

Additive Manufactured Biodegradable and Biocompatible Polymeric Nanocomposite Scaffolds for Bone Tissue Engineering Applications

by

Pedram Karimipour Fard

A thesis submitted to the
School of Graduate and Postdoctoral Studies in partial
fulfillment of the requirements for the degree of

Doctor of Philosophy in Mechanical Engineering

Department of Mechanical and Manufacturing Engineering

Faculty of Engineering and Applied Science

University of Ontario Institute of Technology (Ontario Tech University)

Oshawa, Ontario, Canada

August 2021

© [Pedram Karimipour Fard](#), 2021

THESIS EXAMINATION INFORMATION

Submitted by: **Pedram Karimipour Fard**

Doctor of Philosophy in Mechanical engineering

Thesis title:

Additive Manufactured Biodegradable and Biocompatible Polymeric Nanocomposite Scaffolds for Bone Tissue Engineering Applications

An oral defense of this thesis took place on August 17, 2021 in front of the following examining committee:

Examining Committee:

Chair of Examining Committee	Dr. Vijay Sood
Research Supervisor	Dr. Ghaus Rizvi
Research Co-supervisor	Dr. Remon Pop-Iliev
Examining Committee Member	Dr. Amirkianoosh Kiani
Examining Committee Member	Dr. Sayyed Ali Hosseini
University Examiner	Dr. Scott Nokleby
External Examiner	Dr. Siu Ning Leung, York University

The above committee determined that the thesis is acceptable in form and content and that a satisfactory knowledge of the field covered by the thesis was demonstrated by the candidate during an oral examination. A signed copy of the Certificate of Approval is available from the School of Graduate and Postdoctoral Studies.

ABSTRACT

In this thesis, the focus is on using the fused deposition modeling (FDM) method to manufacture functional biodegradable nanocomposite Polymeric Bone Tissue Scaffolds (PBTs). PBTs are complex products, which have attracted significant attention in the literature in recent decades. In this study, a commercial and user-friendly FDM manufacturing technique was used to fabricate Polycaprolactone (PCL)/Nano-Hydroxyapatite (nHA)/Chitin-Nano-Whisker (CNW) nanocomposite scaffolds with advanced geometrical designs. The fabricated scaffolds were developed to have functional mechanical, biological, and biodegradation properties. Multiple stages of experimental, numerical, and analytical analyses were performed to achieve these goals.

The scaffolds were manufactured in Triply Periodic Minimal Surfaces (TPMS) designs. The impacts of the advanced biomimetic designs, porosity, and biodegradation on the mechanical and morphological properties of the scaffolds were investigated. The nanocomposite filaments for the FDM method were produced using green manufacturing methods. The manufactured novel FDM filaments were characterized using Thermo-Gravimetric Analysis (TGA) and Fourier Transform Infrared Spectroscopy (FTIR) to ensure the precision of the nanocomposite contents. The FDM processing conditions of the novel nanocomposite filaments were optimized using Taguchi's orthogonal array experimental design method to achieve the optimal mechanical properties and structural integrity. The 3D printed nanocomposite bone tissue scaffolds were characterized to assess their mechanical and biological properties. The biodegradation rates of the 3D printed Gyroid-designed nanocomposite PBTs were estimated in sixty weeks of biodegradation, employing numerical, and experimental results. Machine learning methods were used to connect the independent experimental and numerical results and extract objective functions to model properties of the 3D printed nanocomposite PBTs. Multi-objective optimization was performed to propose non-dominated optimal options for the PBTs porosity and the nanocomposite fillers percentages.

The results indicated that the proposed green manufacturing method successfully fabricated the nanocomposite FDM filaments with high precision. The FDM printed PCL/nHA/CNW nanocomposite PBTs with Gyroid structure have high mechanical properties in the practical range of bone tissue scaffolds, enhance cell proliferation and attachment to the scaffolds and biodegrade in the practical period for PBTs. The multi-objective optimization method presents a few significant non-dominated optimal options, which can be selected based on the consumer's priorities.

Keywords: Bone tissue scaffold; Nanocomposite; Additive manufacturing; Chitin-Nano-Whisker; Triply Periodic Minimal Surfaces

AUTHOR'S DECLARATION

I hereby declare that this thesis consists of original work of which I have authored. This is a true copy of the thesis, including any required final revisions, as accepted by my examiners.

I authorize the University of Ontario Institute of Technology (Ontario Tech University) to lend this thesis to other institutions or individuals for the purpose of scholarly research. I further authorize University of Ontario Institute of Technology (Ontario Tech University) to reproduce this thesis by photocopying or by other means, in total or in part, at the request of other institutions or individuals for the purpose of scholarly research. I understand that my thesis will be made electronically available to the public.

Pedram Karimipour Fard

STATEMENT OF CONTRIBUTIONS

Parts of this thesis have been published or are under publication process as follow:

- P. Karimipour-Fard, M. P. Jeffrey, H. Jones-Taggart, R. Pop-Iliev, G. Rizvi (2021) "Development, Processing and Characterization of Polycaprolactone/Nano-Hydroxyapatite/Chitin-Nano-Whisker Nanocomposite Filaments for Additive Manufacturing of Bone Tissue Scaffolds", *Journal of the Mechanical Behavior of Biomedical Materials*, volume 120, 104583.
- P. Karimipour-Fard, R. Pop-Iliev, G. Rizvi (2021) "Design and analysis of triply periodic minimal surface structures produced by additive manufacturing for biomedical applications", 36th International Conference of the Polymer Processing Society – PPS-36 (Accepted).
- P. Karimipour-Fard, H. Jones-Taggart, R. Pop-Iliev, G. Rizvi (2021) "Characterization of novel Polycaprolactone/Nano-Hydroxyapatite/Chitin-Nano-Whisker composites for FDM filaments in biomedical applications", 36th International Conference of the Polymer Processing Society – PPS-36 (Accepted).
- P. Karimipour-Fard, R. Pop-Iliev, G. Rizvi (2021) "Biodegradation assessment of 3D printed Polycaprolactone/Nano-Hydroxyapatite/Chitin-Nano-Whisker nanocomposites", 36th International Conference of the Polymer Processing Society – PPS-36 (Accepted).
- P. Karimipour-Fard, A. Asilian Bidgoli, S. Rahnamayan, R. Pop-Iliev, G. Rizvi (2021) " Meta-modeling based multi-objective optimization of 3D printed Polycaprolactone/Nano-Hydroxyapatite/Chitin-Nano-Whisker nanocomposite bone tissue scaffolds", 36th International Conference of the Polymer Processing Society – PPS-36 (Accepted).
- P. Karimipour-Fard, A.H. Behraves, H. Jones-Taggart, R. Pop-Iliev, G. Rizvi (2020) "Effects of design, porosity and biodegradation on mechanical and morphological properties of additive-manufactured triply periodic minimal surface scaffolds", *Journal of the Mechanical Behavior of Biomedical Materials*, volume 112, 104064.
- P. Karimipour-Fard, R. Pop-Iliev, H. Jones-Taggart, G. Rizvi (2020) "Design of 3D scaffold geometries for optimal biodegradation of poly (lactic acid)-based bone tissue", 35th International Conference of the Polymer Processing Society (PPS-35), *AIP Conference Proceedings*, 2205 (1) 020062.

The following manuscripts resulted from the works and experimentations that were carried out to enhance my understanding of the characterization techniques:

- P. Karimipour-Fard, I. Naeem, A. Mohany, R. Pop-Iliev, G. Rizvi (2020) "Enhancing the Accuracy and Efficiency of Characterizing Polymeric Cellular Structures Using 3D-based Computed Tomography", *Journal of Cellular Plastics*. (Accepted; published online, DOI: 10.1177/0021955X20948556).

- R. Pop-Iliev, W. Y. Pao, P. Karimipour-Fard, and G. Rizvi (2018) "Visualization and Morphological Characterization of Integral Skin Cellular Polymeric Composites Using X-ray Microtomography", *Radiation and Applications* 3 (2), 143-146.
- P. Karimipour-Fard, W. Y. Pao, R. Pop-Iliev, G. Rizvi (2018) "3D Characterization and Mechanical Analysis of Polyethylene Foams Processed in Rapid Rotational Foam Molding", *Annual Technical Conference - ANTEC, Conference Proceedings (Vol. 2018-May)*. Society of Plastics Engineers.
- P. Karimipour-Fard, W. Y. Pao, G. Rizvi, R. Pop-Iliev (2018) "The Use of Microcomputed Tomography to Evaluate Integral Cellular Polyolefin Composites", *Abstract Book; Unilever Res Dev Netherlands: Vlaardingen, The Netherlands, Micro-CT User Meeting 2018*.

I performed the majority of the design, manufacturing, material and mechanical characterizations, and writing of the manuscript.

ACKNOWLEDGEMENTS

First of all, I would like to thank my mother for giving me all the strength in my life. I lost her in the first year of my Ph.D. studies, but her memories, encouragement, and the values she taught me through my lifetime, helped me to withstand all of the obstacles and try my best to make her be proud of me. I dedicate this thesis to her memory, my lovely mother, Shahin Mahmoudi. Also, I want to say thanks to my brother, father, and aunt for their support.

Secondly, I would like to thank my supervisors, Prof. Ghaus Rizvi and Prof. Remon Pop-Iliev, for their constant help, guidance and for providing me the essential requirements to make writing and finishing this thesis possible.

Thirdly, I exclusively grateful to Dr. Holly Jones-Taggart for her significant help and contribution to this thesis. I really appreciate the assistance in granting me access to her research lab for more than two years, helping me with the cell-based assays, and contributing to my published articles.

Next, I want to say thanks to Ms. Anita Nutikka, the laboratory technician of the biology department, for granting us access to their florescent microscopes and the technical assistance while performing the tests. Also, I am thankful to my great friend, Mohamed Nasser, for all his helps and support. In addition, I am grateful to Dr. Azam Asilian Bidgoli for her help and guidance in applying the machine learning and multi-objective optimization methods.

We are also grateful to NSERC's Discovery Grant, NSERC's Discovery Development Grant, and NSERC's Chairs in Design Engineering Program for the financial support of

this research. In addition, we are grateful to BOCO Bio-Nanotechnologies Inc. for providing the Chitin-Nano-Whisker (CNW).

TABLE OF CONTENTS

Thesis Examination Information	ii
Abstract	iii
Authors Declaration	iv
Statement of Contributions	v
Acknowledgements	vii
Table of Contents	ix
List of Tables	xiii
List of Figures.....	xv
List of Abbreviations and Symbols	xxi
Chapter 1 Introduction	1
1.1 Motivations for research and principal research objectives	1
1.2 Summary of thesis contributions	5
1.3 Thesis outline	6
Chapter 2 Background and literature review	8
2.1 The research field focusing on Bone tissue scaffolds	8
2.1.1 Bone tissue	8
2.1.2 Bone disease and conventional therapies for damaged bone tissue	9
2.1.3 Bone tissue scaffold	11
2.1.3.1 Morphological properties	12
2.1.3.2 Materials and manufacturing	13
2.1.3.3 Mechanical properties	17
2.2 Additive manufacturing	19
2.2.1 Selective laser sintering (SLS)	21
2.2.2 Stereolithography (SLA)	22

2.2.3 Fused deposition modeling (FDM)	23
2.2.4 Comparison among the typical commercial AM methods	24
2.2.5 FDM application in 3D printing of composite filaments	26
2.3 PCL/nHA/CNW nanocomposites material selection for the development of novel FDM filaments	29
2.4 Triply Periodic Minimal Surfaces design of bone tissue scaffolds	32
Chapter 3 Manufacturing and analytical methods	36
3.1 Triply Periodic Minimal Surfaces designed scaffolds	36
3.1.1 Manufacturing	37
3.1.2 3D design of Triply Periodic Minimal Surfaces scaffolds	37
3.2 Green manufacturing of the PCL/nHA/CNW nanocomposite FDM filaments	39
3.2.1 Materials	39
3.2.2 Green manufacturing of the FDM filaments	39
3.2.2.1 Stage one: distribution of the nanofillers in the PCL matrix using green solvents	40
3.2.2.2 Stage two and three: extrusion	41
3.2.3 The composition of final nanocomposite filaments	41
3.3 Optimized 3D printing of the nanocomposites using the Taguchi method	43
3.4 Simulation and prediction of long-term biodegradation rate	46
3.4.1 Introduction	46
3.4.2 Hydrolysis of polyesters	48
3.4.3 Mathematical equations	50
3.4.4 3D design and meshing	51
3.4.5 Partial Differential Equation inputs and boundary conditions	52
3.5 Machine learning and Multi-objective optimization	53
3.5.1 Meta-modeling using genetic programming	54
3.5.1.1 Introduction	54
3.5.1.2 Meta-modeling definitions and assumptions	57
3.5.2 Multi-objective optimization	62

Chapter 4 Characterization methods	65
4.1 Effect and impact of design, porosity and biodegradation on the mechanical and morphological properties of the scaffolds	65
4.1.1 Mechanical testing	66
4.1.2 Biodegradation impact assessment	67
4.2 Material characterization	67
4.2.1 Thermo-Gravimetric Analysis (TGA)	67
4.2.2 Fourier Transform Infrared Spectroscopy (FTIR)	68
4.3 Mechanical properties of the 3D printed nanocomposite Polymeric Bone Tissue Scaffolds	68
4.4 Biological properties of the 3D printed nanocomposite Polymeric Bone Tissue Scaffolds	69
4.4.1 MTT assay	70
4.4.2 Fluorescent microscopy	72
4.4.3 Biodegradation and acidity analysis	74
Chapter 5 Results and discussions	75
5.1 Investigation of the effects of design, porosity and biodegradation on the mechanical and morphological properties of the scaffolds	76
5.1.1 Impact of design, porosity and biodegradation on the mechanical properties	76
5.1.1.1 Impact of porosity and design on the mechanical properties	76
5.1.1.2 Effect of biodegradation on the mechanical properties	79
5.1.1.3 Fracture pattern of the scaffolds	81
5.1.2 Impact of design, porosity and biodegradation on the morphological properties	82
5.1.2.1 Impact of the design porosity on the morphological properties	83
5.1.2.2 Effect of compression loading on the morphological properties	85
5.1.2.3 Impact of biodegradation on the morphological properties	88
5.2 Material characterization of the nanocomposite FDM filaments	91
5.2.1 Thermo-Gravimetric Analysis (TGA) results	91

5.2.2 Fourier Transform Infrared Spectroscopy (FTIR) results	96
5.3 Optimization of the 3D printing processing conditions for FDM filaments	97
5.4 Mechanical properties of the 3D printed nanocomposite Polymeric Bone Tissue Scaffolds	109
5.5 Biological properties of the manufactured 3D printed nanocomposite PBTSS	114
5.5.1 Cell proliferation and attachment	115
5.5.2 Biodegradation	121
5.6 Biodegradation rate estimation in the long term	123
5.6.1 Mesh Sensitivity Analysis	123
5.6.2 Validation of the numerical results	125
5.6.3 Impact of 3D printing structure on the average normalized molecular weight variations	126
5.6.4 Mass loss prediction (biodegradation percentage) of the FDM printed Gyroid scaffolds	130
5.6.5 Mass loss prediction (biodegradation percentage) of the FDM printed nanocomposite Polymeric Bone Tissue Scaffolds	132
5.7 Meta-modeling and Multi-objective optimization	137
5.7.1 Meta-modeling	137
5.7.2 Multi-objective optimization	144
Chapter 6 Conclusions and suggestions for future work	150
References	157

LIST OF TABLES

CHAPTER 2

Table 2.1. Conventional therapies for damaged bone tissue	11
Table 2.2. Typical ceramics and glasses materials for bone tissue scaffolds	14
Table 2.3. Trending natural and synthetic polymers for bone tissue scaffolds	14
Table 2.4. The literature review on polymeric, ceramic, and polymer/ceramic composite materials for bone tissue scaffolds	15
Table 2.5. Mechanical properties of cortical bone	18
Table 2.6. Mechanical properties of trabecular bone	18
Table 2.7. The effect of the testing method on the reported mechanical properties of bone tissue	18
Table 2.8. The effect of age on mechanical properties of bone	18
Table 2.9. AM techniques for polymers classified by ISO/ASTM 52900 – 15	20

CHAPTER 3

Table 3.1. Manufactured nanocomposite FDM filaments	42
Table 3.2. Taguchi L9 (four parameters with three levels)	44
Table 3.3. The Taguchi orthogonal array proposed experiments	45
Table 3.4. The filament-based designs for numerical simulations	52

CHAPTER 5

Table 5.1. Mechanical properties of the TPMS scaffolds (ASTM D1621-16)	77
Table 5.2. Mechanical properties of the TPMS scaffolds after biodegradation (ASTM D1621-16)	80
Table 5.3. Morphological properties of the TPMS scaffolds after biodegradation	91
Table 5.4. The responses of the Taguchi orthogonal array proposed experiments	98
Table 5.5. Layer thickness response analyses	101
Table 5.6. Structural integrity response analyses	105

Table 5.7. Compressive strength response analyses	105
Table 5.8. The defined parameters of the numerical analysis	107
Table 5.9. Optimal FDM printing processing conditions	108
Table 5.10. Mechanical properties of the manufactured 3D printed nanocomposite PBTSs	110
Table 5.11. pH level of the media after biodegradation of the nanocomposites	123
Table 5.12. Number of elements for each meshing networks of the mesh sensitivity analysis	124
Table 5.13. Non-dominated optimal options presented by the NSGA-III multi-objective optimization technique for the PCL/nHA/CNW 3D printed nanocomposite PBTSs	147

LIST OF FIGURES

CHAPTER 2

Figure 2.1. Bone structure	9
Figure 2.2. AM processing steps	21
Figure 2.3. Selective Laser Sintering (SLS)	22
Figure 2.4. Stereolithography (SLA)	23
Figure 2.5. Fused Deposition Modeling (FDM)	24
Figure 2.6. A few examples of the Triply Periodic Minimal Surface (TPMS) designs	33

CHAPTER 3

Figure 3.1. Gyroid structure with 60% porosity compared to a one-dollar coin	38
Figure 3.2. TPMS scaffold designs in this study	38
Figure 3.3. The manufactured nanocomposite FDM filaments	42
Figure 3.4. Parameters and their defined levels in the Design-Expert software for the Taguchi design	45
Figure 3.5. Hydrolysis process of polyesters (PLA as an example)	49
Figure 3.6. 3D designed Gyroid scaffold for numerical simulations	52
Figure 3.7. Tree-based representation of GP expressions for an example function	56
Figure 3.8. Parent and offspring expressions created by crossover operation. Parent 1: $\Pi * \tan$; parent 2: $a * r^2$; offspring 1: $\Pi * r^2$; offspring 2: $a * \tan$	56
Figure 3.9. Mutation: before mutation, the function is $10x \tan(2x+3)$, and after mutation, it transforms to $10x / \tan(2x+3)$	57
Figure 3.10. The initial population to extract the f_1 function using the meta-modeling ..	59
Figure 3.11. The initial population to extract the f_2 function using the meta-modeling ..	59
Figure 3.12. The initial population to extract the f_3 function using the meta-modeling ..	60
Figure 3.13. The initial population to extract the f_4 function using the meta-modeling ..	60
Figure 3.14. The initial population to extract the f_5 function using the meta-modeling ..	61
Figure 3.15. The initial population to extract the f_6 function using the meta-modeling ..	61

Figure 3.16. Flowchart of the NSGA-III optimization algorithm	63
---	----

CHAPTER 4

Figure 4.1. Examples of the five mechanical testing specimens (PCL) as required by the ASTM D1621-16 (the circles around the samples are the build plate adhesions)	69
Figure 4.2. 96-well plates prepared for MTT assays	71
Figure 4.3. MTT-assay 96-well plates inside the incubator	71
Figure 4.4. The manufactured chamber slides for cell culture on top of the scaffolds	73
Figure 4.5. Fixed FDM printed nanocomposite scaffold on the manufactured chamber slides	73
Figure 4.6. Chamber slides inside the CO ₂ incubator	74

CHAPTER 5

Figure 5.1. Representative stress-strain curves of the TPMS scaffolds	78
Figure 5.2. Representative stress-strain curve of the Schwarz-D 80% scaffolds	78
Figure 5.3. Representative of Stress-Strain curves of the TPMS scaffolds after biodegradation	80
Figure 5.4. Representative of Stress-Strain curves of the Gyroid 60% scaffolds before and after biodegradation	81
Figure 5.5. Pictures of the failed TPMS structures under compression load before degradation (BD) and after degradation (a: G60 and G60-AD; b: G80 and G80-AD; c: S60 and S60-AD; d: S80 and S80-AD)	82
Figure 5.6. Trabecular thickness distribution of the TPMS scaffolds with different porosities (a: Gyroid; b: Schwarz-D)	84
Figure 5.7. Internal structure of the Gyroid 80% under compression before biodegradation (a: G80 at 0% strain; b: G80 at 5% strain; c: G80 at 10% strain)	85
Figure 5.8. Internal structure of the Gyroid 80% under compression after biodegradation (a: G80-AD6 at 0% strain; b: G80-AD6 at 3% strain)	86
Figure 5.9. Trabecular thickness distribution of the TPMS scaffolds in 0%, 5% and 10% strains (a: G60; b: G80; c: S60; d: S80)	87
Figure 5.10. Trabecular thickness distribution of the TPMS scaffolds after biodegradation in 0% and 3% strains (a: G60-AD6; b: G80-AD6; c: S60-AD6)	88

Figure 5.11. Trabecular thickness distribution of the TPMS scaffolds before and after biodegradation (a: G60 and G60-AD6; b: G80 and G80-AD6; c: S60 and S60-AD6; d: S80 and S80-AD6)	90
Figure 5.12. TGA results of PCL and CNW	92
Figure 5.13. TGA results of the PCL/CNW nanocomposites compared to PCL	93
Figure 5.14. TGA results of the PCL/nHA nanocomposites compared to PCL	94
Figure 5.15. TGA results of the PCL/nHA/CNW nanocomposites compared to PCL	95
Figure 5.16. FTIR spectra of CNW (black), PCL (red), nHA (blue), P-CNW3 (green), P-nHA3 (purple), and P-nHA1-CNW2 (yellow), nanocomposite filaments	97
Figure 5.17. Half-Normal plot of the processing parameters impacts on the layer thickness	99
Figure 5.18. Half-Normal plot of the processing parameters impacts on the layer thickness; 1st step of selecting the effective parameters	99
Figure 5.19. Half-Normal plot of the processing parameters impacts on the layer thickness; 2nd step of selecting the effective parameters	100
Figure 5.20. Half-Normal plot of the processing parameters impacts on the layer thickness; 3rd step of selecting the effective parameters	100
Figure 5.21. Half-Normal plot of the processing parameters impacts on the structural integrity	102
Figure 5.22. Half-Normal plot of the processing parameters impacts on the structural integrity; 1st step of selecting the effective parameters	102
Figure 5.23. Half-Normal plot of the processing parameters impacts on the structural integrity; 2nd step of selecting the effective parameters	103
Figure 5.24. Half-Normal plot of the processing parameters impacts on the compressive strength	103
Figure 5.25. Half-Normal plot of the processing parameters impacts on the compressive strength; 1st step of selecting the effective parameters	104
Figure 5.26. Half-Normal plot of the processing parameters impacts on the compressive strength; 2nd step of selecting the effective parameters	104
Figure 5.27. Setting the optimal target for numerical analyses of the layer thickness	106
Figure 5.28. Setting the optimal target for numerical analyses of the structural integrity	106

Figure 5.29. Setting the optimal target for numerical analyses of the compressive strength	107
Figure 5.30. Interaction of critical design factors in the limits of the optimal processing condition	108
Figure 5.31. Average compressive strength (MPa) of 3D printed nanocomposite PBTSSs with nHA or CNW nanofillers, including statistical analysis (statistically significant: P-value ≤ 0.05). * stands for not statistically significant and ** for significant.	110
Figure 5.32. Stress-strain curves of the 3D printed nanocomposite PBTSSs with nHA nanofiller	111
Figure 5.33. Stress-strain curves of the 3D printed nanocomposite PBTSSs with CNW nanofiller	112
Figure 5.34. Average compressive strength (MPa) of 3D printed nanocomposite PBTSSs with nHA/CNW nanofillers, including statistical analysis (statistically significant: P-value ≤ 0.05). * stands for not statistically significant and ** for significant.	113
Figure 5.35. Stress-strain curves of the manufactured 3D printed nanocomposite PBTSSs	114
Figure 5.36. Cell viability results after 1, 3, and 7 days of MC3T3-E1 cells culture on the 3D printed nanocomposite PBTSSs	115
Figure 5.37. Cell viability results after seven days of cell culture on the 3D printed nanocomposite PBTSSs including statistical analysis. * stands for not statistically significant and ** for significant.	116
Figure 5.38. Nuclei and actin filaments of MC3T3-E1 cells growing on top of the 3D printed nanocomposite PBTSSs	118
Figure 5.39. Nuclei of MC3T3-E1 cells (fluorescent microscopy results of DAPI staining) after 1, 3, and 7 days of cell culture on the 3D printed nanocomposite PBTSSs	119
Figure 5.40. Actin filaments of MC3T3-E1 cells (fluorescent microscopy results of Phalloidin CF@640R staining) after 1, 3, and 7 days of cell culture on the 3D printed nanocomposite PBTSSs	120
Figure 5.41. Biodegradation rates of the manufactured nanocomposites after 7, 14, and 28 days	122
Figure 5.42. Biodegradation rate of the nanocomposites after 28 days, including statistical analysis. * stands for not statistically significant and ** for significant.	122
Figure 5.43. The defined meshing systems of the mesh sensitivity analysis	124

Figure 5.44. Normalized molecular weight variations in a 10-week period of biodegradation for meshing networks of the mesh sensitivity analysis	125
Figure 5.45. Comparison of simulation results in this study with the experimental data presented by Grizzi et al.	126
Figure 5.46. Normalized molecular weight variations for a 3D printed and a solid cube	128
Figure 5.47. The designs with the repeating overlapped extruded shape units	128
Figure 5.48. Normalized molecular weight variation of the designs with repeating overlapped extruded shape units	129
Figure 5.49. Normalized molecular weight variations of the 3D printed Gyroid structures in 70 weeks of biodegradation	129
Figure 5.50. Mass loss trends due to internal and surface erosion over time	131
Figure 5.51. Mass loss estimation of the FDM Gyroid scaffolds over time	132
Figure 5.52. Estimation of the slope of surface erosion biodegradation and the critical point of the internal erosion initiation, using the experimental results	133
Figure 5.53. Estimated biodegradation rate of the 3D printed nanocomposite PBTs with nHA nanofiller over 60 weeks	134
Figure 5.54. Estimated biodegradation rate of the 3D printed nanocomposite PBTs with CNW nanofiller over 60 weeks	135
Figure 5.55. Estimated biodegradation rate of the 3D printed nanocomposite PBTs with hybrid nHA/CNW nanofillers over 60 weeks	136
Figure 5.56. Compressive strength of the 3D printed nanocomposite PBTs for 70% porosity Gyroid design	139
Figure 5.57. Average apparent modulus of the 3D printed nanocomposite PBTs for 70% porosity Gyroid design	140
Figure 5.58. Compressive strength after four months of biodegradation of the 3D printed nanocomposite PBTs for 70% porosity Gyroid design	141
Figure 5.59. Average apparent modulus after four months of biodegradation of the 3D printed nanocomposite PBTs for 70% porosity Gyroid design	142
Figure 5.60. Biodegradation percentage of the 3D printed nanocomposite PBTs after six months for 70% porosity Gyroid design	143
Figure 5.61. Cell proliferation of the 3D printed nanocomposite PBTs for 70% porosity Gyroid design	144

Figure 5.62. Non-dominated optimal options presented by the NSGA-III multi-objective optimization technique for compressive strength, average apparent modulus, cell proliferation, and biodegradation after six months 146

Figure 5.63. Non-dominated optimal options presented by the NSGA-III multi-objective optimization technique for compressive strength and average apparent modulus after four months of biodegradation, cell proliferation, and biodegradation after six months 147

LIST OF ABBREVIATIONS AND SYMBOLS

AM	Additive manufacturing
AD	After degradation
AD4	After 4 months of degradation
AD6	After 6 months of degradation
ABS	Acrylonitrile butadiene styrene
BMIMCl	1-butyl-3-methylimidazolium chloride
BTE	Bone tissue engineering
CAD	Computer-aided design
CNW	Chitin-Nano-Whisker
CF	Carbon fiber
CW	Chitin Whisker
CFD	Computational fluid dynamics
C_e	Concentration of ester bonds
C_{H^+}	Concentration of H^+
C_{ol}	Mole concentration of dissolvable small molecules
C_{e0}	Initial mole concentration of ester bonds of the polymer chain
C_{o10}	Concentration of residual monomers
DoE	Design of Experiment
Dev	Deviation
DL-PLGA	Poly(d,l-lactide:glycolide)
D	Diffusion coefficient of small molecules
$D_{polymer}$	Diffusion coefficients of the small molecules in the non-degraded polymer
D_{pore}	Diffusion coefficients of the small molecules in the liquid-filled pores
DLP	Digital light processing
d_a	Damping coefficient
ECM	extracellular matrix

e_a	Mass coefficient
FDM	Fused deposition modeling
f	Source term
FTIR	Fourier Transform Infrared Spectroscopy
f_1	Mathematical function for compressive strength
f_2	Mathematical function for average apparent modulus
f_3	Mathematical function for compressive strength after four months of biodegradation
f_4	Mathematical function for average apparent modulus after four months of biodegradation
f_5	Mathematical function for biodegradation percentage after six months
f_6	Mathematical function for cell proliferation
GnP	Graphene nanoplatelets
GP	Genetic programming
G60	Gyroid design with 60% porosity
G80	Gyroid design with 80% porosity
k_1	Rate of non-catalytic hydrolysis reaction
k_1'	Reaction constant
k_2	Rate of autocatalytic hydrolysis reaction
LDPE	Low-density polyethylene
Mn	Averaged molecular weight
M_{n0}	Initial averaged molecular weight
M_0	Molecular weight of a single repeating unit of the polymer
m	Average degree of polymerization of the small molecules
ME	Material extrusion
MWCNT	Multi-walled carbon nanotube
Micro-CT	Microcomputed tomography
nHA	Nano-Hydroxyapatite
n	Exponent for acid dissociation

N_{dp0}	The ratio of initial averaged molecular weight by molecular weight of a single repeating unit of the polymer
NSGA-III	Non-dominated Sorting Genetic Algorithm III
N60	Neovius design with 60% porosity
N80	Neovius design with 80% porosity
OD	Optical density
PDE	Partial differential equation
PCL	Polycaprolactone
PBTS	Polymeric bone tissue scaffold
PLA	Polylactic acid
PBF	Powder bed fusion
PEEK	Reinforced polyetheretherketone
PP	Polypropylene
PEA	Polyester amide
PBS	Phosphate buffer saline
R_s	Total number of chain scissions of the ester bonds per unit volume
SLS	Selective laser sintering
SLA	Stereolithography
SLM	Selective laser melting
S60	Schwarz-D design with 60% porosity
S80	Schwarz-D design with 80% porosity
St	Standard
TPMS	Triply Periodic Minimal Surfaces
TGA	Thermo-gravimetric Analysis
TE	Tissue engineering
TPU	Thermoplastic polyurethane
TCP	Tricalcium phosphate
VPP	Vat photopolymerization

V_{pore}	Porosity of the polymer caused by the loss of the small molecules
X_1	Percentage of nHA nanofiller
X_2	Percentage of CNW nanofiller
X_3	Porosity percentage of the Gyroid structural design
α	Empirical parameter of the production rate of the small molecules by chain scission
β -TCP	β -tricalcium phosphate
β	Empirical parameters of the production rate of the small molecules by chain scission
Ω	Computational domain
$\partial\Omega$	Domain boundaries
Γ	Conservative flux vector

Chapter 1. Introduction

Bone diseases are currently estimated to be a significant public health threat for almost 1.4 million Canadians and 44 million U.S. citizens aged 50 and older. For example, as a major bone disease, osteoporosis caused almost nine million new bone fractures worldwide in the year 2000, and it has been estimated that more than 200 million people are suffering from osteoporosis. Every year thousands of bone grafting surgeries are performed worldwide to treat bone defects and diseases [1-4]. In recent decades, tissue engineering (TE) is advancing significantly to replace the conventional approaches for restoring and repairing damaged bone tissue. Bone tissue scaffolds prepare a suitable environment for native tissue to grow and shape the extracellular matrix (ECM). Bone tissue scaffolds have to acquire specific properties to meet the bone cell regeneration requirements and be practical products. The morphological, mechanical, biodegradation, and biological properties are the key factors to develop and manufacture a practical product. Polymeric bone tissue scaffolds (PBTS) are significantly pursued in recent decades as a response to address all of the required standards of the practical bone tissue scaffolds. This study focuses on developing, processing, and characterizing biodegradable PBTSs with novel nanocomposites and advanced geometrical designs using the fused deposition modeling (FDM) manufacturing method.

1.1 Motivations for Research and Principal Research Objective

Bone Tissue Engineering (BTE) is a very active interdisciplinary scientific research area within the Tissue Engineering (TE) field, which addresses a global health threat by focusing on developing bone regeneration processes that result in functional biological

substitutes that can restore, maintain, improve or entirely replace the biological functions of the damaged bones. Biodegradable polymeric bone tissue scaffolds (PBTS) research field is one of the most active areas of BTE, which is advancing parallel to other techniques and sciences in the BTE knowledge. As the research field on PBTSs continues to advance in many directions, as indicated in the open research literature, further advancement of the bone scaffold properties and the improvement of the current state-of-the-art in this specific field were the principal motivations for undertaking this research study.

The principal objective of the research presented in this thesis was to develop and introduce novel nanocomposite filaments as building materials into the additive manufacturing to fabricate biodegradable biocompatible PBTSs with advanced material compositions and geometrical designs, to achieve products with functional mechanical, biological, and biodegradation properties and add more information to the current state of the art. Biodegradable PBTSs have a few critical requirements that have to be satisfied to manufacture a practical product. Manufacturing techniques and the material composition of the products are under improvement in the literature to develop products with higher mechanical, biological, and biodegradation qualities. Many conventional manufacturing techniques cannot fabricate advanced 3D-designed PBTS or lack practical material selection opportunities. These two challenges have to be addressed in order to produce practical PBTSs. The scaffolds have to be designed and manufactured in advanced biomimetic structures with novel nanocomposites to respond to the products' biodegradation, biological, and mechanical requirements.

FDM manufacturing is a commercial and user-friendly desktop 3D printer with fast prototyping capabilities. The accessibility of this manufacturing technique brings up the

opportunity of improving the properties of its products to fit the standards of bone tissue scaffolds. The FDM technique can fabricate parts with advanced 3D designs and operate with a wide range of materials. Improvement in the FDM filament's material compositions can enhance this manufacturing method's application for biomedical products. The manufacturing techniques of the biocomposites for bone tissue scaffolds are time-consuming and expensive; thus, having a commercially available manufacturing technique can have financial efficacy implications as well.

After choosing the manufacturing technique, the material composition of the products for tissue scaffolds needs significant attention, and always there are opportunities to improve the current state of the art. The final products have to be biodegradable and biocompatible PBTs, which can be 3D printed in advanced biomimetic geometries using the FDM technique. Based on the product definition, literature review, and the manufacturing technique, novel nanocomposites have to be introduced to satisfy these requirements. Therefore, Polycaprolactone (PCL)/Nano-Hydroxyapatite (nHA)/Chitin-Nano-Whisker (CNW) nanocomposites were introduced as the composition of PBTs in this study. The FDM filaments were manufactured with these compositions and were 3D printed to fabricate the final product.

Another challenge to overcome was the manufacturing of the FDM filaments with the mentioned composition. In general, for blending nanofillers with a polymeric matrix, solvents are needed, and the majority of the solvents for practical polyesters like Polylactic acid (PLA) and PCL are highly toxic. Also, the solubility of Chitin-Nano-Whisker and evenly dispersion of its nanoparticles in the polymeric matrix using the conventional methods were not feasible for practical percentages. A green manufacturing technique

using ionic solvents was employed to overcome these challenges in this study. Using ionic solvents that are commonly referred to as green solvents with excellent temperature stability, made the precise manufacturing of the FDM filaments possible. After manufacturing the nanocomposite filaments, to enhance the 3D printed bone tissue scaffolds' properties, the FDM processing conditions of the nanocomposites were optimized using Taguchi's orthogonal array experimental design method.

In parallel to introducing a new material composition for FDM-based PBTSSs, the 3D mechanical design of the products was considered to improve the quality of the products. The 3D design of the scaffolds has a significant and direct impact on cell proliferation, biodegradation, and mechanical properties of the scaffolds. In this study, a few Triply Periodic Minimal Surfaces (TPMS) designs with different porosities were manufactured, and the critical effects of the design on the properties of the PBTSSs were assessed. Based on the assessments in this part of the research, the Gyroid design was selected as the primary option for the design of the PBTSSs. One of the significant contributions of the current work to the literature was the experimental assessment of the long-term biodegradation impact on the mechanical properties of the TPMS designed PBTSSs.

Although the presented research is mainly an experimental study, numerical simulation was added to estimate and predict the biodegrading percentage of the bone tissue scaffolds in extended periods. The prediction of the exact biodegradation rate for the nanocomposites with advanced geometries is not practically feasible, but employing hybrid techniques can provide an educated estimation. Although the prediction is based on numerical results, the experimental data and analytical study assisted and directed the simulation results to achieve a more realistic prediction. Another non-experimental component of this study is

using machine learning techniques to connect and relate all of the experimental and simulation data and provide formulations for the critical properties of the manufactured PBTSs in this study. A multi-objective optimization method followed the formulation process to generate a set of non-dominated optimal suggestions for the final products with estimated properties.

1.2 Summary of Thesis Contributions

The novelties and contributions of the current research can be summarized as follows:

- PCL/nHA/CNW nanocomposite FDM filaments for bone tissue scaffolds were introduced, manufactured, and characterized for the first time.
- A green manufacturing method was employed to fabricate the nanocomposite FDM filaments. The employed manufacturing method effectively overcame the significant challenge of distributing Chitin-Nano-Whisker evenly in the polymeric matrix.
- 3D printing of bone tissue scaffolds using PCL/nHA/CNW nanocomposites was performed. The Taguchi orthogonal array method was employed to optimize the FDM 3D printing of the nanocomposites.
- 3D printing and characterization of bone tissue scaffolds with TPMS designs were carried out. The impact of design, porosity, and biodegradation on the scaffolds' mechanical and morphological properties were reported.
- 3D printed nanocomposite scaffolds were characterized to assess their mechanical, biodegradation, and biological properties. A mouse preosteoblast bone cell line was employed to assess cell proliferation and attachment to the scaffolds.

- The long-term biodegradation rate and pattern of the nanocomposite Gyroid 3D printed bone tissue scaffolds were predicted using numerical simulations, and experimental data.
- Meta-modeling (a machine learning technique) was employed to formulate the properties of the PBTs based on the Gyroid design porosity percentage and the nanofiller contents of the nanocomposites. Non-dominated Sorting Genetic Algorithm III (NSGA-III) multi-objective optimization method was employed to propose non-dominated optimal options for the 3D printed nanocomposite PBTs with Gyroid design.

1.3 Thesis Outline

Chapter 2 includes background knowledge and literature review. The general research field of bone tissue scaffolds, additive manufacturing (AM), nanocomposites material selection, and background on the biomimetic geometrical designs were discussed.

Chapter 3 describes the manufacturing processes and analytical methods of this thesis. In details, this chapter describes the design and manufacturing of the scaffolds with TPMS designs, explains the green manufacturing process of the FDM nanocomposite filaments and their optimal 3D printing assessment using the Taguchi method, describes the methods of numerical simulation and prediction of biodegradation rate, and explains the employed machine learning technique and multi-objective optimization method in the last section.

Chapter 4 presents the experimental characterization methods to investigate the properties of the manufactured PBTs. The methods to analyze the impact of design, porosity and

biodegradation on the mechanical and morphological properties of the TPMS scaffolds are described. Material characterization, mechanical testing, and biological properties assessment techniques to analyze the PCL/nHA/CNW nanocomposite PBTs are explained, as well.

Chapter 5 presents the results and discussions. The impact of design, porosity, and biodegradation on the scaffolds' mechanical and morphological properties is assessed. Material characterization results of the novel nanocomposite FDM filaments are reported in detail, and the FDM processing conditions are optimized using the Taguchi method. The mechanical and biological properties of the 3D printed nanocomposite PBTs are investigated and explained. The products' Biodegradation rates are estimated in the long term, based on numerical simulation and analytical assessment results. In the last section of this chapter, meta-modeling and multi-objective optimization results are presented.

Chapter 6 is devoted to discussions and conclusions. Also, a few recommendations for future works are discussed in this chapter.

Chapter 2. Background and Literature Review

2.1 The Research Field Focusing on Bone Tissue Scaffolds

2.1.1 Bone Tissue

Bone is a composite structure of hydroxyapatite ($\text{Ca}_{10}(\text{PO}_4)_6(\text{OH})_2$) crystals deposited within an organic matrix (95% is the type I collagen) [5]. Bone architecture is hierarchical and complex. The bone structure is divided into two main regions, including cancellous (spongy) bone and compact bone. As shown in Figure 2.1, cortical (compact) bone is shaped by a group of Osteons, which are multiple layer collagen fibers. The rest of the structure is a microcellular porous structure that is the spongy bone. The levels of bone hierarchy are shown part by part in Figure 2.1. These hierarchical levels are: (1) the macrostructure: cancellous and cortical bone; (2) the microstructure (from 10 to 500 μm): Haversian systems, osteons, single trabeculae; (3) the sub-microstructure (1–10 μm): lamellae; (4) the nanostructure (from a few hundred nanometers to 1 μm): fibrillar collagen and embedded mineral; and (5) the sub-nanostructure (below a few hundred nanometers): molecular structure of constituent elements, such as mineral, collagen, and non-collagenous organic proteins. This structure is heterogeneous, anisotropic, has an optimized arrangement of components, and is irregular [6].

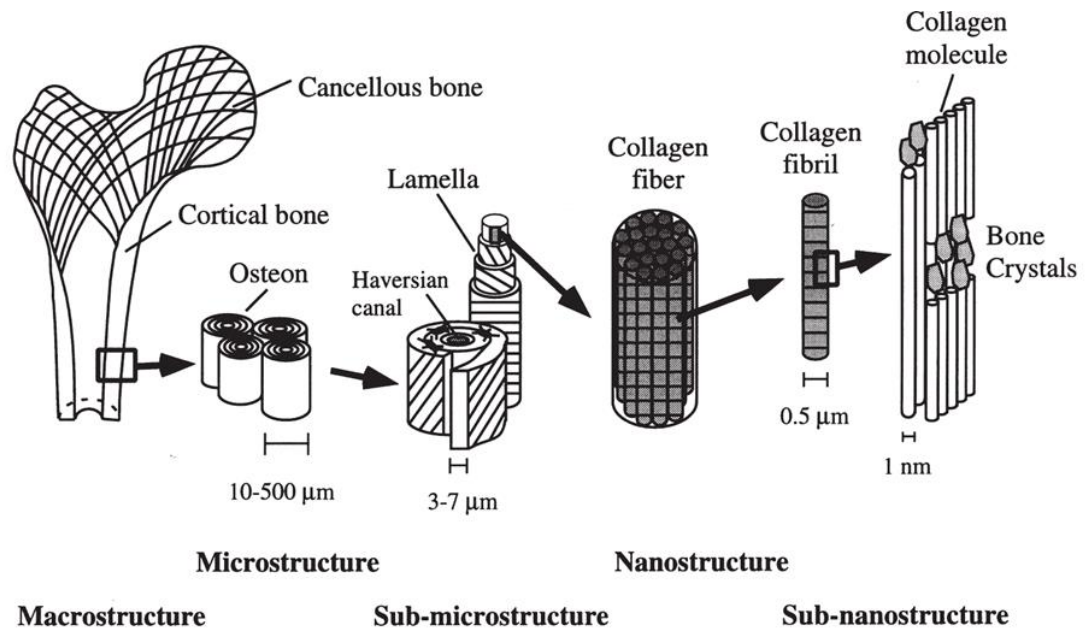


Figure 2.1. Bone structure (Reprinted from Medical Engineering & Physics, Volume 20, Rho et al., Mechanical properties and the hierarchical structure of bone (reference [6]), Pages 92-102., Copyright (1998), with permission from Elsevier)

2.1.2 Bone Disease and Conventional Therapies for Damaged Bone Tissue

Bone diseases include infections, bone tumors, implant revisions, joint fusion, and bone loss by trauma. Conventional techniques for bone regeneration revolve around the natural bone structure and its derivatives. The primary practice is called grafting. Every year more than 500,000 bone grafting surgeries are carried out in the United States and almost 2.2 million worldwide to repair bone defects [1, 2]. It is essential to understand the difference between grafting and implant. Implants do not contain cells, but the grafts contain cells. Grafting can be of three types; autograft, allograft, and xenograft [7, 8].

It is important to understand osteogenesis, osteoinduction, and osteoconduction to compare grafting processes. These processes occur through bone healing and new bone formation after the implantation of a graft. Osteoprogenitor cells live within the donor graft and could

proliferate and differentiate to osteoblasts and eventually to osteocytes. These cells represent the osteogenic potential of the graft. Osteoinduction is the host mesenchymal stem cells activation process that forms osteoblasts. Finally, osteoconduction pronounces the new Haversian systems' generation and shapes blood-vessel into the bone structure [7, 8]. These three definitions characterize a highly effective graft.

Autograft of bone uses the patient tissue as a donor to implant the bone in the same patient. Generally, the iliac crest is used in autografts [9]. Autografts are the gold standard in grafting practice. The first reason is that the autografts satisfy all of the mentioned bone regeneration criteria (processes of osteogenesis, osteoinduction, and osteoconduction). This type of grafting has ideal biological signals for integrating the new bone to the damaged site. On the contrary, Autografts have disadvantages of limitation in donor sites, restrictions in geometry, expensive past processing, and surgery complications [7, 10].

Allograft is the process of harvesting tissue from a healthy human donor and its implantation in a patient. The main benefit of allografts is to eliminate the number of surgeries on the patient. This benefit brings the disadvantage of possible immune response activation in the patient's body as the tissue origin is from another donor. Also, allografts pass through washing, freeze-drying, and a few other processes to decrease the risk of disease transmission and immunological responses, which reduces the osteogenic potential of the allograft [7, 11].

Xenograft is an alternative to autograft and allograft by replacing a human tissue donor with a non-human donor. The main concern is to ensure sterility and biocompatibility to avoid disease transmission. This type of grafting is mainly used as bone void fillers.

Xenografts critical disadvantages are disease transmission and ethical issues [7, 12]. Grafting processes, their advantages, and complications are summarized in Table 2.1.

Table 2.1. Conventional therapies for damaged bone tissue

Therapies	Source	Advantages	complications
Allograft	a human donor	Eliminating the need for a second surgical site.	Activate an immune response in the new host. Reduce the osteogenic potential because of freeze-drying, washing, gamma irradiation, and ...
Autograft	patient's tissue (usually the iliac crest)	Mitigating the risk of immunological sequelae. High cell regeneration rate.	Limited in quantity, shape restrictions, require extensive intra-operative modifications. Surgery includes inflammation, infection, chronic pain, and donor site morbidity.
Xenograft	non-human species	Elimination of the need for human tissue	Almost the same as allograft Risks of disease transmission Ethical issues

2.1.3 Bone Tissue Scaffold

TE is an alternative to the earlier mentioned conventional approaches (autografts, allografts, and xenografts) for restoring and repairing damaged bone tissue [13]. Bone tissue scaffolds prepare a suitable environment for native tissue to grow and shape the extracellular matrix (ECM). Bone tissue scaffolds have to acquire specific properties to meet the bone cell regeneration requirements. These properties can be categorized as morphological, materials and mechanical properties.

2.1.3.1 Morphological Properties

Bone morphology consists of the spongy and cortical bone. Spongy bone has 50-90% porosity, 1.85 ± 0.06 g/cm³ apparent density, and pore sizes in the order of 1mm [14, 15]. The cortical bone has an almost a solid structure with a series of canals that results in 3-12% porosity and an apparent density of 0.3 ± 0.10 g/cm³ [15, 16]. Porosity is the percentage of void space in a solid structure, and this morphological property of bone tissue scaffolds is independent of the material that is used to fabricate the structure. Porosity is essential for native tissue formation because of the need for cell migration and proliferation, and vascularization inside the scaffold. Pores are also improving mechanical interlocking in implantation and provide better mechanical stability [17]. Based on previous research works in the literature, a few limits and recommendations are proposed for the optimal porosity and pore size. In general, these recommendations are helpful to find a limit for the porosity and pore size, and then these factors should be optimized for specific designs and materials. The minimum pore size required to regenerate mineralized bone is considered to be 100 μ m, although, in a recent research, this limit has been challenged. Large pores have substantial bone ingrowth, medium-sized pores (75–100 μ m) are resulting in the ingrowth of mineralized tissue, and smaller pores are just helpful for the regeneration of fibrous tissue. Pore sizes smaller than 200 μ m, because of the decreased oxygen and nutrient diffusion through the scaffolds, negatively affect the bone tissue regeneration process. In sum, scaffolds with a mean pore size of equal or higher than 300 μ m cause osteoblast proliferation and differentiation throughout the entire scaffold due to improved neovascularization and passage of oxygen and nutrients [15, 18-22]. Technically, by employing this information and considering the other related factors like mechanical

and biological properties of a bone tissue scaffold, an optimal customized porosity for the designed scaffolds is achievable.

2.1.3.2 Materials and Manufacturing

Bone native tissue is a structure composed of hydroxyapatite ($\text{Ca}_{10}(\text{PO}_4)_6(\text{OH})_2$) crystals deposited within an organic matrix (95% is the type I collagen), as mentioned in previous sections [5]. By consideration of this composition, the materials and manufacturing methods are developed to fabricate bone tissue scaffolds. The materials and manufacturing processes are tightly related in bone tissue scaffolds production because of different limitations of the manufacturing methods in processing diverse raw materials. The main group of materials for bone scaffolds are ceramics, glasses, metals, natural polymers, polymers, and their composites. In Table 2.2, a few typical ceramics and glasses that are used in the literature with their related manufacturing methods, pore sizes, and porosity are reported. Polymeric and ceramic/polymer composites are among the trending materials for bone tissue engineering because they can simulate the natural composition of bone tissue scaffolds with high precision. Polymeric composites for bone tissue scaffolds mainly consist of synthetic polymers for their mechanical strength and one type of natural polymer for their biological properties. In Table 2.3, trending natural and synthetic polymers that are commonly used in the literature are reported [13]. There are numerous articles in the literature using polymeric, ceramic, and polymer/ceramic composites with different manufacturing processes. Although it is not possible to cover all of the related scientific articles in this section, in Table 2.4, a few studies on these types of composite materials and their related manufacturing processes are listed to represent the wide range of studies

and indicate the basic types of materials and fabrication methods that are used in the literature.

Table 2.2. Typical ceramics and glasses materials for bone tissue scaffolds

Type	Material	Manufacturing technique	Pore size (μm)	Porosity (%)
Ceramics	Hydroxyapatite [23]	Sintering	400 and 800	60 and 70
	Hydroxyapatite [24]	Sintering	500	77
	Hydroxyapatite [25]	Sintering	400–600	80
	Hydroxyapatite/tricalcium Phosphate [26]	Sintering	100-150	36
Bioglass [27]	-----	Foaming	100-600	-----
Glass/ceramics [28]	-----	Phase transformation	10-300	43-51

Table 2.3. Trending natural and synthetic polymers for bone tissue scaffolds

Type	Material	Properties
Natural	Collagen	Hydrophilic, cell adhesive, low mechanical properties
	Fibrin	
	Chitosan	
	Chitin	
Synthetic	Poly lactide (PLA)	Slow degrading, high mechanical properties, satisfactory biological property
	PCL	
	poly lactide-co-glycolide (PLGA)	
	Polyglycolide (PGA)	

Table 2.4. The literature review on polymeric, ceramic, and polymer/ceramic composite materials for bone tissue scaffolds

Material	Manufacturing technique	Pore size (µm)	Porosity (%)
Hydroxyapatite/poly(ϵ -caprolactone) [29]	Sintering	150–200	87
Collagen/hydroxyapatite [30]	Freeze-drying	30–100	85
Hydroxyapatite/b-tricalcium phosphate/chitosan [31]	Sintering	300–600	-----
Hydroxyapatite/chitosan-gelatin [32]	phase separation	<500	90.6
calcium phosphate /poly(hydroxybutyrate-co-hydroxyvalerate) And carbonated hydroxyapatite/poly(L-lactic acid) [33]	selective laser sintering (SLS)	500-800	60-70
diethyl fumarate-Hydroxyapatite/poly (propylene fumarate) [34]	Micro-Stereolithography (mSLA)	125–135 and 330–360	-----
PCL [35]	FDM	-----	70
β -tricalcium phosphate (β -TCP) [36]	SLS	600, 1300	-----
HA/PLA, HA/PCL, 6P53B glass/PLA [37]	Robocasting/Robotic assisted deposition	200–500	75
PLA [38]	FDM and gas foaming	100–800 1–10	-----
β -TCP/PCL [39]	3D printing	300	-----
High molecular weight PCL/Low molecular weight PCL/HA [40]	Supercritical CO ₂ gas foaming	132-612	22.4-73
poly(vinyl alcohol)/ β -TCP [41]	FDM	675	40

PCL composites with: tricalcium phosphate (TCP), HA, Bio-Oss (BO), and decellularized bone matrix (DCB) [42]	FDM	800	60 (design porosity)
PCL/ β -TCP [43]	SLS	-----	-----
poly(trimethylene carbonate) (PTMC)/HA [44]	SLA	600	70
PCL coated by HA/TCP [45]	FDM	-----	-----
PLA [46]	FDM	0, 150, 200, 250	-----
PLA/Akermanite [47]	FDM	200–400	-----
PLLA/HA [48]	FDM	-----	60

One of the critical features of PBTS materials is their biodegradability [49-51]. PBTSs should bio-absorb at a predicted rate, and the regenerated tissue should occupy the scaffolds 3-dimensional space in an ideal case [52]. Different wound conditions in individual patients need different biodegradation rates. For example, the degradation rate can be nine months or more for scaffolds in spinal fusion or less for scaffolds in the craniomaxillofacial applications [53, 54]. This fact makes the design of a scaffold with optimal biodegradation rate an engineering challenge [7]. Bone tissue scaffolds have to maintain mechanical strength for a particular amount of time, so materials should not degrade before transferring mechanical load to the newborn tissue; otherwise, the therapy would fail. On the other hand, the scaffold should not degrade too slow, as it would damage the surrounding tissues and impede the regeneration process [55, 56]. In sum, the bone scaffolds have to maintain part of their mechanical properties for a few months, and then they should be metabolized by the body after 12-18 months [50].

2.1.3.3 Mechanical Properties

Bone tissue scaffolds have to provide temporary mechanical support until the bone tissue is repaired and regenerated to restore the native biomechanical function. One of the most essential properties of a bone scaffold to be functional immediately after implantation is biomechanical properties that match the physical demand of the healthy surrounding bone to some extent [20, 50, 57, 58]. Also, the scaffold's mechanical strength affects the mechanotransduction of the adherent bone cells on the scaffold. These cells show a crucial role in bone repair and remodeling [59]. TE struggles to repair or replace the tissues with predominantly biomechanical functions, like bone tissue scaffold [57]. In Table 2.5 and 2.6, mechanical properties of bone tissue are reported. The test method to assess mechanical properties of native bone tissue affects the final results, as shown in Table 2.7. The mechanical properties achieved by compression test on the whole bone structure are almost 60% lower than mechanical testing results on a rod or beam of the bone structure [60]. Another factor that affects the mechanical properties of the scaffold is age. The mechanical strength increases until an adult person is 35 years old, and then it declines 2% after each decade [15]. The statistics are listed in Table 2.8. Therefore, by considering the presented literature and the ratio numbers in Table 2.7, the compressive mechanical strength requirement of a bone tissue varies from almost 0.5 to 16 GPa for the elastic modulus and from almost 6 to 124 MPa for the ultimate strength, from Trabecular bones to cortical bones, and the target manufactured bone tissue scaffolds have to stand in the mentioned range of the mechanical properties [15, 60].

Table 2.5. Mechanical properties of cortical bone

Cortical bone [60]	Elastic modulus (GPa)	Ultimate strength (MPa)
Compression test	23 ± 4.8	200 ± 36
Tensile Test	19.6 ± 6.2	141 ± 28
Torsional Test	3.3 ± 0.1	69 ± 9
Bending test [60, 61]	15.5	181

Table 2.6. Mechanical properties of Trabecular bone

Trabecular bone [15]	Elastic modulus (GPa)	Ultimate strength (MPa)
Compression test [62, 63]	0.443 ± 0.002	6.05 ± 0.75

Table 2.7. The effect of the testing method on the reported mechanical properties of bone tissue

Compression test Cortical bone [60]	Whole Bones	Rods or Beams	Difference	Ratio (%)
Ultimate strength (MPa)	125 ± 58	202 ± 40	77	61.8
Elastic modulus (GPa)	10.3 ± 5.7	16.5 ± 3.6	6.2	62.4

Table 2.8. The effect of age on mechanical properties of bone

Age [15]	3	5	35	after maturation
Elastic modulus (GPa)	7.0	12.8	16.7	Decline 2% after each decade

2.2 Additive Manufacturing

Additive Manufacturing (AM) is a manufacturing technique that fabricates computer-based 3D models by successively printing computer generated 2D layer slices layer-by-layer on top of each other [64, 65]. AM applications are limitless in various research fields and industries, including biomedical, healthcare, aerospace, construction, and automotive [66-75]. Figure 2.2 represents the AM processing steps, which starts with a computer-aided design (CAD) 3D model and employs a slicing software to generate a G-code file that defines the pathway to fabricate the part, and at the end, it deposits the materials layer by layer and delivers the product [70]. AM techniques can 3D print a wide diverse range of polymeric materials, including thermoplastics and thermosets [76]. In addition to the conventional polymers, composite materials can be manufactured in precise geometries employing the AM technique [64, 67, 76]. AM includes many diverse technologies, which are developed to respond wide range of applications and the necessity of manufacturing complex parts. ISO/ASTM 52900 – 15 describes the AM processes into seven categories [77], including material extrusion (ME), powder bed fusion (PBF), vat photopolymerization (VPP), binder jetting, directed energy deposition, material jetting, and sheet lamination.

ME is one of the most developed and extended AM techniques that include FDM, the most popular technique in the field. The ME technique employs a type of filament and extrudes the material through a nozzle and deposits the layers on top of each other on a movable build platform [64, 65]. PBF is another major AM technique, which includes selective laser sintering (SLS), as one of the most reputable techniques in the literature [64, 65]. PBF employs thermal energy to fuse regions of the build material's powder bed to fabricate the

final product. VPP operates by a liquid photopolymer in a vat, which is selectively cured by light-activated polymerization, based on the CAD design [64, 65]. VPP includes two other types of well-known and reputable AM techniques called Stereolithography (SLA) and Digital Light Processing (DLP) [64, 65]. Three of the mentioned subsections (SLS, SLA, and FDM) are the most common AM techniques in the literature and will be discussed in more detail in the following sections [65]. The other techniques mentioned in the ISO/ASTM 52900-15 with a short description are mentioned in Table 2.9 (directed energy deposition is not mentioned, because it is used for metallic materials that are not related to this study's topic).

Table 2.9. AM techniques for polymers classified by ISO/ASTM 52900 – 15 [77]

AM technique	Process technique for polymers	State of fusion
Material extrusion	Extrusion of melted materials through a deposition nozzle	Thermal reaction bonding
Powder bed fusion	Selective fusion of material in a powder bed	Thermal reaction bonding
Vat photopolymerization	Light reactive photopolymer curing	Chemical reaction bonding
Binder jetting	Reactive curing	Chemical reaction bonding
Material jetting	Multi-jet melted material printing / Light reactive photopolymer curing	Thermal reaction bonding/ Chemical reaction bonding
Sheet lamination	Fusion of stacked sheets of material	Chemical reaction bonding

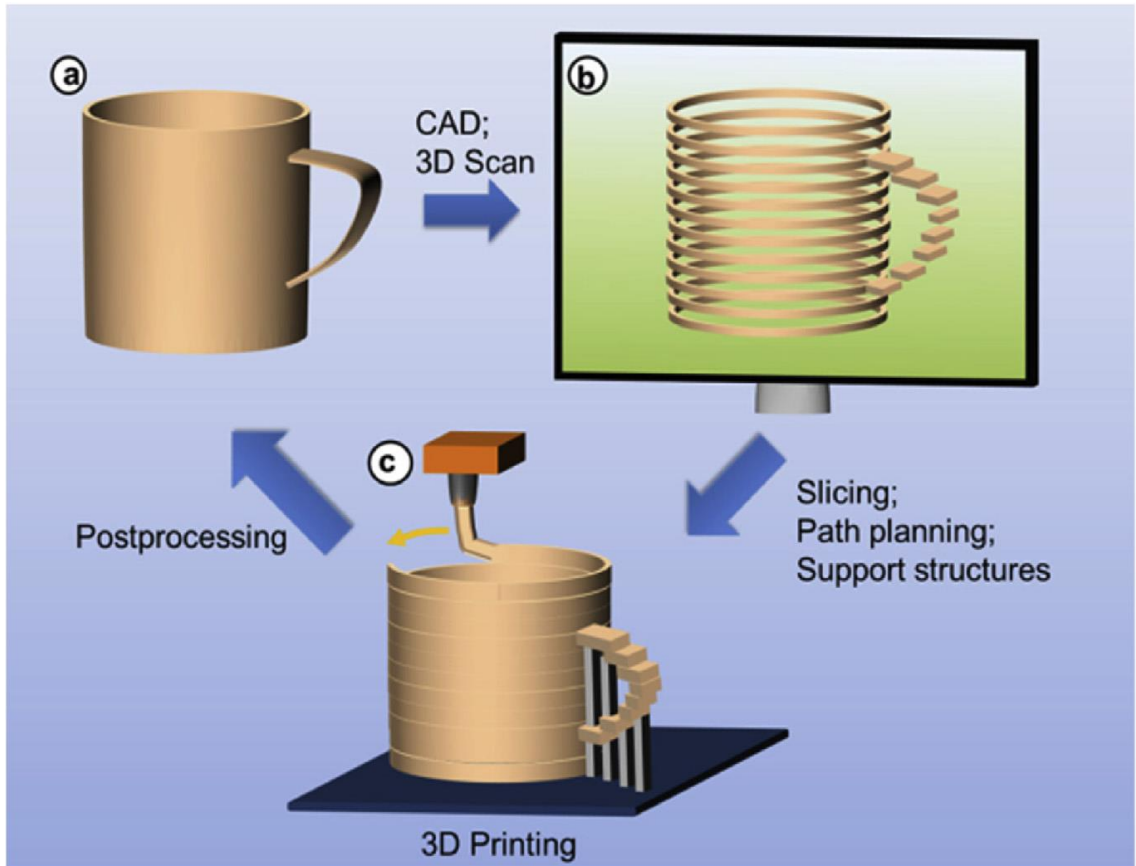


Figure 2.2. AM processing steps (the figure was used from the references [65, 70])

2.2.1 Selective Laser Sintering (SLS)

SLS is a powder-based AM method that employs a high-energy laser to fuse the powder particles, layer by layer. The laser is focused on the bed of polymer powder, as shown in Figure 2.3 [78]. The laser path and the shape of the related layer are determined by a CAD design in STL file format. Then the bed moves down, and a new layer is manufactured with the same process [79]. The processing conditions, including the laser scan speed, the powdered layer's thickness, the laser power, and the laser focusing radius, control the morphology of the scaffolds [80]. One of the benefits of SLS is that it does not require

support material or a separate feeder to fabricate the complex structures since unsintered powder supports each layer [81].

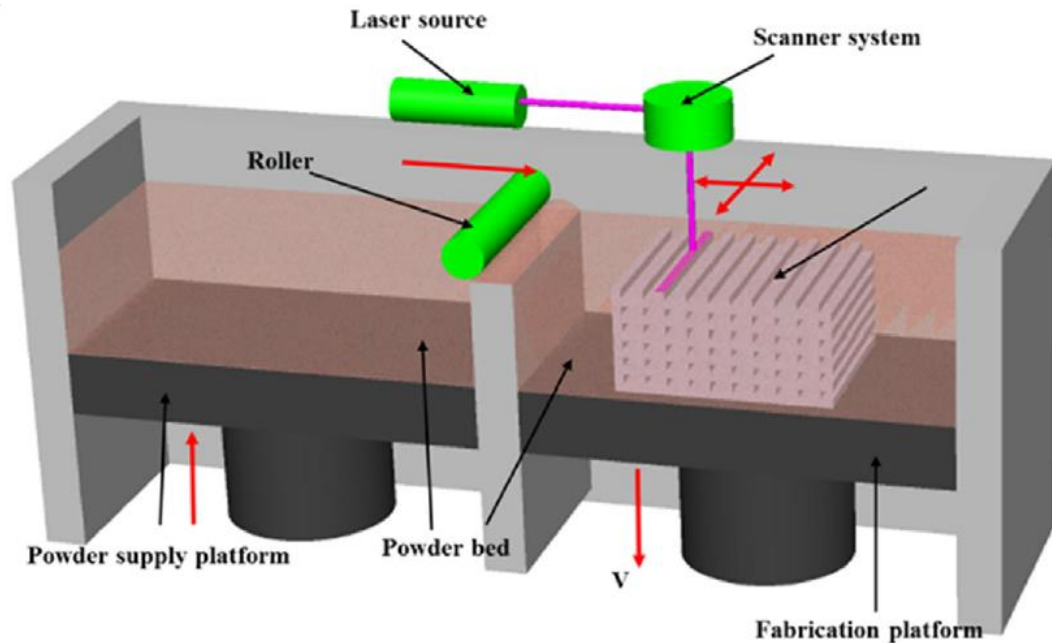


Figure 2.3. Selective Laser Sintering (SLS) (Reprinted from Composites Part B: Engineering, Volume 110, Wang et al., 3D printing of polymer matrix composites: A review and perspective (reference [67, 76]), Pages 442-458, Copyright (2017), with permission from Elsevier)

2.2.2 Stereolithography (SLA)

SLA is an AM method that utilizes UV light to polymerize liquid photopolymers. The first step is the exposure of the liquid's desired area to UV light, and then the photopolymer is polymerized and cured to form the first layer. The typical UV light wavelengths are 356, 385, and 405 nm, respectively [82, 83]. This process continues to form the designed 3D structure. The SLA process is shown in Figure 2.4. SLA has two main branches of laser direct writing and mask image-projection. Mask image-projection employs a digital

micromirror device to polymerize and cure the photopolymers using UV or another light source. Laser direct writing uses a laser that is focused through an objective lens to crosslink and solidify the photopolymers [84, 85]. The most crucial advantage of SLA is using lasers that increase the resolution of the designed scaffolds [82]. The critical problem of SLA is the difficulty of developing proper photopolymeric solution composition for bone tissue scaffold.

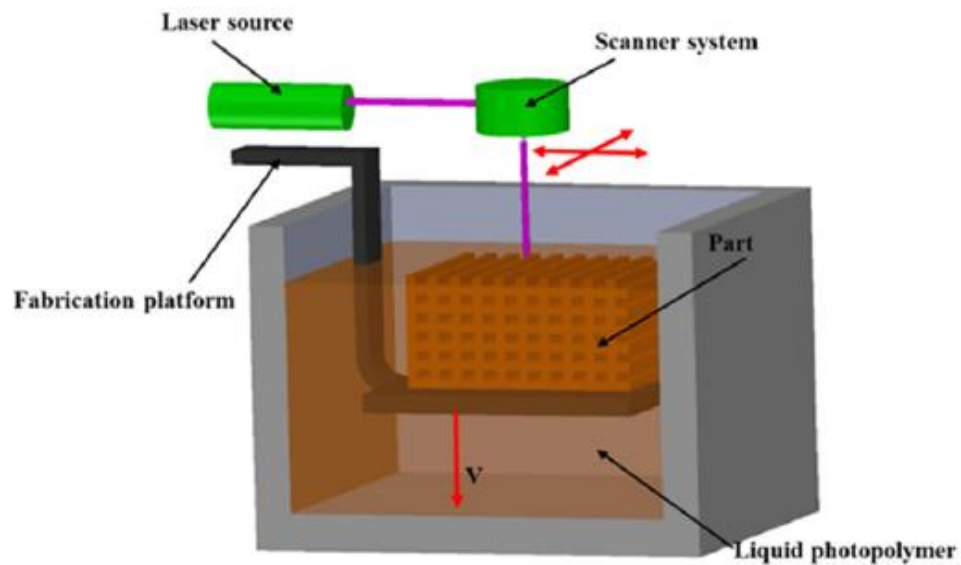


Figure 2.4. Stereolithography (SLA) (Reprinted from Composites Part B: Engineering, Volume 110, Wang et al., 3D printing of polymer matrix composites: A review and prospective (reference [67, 76]), Pages 442-458, Copyright (2017), with permission from Elsevier)

2.2.3 Fused Deposition Modeling (FDM)

FDM is a material extrusion based AM technique. The main components of the FDM 3D printers are shown in Figure 2.5. The filament is the FDM input material, which is in a standard radius depending on the FDM machine. The filament is inserted into the extruder nozzle's feeder, and the layer-by-layer deposition on the print bed starts [76]. The print

head moves in the X-Y plane, and the print bed moves on the Y-axis. The movements are defined by a G-code file, which is sliced based on the STL design file. FDM is the most popular AM technique because of its cost-effectiveness and flexibility in using a wide range of polymeric materials [86]. The main processing conditions to control FDM manufacturing are print speed, nozzle temperature, build plate temperature, and fan speed.

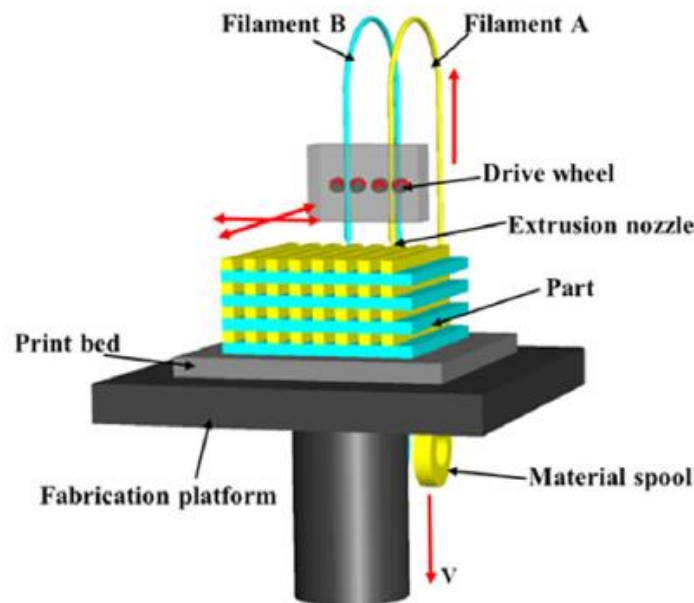


Figure 2.5. Fused Deposition Modeling (FDM) (Reprinted from Composites Part B: Engineering, Volume 110, Wang et al., 3D printing of polymer matrix composites: A review and perspective (reference [67, 76]), Pages 442-458, Copyright (2017), with permission from Elsevier)

2.2.4 Comparison Among the Typical Commercial AM Methods

Most commercial AM methods can be divided into three categories of VPP, PBF, and ME, which include FDM, SLS, SLA and a few other techniques. The manufactured products by these methods have a few advantages and disadvantages that are critical to be used in biomedical applications.

VPP methods operate by photopolymers, which the definition itself is a significant disadvantage in material selection perspective. VPP methods are beneficial in the manufacturing of large parts, they have excellent process accuracy, and the parts have high surface quality with great details. Other than the critical material selection disadvantage, VPP products mostly have poor mechanical properties, and their precursors are expensive. SLA and digital light processing (DLP) printers are the most common VPP systems [65, 69, 70, 87, 88].

PBF methods are relatively inexpensive and capable of fabricating parts using metals, ceramics, polymers, and their composites. The manufactured parts have high specific strength and relatively high resolution. Also, the powder bed acts as integrated support in the fabrication process. Although the mentioned advantages are significant, the PBF techniques have a few critical disadvantages too. The method is relatively slow, requires high power, and has limited scalability. The manufactured parts lack proper structural integrity, and their finish quality depends on the precursor. The other deficiencies of PBF are restriction in the powder particle size and poor reusability of unsintered powder. SLS is one of the most common PBF methods [65, 69, 70, 87, 88].

ME methods have the broadest range of material selection options, including polymers, ceramics, composites, hybrid materials, and biological contents. This property of ME methods is a significant advantage in the manufacturing of biodegradable bone tissue scaffolds. ME fabrication systems are inexpensive and can produce multi-material and multicolor parts. They can also manufacture fully functional parts, the process is easily scalable, and they are capable of 3D printing complex structures using nanocomposites. There are a few drawbacks in employing ME methods, including stepped-structured surface,

relatively low resolution, and the requirement for relatively medium-high temperature processes (depend on the materials). FDM, the most common AM technique, is categorized as a ME method [65, 69, 70, 87, 88].

By considering the advantages and disadvantages of the VPP, PBF, and ME methods of the AM, the ME has advantages that can be critical in manufacturing biodegradable PBTSs. Also, it is easier to enhance the ME systems' fabrication process to diminish their disadvantages. VPP methods have the significant disadvantage of materials selection, and PBF is not operational for biological contents and has a few processing deficiencies that cannot be ignored in manufacturing biodegradable PBTSs using nanocomposite materials. Therefore, ME is more suitable for the mentioned application among the well-known commercial AM methods, and this conclusion brings up the FDM as the leading ME method.

2.2.5 FDM Application in 3D Printing of Composite Filaments

In this section, applications of the FDM method in the 3D printing of composites and its specific application in the biomedical research field are reviewed. AM enables efficient and cost-effective fabrication of the final products (bone scaffolds) with advanced geometrical designs [89, 90]. AM, especially FDM, can manufacture polymeric products using a broad range of thermoplastic composites [67, 91-94]. There are several recent publications on the FDM printing of polymeric composites in diverse fields of research. In a study by Masood et al. [95], they introduced a metal/polymer composite filament for the FDM technique in the application of rapid tooling for injection molding. Their results indicated that the thermal properties of the products are acceptable for the application. In a research work by Perez et al. [96], the impact of reinforcement on the properties of

acrylonitrile butadiene styrene (ABS) matrix in FDM printing was analyzed. They assessed two ABS-based composites and one ABS/elastomer blend. Their result showed that ABS reinforced with 5% by weight TiO₂ had superior ultimate tensile strength, and ABS/elastomer blend enhanced the parts' surface finish. In improving creep and wear resistance of FDM printed parts, Bustillos et al. [97] employed graphene reinforced PLA composites to fabricate 3D printed parts. The composite improved the wear resistance of the parts by 14% and indicated a significant improvement in the related properties. In another study on FDM printing of wear-resistant composites, Olesik et al. [98] introduced Low-density polyethylene (LDPE) composites reinforced by the powdered waste glass. The reinforcement improved LDPE's wear resistance by 50%, and the composite indicated promising results for low-duty frictional applications. In a research by Christ et al. [99], highly elastic strain sensors were developed utilizing FDM printing of thermoplastic polyurethane/multiwalled carbon nanotube (TPU/MWCNT) nanocomposites. They reported that MWCNT improved the printability of the TPU, and the introduced nanocomposite is an exceptional piezoresistive filament for FDM printing of the desired parts. In another research work, Caminero et al. [100] assessed the impact of graphene nanoplatelets reinforced PLA on the mechanical properties, dimensional accuracy and texture of FDM printed parts. They reported a significant increase in mechanical properties of the 3D printed parts and indicated that the graphene did not decrease the dimensional accuracy of the parts. In a recent research publication by Alam et al., [101], 3D printing of PLA reinforced by magnetic and conductive fillers using the FDM technique was investigated. Their findings indicated that the PLA composites exhibited a higher degradation rate and enhanced bioactivity than the pure PLA matrix. In another research

by Lin et al. [102], manufactured carbon fiber (CF) reinforced polyetheretherketone (PEEK) composites by FDM technique and reported improvement in tribological properties of the composites compared to PEEK. Dul et al. [103] manufactured graphene nanoplatelets (GnP)/acrylonitrile-butadiene-styrene (ABS) composite filaments in a solvent-free process to be used as FDM raw material. They indicated an increase in elastic modulus and reduction in ultimate strength by increasing the GnP content of the composites. Also, the GnP content caused higher thermal stability in the matrix.

There are a significant number of scientific articles on applications of FDM printing in the biomedical research field. In an early research by Zein et al. [104], PCL as a bioabsorbable polymer was employed to fabricate honeycomb-like pattern scaffolds using the FDM technique for TE application. In a later study by Kalita et al. [105], polymer-ceramic composites were manufactured using the FDM technique with 3D interconnected designs to promote biocompatibility of the bone tissue scaffolds. They used polypropylene (PP) polymer and tricalcium phosphate (TCP) ceramic to produce the polymer-ceramic composites. They indicated that their proposed composites were not toxic to the human bone cells, cell growth was decent on the scaffolds, and the scaffold's mechanical properties with the lowest porosity were higher. In a research by Kim et al. [106], bone tissue scaffolds were manufactured by the FDM method using poly(d,l-lactide:glycolide) (DL-PLGA) and β -tricalcium phosphate (β -TCP) nanocomposites, which were coated by hydroxyapatite (HA). Their scaffolds were implanted into rabbit hosts, and the results indicated the native bone tissue cell growth and high biocompatibility of the scaffolds. Zhang et al. [107], 3D printed Fe₃O₄ nanoparticles/bioactive glass/Polycaprolactone (Fe₃O₄/MBG/PCL) composites to manufacture multifunctional tissue scaffolds. Their scaffolds exhibited

decent mechanical and biological properties, which proved their product's relative effectiveness as a multifunctional tissue scaffold. In producing scaffolds for the hard-tissue engineering field of research, Ergul et al. [108] used a 3D printing technique to manufacture chitosan/poly (vinyl alcohol) hydrogels containing HA. They reported that HA content could improve the properties of the 3D printed bone tissue scaffolds significantly. In another recent research by Gloria et al., [109], polyester amide (PEA) impact on the properties of additive manufactured PCL scaffolds were assessed, and they reported improvements in the properties of the PCL matrix. Based on the discussed research articles, the FDM technique is a significantly beneficial manufacturing method to 3D print composite tissue scaffolds.

2.3 PCL/nHA/CNW Nanocomposites Material Selection for the Development of Novel FDM Filaments

In recent decades, advanced polymeric nanocomposite materials for biomedical applications with properties superior to traditional composites are rapidly developed. Nanofiller reinforcements, including nanoparticles, nanofibers, and nanoplatelets due to their large interfacial interaction area with the polymeric matrix, can improve properties of the matrix more significantly than traditional biocomposites [110]. PCL is an aliphatic polyester that is biodegradable and biocompatible. PCL is an invaluable polymeric matrix for tissue scaffolds because of its outstanding properties, including nontoxicity, biocompatibility, gradual resorption after implantation, and stable mechanical properties [111-114]. PCL has a melting point of under 100°C that makes it an excellent polymeric matrix for biological natural fillers. Because the natural nanofillers mainly do not degrade in the range of PCL melting point in the polymeric processes that include thermal melting.

This fantastic property offers the opportunity of blending with novel fillers to improve the properties of the matrix [115-118].

The global interest in the scientific and industrial communities to employ chitin for improving their products' properties is increasing in many diverse fields, including pharmaceutical, drug delivery, and biocomposites. Chitin is the second most abundant natural polymer after cellulose and most commonly is extracted from crustacean shells [119, 120]. Crystalline whiskers are formed by acetyl-glucosamine monomers connected by $\beta - (1 \rightarrow 4)$ linkages as repeating units in the chitin structure. The CNW form of the chitin is characterized by its rod-like structure with dimensions of approximately 200-500 nm and 10-20 nm in the length and width, respectively [121, 122]. One of the significant advantages of CNW is its high modulus of 200 GPa, which makes it a satisfactory substitute for more common natural polymers to be employed as nanofiller [123, 124]. In a study by Feng et al. [125], Chitin Whisker (CW)- graft- Polycaprolactone (PCL) thermoformable composite was manufactured for biomedical applications. They reported the results on hydrophobicity, mechanical strength, and elongation for three different CW-PCL combinations, and their reported results showed a slight decrease in tensile strength by increasing the CW content. However, the young modulus indicated an opposite pattern. In another research, CW content was proven to be effective in mechanical properties stabilization of PCL matrix over a more extensive temperature range than pure PCL products [126]. In a recent research by Anwer et al. [124], CNW was used as reinforcement for epoxy and they analyzed the morphological, fracture, mechanical, dynamic mechanical, and thermal characteristics of the final products. They indicated that the CNW was effective in improving the properties of the epoxy matrix. They experienced self-

agglomeration of CNWs in concentrations over 0.5% while using the traditional solvents. In another application of CNW in the biomedical field of research, Wang et al. [127], employed CNW to enhance the properties of chitosan based injectable hydrogels. They reported improved mechanical properties of the hydrogels with CNW content and indicated high biocompatibility of the products.

Hydroxyapatite (HA) is a commonly used filler to reinforce biomedical products, especially in orthopedic, dental, and maxillofacial applications, because it is biocompatible, bioactive, and osteoconductive [13, 128, 129]. In addition to the mentioned advantages, multiple studies indicate that no inflammation was observed around implanted HA scaffolds, and HA was surrounded by bone tissues and formed an osseous combination with bone tissues in those types of implants [130-133]. Many studies in the literature employ HA as filler in the PCL matrix to improve bioactivity and mechanical properties. In a research work by Xiao et al. [134], HA and chitosan were used as fillers to improve the PCL matrix properties. They indicated that HA initially improves the composite's mechanical properties, but by increasing the content by more than 5%, the mechanical properties experienced a decrease afterward. In another research publication by El-Habashy et al. [135], the HA/PCL blend was investigated to enhance the osteogenic properties of bone tissue scaffolds. They indicated that hybrid bioactive HA/PCL composites have higher osteogenic properties than HA for bone regeneration. Trakoolwannachai et al. [136], assessed a broader range impact of HA in the PCL matrix. They extracted the HA from eggshell waste and manufactured the composites in three different combinations. Their results show that HA as a filler increased the thermal stability

of the PCL matrix and improved the swelling behavior of the composite. Also, the presence of HA caused an increase in the degradation rate of the PCL matrix.

Considering the current state of the art in the field and the literature review, PCL was chosen as the polymeric matrix of the nanocomposite FDM filaments in this study and, CNW and nHA were selected as nanofillers to enhance the properties of the matrix. To the best of the authors' knowledge, PCL/nHA/CNW nanocomposites are being manufactured for the first time to be used as FDM filaments, especially by employing green manufacturing methods.

2.4 Triply Periodic Minimal Surfaces Design of Bone Tissue Scaffolds

In recent decades, TE applications are receiving significant attention in replacing damaged tissues with 3D biomimetic porous scaffolds. The properties of such structures are highly dependent on the architecture of the scaffolds; therefore, advanced manufacturing methods are employed to manipulate the pore distributions and 3D designs [137-139]. AM has proven to be highly effective at fabricating advanced geometric scaffolds with a wide range of materials [89].

The morphological properties of PBTSs considerably affect the biological and mechanical properties of the scaffolds [140-142]. High porosity is essential for native tissue formation due to the importance of cell migration and proliferation on the scaffolds, as well as vascularization [15]. Pores also improve mechanical interlocking in implantation and provide better mechanical stability [17]. On the contrary, high porosity can reduce mechanical strength, and the scaffolds have to be immediately functional after implantation and be responsive to the physical demands of the healthy surrounding tissue [50, 57]. Thus,

advanced 3D designs of highly porous scaffolds are necessary to achieve an acceptable balance between the products' biological and mechanical properties [143]. Triply Periodic Minimal Surfaces (TPMS) are biomimetic or biomorphic designs that are under assessment for 3D scaffolds and have shown favorable performances in many cases [41, 144-147]. TPMS scaffolds have a mean curvature of zero that can facilitate the cell regeneration because of the agreement with the mean curvature of trabecular bone. In addition, TPMS designs have high surface per volume ratio, which can be a favorable property for tissue scaffolds. A few examples of the TPMS designs are presented in Figure 2.6 [148]. AM techniques, including FDM, can manufacture these structures with tunable porosity and acceptable surface quality [109, 149, 150].

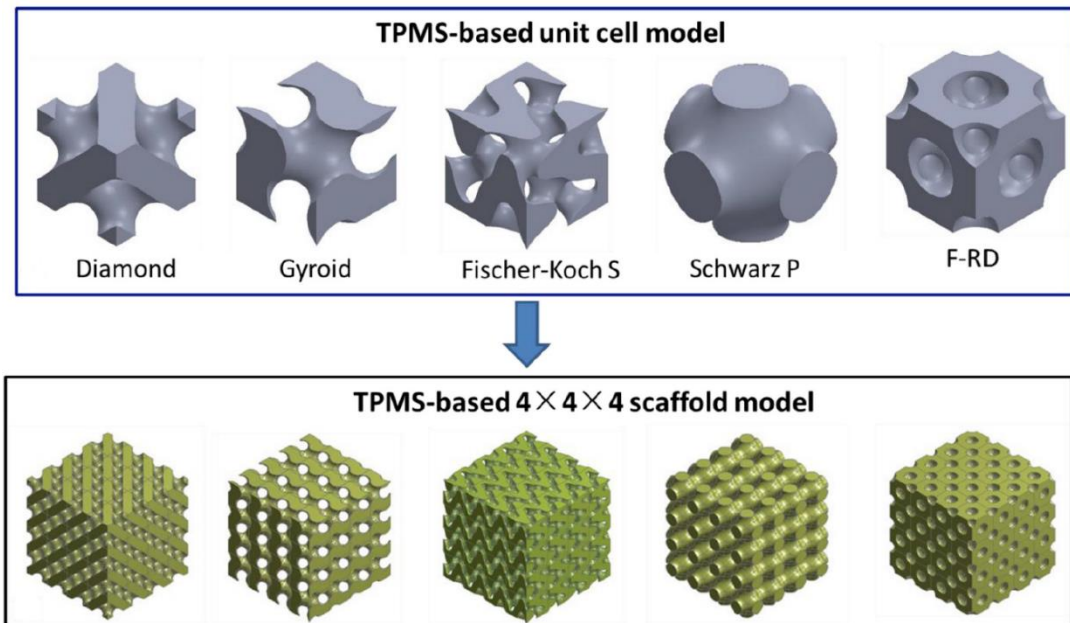


Figure 2.6. A few examples of the Triply Periodic Minimal Surface (TPMS) designs (Reprinted from Journal of the Mechanical Behavior of Biomedical Materials, Volume 99, Lu et al., the anisotropic elastic behavior of the widely-used triply-periodic minimal surface based scaffolds (reference [148]), Page 58, Copyright (2019), with permission from Elsevier)

Research focus on 3D design, simulation, and manufacturing of TPMS scaffolds is increasing in the recently published articles. Ma et al. [151] employed the selective laser melting (SLM) technique to manufacture and analyze 316L stainless steel bone tissue scaffold with the Gyroid structure. They indicated that as the volume fraction increased, the elastic moduli and yield stresses of the structures improved. Also, they assessed mass-transport properties through the metallic Gyroid scaffolds by computational fluid dynamics (CFD) simulation and reported promising results. In another numerical study, Ali et al. [137] used the finite element method to assess the mechanical behavior and permeability of Gyroid and lattice-based rectangular unit-cell scaffolds. Lozanovski et al. [152] presented a modeling technique to consider the AM defects in predicting mechanical properties and reducing the computational cost. They employed a Monte Carlo simulation approach to predict the stiffness of lattice additive manufactured scaffolds. Yang et al. [41] proposed an analytical approach to predict the Gyroid porous structures' mechanical properties and verified the model by finite element modeling and SLM experimental results. They proved that the proposed model is reasonable for low volume fraction designs. Lu et al. [148] presented a numerical method and an analytical approach to assess the anisotropic elastic behavior of a few TPMS designs. Their results could facilitate the selection of TPMS designs for different applications. Al-Ketan et al. [153] manufactured metallic parts of Gyroid and diamond TPMS designs and assessed the effects of relative density grading and cell size grading on the structures' mechanical properties. They investigated the effects of loading direction and force transfer patterns through the structures. Shi et al. [154] analyzed the rabbit bone morphology by CT scans and proposed geometrical parameters for TPMS structures to match the mechanical properties of the

native rabbit bone. Speirs et al. [155] studied the fatigue behavior of SLM 3D printed designs including TPMS scaffolds. They indicated that TPMS designs show superior mechanical properties compared to the conventional octahedron lattice structures. They also indicated that the metallic Gyroid structures fail in 45-degree shear plain. In another study, Abueidda et al. [156] employed 3D printing technique to manufacture polymeric Gyroid structures and investigated the mechanical properties experimentally and numerically. They concluded that their products have acceptable mechanical strength and can compete with other TPMS designs.

One of the essential features of advanced bone tissue scaffolds is biodegradability [49, 50], which biodegradable polymeric scaffolds can perform this capability. PBTSs should degrade at a predicted rate, and ideally, the regenerated tissue should occupy the 3-dimensional space created due to the degradation [52]. Different wound conditions in individual patients demand different biodegradation rates [53, 54]. This fact makes the design of a scaffold with optimal biodegradation rate an engineering challenge. Understanding the impact of design on biodegradation is essential, but it is sparse in the literature [157]. In sum, the TPMS designs exhibited significantly promising results to be employed as bone tissue scaffolds, but there are many opportunities to continue research in this area, and there are many aspects of this topic to be explained by new experiments.

Chapter 3. Manufacturing and Analytical Methods

In this chapter, the manufacturing methods of the PBTSs were discussed along with analytical and numerical methods to predict the scaffolds' biodegradation rate in the long term and perform optimization. In the first section, the design and manufacturing of the TPMS scaffolds with different porosities were discussed to assess the impact of design, porosity, and biodegradation on the mechanical and morphological properties of the PBTSs with advanced designs. Then, green manufacturing of the FDM nanocomposite filaments was explained in detail. Afterward, the Taguchi orthogonal array method was discussed to optimize the processing conditions of the FDM 3D printing. In the next section, the numerical simulation method and analytical analyses were explained to assist prediction of the biodegradation rate in the long term. In the last section of this chapter, a machine learning method was described to relate and formulate the experimental and numerical results, and NSGA-III multi-objective optimization method was explained to optimize the extracted equations.

3.1 Triply Periodic Minimal Surfaces Designed Scaffolds

Triply Periodic Minimal Surfaces (TPMS) designed scaffolds were manufactured using a single polyester material to assess the impact of design, porosity, and biodegradation on the scaffolds' mechanical and morphological properties independent of their material composition. In this section, the manufacturing and the design process of the TPMS scaffolds were explained.

3.1.1 Manufacturing

In this section, the scaffolds were manufactured with a nozzle size of 250 μm . The scaffolds were 3D printed with a wall thickness of 250 μm , layer thickness of 100 μm , printing speed of 10 mm/min, and 100% fan speed. The g-code files of the structural designs were generated by employing Ultimaker-Cura 4.2.1 slicing software. PLA filament of 2.85 mm in diameter, manufactured by Ultimaker, was used to produce all the scaffolds. PLA is a cost-effective, standard, and commercially available biodegradable polyester with the same dominant biodegradation mechanism as PCL. Because of the mentioned reasons, PLA was used for this section's analyses.

3.1.2 3D Design of Triply Periodic Minimal Surfaces Scaffolds

The scaffold architectures were designed according to three types of TPMS: Gyroid, Schwarz-D, and Neovius. Gyroid (this surface is an infinitely connected TPMS and does not contain straight lines or planar symmetries) and Schwarz-D (this surface is in the same associate family as Gyroid surface. The Gyroid's angle of association with respect to Schwarz-D is approximately 38°) were chosen because they are well-known TPMS designs for biomedical applications in the literature. The Neovius design was investigated as it has not been sufficiently assessed in the literature. Each structure was designed with 60% and 80% porosities to assess the effect of porosity on the properties. All of the structures were fabricated as cubes of 10 mm on each side. The Gyroid structure with 60% porosity is shown in Figure 3.1 compared to a one-dollar Canadian coin to show the precision of the designs. Gyroid structure was designed using the approximated surface formulated by Equation 3.1 [90, 148, 158]. The approximated formulations for Schwarz-D (diamond) and

the Neovius surfaces are presented in Equations 3.2 [148] and 3.3 [158], respectively. The corresponding designed structures are illustrated in Figure 3.2.

$$\sin(2\pi x) \cos(2\pi y) + \sin(2\pi y) \cos(2\pi z) + \sin(2\pi z) \cos(2\pi x) = 0 \quad (3.1)$$

$$\begin{aligned} \sin(x) \sin(y) \sin(z) + \sin(x) \cos(y) \cos(z) + \cos(x) \sin(y) \cos(z) \\ + \cos(x) \cos(y) \sin(z) = c \end{aligned} \quad (3.2)$$

$$6(\cos(2\pi x) + \cos(2\pi y) + \cos(2\pi z)) - 4 \cos(2\pi x) \cos(2\pi y) \cos(2\pi z) = -3 \quad (3.3)$$

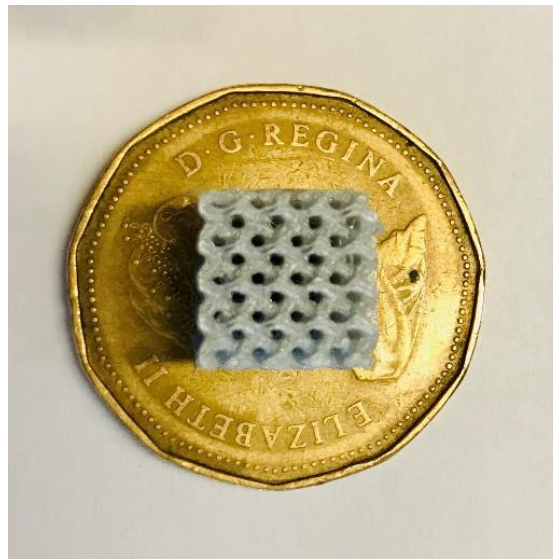
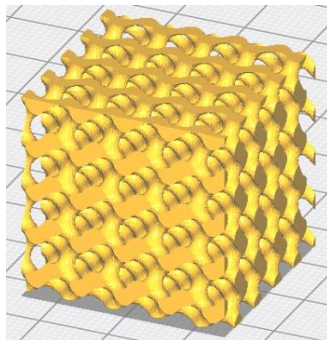
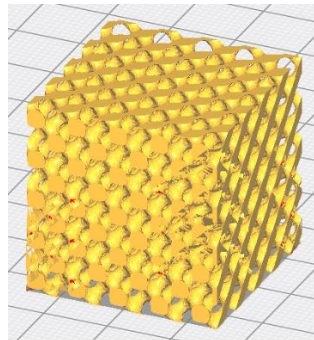


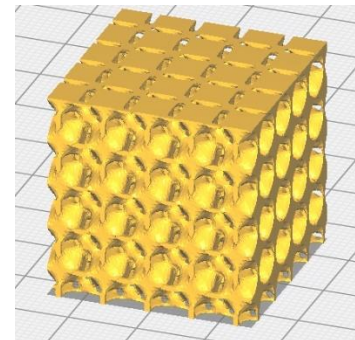
Figure 3.1. Gyroid structure with 60% porosity compared to a one-dollar coin



Gyroid 60%



Schwarz-D 60%



Neovius 60%

Figure 3.2. TPMS scaffold designs in this study

3.2 Green Manufacturing of the PCL/nHA/CNW Nanocomposite FDM Filaments

3.2.1. Materials

As discussed in the background and literature survey section, the novel PCL/nHA/CNW nanocomposites are selected for this study. As mentioned, to the best of our knowledge, these nanocomposites are being manufactured for the first time as FDM filaments and especially by using a green manufacturing method. Polycaprolactone (PCL), with an average Mn of 80,000 (melt flow index equal to 2.01 - 4.03), in the form of pellets (by Sigma-Aldrich), was used as the main polymeric matrix for the FDM filaments. Hydroxyapatite (nHA) nanopowder with particle size of lower than 200 nm from Sigma-Aldrich (molecular weight of 502.31 g/mol and specific surface area of higher than 9.4 m²/g) and Chitin-Nano-Whisker (CNW) provided by BOCO Bio-Nanotechnologies Inc. (density of 1.45 g/cm³, dimensions (L/W) of 200-500 nm/10-20 nm and specific surface area of 200-300 m²/g) were used as the nanofillers.

3.2.2. Green Manufacturing of the FDM Filaments

The green manufacturing of bio-nanocomposites is necessary due to health risk issues of commonly used toxic solvents, and the ionic solvents present a solution [159-161]. Ionic solvents are referred to as green solvents because they have significant advantages, including nontoxicity, non-volatility, easy recycling, non-flammability, and thermal stability [162, 163]. Many recent research works are using ionic solvents for manufacturing biocomposites. In a research study by Xiong et al., [160], 1-butyl-3-methylimidazolium chloride (BMIMCl) was used as an ionic solvent to manufacture cellulose/PCL blend films. They reported promising results on producing the proper solution blend, and their final

product quality was improved as well. These types of solvents specifically presented the opportunity to use the chitin more commonly in bio-nanocomposites; chitin shows dissolubility in most of the common solvents due to its structure, and the ionic solvents can be the solution [161]. In a research by Xie et al. [159], BMIMCl was employed to dissolve chitin and chitosan in the application of reversible sorbents of CO₂. The solvent was effective in dissolving chitin and chitosan, and the products show significant CO₂ sorption capacity.

In this study, the composites were manufactured using green methods, and no toxic solvents were employed to distribute the nanoparticles in the matrix. The nanocomposite filaments were manufactured in three stages. The first stage was the distribution of the nanofillers in the PCL matrix using a green solvent. The second and third stages were extrusion based to inspect the quality, enhance the blending and manufacture the standard FDM filament.

3.2.2.1 Stage One: Distribution of the Nanofillers in the PCL Matrix Using Green Solvents

1-Butyl-3-Methylimidazolium chloride (BMIMCl) purchased from Sigma-Aldrich was employed as an ionic solvent to manufacture the green nanocomposites. This stage is the most critical part of the manufacturing process because it is essential to distribute the nanofillers evenly in the matrix and avoid the accumulation of the nanofillers in one spot (especially CNW), which makes obstacles to the FDM printing of the filaments.

The BMIMCl solvent was added to a beaker, and then the nanofillers were added to the solvent [160] and heated up to 90°C. After 4 hours of mechanical stirring, the PCL pellets

were added to the solvent gradually in the next 5 hours, and the final solution was stirred for 30 hours, and at the end, the ionic solvent was removed [160, 164, 165].

3.2.2.2 Stages Two and Three: Extrusion

The previous section's produced composites were extruded using a single screw extruder with a nozzle diameter of 1.75 mm and nozzle temperature of $90^{\circ}\text{C} \pm 5^{\circ}\text{C}$. This first extrusion stage was intended to enhance the mixing process, and also the product was used to inspect the quality of the composites. If the ionic solvent was not completely removed before extrusion, the color of the material would change to dark brown during the extrusion. In such cases, the extruded composites were discarded. At the next inspection level, the Thermo-Gravimetric Analysis (TGA) results were used to confirm the solvent's removal. The acceptable nanocomposites were pelletized and again extruded with a nozzle size of 2.85 mm to produce standard filaments for FDM printing. The extrusion nozzle temperature was set to 100°C in all of the extrusion processes.

3.2.3 The Composition of Final Nanocomposite Filaments

The compositions of the manufactured nanocomposite filaments are listed in Table 3.1. The maximum percentage of the fillers was kept at 3% by weight; because CNW is in emulsion form in water, distributing high percentages of CNW in the matrix is a great challenge as they intrinsically intend to accumulate [124]. Also, successful FDM printing of the nanocomposite filaments was possible just for under 4% of CNW content; with the 4% CNW content, the extruder was clogged, and continuous printing was impossible. Multiple batches of each type of filament were produced to ensure the repeatability of the characterization results. Figure 3.3 represents the manufactured filaments.

Table 3.1. Manufactured nanocomposite FDM filaments

Nanocomposite	PCL (wt. %)	nHA (wt. %)	CNW (wt. %)
PCL	100	0	0
P-nHA1	99	1	0
P-nHA2	98	2	0
P-nHA3	97	3	0
P-CNW1	99	0	1
P-CNW2	98	0	2
P-CNW3	97	0	3
P-nHA1.5-CNW1.5	97	1.5	1.5
P-nHA1-CNW2	97	1	2
P-nHA2-CNW1	97	2	1

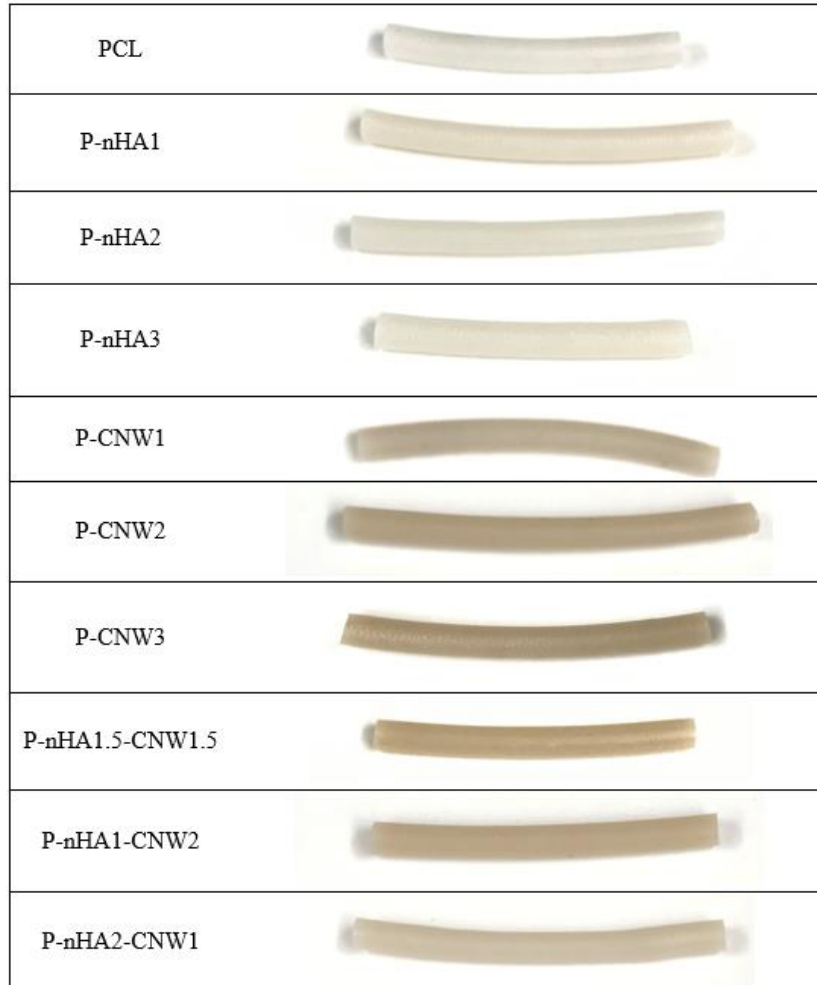


Figure 3.3. The manufactured nanocomposite FDM filaments

3.3 Optimized 3D Printing of the Nanocomposites Using the Taguchi Method

Numerous experiments have to be performed to achieve optimal processing conditions for 3D printing of the nanocomposites. Taguchi orthogonal array is a method to save time and resources in these types of investigations and reduces the number of experiments to a reasonable number. This technique performs optimization by considering control parameters and their responses, which are defined and calculated by the operator. The optimal results of the processing conditions are predicted by analysis of variance [166-169]. Taguchi method is introducing the variations by the signal-to-noise ratio factor, and the optimal parameters are selected based on the experimental processing conditions with the highest signal-to-noise ratio [170, 171].

Therefore, the Design of Experiment (DoE) and Taguchi orthogonal array were used to optimize the processing conditions of the newly introduced nanocomposite filaments. Print speed, nozzle temperature, build plate temperature, and fan speed of the FDM 3D printing of the manufactured composites are the critical processing condition for the experiments; three levels of variations were defined for each of the parameters. The L₉ three-level Taguchi orthogonal arrays were proposed to address the experimentation of four parameters with three levels of variation. Table 3.2 lists the standard Taguchi L₉ proposed experiments [172]. In Table 3.2, the numbers 1, 2, and 3 represent the low, medium, and high levels of a factor, respectively.

The Design-Expert DoE software was employed to apply the Taguchi method and optimize the results. As shown in Figure 3.4, the Taguchi method was selected, and the four parameters, their units, and the three levels are defined in the software. The study type was set to randomized factorial analysis. Based on the defined parameters in this study, the

Taguchi orthogonal array recommended experiments are shown in Table 3.3 (the run numbers are not listed in the standard order of the Taguchi method). The experiments were performed, and the results were analyzed by Design-Expert software. The final products' layer thickness, structural integrity, and compressive strength were analyzed to investigate the optimal processing conditions. Structural integrity was defined as a qualitative factor in the range of 0-100 (0, 25, 50, 75, 100) based on regular 3D printed parts visual inspections; 100 for the best structural integrity and 0 for the worst.

Table 3.2. Taguchi L_9 (four parameters with three levels) [172]

Experiment Number	Parameter 1	Parameter 2	Parameter 3	Parameter 4
1	1	1	1	1
2	1	2	2	2
3	1	3	3	3
4	2	1	2	3
5	2	2	3	1
6	2	3	1	2
7	3	1	3	2
8	3	2	1	3
9	3	3	2	1

Taguchi OA Design

Orthogonal array designs from Taguchi's textbook. Explore Regular Two-Level Factorial and Optimal (custom) designs as alternatives. Pay attention to the alias structure for these designs to ensure estimation of the effects needed.

Design Designation: Horizontal
 Vertical

	Name	Units	Levels	L[1]	L[2]	L[3]
A [Categorical]	Print speed	mm/s	3	10	15	20
B [Categorical]	Nozzle Temp	celsius	3	80	100	120
C [Categorical]	Build plate te	celsius	3	30	40	50
D [Categorical]	Fan speed	%	3	80	90	100

3-level factors: 4 Runs: 9

Figure 3.4. Parameters and their defined levels in the Design-Expert software for the Taguchi design (Screenshot)

Table 3.3. The Taguchi orthogonal array proposed experiments

Run	Print speed (mm/s)	Nozzle Temperature (°C)	Build plate temperature (°C)	Fan speed (%)
1	15	100	50	80
2	20	80	50	90
3	15	120	30	90
4	10	100	40	90
5	15	80	40	100
6	20	120	40	80
7	10	120	50	100
8	20	100	30	100
9	10	80	30	80

3.4 Simulation and Prediction of Long-term Biodegradation Rate

In this section, the finite element analysis method was employed to estimate the biodegradation rate and behavior of 3D printed polyester-based scaffolds with Gyroid designs in the long term. Understanding the degradation properties of polymeric scaffolds in biomedical applications is essential as it has considerable impact on the cell growth and structural integrity of the scaffolds with time. Gyroid structures were studied as they are one of the most commonly used TPMS scaffolds for biomedical applications [90]. Hydrolytic degradation was simulated by employing the COMSOL software package. In the first stages, the biodegradation of a polyester (PLA) was estimated by considering bulk and surface erosion, and mass loss of the scaffolds was predicted using the methods in the literature. PLA was used initially to validate the numerical results with the literature. Finally, the methods and analyses were linked to PCL matrix properties, and the biodegradation behavior of the manufactured nanocomposites was estimated in the long term. Although many factors affect the degradation rate of 3D printed scaffolds, which makes precise prediction not feasible, the method used in this study can help predict and understand the scaffolds' biodegradation rate in the long term by connecting numerical simulation, analytical assessments, and experimental data.

3.4.1 Introduction

Biodegradation of aliphatic polyesters including PLA and PCL is affected by five major chemical and physical factors, including polymer composition [173], degradation media [174], crystallinity and polymer morphology [175, 176], molecular weight [177, 178] and, the scaffolds geometry and morphology [179, 180]. Due to the high importance of the geometry of the scaffolds [181, 182], the 3D design of the tissue scaffolds is relevant to the

biodegradation rate and pattern of the structures [90, 157, 183, 184] and can be one of the factors to manipulate the biodegradation rate and pattern. In recent experimental research on the effect of design on biodegradation, it was shown that the Gyroid structure exhibits a very different pattern of biodegradation than simple cubic designs of bone tissue scaffolds, which makes Gyroid structure a more favorable design to manufacture a biodegradable bone tissue scaffold [90].

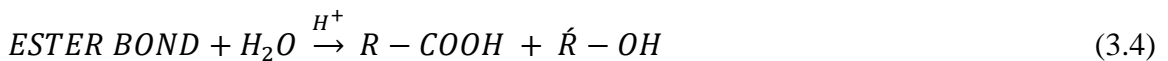
The study of the biodegradation process is time-consuming, as the experimental analysis has to be done in an extended period. Therefore, numerical modeling of the scaffolds' biodegradation process receives significant attention in the literature [185]. Polymer chain scission is the primary chemical reaction that causes biodegradation of the aliphatic polyesters and follows by diffusion of monomers and oligomers [186]. Various mathematical models were developed to analyze this phenomenon. In a few studies, stochastic hydrolysis and erosion models were developed to predict mass loss and drug release, but they could not consider the autocatalytic effect in the hydrolysis reaction, which is a critical factor in many polyesters [187-189]. In a study by Zhang et al. [190], a model was presented which combined degradation and erosion phenomena. The model was over-complicated in practical applications and did not consider the autocatalytic effect of the hydrolysis process. In the model developed by Gopferich [191], biodegradation was divided into two phases by defining a critical molecular weight. They considered that before the molecular weight reaches the critical value, the mass loss can be neglected, but afterward, the structure would experience a large immediate mass loss [192]. Their model was incapable of linking degradation and erosion phenomena, and there was a considerable gap between their results and the available experimental data [193, 194]. Pan and Wang et

al. developed a reaction-diffusion model that considers the autocatalytic effect of the hydrolysis process and is valid for polyesters [184, 195]. The developed model can be applied in commercial software, including COMSOL, to simulate the hydrolytic biodegradation for the advanced geometries [184]. In a recent study by Sevim et al. [186], a proper connection was made between hydrolytic biodegradation and erosion to improve the previous model and provide a complete picture of the mass loss.

In this study, the hydrolytic biodegradation process of Gyroid-based scaffolds was simulated using COMSOL commercial software, coupled with the SOLIDWORKS part design, using the presented mathematical models in the literature. The inherent property of FDM 3D printed structures, which are consist of repeating units of extruded filaments, was used to present an interpretation for hydrolytic biodegradation of 3D printed Gyroid scaffolds. In the end, the mass loss of the scaffolds was estimated by considering both bulk and surface erosion.

3.4.2 Hydrolysis of Polyesters

Hydrolysis of polyesters (PLA, PCL, and ...) is defined as the reaction of water molecules with the polyester's ester bonds. This process results in the chain scission process of the polyester. Figure 3.5 and Equation 3.4 demonstrate the chain scission process of polyesters that was used for numerical simulation in this study [184]. The reaction of water molecules with the ester bonds yields two products, including a hydroxyl alcohol group ($R' - OH$) and a carboxylic acid end group ($R - COOH$), as shown in Equation 3.4:



where R and R' stand for the remainders of the polymeric chain. H^+ catalyzes the reaction and because of the high degree of acid dissociation in the carboxylic end groups the reaction is autocatalytic.

The total number of chain scissions of the ester bonds per unit volume of the material is defined as R_s . The changing rate of R_s is represented in Equation 3.5 [195, 196]:

$$\frac{dR_s}{dt} = k_1 C_e + k_2' C_e C_{H^+} \quad (3.5)$$

where k_1 and k_2' stand for the reaction constants, C_e is the concentration of ester bonds, and C_{H^+} is the concentration of H^+ . The hydrolytic biodegradation process depends on the defined terms. The next section presents the evolved and final equations, which were employed in this study.

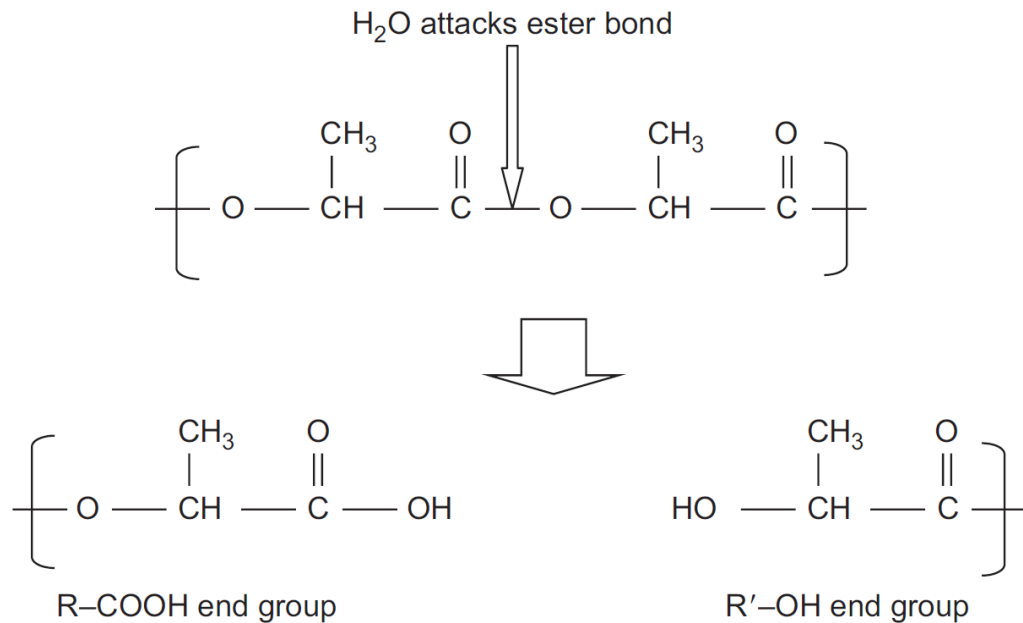


Figure 3.5. Hydrolysis process of polyesters (PLA as an example) (Reprinted from Modelling degradation of bioresorbable polymeric medical devices, Pan et al. (reference [184]), Modelling degradation of amorphous biodegradable polyesters: basic model,

Pages 15-31, Copyright (2015), with permission from Elsevier)

3.4.3 Mathematical Equations

The mathematical equations were defined based on the chain scission and the short chains' diffusion (small dissolvable molecules) [184]. Equation 3.6 is the partial differential equation (PDE) of the polymer chain scissions:

$$\frac{dR_s}{dt} = C_{e0} \left[1 - \alpha \left(\frac{R_s}{C_{e0}} \right)^\beta \right] \left[k_1 + k_2 C_{e0}^n \left[\frac{1}{m} \left(\frac{C_{ol}}{C_{e0}} \right) \right]^n \right] \quad (3.6)$$

where R_s is the mole concentration of polymer chain scissions, C_{ol} is the mole concentration of dissolvable small molecules, and C_{e0} is the initial mole concentration of ester bonds of the polymer chain. k_1 and k_2 stand for the rates of non-catalytic and autocatalytic hydrolysis reactions, respectively. Parameters α and β are empirical parameters of the production rate of the small molecules by chain scission, m is the average degree of polymerization of the small molecules, and n is the exponent for acid dissociation.

Equation 3.7 defines the PDE for the diffusion of the short chains:

$$\frac{dC_{ol}}{dt} = \alpha \beta \left(\frac{R_s}{C_{e0}} \right)^{\beta-1} \frac{dR_s}{dt} + \sum_{i=1}^3 \frac{\partial}{\partial x_i} \left(D \frac{\partial C_{ol}}{\partial x_i} \right) \quad (3.7)$$

where D is the diffusion coefficient of small molecules in the biodegrading polymer and is defined by Equation 3.8. Parameter V_{pore} in the Equation 3.8 is defined in Equation 3.9, which stands for the porosity of the polymer caused by the loss of the small molecules.

$$D = D_{polymer} + (1.3V_{pore}^2 - 0.3V_{pore}^3)(D_{pore} - D_{polymer}) \quad (3.8)$$

$$V_{pore} = \frac{R_{ol} - (C_{ol} - C_{ol0})}{C_{e0}} = \alpha \left(\frac{R_s}{C_{e0}} \right)^\beta - \frac{C_{ol} - C_{ol0}}{C_{e0}} \quad (3.9)$$

In Equation 3.8, $D_{polymer}$ and D_{pore} are diffusion coefficients of the small molecules in the non-degraded polymer and liquid-filled pores, respectively. In Equation 3.9, C_{oI0} stands for the concentration of residual monomers that may exist in the polymer. Equation 3.10 is the final equation that calculates the average molecular weight using the results of the previously defined PDEs:

$$\frac{M_n}{M_{n0}} = \frac{1 - \alpha \left(\frac{R_s}{C_{e0}} \right)^\beta}{1 + N_{dp0} \left(\left(\frac{R_s}{C_{e0}} \right) - \left(\frac{\alpha}{m} \right) \left(\frac{R_s}{C_{e0}} \right)^\beta \right)} \quad (3.10)$$

where M_{n0} is the initial averaged molecular weight and N_{dp0} was defined in Equation 3.11, which M_0 is the molecular weight of a single repeating unit of the polymer. The constant values for the simulation were used, as reported by Pan [184].

$$N_{dp0} = \frac{M_{n0}}{M_0} \quad (3.11)$$

3.4.4 3D Design and Meshing

Gyroid structures were designed using SOLIDWORKS commercial software, and they were imported to COMSOL geometry afterward. Figure 3.6 represents the designs in the 3D space, x-y plane, and z-x plane. In addition to Gyroid design, three geometries, based on the shape of 3D printed filaments, were designed to reach an approximation factor for the 3D printed parts, as reported in Table 3.4. In the filament-based scaffolds' design, the extruded filaments were considered to be cylindrical and have the same percentage of overlapping volume for each deposition layer. The initial 3D simulation of Gyroid structures was performed for the uniform Gyroid scaffold, but the 3D printed structures are made by the deposition of filaments, and an approximation factor is crucial to relate the

simulation results. Three different mesh networks were used for the numerical simulation, and a mesh sensitivity analysis was performed to reach a precise meshing network with the lowest computational cost. This analysis was discussed in a separate section of the results and discussions.

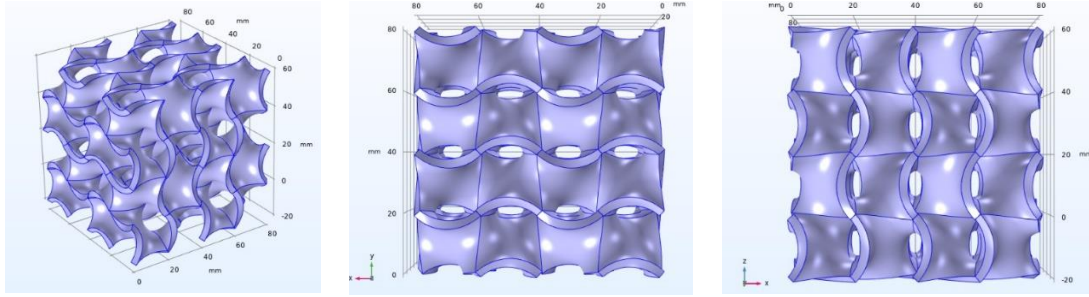


Figure 3.6. 3D designed Gyroid scaffold for numerical simulations

Table 3.4. The filament-based designs for numerical simulations

Sample	Filament diameter (μm)	Number of adjacent extruded filaments
F-TH0.5	240	2
F-TH1	240	4
F-TH1.5	240	6

3.4.5 Partial Differential Equation Inputs and Boundary Conditions

A transient form was defined in Equation 3.12 to solve the general form PDE equations in the COMSOL.

$$\begin{cases} e_u \frac{\partial^2 u}{\partial t^2} + d_a \frac{\partial u}{\partial t} + \nabla \cdot \Gamma = f & \text{in } \Omega \\ -n \cdot \Gamma = G + \left(\frac{\partial R}{\partial u} \right)^T \mu & \text{on } \partial\Omega \\ 0 = R & \text{on } \partial\Omega \end{cases} \quad (3.12)$$

In this equation, Ω is the computational domain, and $\partial\Omega$ is the domain boundaries. u represents the PED variable and is equal to $(R_s, C_{ol})^T$ in this study. The terms of e_a, d_a, Γ and f are mass coefficient, damping coefficient, conservative flux vector, and the source term, which were defined based on Equations 3.6 and 3.7. Equations 3.13 – 3.16 represent these terms of the numerical model.

$$e_a = \begin{bmatrix} 0 & 0 \\ 0 & 0 \end{bmatrix} \quad (3.13)$$

$$d_a = \begin{bmatrix} 1 & 0 \\ (-\alpha\beta) \left(\frac{R_s}{C_{e0}}\right)^{\beta-1} & 1 \end{bmatrix} \quad (3.14)$$

$$\Gamma_{R_s} = \begin{bmatrix} 0 \\ 0 \\ 0 \end{bmatrix}, \Gamma_{C_{ol}} = \begin{bmatrix} -D_x \frac{\partial C_{ol}}{\partial x} \\ -D_y \frac{\partial C_{ol}}{\partial y} \\ -D_z \frac{\partial C_{ol}}{\partial z} \end{bmatrix} \quad (3.15)$$

$$f = \begin{bmatrix} C_{e0} \left[1 - \alpha \left(\frac{R_s}{C_{e0}}\right)^\beta \right] \left[k_1 + k_2 C_{e0}^n \left[\frac{1}{m} \left(\frac{C_{ol}}{C_{e0}}\right) \right]^n \right] \\ 0 \end{bmatrix} \quad (3.16)$$

The initial values of the numerical simulations were considered as follow [184]:

$$R_{sin} = 0, C_{ol_{in}} = C_{ol0}, \frac{\partial R_{sin}}{\partial t} = 0, \frac{\partial C_{ol_{in}}}{\partial t} = 0$$

3.5 Machine Learning and Multi-Objective Optimization

In this study, many experiments and simulations were performed to assess the impact of various factors on the performance of the bone tissue scaffolds. The impact of the TPMS designs and their porosity on the mechanical and morphological properties of the PBTS, before and after biodegradation, was assessed in an independent study from the variations of the material composition. The logical relations between the properties were extracted

and discussed. In another part of the experimental works, the PCL/nHA/CNW 3D printed nanocomposite PBTSs were developed, processed, and characterized, and all of the properties were reported independent from the structural design of the scaffolds. These experiments revealed explanations and relations to understand the impact of the nanocomposite materials on the properties of the scaffolds. These two parts were connected to achieve more comprehensive formulations to model the properties of the PBTSs. Because the impacts of the design and porosity were analyzed independently from the material composition (were achieved for a single polyester), the relations were applied to the experiments' results on PCL/nHA/CNW PBTSs, as those experimental results were achieved in an independent study (from the 3D design properties) too. These experimental works have been followed by numerical simulation and analytical assessments to extrapolate the results on the biodegradation rate of the products to the long term.

All of the achieved results were analyzed using machine learning to predict and formulate the responses and generate multiple functions, one for each response. Afterward, these functions were optimized to recommend non-dominated options employing multi-objective optimization.

3.5.1 Meta-Modeling Using Genetic Programming

3.5.1.1 Introduction

Machine learning is used for meta-modeling of discrete experimental and numerical simulation data. Eureqa software, which uses Genetic Programming (GP), was employed to perform the meta-modeling of the data [197]. GP is a sub-branch of evolutionary algorithms that is used to achieve a symbolic regression tree corresponding to a

mathematical formula to fit a data set [198]. The fitting process is based on the optimization structure that minimizes the error of the symbolic tree (compared to the original set of data) by regression. This property makes the GP an excellent candidate for meta-modeling of complex experimental sets of data [199, 200].

The symbolic regressions (solutions) are generated to shape an initial population, which is a set of solutions at an iteration of the algorithms. A tree-based encoding creates these initial expressions. An example of these expressions is shown in Figure 3.7 for the example of $10x \tan(2x + 3)$. The expressions are consist of two types of parameter groups, including functional primitives and a terminal set. For example, the functional primitives of the expression in Figure 3.7 are \times , $+$, and \tan , which are generally n-ary arithmetic functions. A terminal set consists of constants, decision variables, and other system parameters that supply the functions' arguments. The initial expressions are evolving through the process, and in each stage, they are associated with a fitness value that indicates the expression's accuracy. In each stage, the algorithm evolves new solutions by using the previously generated solutions. Evolutionary variation mechanisms, including crossover and mutation, lead to many solutions constituting a population. After creating a population, the system operates by parent selection procedure, which means to choose solutions to extract new solutions from them. These expressions are called parent and offspring expressions. Crossover creates two offspring by interchanging parts of the parent expression trees, as shown in Figure 3.8. The mutation is applied in random alterations on a node-by-node basis of a branch or terminal node to produce new solutions, as shown in Figure 3.9. The final goal is to achieve a meta-model with an acceptable fitness value to the original data sets [198, 200].

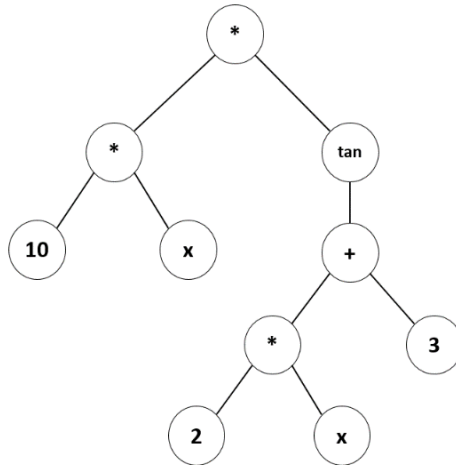


Figure 3.7. Tree-based representation of GP expressions for an example function

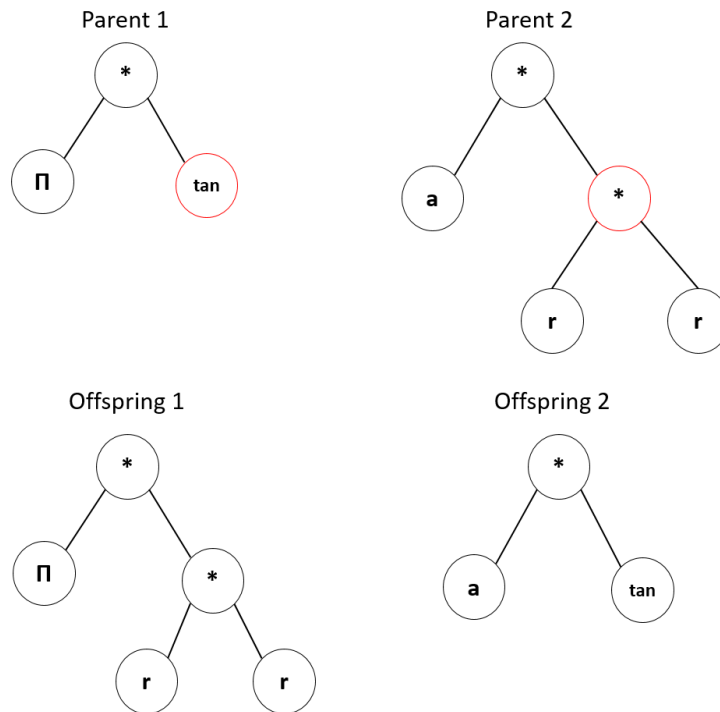


Figure 3.8. Parent and offspring expressions created by crossover operation. Parent 1: $\pi * \tan$; parent 2: $a * r^2$; offspring 1: $\pi * r^2$; offspring 2: $a * \tan$

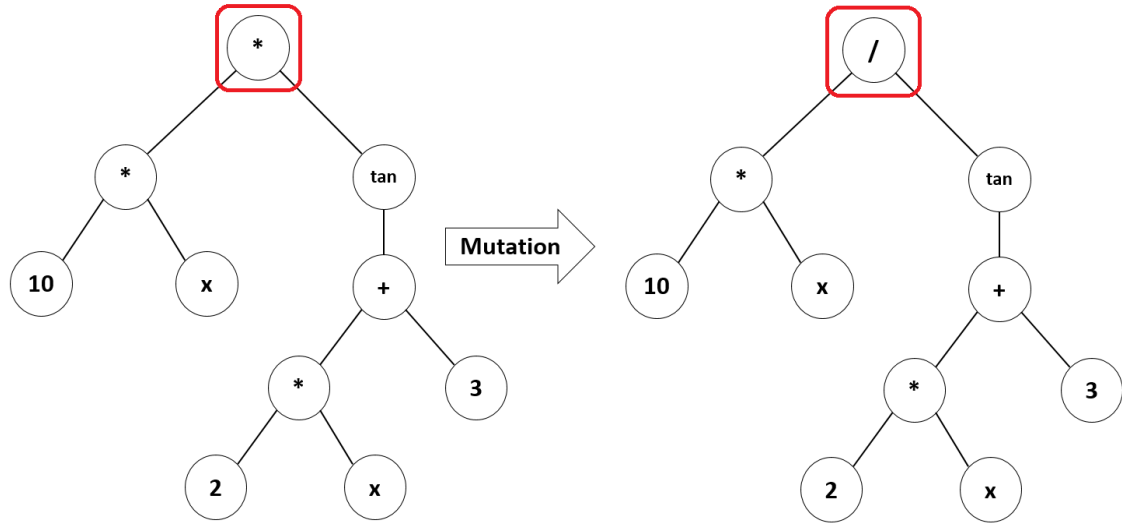


Figure 3.9. Mutation: before mutation, the function is $10xtan(2x + 3)$, and after mutation, it transforms to $10x/tan(2x + 3)$

3.5.1.2 Meta-modeling Definitions and Assumptions

An initial population has to be defined to perform the meta-modeling of an experimental or a numerical simulation set of data. In this study, six objective functions as $f_1 - f_6$ were extracted, which are the functions for (1) compressive strength, (2) average apparent modulus, (3) compressive strength after four months of biodegradation, (4) average apparent modulus after four months of biodegradation, (5) biodegradation percentage after six months, and (6) cell proliferation ($OD \times 1000$), respectively. These functions were defined based on three variables of X_1, X_2 and X_3 , which stand for the percentage of nHA filler in the nanocomposites, percentage of CNW filler in the nanocomposites, and porosity percentage of the Gyroid structural design of the scaffolds, respectively.

The initial populations to extract these objective functions were defined using the data reported in sections 5.1, 5.4, 5.5, and 5.6. In the f_1 and f_2 , the impact of design and porosity

on the mechanical properties that were reported in section 5.1, were superimposed on the impact of the nanocomposite filaments on the mechanical properties of the 3D printed PBTSs, which were reported in section 5.4; the initial population results were also experimentally confirmed for the PCL scaffolds, to assure the acceptable accuracy. The initial populations to extract the f_1 and f_2 objective functions are demonstrated in Figures 3.10 and 3.11. In the f_3 and f_4 , the impact of biodegradation on the mechanical properties of the Gyroid scaffolds that were reported in section 5.1, The results reported in section 5.4 and the results of biodegradation rate in the long term that were achieved in section 5.6, were combined to define the initial population; these initial population results were also experimentally confirmed for the PCL scaffolds, to guarantee the acceptable precision. The initial populations to extract the f_3 and f_4 objective functions are demonstrated in Figures 3.12 and 3.13. The initial population to extract the f_5 , was defined based on the reported results in section 5.6 and is shown in Figure 3.14. The initial population to extract the f_6 , was defined using the reported data in section 5.5 and by considering a positive impact factor for an increase in the porosity of the design that was experimentally confirmed for the PCL scaffolds to assure the acceptable accuracy. The initial population to extract the f_6 objective function is demonstrated in Figures 3.15.

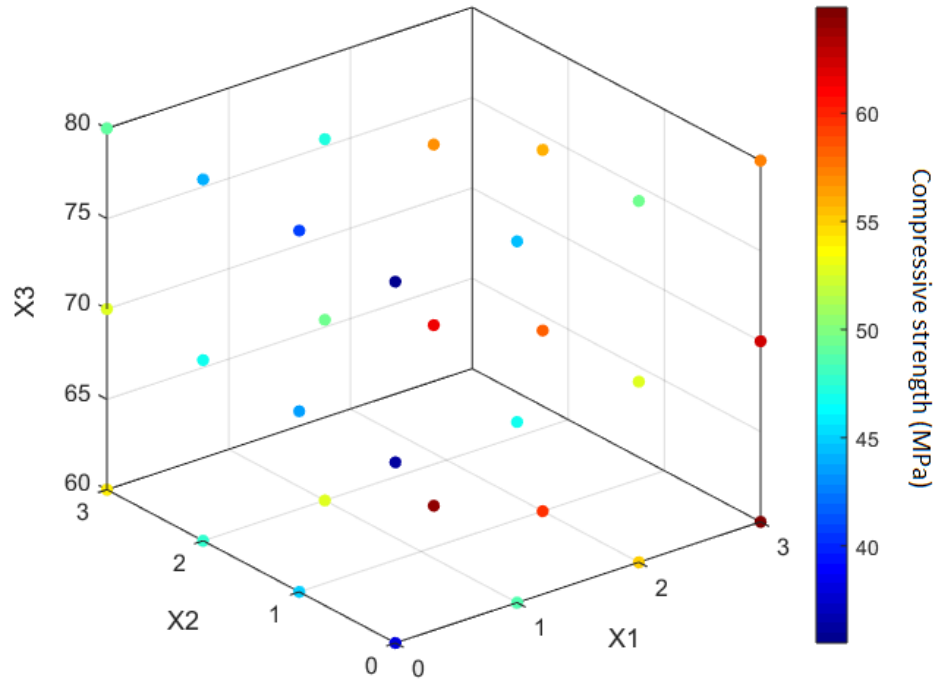


Figure 3.10. The initial population to extract the f_1 function using the meta-modeling

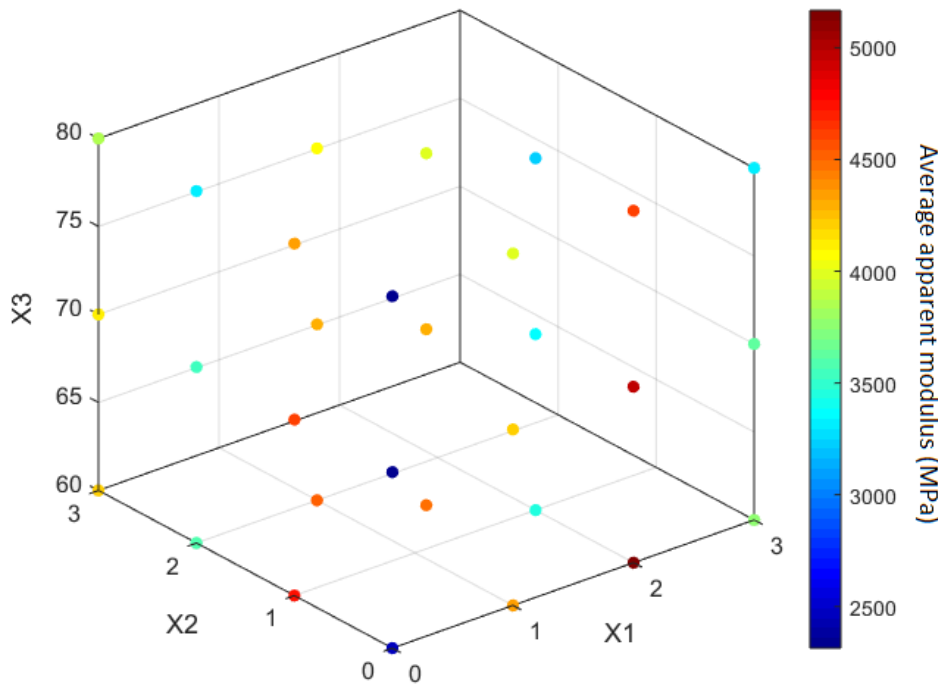


Figure 3.11. The initial population to extract the f_2 function using the meta-modeling

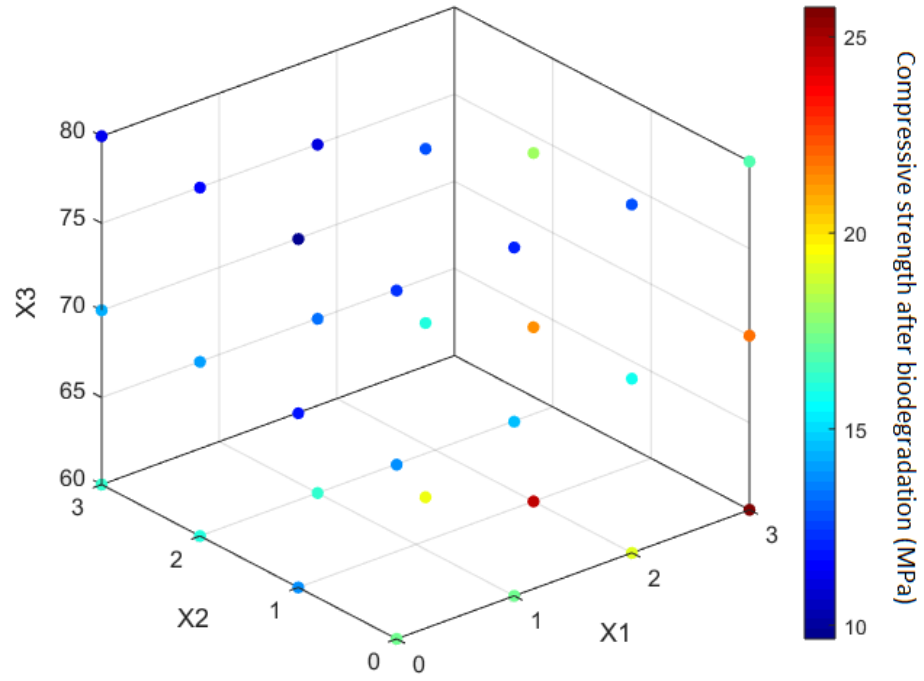


Figure 3.12. The initial population to extract the f_3 function using the meta-modeling

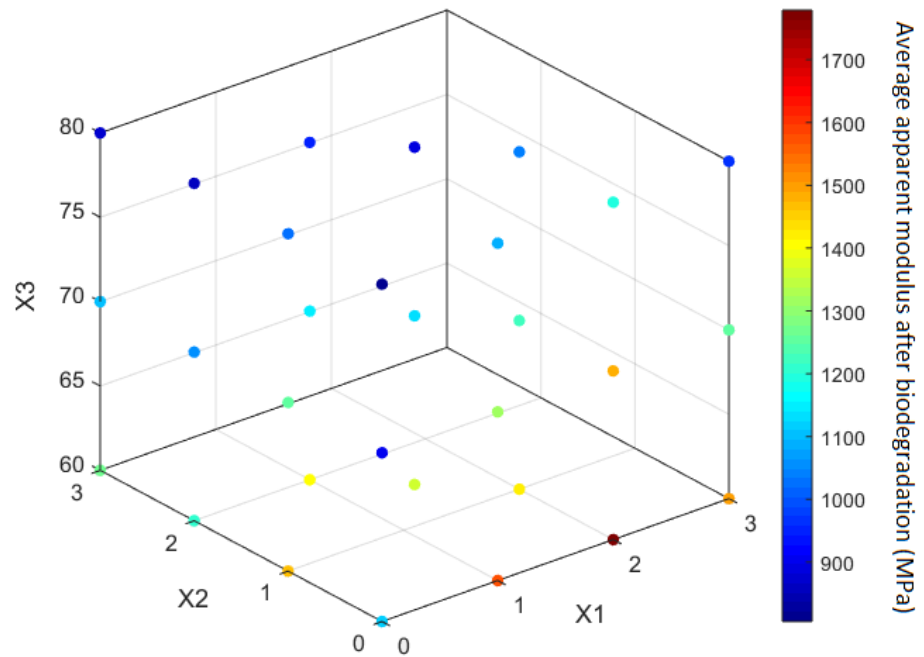


Figure 3.13. The initial population to extract the f_4 function using the meta-modeling

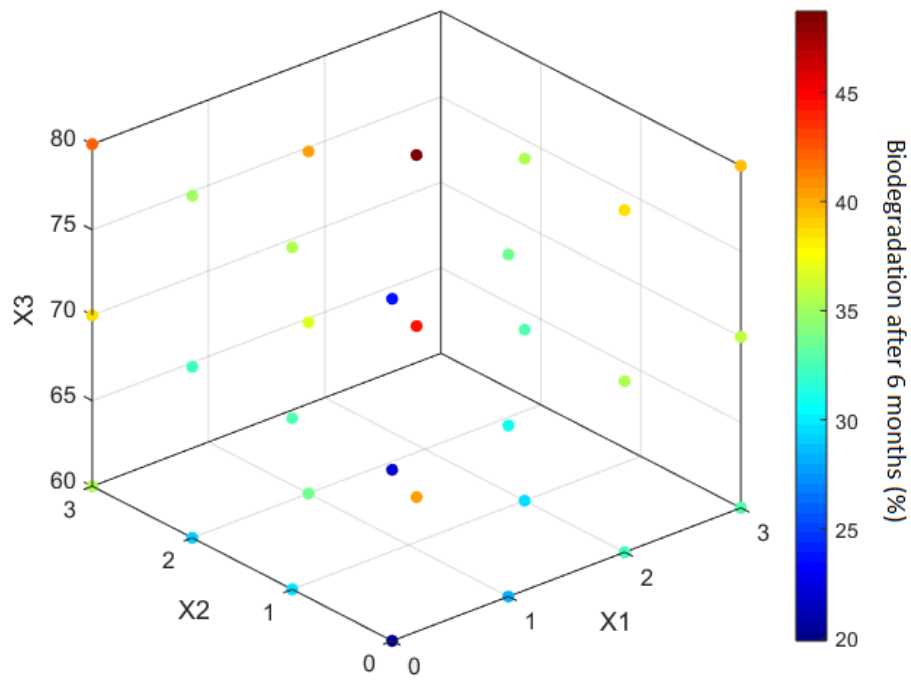


Figure 3.14. The initial population to extract the f_5 function using the meta-modeling

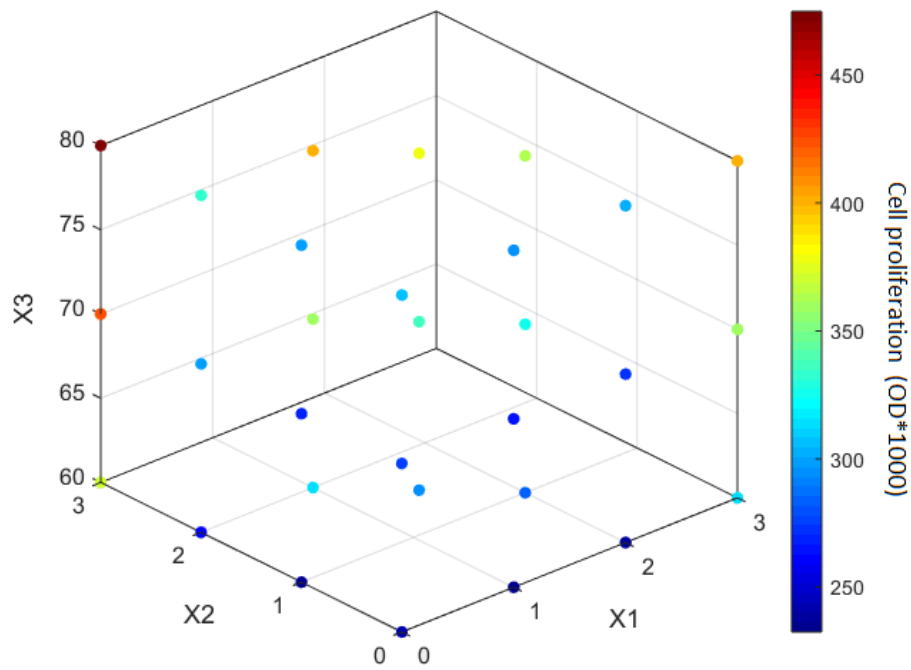


Figure 3.15. The initial population to extract the f_6 function using the meta-modeling

3.5.2 Multi-Objective Optimization

The achieved objective functions by meta-modeling are optimized using the NSGA-III method. The NSGA-III algorithm was performed employing the PlatEMO MATLAB-based platform [201]. This method is designed to encounter numerous objectives at the same time. The algorithm is the third generation of NSGA algorithms proposed by Deb and Jain [202, 203] to handle many-objective constrained optimization problems. The algorithm steps of NSGA-III (NSGA-III algorithm flowchart is shown in Figure 3.16) are described as follow [202, 204]:

1. Calculating the number of reference points to place on a Hyper-Plane
2. Generating the initial population randomly by considering the resources assignment constraints
3. Applying the non-dominated population sorting mechanisms
4. **for** $i = 1$ stopping criteria **do**
5. Selecting two parents P1 and P2, using the tournament method
6. Applying the crossover with a probability of P_c
7. Applying the non-dominated population sorting mechanisms
8. Normalizing the population members
9. Associating the population members with the reference points
10. Applying the niche preservation operation
11. Keeping the niche obtained solutions for the next generation
12. **end for**

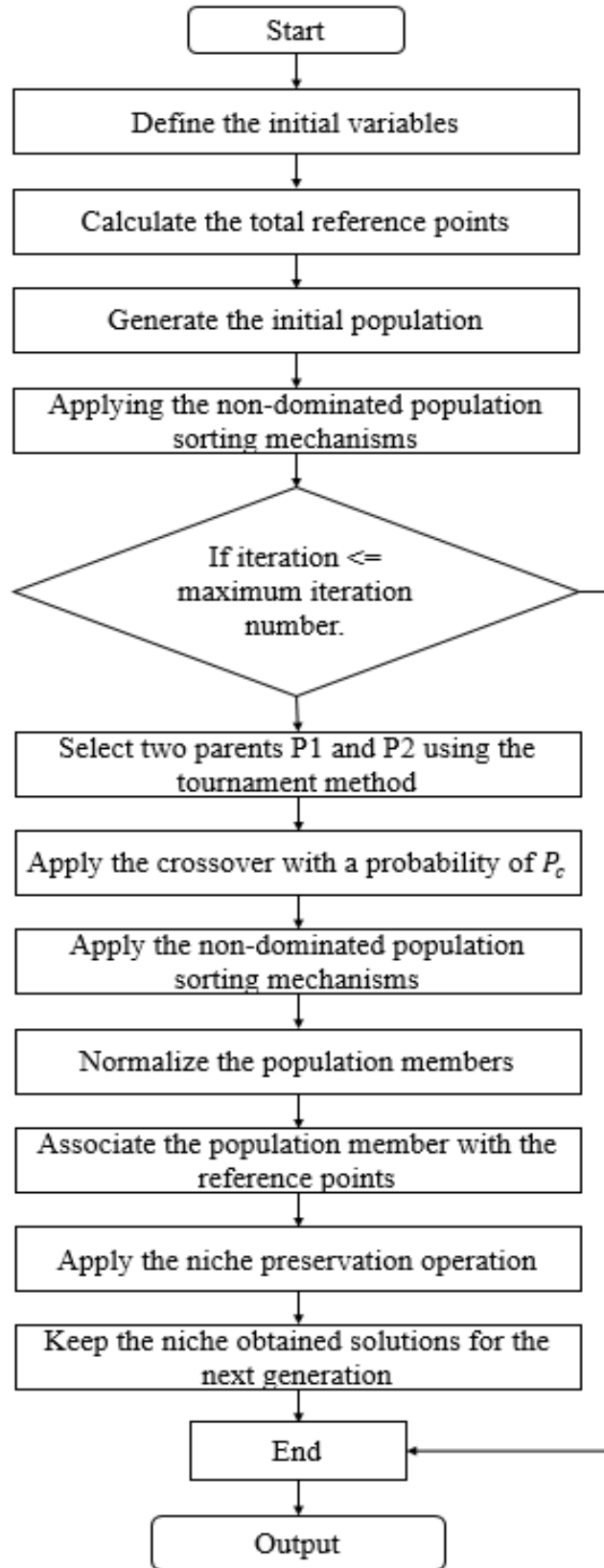


Figure 3.16. Flowchart of the NSGA-III optimization algorithm

In the optimization process, the six objective functions are defined as $f_1 - f_6$. The percentage of nHA content in the nanocomposites (X_1) and percentage of CNW content in the nanocomposites (X_2) were considered $0 \leq X_1 \leq 3$ and $0 \leq X_2 \leq 3$ to match the experimental results and the manufacturing restrictions. Also, $X_1 + X_2$ was defined to be equal and lower than 3. The porosity percentage of the Gyroid designed scaffolds (X_3) was defined as $60 \leq X_3 \leq 90$ to match the practical region close to the experimental data. Optimization was performed to maximize all of the functions to have maximum initial mechanical properties, mechanical properties after four months of biodegradation, biodegradation rate after six months, and cell proliferation. The results are reported as a set of non-dominated options for the optimal responses of the functions.

Chapter 4. Characterization Methods

In this chapter, the employed methods to experimentally characterize the manufactured experimental specimen are introduced and explained. This study has been focused on two general types of products, including polyester scaffolds with advanced TPMS designs and PCL/nHA/CNW nanocomposite PBTSs. To assess the impact of design, porosity, and biodegradation on the mechanical and morphological properties of the PBTS, 3D structures with advanced TPMS designs and different porosities were manufactured using PLA, which is a polyester with the same type of dominant biodegradation mechanism of PCL. These experiments were defined to investigate the mentioned characteristics independent of the material composition of the scaffolds. In the next set of experiments, the nanocomposite 3D printed scaffolds were characterized to assess their material composition precision, mechanical properties, and biological characteristics. These characterizations are designed to assess the properties of FDM printed nanocomposites independent from their 3D design. The combinations of methods and analyses explained in this chapter will lead to analyzing the essential properties of the scaffolds.

4.1 Effect and Impact of Design, Porosity, and Biodegradation on the Mechanical and Morphological Properties of the Scaffolds

The main aim of this section is to assess the effects of design, porosity, and biodegradation on the mechanical and morphological properties of triply periodic minimal surface (TPMS) scaffolds. The TPMS scaffolds were designed and manufactured with different porosities using the fused depositing modeling (FDM) technique. The biodegradation tests on the scaffolds were performed for four and six months. The mechanical properties were

assessed employing ASTM standard compression test and an in-situ mechanical testing stage. The Microcomputed tomography (Micro-CT) technique was used to investigate detailed morphological properties of the scaffolds in 3D.

4.1.1 Mechanical Testing

Two methods were used to measure the mechanical properties of the designed scaffolds. In one, an in-situ testing stage of Micro-CT scanner SkyScan 1172 Bruker was employed at different stages of compression testing. The compression tests were carried out with a very low displacement rate. 3D scanning of the experimental samples was carried out at strains of 0%, 5%, and 10% before biodegradation and at strains of 0% and 3% after biodegradation to observe the effect of load on the morphology of the structures. The strain values for the 3D scans were chosen before reaching the mechanical failure of the scaffolds. All the tests were performed on the scaffolds before and after biodegradation to assess the impact of biodegradation on the mechanical properties. The images were captured with a pixel size of 8.99 μm , and the flat field correction was done to ensure the quality of the captured images [205-208]. The voltage and current of the X-Ray source were adjusted at 67 kV and 147 μA , respectively. The 360° scans were performed with 0.6° steps, and an average of 5 images per step were taken.

In the other method, the compression tests were performed on the scaffolds before and after biodegradation, using ASTM D1621-16 standard [209]. The tests were performed on at least five samples per design, as required by the ASTM standard. The tests were done using Lloyd LS100 Plus Materials Testing Machine with a displacement rate of 0.75 mm/min and test termination strain of 50%.

4.1.2 Biodegradation Impact Assessment

The biodegradation assessments of the designed structures were performed after extended periods of 4 and 6 months. PBTS should preserve a portion of their mechanical strength and morphological properties over the biodegradation period to assist the native tissue to grow appropriately. This process will take a few months for the majority of applications [53]. Therefore, 4 and 6 months of biodegradation periods were chosen to analyze the variations of these properties. The scaffolds were kept in RPMI-1640 medium (from Sigma-Aldrich) inside an incubator, at the temperature of 37°C with 5% carbon dioxide atmospheric condition. Multiple samples of each design were assessed. After the biodegradation period, the samples were washed using phosphate buffer saline (PBS) solution and iso-propyl alcohol 70%, and then they were air-dried at 40°C for 8 hours before the assessments.

High-resolution SkyScan 1172 (Bruker, Belgium) Micro-CT scanner was employed to study the biodegradation effects on the scaffolds' morphology. A Hamamatsu C9300 11 Mp camera with a pixel size of 8.99 μm was used to capture the images. The details of the Micro-CT conditions were maintained the same as the conditions explained in Section 4.1.1.

4.2 Material Characterization

4.2.1 Thermo-Gravimetric Analysis (TGA)

The nanocomposites matrix (PCL) and the nanofillers employed in this study have distinguished thermal degradation behaviors, including mass loss patterns and the final residual weight percentage. By taking advantage of these properties, TGA was employed

to investigate the accuracy of the manufactured composites based on ASTM E1131 – 20 standard [210]. PCL and CNW, along with all of the manufactured nanocomposite filaments, were heated at the rate of 10 °C/min from 0°C to 600°C. The patterns and residual weight of the composites were compared with the raw materials' patterns, and the content percentages of the nanocomposites were investigated. This process was done as the final material characterization method and as a quality control step during the manufacturing of the nanocomposites.

4.2.2 Fourier Transform Infrared Spectroscopy (FTIR)

FTIR spectra of the selected manufactured nanocomposite filaments were recorded employing a Perkin Elmer Spectrum 100 FT-IR spectrometer to identify the presence of the functional groups related to the nanofiller components in the nanocomposites. KBr powder was used as the matrix to fabricate the FTIR pellets for the tests. The transmission method was employed for the tests at room temperature. The spectra were recorded at an average of 16 scans in the standard wavenumber range of 400–4000 cm^{-1} at a resolution of 4 cm^{-1} .

4.3 Mechanical Properties of the 3D Printed Nanocomposite Polymeric Bone Tissue Scaffolds

The mechanical properties of the final 3D printed nanocomposite Polymeric Bone Tissue Scaffolds (PBTSS) were analyzed employing the ASTM D1621-16 standard [90, 209]. The structures were 3D printed in cylindrical form with a height of 4 mm and a diameter of 8 mm. All tests were performed at least on five specimens of each nanocomposite PBTSS. Lloyd LS100 Plus Materials Testing Machine with a displacement rate of 0.75 mm/min

and the test termination strain of 50% was used for the compression tests. Figure 4.1 represents examples of the 3D printed mechanical testing specimens.



Figure 4.1. Examples of the five mechanical testing specimens (PCL) as required by the ASTM D1621-16 (the circles around the samples are the build plate adhesions)

4.4 Biological Properties of the 3D Printed Nanocomposite Polymeric Bone Tissue Scaffolds

A preosteoblast bone cell line was employed to assess the biological properties of the FDM manufactured nanocomposite PBTs. MTT assay and fluorescent microscopy were performed to assess cell proliferation and attachment to the scaffolds. Experimental biodegradation assessments were performed, and during the biodegradation process, the impact of the degraded materials on the pH of the media was assessed as well.

Preosteoblast mouse bone cell line, MC3T3-E1 Subclone 4 (ATCC® CRL-2593™) [211], was employed for cell-based assays. Alpha Minimum Essential Medium without ascorbic acid (by GIBCO, Custom Product, Catalog No. A1049001) was employed as the growth medium. The cells were double-stained by DAPI (purchased from Sigma-Aldrich) and Phalloidin CF®640R (provided by Biotium Inc.) for fluorescent microscopy purposes. MTT (3-(4,5-Dimethylthiazol-2-yl)-2,5-Diphenyltetrazolium Bromide) assay provided by Thermo-Fisher Scientific was employed for cell proliferation assays.

4.4.1 MTT Assay

MTT assay was performed to investigate cell proliferation on the manufactured nanocomposites. The composites were 3D printed in the exact size of the standard 96-well plates to enhance the quality of the test results, and they were fixed mechanically on the bottom of each well. The contact surface of each well with the cells was covered 100% by the nanocomposites by implementing this approach. As mentioned, the tests were all performed on the final 3D printed PBTSs. The scaffolds were sanitized before the cell culture in three consecutive steps, including rinsing with 70% isopropyl alcohol, rinsing three times with PBS, and exposure to UV light for 15 minutes.

MTT assays were done after 1, 3, and 7 days of cell culture on each nanocomposite product. For each of the tests, five replicates of each composite were tested (cell culture was also done on the original surface of the wells as control samples). Figure 4.2 presents the 96-well plates, which were prepared for the MTT assay for 1, 3, and 7 days, and Figure 4.3 shows the plates inside the incubator. The number of initially seeded preosteoblast cells has to be selected to not confluent the plates before seven days to achieve reliable results for cell proliferation assessments. Based on previous studies in the literature [22, 211-215], 3000 MC3T3-E1 cells per well were seeded on the scaffolds in the first stages (the initial number of cells per well was chosen by considering the number of cells seeded in the literature and their results). Based on the final results, most of the plates were confluent after 3-4 days of cell culture, and no comparison could be made to understand cell proliferation. Thus, the number of the seeded cells was reduced to 1000 MC3T3-E1 cells per well; this cell density demonstrated favorable results, and the cell proliferation comparative results after seven days of cell culture were achieved.

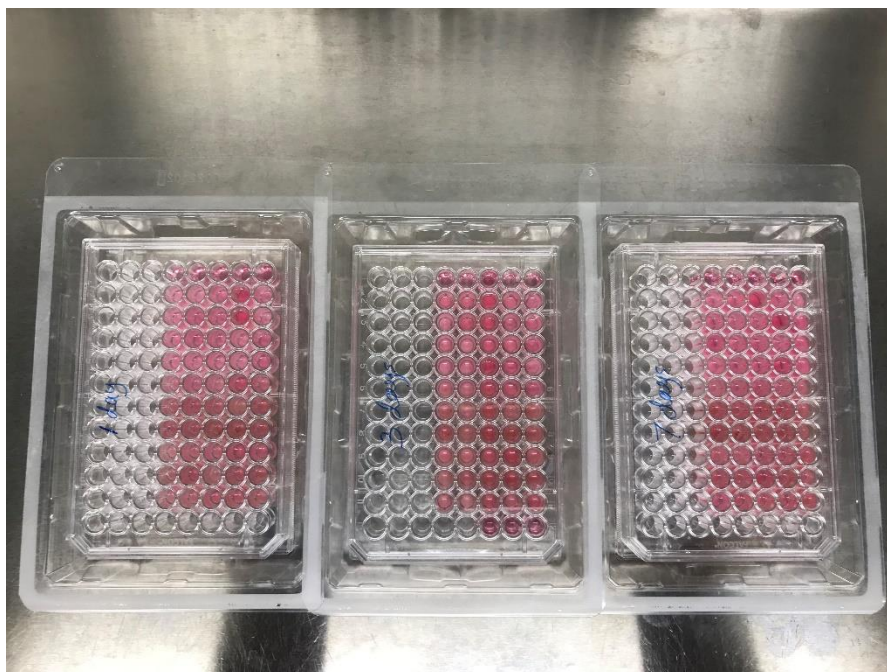


Figure 4.2. 96-well plates prepared for MTT assays



Figure 4.3. MTT-assay 96-well plates inside the incubator

4.4.2 Fluorescent Microscopy

Fluorescent microscopy was carried out to visualize the cell nuclei and actin filaments of the seeded MC3T3-E1 cells on the scaffolds after 1, 3, and 7 days of cell culture. A specific slide chamber was designed and manufactured using the FDM technique to culture the cells on the scaffolds embedded on a microscope slide. PLA filaments were used to manufacture the slide chamber because of the significant melt temperature difference with the main matrix of the manufactured scaffolds. The design consists of a base and a chamber (top part), as shown in Figure 4.4. The base was thermally fixed on the glass slides by heating the slides up to 140°C and sealed using commercially available nail polish. The chamber was installed on the top of the area of interest to increase the slide chamber's capacity to hold the growth medium for the cells and was sealed around the edges. Afterward, the 3D-printed scaffolds were fixed in the area of interest on the glass slides, and the gap was sealed using the raw material of each scaffold, as shown in Figure 4.5.

The MC3T3-E1 cells were cultured for 1, 3, and 7 days on the scaffolds (Figure 4.6 presents the chamber slides inside the CO₂ incubator). The cells were fixed using paraformaldehyde 4% solution in PBS, and the 0.5% Triton X-100 solution was employed for permeabilization of the cells after fixation. After permeabilization of the cells, DAPI (by Sigma-Aldrich) and Phalloidin CF®640R (by Biotium Inc.) dilutions were used to stain the nuclei and actin filaments of the cells using the provided instructions by each of the manufacturing companies. Between each of the above steps, the cells were washed by rinsing three times with PBS. In the final stage, Invitrogen™ ProLong™ Gold Antifade Mountant with DAPI was used as the antifade mounting media. The cells were covered by

the slide cover glass and were cured for 24 hours before being sealed, and were refrigerated before visualization with a Leica DML fluorescent microscope.

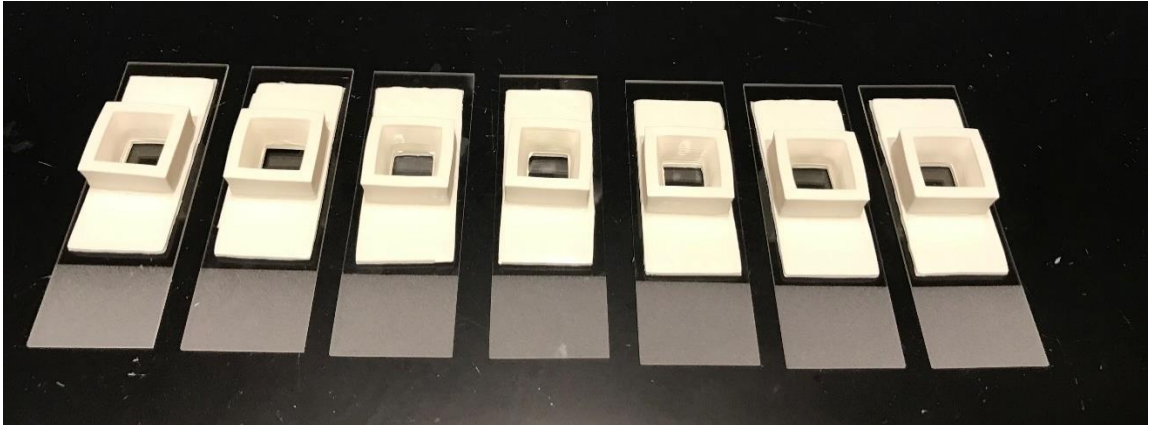


Figure 4.4. The manufactured chamber slides for cell culture on top of the scaffolds

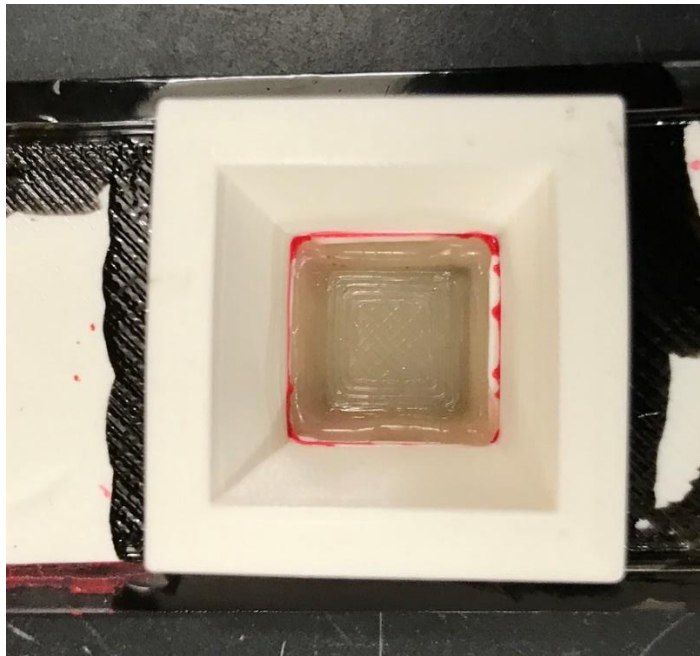


Figure 4.5. Fixed FDM printed nanocomposite scaffold on the manufactured chamber slides



Figure 4.6. Chamber slides inside the CO₂ incubator

4.4.3 Biodegradation and Acidity Analysis

The 3D printed products of the manufactured nanocomposite filaments were kept in the Alpha Minimum Essential Medium without ascorbic acid (by GIBCO, Custom Product, and Catalog No. A1049001), which was initially used as the growth medium of MC3T3-E1 cells, for four weeks inside a carbon dioxide incubator. The environmental factors were set on 37°C and 5% carbon dioxide for the biodegradation period. The samples were weighted initially before biodegradation. After the degradation period, the samples were washed three times by PBS, air-dried at 40°C for 4 hours, and weighted again. The weight difference was reported as the biodegradation percentage. In addition to the biodegradation percentage, the pH level of the buffer solution was tested after each step to test the impact of biodegraded content on the pH of the buffer solution using the HI-2211 pH meter (Hanna instruments).

Chapter 5. Results and Discussion

In this chapter, the experiments, simulations, and data analyses results are reported and discussed in detail. The impacts of design, porosity, and biodegradation on the mechanical and morphological properties of the scaffolds were experimentally assessed, independent from the material composition of the 3D printed structures. In the next set of experimental analyses, the properties of the FDM manufactured nanocomposite Polymeric Bone Tissue Scaffolds (PBTSS) are investigated in detail, independent of their 3D design impact. The material characterization results were reported to investigate the accuracy of the manufactured nanocomposite FDM filaments, and the optimized FDM processing conditions of the nanocomposite filaments were discussed using the Taguchi orthogonal array method. Mechanical, biological, and biodegradation properties of the manufactured nanocomposite PBTSS were discussed using experimental characterizations. After a detailed discussion of the experimental data, numerical simulation was employed to estimate the biodegradation rate of the 3D printed nanocomposite Gyroid scaffolds in the long term. The Biodegradation rates of the PBTSS were estimated for sixty weeks of biodegradation based on the numerical analyses along with the state of the art biodegradation estimation techniques in the literature. In the mentioned sections, a significant amount of experimental and numerical data were achieved. The results were achieved in independent analyses and were required to be connected to analyze the impact of design and the nanocomposite contents of the bone tissue scaffolds altogether. For this purpose, machine learning techniques and multi-objective optimization were employed to analyze all sets of the available results and propose non-dominated optimal options for the

porosity and the nanocomposite contents of the PBTSs. Meta-modeling and NSGA-III multi-objective optimization methods were employed to achieve the mentioned goal.

5.1 Investigation of the Effects of Design, Porosity, and Biodegradation on the Mechanical and Morphological Properties of the Scaffolds

5.1.1 Impact of Design, Porosity, and Biodegradation on the Mechanical Properties

In this section, part of the results of the characterization methods described in Section 4.1 were analyzed in three stages. In the first step, the mechanical properties of the TPMS designs were compared for different porosities to assess the impact of design and porosity on the mechanical strength. In the second stage, the effect of biodegradation was investigated after six months of biodegradation. In the end, the effect of biodegradation on the failure patterns of the designs was assessed.

5.1.1.1 Impact of Porosity and Design on the Mechanical Properties

Table 5.1 shows the results of the compression mechanical testing on the scaffolds. The results indicate that Neovius structures (N60 and N80 stand for Neovius with 60% and 80% porosity) have inferior mechanical strength compared to Gyroid (G60 and G80 stand for Gyroid with 60% and 80% porosity) and Schwarz-D structures (S60 and S80 stand for Schwarz-D with 60% and 80% porosity).

The N80 design exhibits a compressive strength close to S80, but its apparent modulus is inferior. The S60 scaffold showed the highest compressive strength and apparent modulus among all of the designs, but its mechanical properties dropped drastically on increasing the porosity. S80 exhibited much lower compressive strength than S60, as shown in Figure 5.1. The Gyroid structure shows better stability with the increase in the design porosity.

G60 has lower mechanical properties than S60, but the compressive strength and apparent modulus did not change considerably on increasing the porosity. It can be concluded from the results that the Gyroid structure is the best choice for the high porosity scaffolds.

The Schwarz-D structure exhibited an unusual response to mechanical loading in the case of the high porosity structures. The scaffold's response to the compression load changed from a single-stage mechanical failure to multiple stages of failures. When the porosity was increased from 60% to 80%, the mechanical response indicated layer by layer failure, as shown in Figure 5.2. After each layer's failure, which follows by a sudden decrease in the mechanical properties, the remaining structure regains strength; this occurs multiple times before the total failure.

Table 5.1. Mechanical properties of the TPMS scaffolds (ASTM D1621-16)

Sample	Average Compressive strength (MPa)	St. dev. (MPa)	Average Apparent modulus (GPa)	St. dev. (GPa)
G60	126.47	5.84	2.63	0.25
G80	124.39	1.45	2.09	0.07
S60	204.97	9.51	3.66	0.09
S80	52.08	1.59	1.41	0.29
N60	92.83	1.90	1.13	0.25
N80	45.18	2.35	0.95	0.37

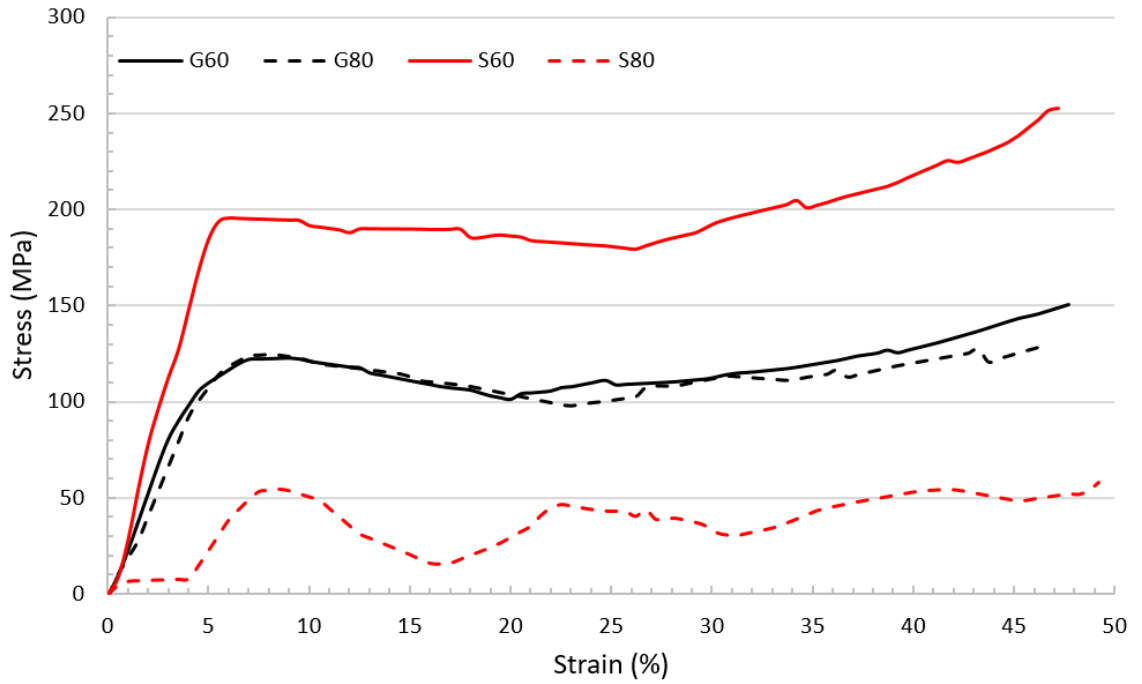


Figure 5.1. Representative stress-strain curves of the TPMS scaffolds

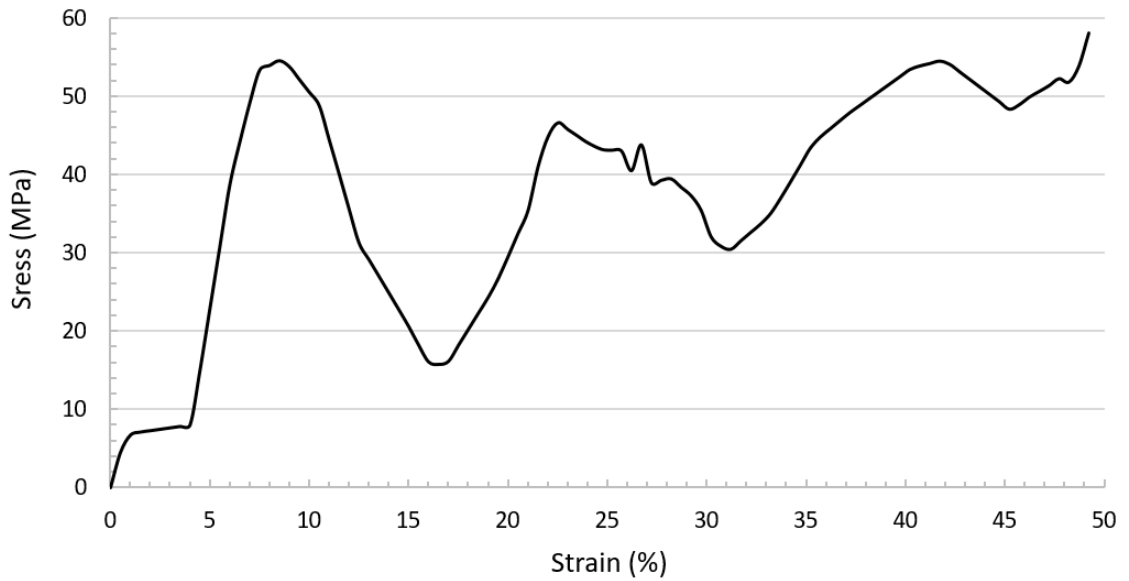


Figure 5.2. Representative stress-strain curve of the Schwarz-D 80% scaffolds

5.1.1.2 Effect of Biodegradation on the Mechanical Properties

Due to the significantly inferior mechanical properties of the Neovius scaffolds, they were not used for further evaluations. Mechanical properties of the other scaffolds after six months of biodegradation are given in Table 5.2 and shown in Figure 5.3 (AD stands for After Degradation).

The results clearly show that the G60-AD scaffolds had the highest mechanical properties among the biodegraded scaffolds. The loss in the initial mechanical properties of the G60 after six months of biodegradation was lower than the Schwarz-D scaffolds. The G60 scaffolds initial compressive strength suffered a loss of 73% (G60-AD) after biodegradation, whereas the S60 scaffold lost almost 85% of its strength after biodegradation (S60-AD). More significantly, G80-AD lost 83% of their strength but retained strength of almost 20 MPa, which was still approximately more than half of the G60-AD scaffolds. The results for G60-AD and G80-AD indicate the same understanding regarding the effect of porosity on the mechanical properties of Gyroid structures, as the values are not considerably lower for G80-AD. S80 scaffolds lost all of their strength and completely disintegrated (S80-AD).

Another significant observation was the transformation of the failure mode from ductile to brittle after six months of biodegradation. Figure 5.4 compares the stress-strain curves of G60 and G60-AD to emphasize on the differences. The results indicate that in addition to the reduction in the compressive strength and the apparent modulus, the mechanical failure mode changes to brittle in G60-AD. Similar results are shown in Figure 5.3 for the other scaffolds after biodegradation.

Table 5.2. Mechanical properties of the TPMS scaffolds after biodegradation (ASTM D1621-16)

Sample	Average Compressive strength (MPa)	St. dev. (MPa)	Average Apparent modulus (GPa)	St. dev. (GPa)
G60-AD	34.43	0.72	0.79	0.08
G80-AD	21.01	6.52	0.63	0.22
S60-AD	31.62	3.99	1.51	0.12
S80-AD	0	0	0	0

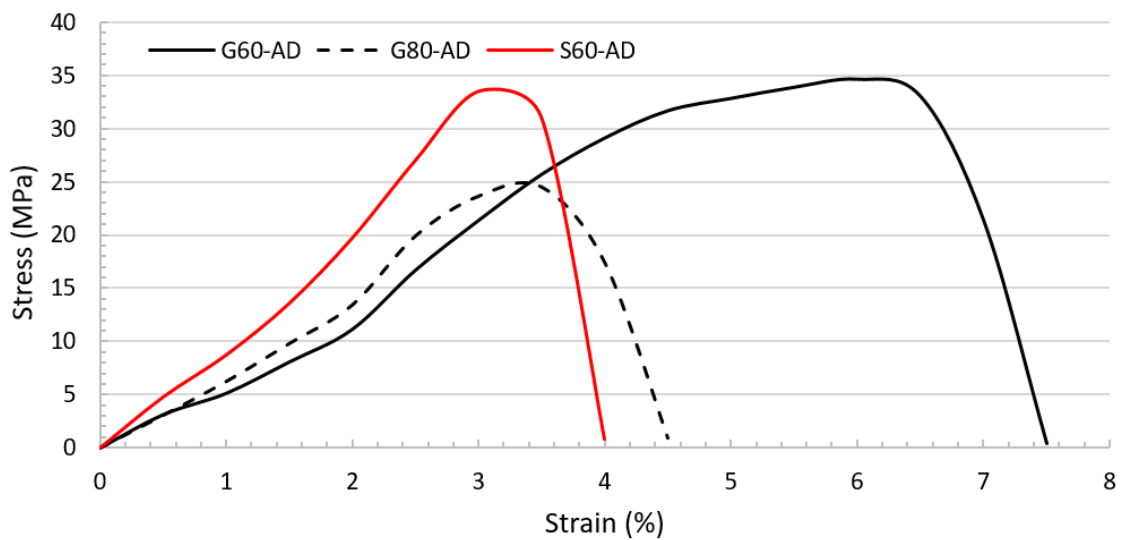


Figure 5.3. Representative of Stress-Strain curves of the TPMS scaffolds after biodegradation

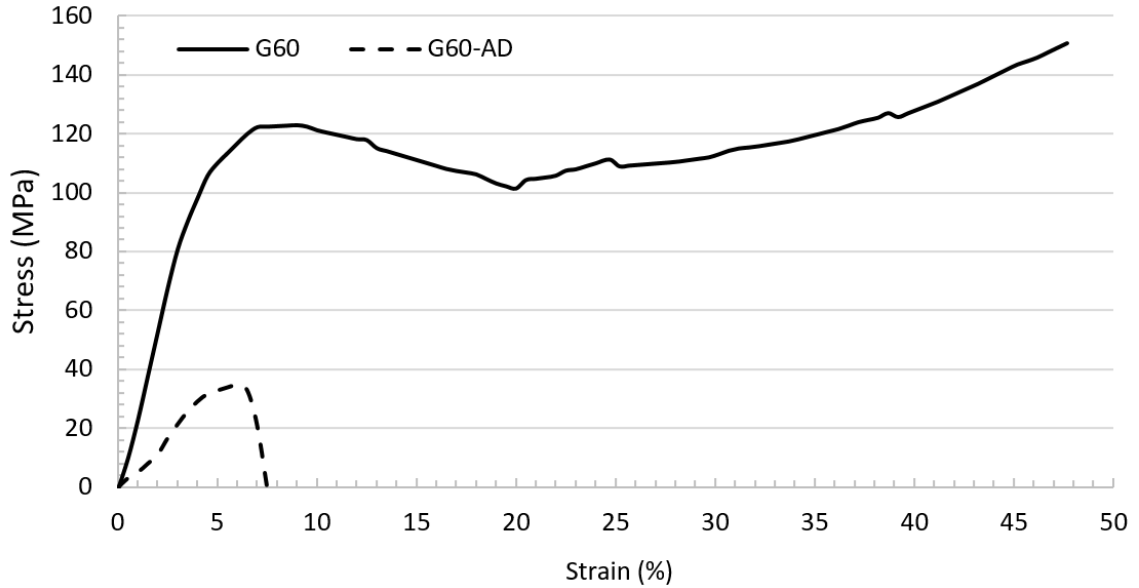


Figure 5.4. Representative of Stress-Strain curves of the Gyroid 60% scaffolds before and after biodegradation

5.1.1.3 Fracture Pattern of the Scaffolds

Figure 5.5 shows the pictures of the mechanically failed scaffolds under the compression test before and after biodegradation. The G60, G80, and S60 scaffolds exhibited uniform deformation through all layers of the structure, which indicates the proper force transmission through the structures' layers. In the S80 scaffolds, the upper layers were crushed without any sign of failure in the lower layers, which can be due to weaker connections between the layers. After six months of biodegradation, all of the scaffolds experienced brittle failure, as demonstrated in Figure 5.5 for G60-AD, G80-AD, and S60-AD. The failure occurs along the diagonal plane of the 3D structures, the normal failure plane under the compressive forces [155], which is the dominant cause of the failure. The comparison of S60 and S80, as well as S60-AD and S80-AD, reveals that by increasing the

porosity from 60% to 80%, the diagonal networks between the layers were significantly weakened, and the structure could not withstand compressive load on the diagonal plane anymore. S80-AD did not show any mechanical strength after biodegradation, and the structure failed just on touching the scaffolds. The S80-AD picture shows the structure after biodegradation without applying any compression load.

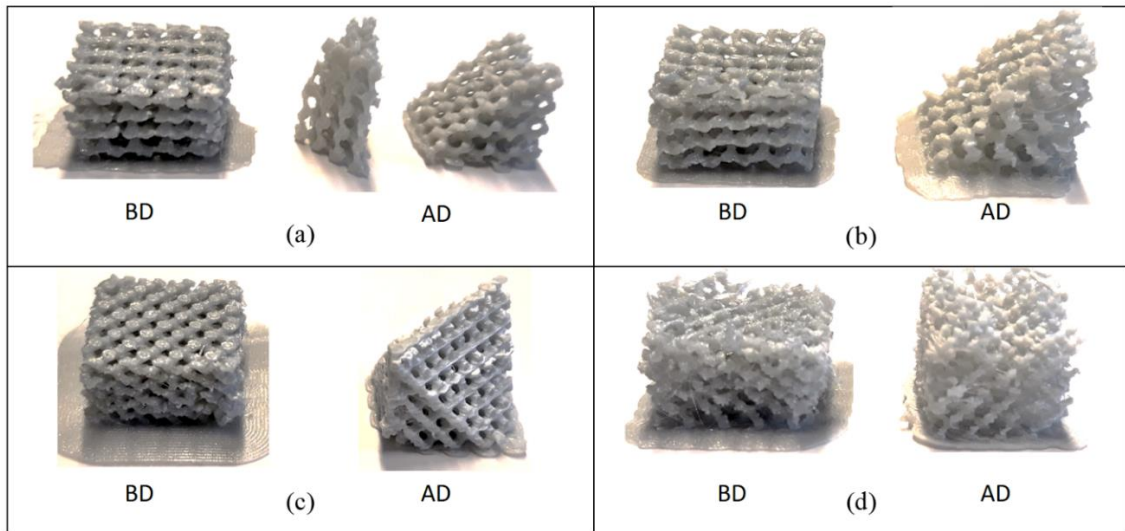


Figure 5.5. Pictures of the failed TPMS structures under compression load before degradation (BD) and after degradation (a: G60 and G60-AD; b: G80 and G80-AD; c: S60 and S60-AD; d: S80 and S80-AD)

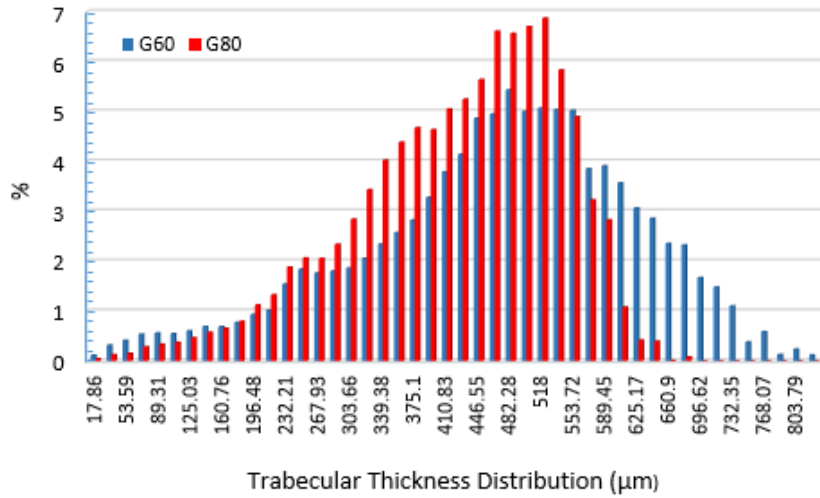
5.1.2 Impact of Design, Porosity, and Biodegradation on the Morphological Properties

The most critical morphological properties of PBTSs based on the literature are porosity, size (in this study, trabecular thickness distribution represents the variations in the size of wall thickness in the scaffolds), the shape of pores, and surface area per volume ratio [110, 183]. These factors have diverse effects on the biological and mechanical properties of the

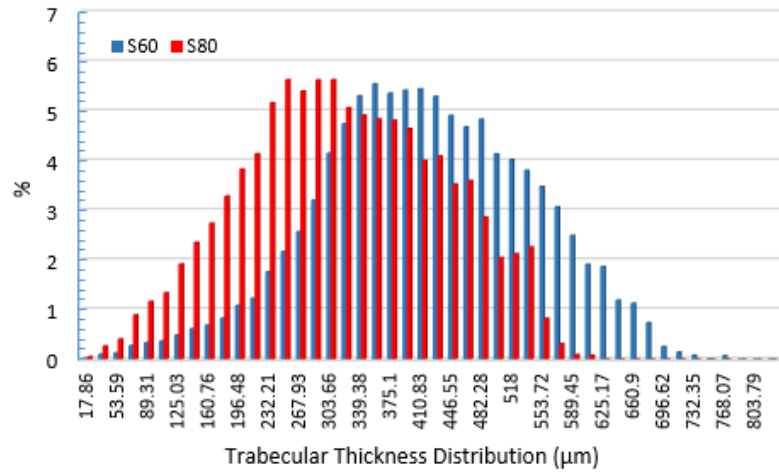
scaffolds. High porosity is a valuable asset for PBTSs as it improves cell migration and proliferation, which also increases the biodegradation rate [15, 183]. The impact of wall thickness depends on the design and is mostly effective on the biodegradation rate [179, 181, 182]. The shape of pores (pore size, homogeneity, and the proportion of closed, blind-end, or open pores) is defined by the manufacturing process or 3D design, which should be biomimetic to improve cell attachment and proliferation properties of the 3D scaffolds (in this study, the shape of pores vary by the TPMS designs) [183]. High surface area per volume is preferable for cell growth and increases the scaffolds' biodegradation rate [181]. All of the mentioned relations are applicable when the other factors remain constant. Therefore, assessment of these properties is of high importance. In each part of this section, the most related mentioned morphological properties were reported and assessed. The detailed morphological characteristics of the specimens, studied by Micro-CT scanning, are discussed in three major sections to separately assess the design, mechanical loading, and biodegradation impacts on the scaffolds morphology. The results of biodegradation were assessed after four (AD4) and six months (AD6).

5.1.2.1 Impact of the Design Porosity on the Morphological Properties

Figure 5.6.a shows the trabecular thickness distribution of the G60 scaffolds, which exhibits a skewed distribution with a median thickness of 464 μm and tissue surface area per volume of 577 μm^{-1} . On increasing the porosity to 80% (G80 scaffolds), the median of trabecular thickness distribution reduced to 428 μm . The tissue surface per volume remained unchanged, which indicates that the surface properties remained intact in the design process.



(a)



(b)

Figure 5.6. Trabecular thickness distribution of the TPMS scaffolds with different porosities (a: Gyroid; b: Schwarz-D)

The S60 trabecular thickness distribution is shown in Figure 5.6.b. The median thickness is 410 μm , and surface area per volume is 574 μm^{-1} . With an increase in porosity to 80% (S80), the trabecular thickness decreased, and the distribution shifted to the left (smaller thicknesses) by almost 127 μm , and the thickness median was reduced to 303 μm , but the tissue surface per volume slightly increased to 589 μm^{-1} . The decrease in the median of

the S80 design was considerable, which caused a significant increase in the population density of very thin walls, as shown in Figure 5.6.b. This property could be the reason for the specific detected mechanical responses of the S80 scaffolds in Section 5.1.1.1. The decrease in the G80 median had effect mainly on the midrange of wall thicknesses, leading to higher mechanical stability after the increase in the porosity. To assess the mentioned fact quantitatively, the margin of the first 20% of the trabecular thickness spectrum can be considered as the range with the lowest wall thicknesses; the population density of the mentioned range had changed from 3% to 11% and from 4.5% to 3% for Schwarz-D and Gyroid scaffolds by the increase in the porosity, respectively.

5.1.2.2 Effect of Compression Loading on the Morphological Properties

In this section, the morphology of the TPMS designs before and after biodegradation was analyzed under mechanical loading. Figure 5.7 illustrates the internal structure of the G80 scaffolds under compression loading at 0%, 5%, and 10% strains, and Figure 5.8 demonstrates the internal structure of G80-AD6 at 0% and 3% strains acquired by the Micro-CT scanning technique.

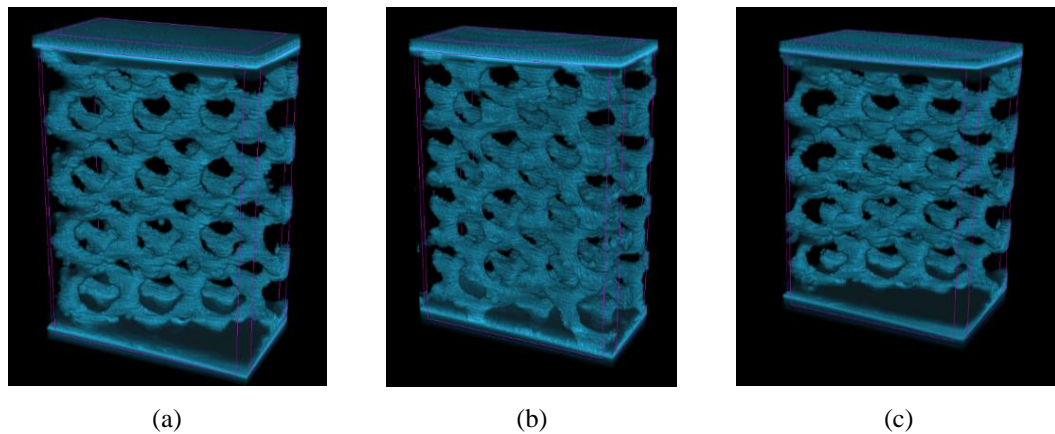


Figure 5.7. Internal structure of the Gyroid 80% under compression before biodegradation (a: G80 at 0% strain; b: G80 at 5% strain; c: G80 at 10% strain)

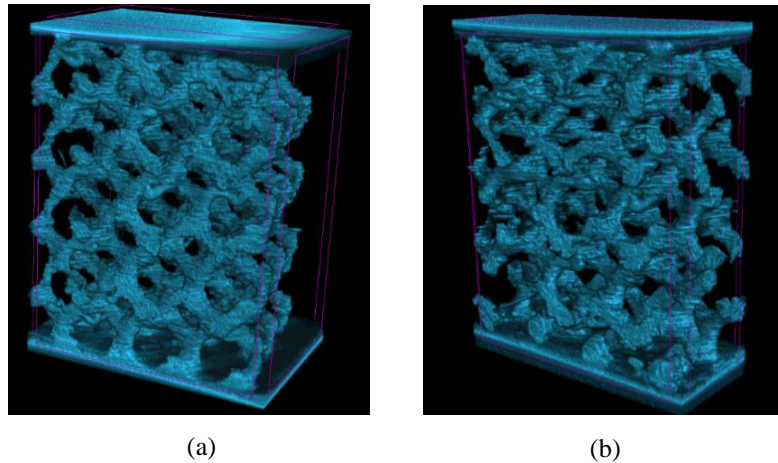


Figure 5.8. Internal structure of the Gyroid 80% under compression after biodegradation
(a: G80-AD6 at 0% strain; b: G80-AD6 at 3% strain)

Figures 5.9 and 5.10 demonstrate the effects of compression loading on the scaffolds' trabecular thickness distribution, at 0%, 5%, and 10% strains and at 0% and 3% strains, before and after biodegradation, respectively. The results showed an initial minor shift to the left in the trabecular thickness distribution of the G60 scaffolds at 5% strain, which remained almost unchanged for the rest of the deformation (10% strain). Deformation in the layers due to their ductile mechanical responses could be the reason. The variations in the rest of the morphological properties of the G60 were not significant. After six months of biodegradation, the porosity of the G60 increased by almost 2%, and the surface area per volume decreased by almost 3%, under mechanical load. G80 and G80-AD6 show the same morphological variation trends as G60 and G60-AD6.

S60 scaffolds experienced a 3% and 5% decrease in the porosity and increase in surface area per volume from $574 \mu\text{m}^{-1}$ to $599 \mu\text{m}^{-1}$ and $613 \mu\text{m}^{-1}$ at the strains of 5% and 10%, respectively. These variations can be due to the effects of deformation on the S60 scaffolds, which reduces the space between the adjacent layers and results in lower porosity and a very slight increase in the population density of thicker layers. After biodegradation, S60-

AD6 experiences a decrease in the tissue surface per volume (from $578 \mu\text{m}^{-1}$ to $536 \mu\text{m}^{-1}$) and a notable increase in porosity by almost 6%. The S80 scaffold shows the same pattern of variations as the S60 under mechanical load. Due to the lack of sufficient mechanical strength in the specimen S80-AD6, the morphological results were not attainable under mechanical loading.

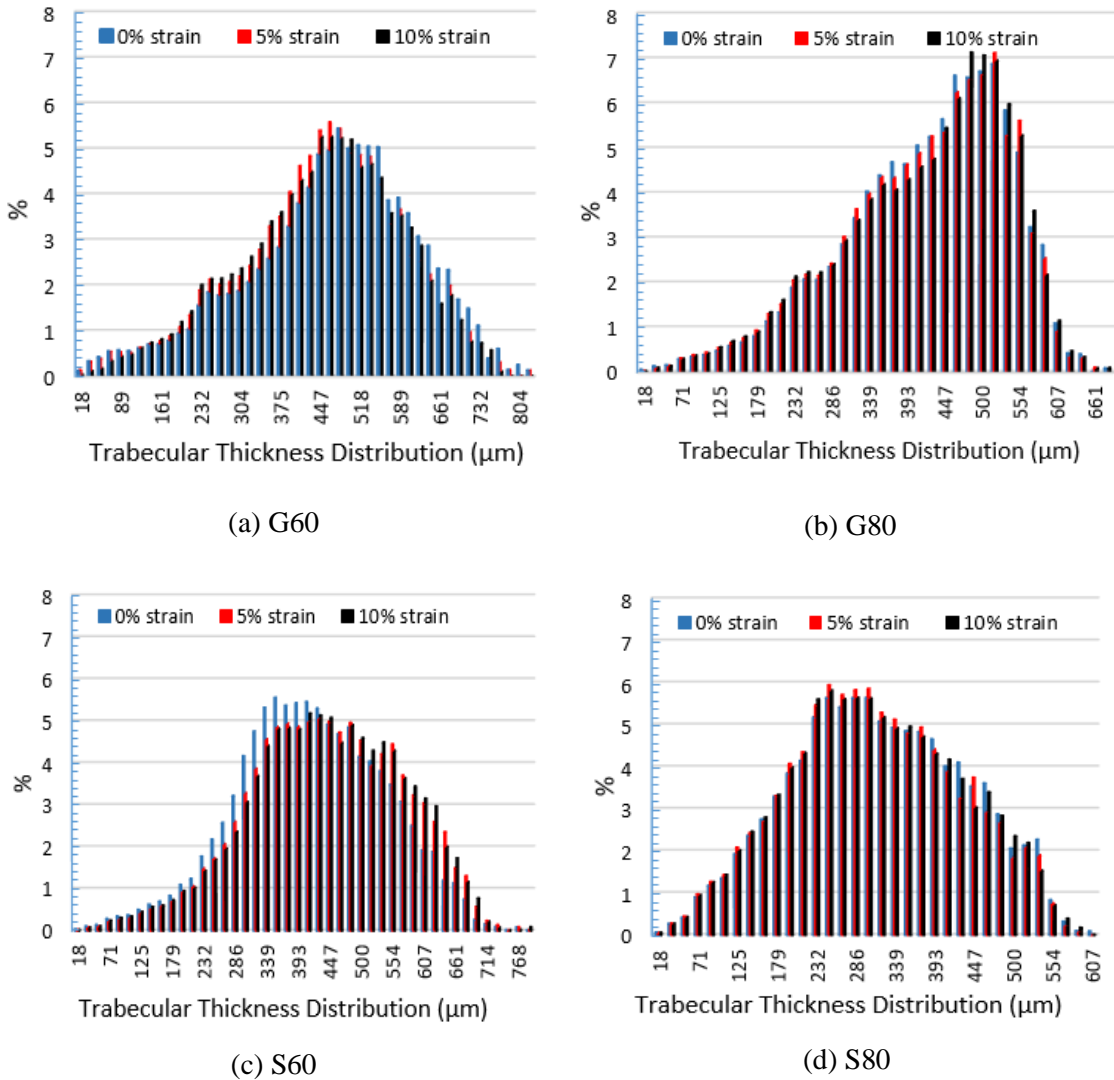
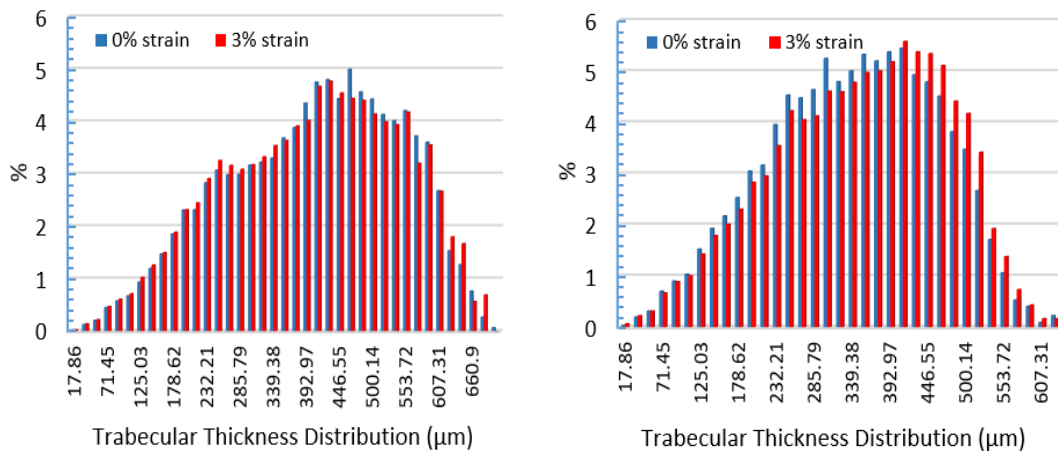
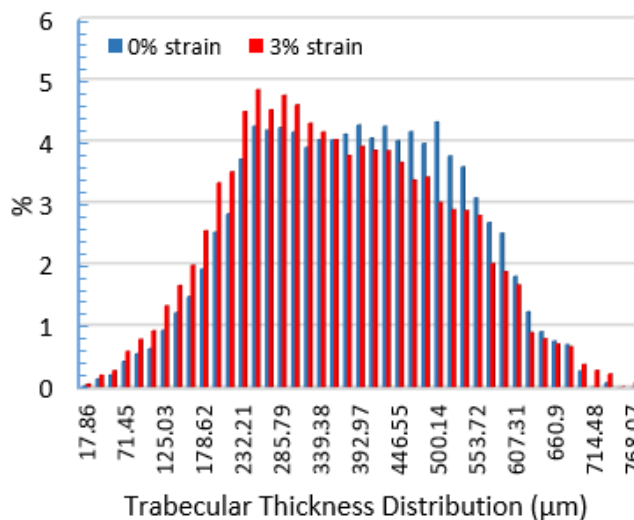


Figure 5.9. Trabecular thickness distribution of the TPMS scaffolds in 0%, 5% and 10% strains (a: G60; b: G80; c: S60; d: S80)



(a) G60-AD6

(b) G80-AD6



(c) S60-AD6

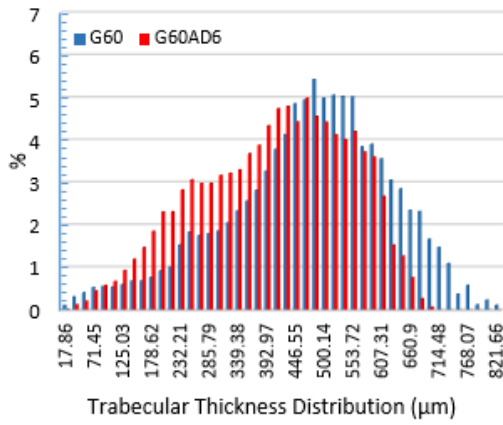
Figure 5.10. Trabecular thickness distribution of the TPMS scaffolds after biodegradation in 0% and 3% strains (a: G60-AD6; b: G80-AD6; c: S60-AD6)

5.1.2.3 Impact of Biodegradation on the Morphological Properties

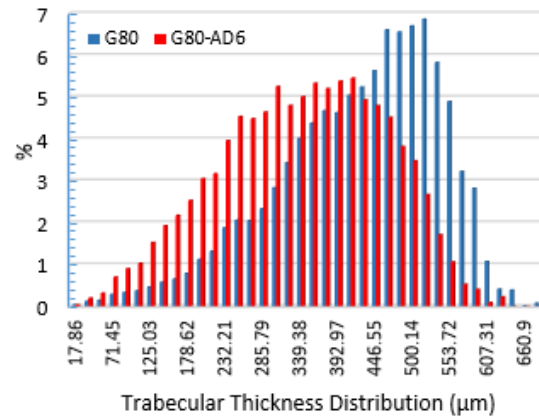
The effects of the biodegradation process on the TPMS scaffolds morphology are shown in Figure 5.11 and Table 5.3. In the G60 and G80 scaffolds, a decrease in the trabecular

thicknesses was observed upon biodegradation (Figure 5.11.a and b), which led to an increase in the porosity, as shown in Table 5.3. Increased porosity could be helpful in cell growth and expedite the biodegradation process afterward. Tissue surface per volume did not significantly change in Gyroid structures due to biodegradation, which indicates that the scaffolds surface properties were preserved during the biodegradation.

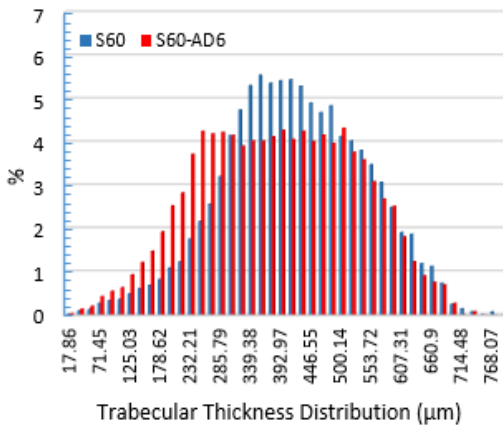
Figure 5.11.c shows that the S60 scaffold experienced trabecular thickness reduction mostly at the midrange of thickness distribution under biodegradation, and as a result, the population density at the lower thickness range increased. Figure 5.11.d indicates that after biodegradation, the trabecular thickness distribution of the S80-AD6 scaffolds experienced a considerable increase compared to S80 scaffolds. The reason is the collapse of walls and their coalescence. These structures, after biodegradation, did not possess any mechanical strength, and while loading the sample in the Micro-CT stage and even during the CT-scan process (which contains movement and rotation), parts of the structure were collapsing and coalescing. The significant increases of 5.49% and 7.32% in porosity after four and six months of biodegradation, respectively, demonstrated a high biodegradation rate for the S80 scaffolds. Due to this high biodegradation rate, the structure did not show any mechanical strength after biodegradation. Based on these results, S80 scaffolds just can be utilized in applications that require a high biodegradation rate and low mechanical properties.



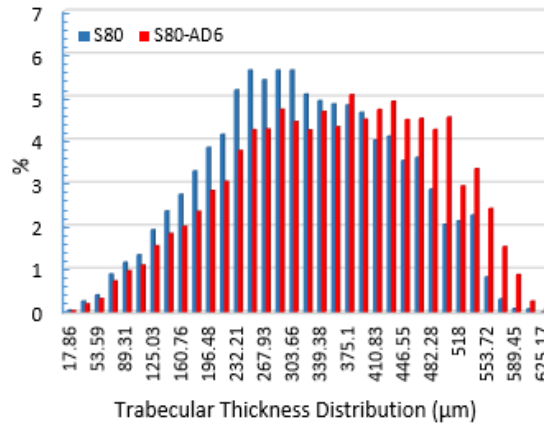
(a)



(b)



(c)



(d)

Figure 5.11. Trabecular thickness distribution of the TPMS scaffolds before and after biodegradation (a: G60 and G60-AD6; b: G80 and G80-AD6; c: S60 and S60-AD6; d: S80 and S80-AD6)

Table 5.3. Morphological properties of the TPMS scaffolds after biodegradation

Structure	Porosity increase by biodegradation (%)	Tissue surface per volume (μm^{-1})	Trabecular thickness median (μm)
G60	Reference	577 ± 2	464 ± 9
G60-AD4	3.25 ± 0.72	580 ± 1	426 ± 9
G60-AD6	4.89 ± 0.69	580 ± 2	410 ± 9
G80	Reference	577 ± 2	428 ± 9
G80-AD4	3.61 ± 0.74	581 ± 1	415 ± 9
G80-AD6	4.56 ± 0.72	592 ± 2	339 ± 9
S60	Reference	574 ± 2	410 ± 9
S60-AD4	2.79 ± 0.53	575 ± 2	401 ± 9
S60-AD6	3.14 ± 0.78	578 ± 2	375 ± 9
S80	Reference	589 ± 2	303 ± 9
S80-AD4	5.49 ± 0.64	589 ± 1	357 ± 9
S80-AD6	7.32 ± 0.81	591 ± 2	381 ± 9

5.2 Material Characterization of the Nanocomposite FDM Filaments

5.2.1 Thermo-Gravimetric Analysis (TGA) Results

The nanocomposites' TGA results were analyzed after careful consideration of the PCL and CNW thermal degradation patterns. The characterizations were performed after dividing the nanocomposites into three groups based on the types of nanofillers in each composite. Nanocomposites containing CNW, nHA, and hybrid nHA/CNW were analyzed separately.

Figure 5.12 shows the TGA results of PCL and CNW up to 600°C. PCL was completely degraded at 500°C, and only $0.2\% \pm 0.06\%$ of the weight percentage had remained. CNW

is the natural content of the nanocomposites, and its observed initial weight loss from 120°C to 200°C is mainly due to the loss of adsorbed water molecules, which is followed by a rapid weight loss starting after 250°C; at the end of the test, $28.5\% \pm 0.19\%$ of the initial mass had remained. The nHA is not degrading in this range of temperature change, and its residual mass at the end of the tests will be 100%.

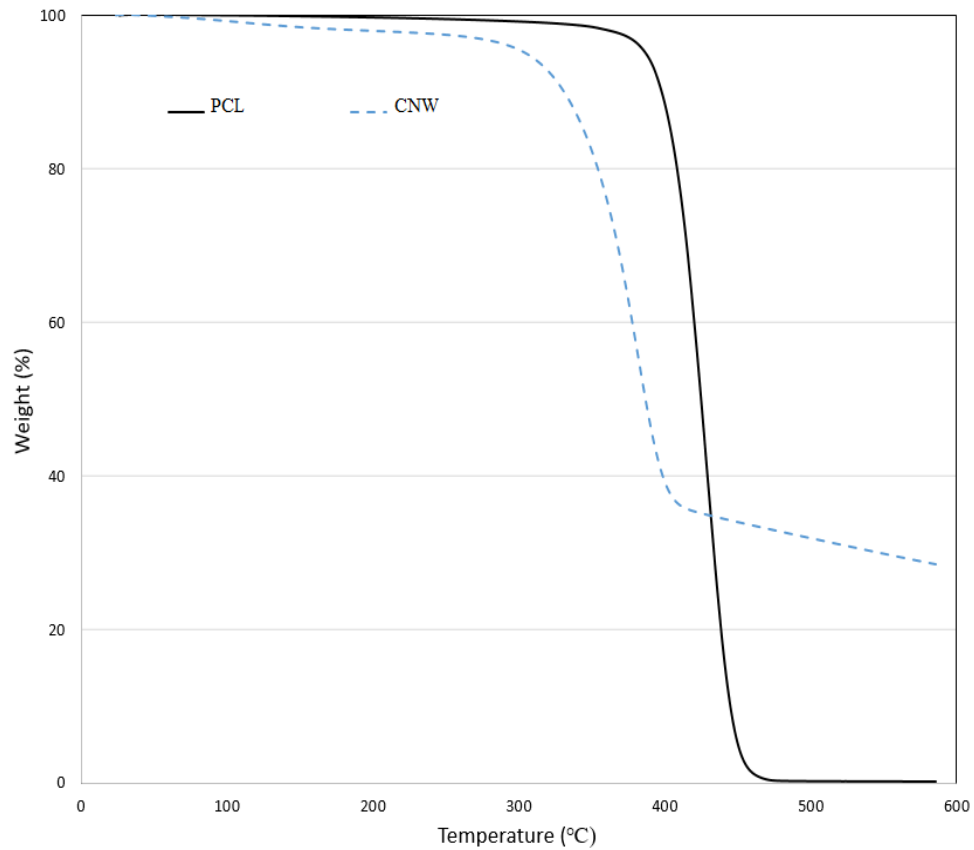


Figure 5.12. TGA results of PCL and CNW

The characterization of the nanocomposites precision was done based on the above analyses. In Figure 5.13, the TGA results for the composites with CNW nanofiller are demonstrated. The general trend of the TGA results was almost the same as PCL, but the mass residuals at the end of the experiment demonstrated a noticeable difference among the composites. The residual mass percentage was higher for higher percentages of the

CNW content, and the differences were evenly spaced in the graph. As shown in Figure 5.12, $28.5\% \pm 0.19\%$ of CNW mass would remain at the end of the experiment, which theoretically has to be almost 0.29%, 0.58%, and 0.87% for P-CNW1, P-CNW2, and P-CNW3, respectively. By closer inspection of the temperature range of 460°C to 600°C in Figure 5.13, P-CNW1 residual mass was $0.52\% \pm 0.04\%$ that is consist of $0.2\% \pm 0.06\%$ PCL, and the rest is CNW that precisely proves the 1% content of CNW in the nanocomposites. The residual mass for P-CNW2 and P-CNW3 were $0.93\% \pm 0.05\%$ and $1.33\% \pm 0.08\%$, respectively. These results are clearly confirming the precise percentage of CNW content in the nanocomposites.

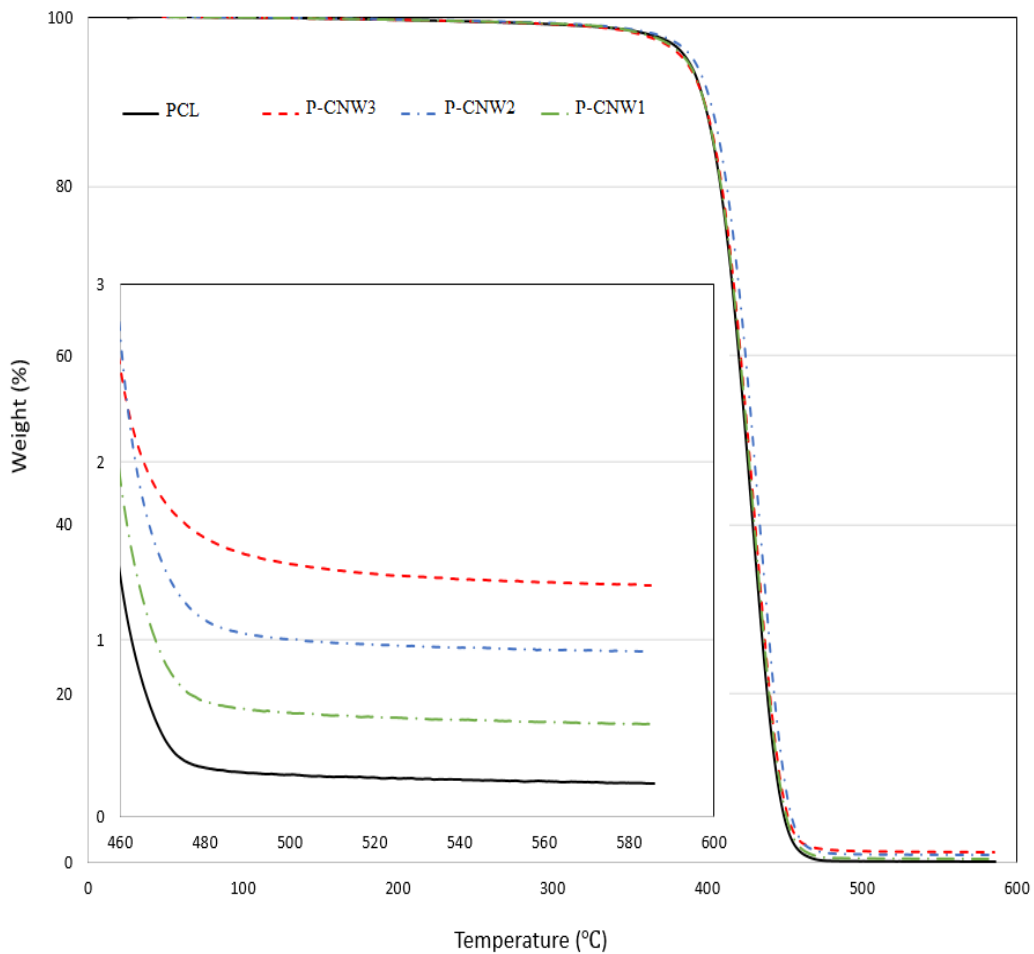


Figure 5.13. TGA results of the PCL/CNW nanocomposites compared to PCL

The nanocomposites with nHA nanofiller have a straightforward factor for characterization, as the nHA content will not degrade in the range of under 600°C. Figure 5.14 presents the TGA results of the nanocomposites with nHA nanofiller. By investigating the temperature range of 460°C to 600°C, it is clear that the remained mass percentages for the nanocomposites are evenly spaced with variation values of close to 1%. P-nHA1 had $1.19\% \pm 0.09\%$ residual mass percentage at the end of the test, which stands for almost 1% of nHA content, and the rest is PCL, as mentioned above. The P-nHA2 and P-nHA3 tests exhibited remained mass percentages of $2.23\% \pm 0.11$ and $3.18\% \pm 0.08$, respectively. The results clearly confirm the precise nHA contents in the manufactured nanocomposites.

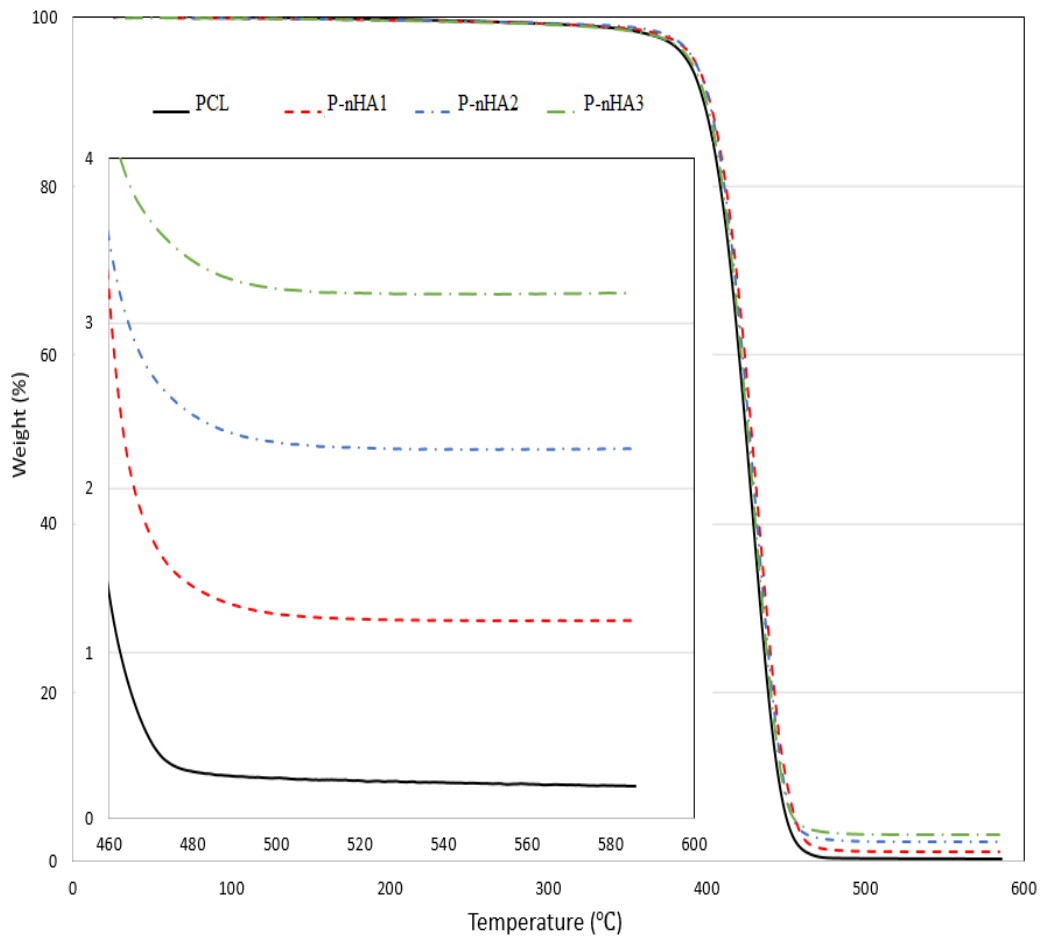


Figure 5.14. TGA results of the PCL/nHA nanocomposites compared to PCL

Figure 5.15 demonstrates the TGA results of PCL/nHA/CNW nanocomposites in comparison to PCL. As discussed before, we expect almost 0.29% and 1% residual mass percentages for each 1% content of CNW and nHA, respectively. The P-nHA1-CNW2 nanocomposites TGA results showed $1.85\% \pm 0.16\%$ residual mass percentage at the end of the experiment, which perfectly confirms the nanofillers contents percentages, considering the $0.2\% \pm 0.06\%$ remained mass of the PCL matrix. The TGA residual mass percentage results for P-nHA2-CNW1 and P-nHA1.5-CNW1.5 were $2.72\% \pm 0.13\%$ and $2.31\% \pm 0.08\%$, respectively. These percentages evidently confirmed the precision of the nanocomposites.

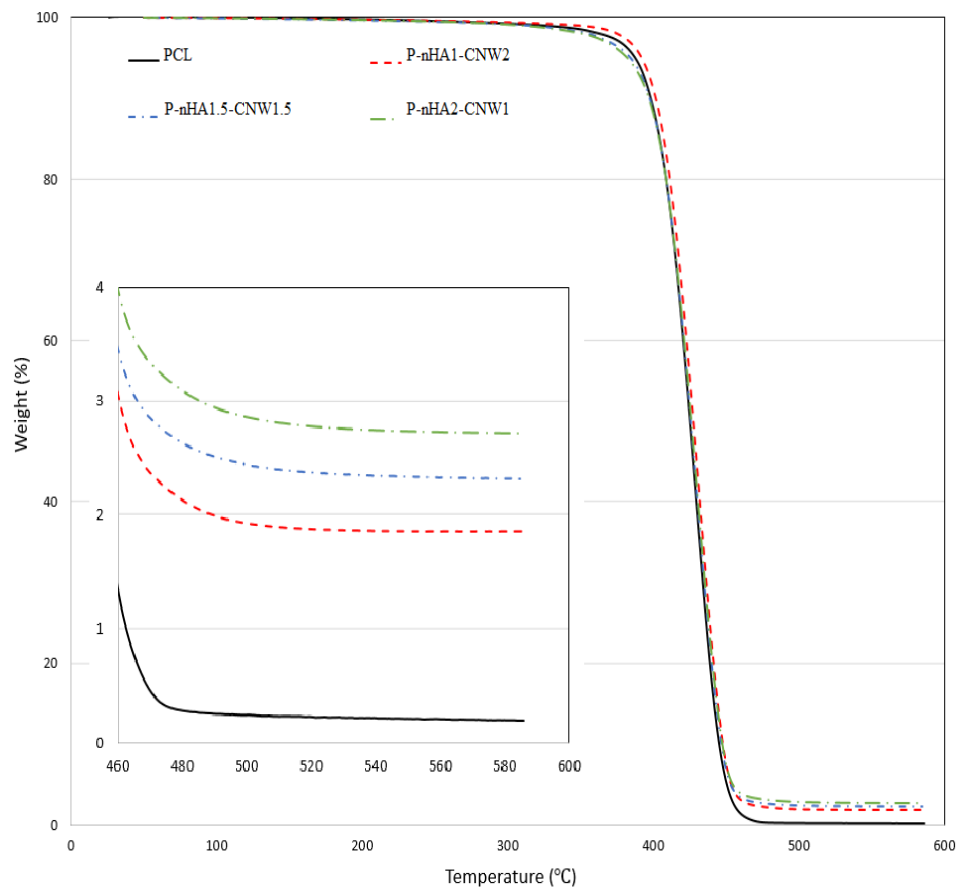


Figure 5.15. TGA results of the PCL/nHA/CNW nanocomposites compared to PCL

5.2.2 Fourier Transform Infrared Spectroscopy (FTIR) Results

The FTIR spectra of PCL, CNW, and nHA along with P-CNW3, P-nHA3, and P-nHA1-CNW3 nanocomposite FDM filaments are reported in Figure 5.16 in the range of 900-2000 cm^{-1} wavenumbers (this range was selected because it contains all of the required information to characterize the PCL matrix and the nanofillers). These nanocomposites are selected to represent each group of the fabricated FDM filaments (nanocomposites with nHA, CNW, and nHA/CNW nanofillers). The characteristic functional groups of PCL, CNW, and nHA were assessed to investigate the presence of the nanofillers in the matrix qualitatively. The ester carbonyl (C=O) functional group at the peak of 1733 cm^{-1} wavenumber and the stretching C-O functional group at the peak of 1173 cm^{-1} wavenumber are the characteristic bonds of PCL [216-218], as shown in Figure 5.16. The amides (C=O) functional groups at the peak range of 1624 cm^{-1} -1661 cm^{-1} wavenumbers are the characteristic bonds of the CNW [219] in the nanocomposites, and the peak of the Phosphate functional group at the range of 1047 cm^{-1} -1062 cm^{-1} characterizes the nHA in the nanocomposites [136, 218, 220]. The FTIR spectrum of P-CNW3 indicated characteristic peaks of the amides and the ester carbonyl bonds at the expected wavenumbers, which characterizes both the PCL matrix and the presence of the CNW nanofiller. The FTIR spectrum of P-nHA3 showed a clear phosphate peak that indicates the presence of the nHA nanofiller. The P-nHA1-CNW2 nanocomposite filaments have nHA and CNW nanofillers, so the amides and phosphate peaks were trackable in the FTIR spectrum, as shown in Figure 5.16. In sum, the FTIR analysis of the selected nanocomposites proved the qualitative presence of the nanofillers in the nanocomposite FDM filaments.

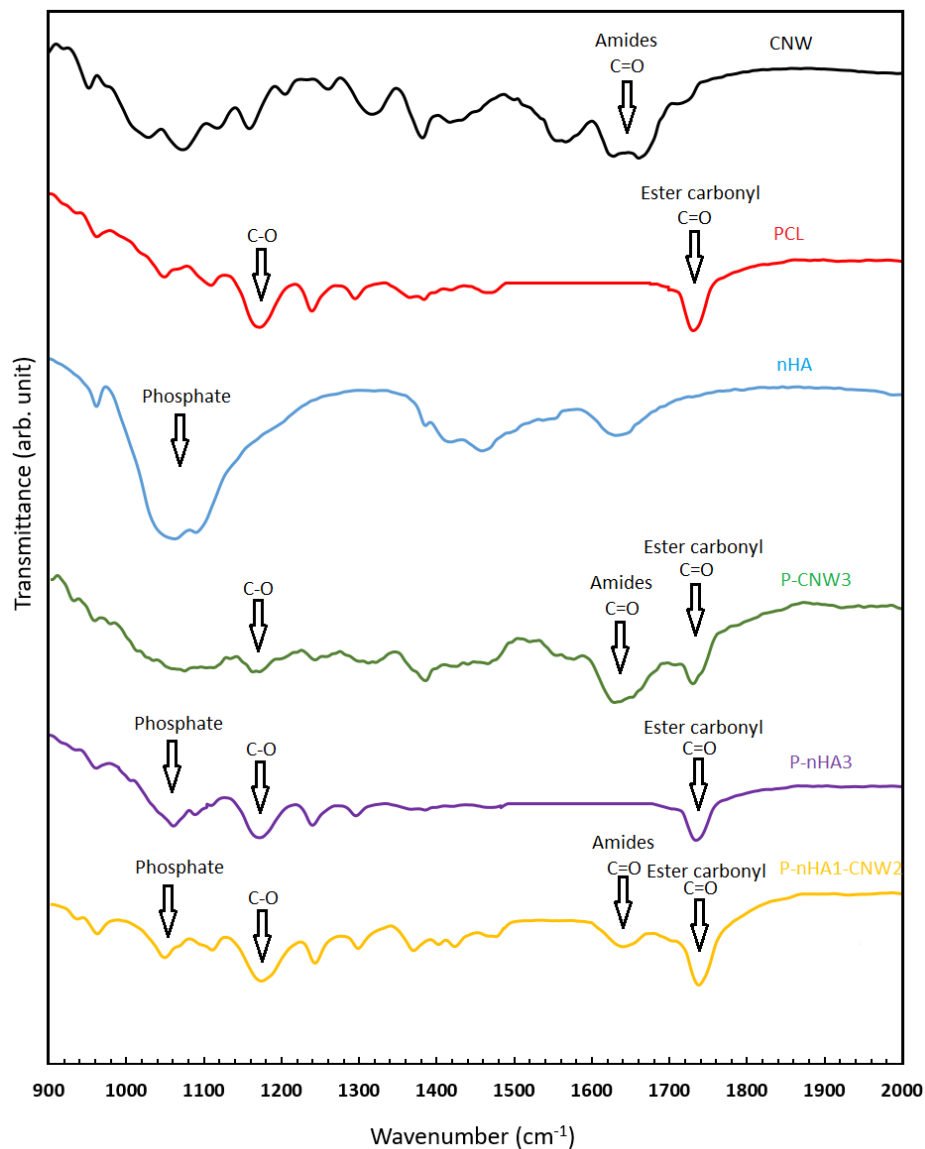


Figure 5.16. FTIR spectra of CNW (black), PCL (red), nHA (blue), P-CNW3 (green), P-nHA3 (purple), and P-nHA1-CNW2 (yellow), nanocomposite filaments

5.3 Optimization of the 3D Printing Processing Conditions for FDM Filaments

The experiments to optimize the 3D printing conditions of the nanocomposites were performed as instructed by the Taguchi method. The experimental results were inserted in the DoE software, and the analyses were performed based on those outcomes. Table 5.4

lists the responses for the nine experiments recommended by the Taguchi orthogonal array technique.

Table 5.4. The responses of the Taguchi orthogonal array proposed experiments

Run	Print speed	Nozzle Temperature	Build plate temperature	Fan speed	Layer thickness	Structural integrity	Compressive strength
	mm/s	Celsius	Celsius	%	µm		MPa
1	15	100	50	80	85	75	16.09
2	20	80	50	90	102	0	0
3	15	120	30	90	92	75	10.48
4	10	100	40	90	115	100	13.78
5	15	80	40	100	89	50	8.81
6	20	120	40	80	74	25	0
7	10	120	50	100	81	0	0
8	20	100	30	100	107	100	26.72
9	10	80	30	80	128	25	4.17

The analyses were performed factor by factor after achieving the experimental results. Figure 5.17 represents the half-normal plot for layer thickness analyses of the parts. In the analyses, the most outlined parameters have to be selected to analyze their significance. Figures 5.18 to 5.20 show the selection process of the factors in consecutive order. Based on the plot, print speed, nozzle temperature, and build plate temperature were chosen, and Table 5.5 presents the analyses results of these parameters. The P-value of the model does not show high significance for the selected parameters (a P-value lower than 0.05 indicates the statistical significance of the parameters). Among the three parameters, nozzle temperature had the highest impact on the layer thickness, and build plate temperature was the next.

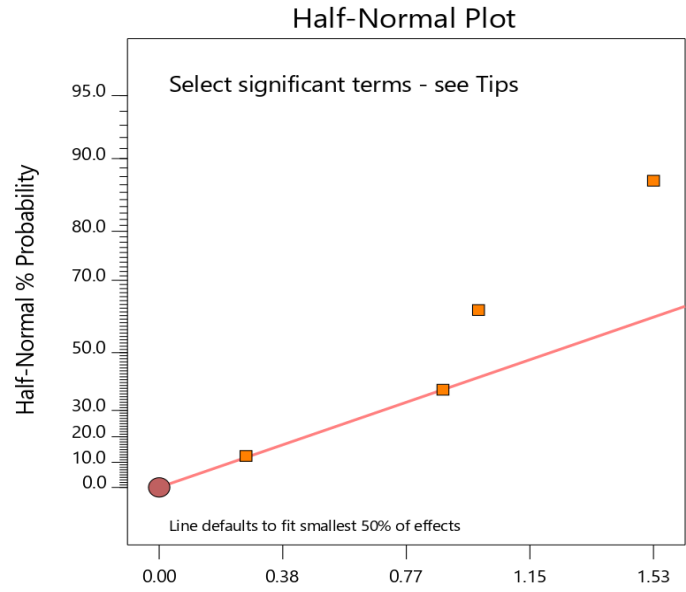


Figure 5.17. Half-Normal plot of the processing parameters impacts on the layer thickness

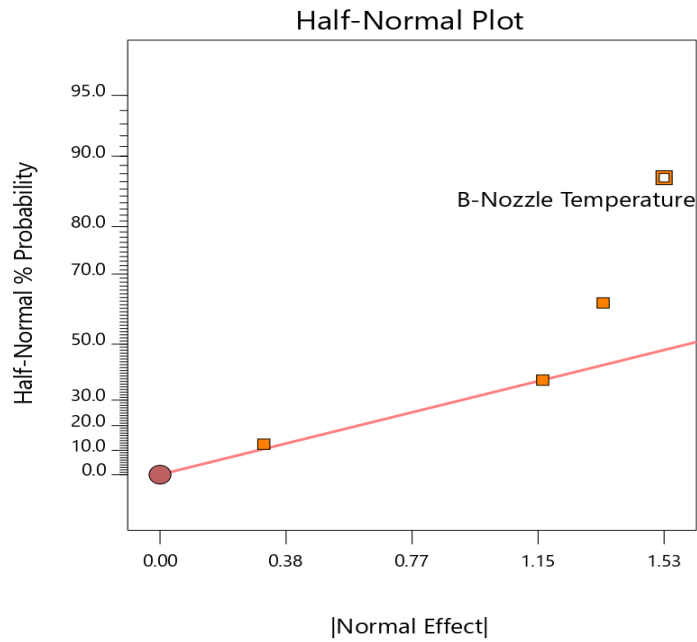


Figure 5.18. Half-Normal plot of the processing parameters impacts on the layer thickness; 1st step of selecting the effective parameters

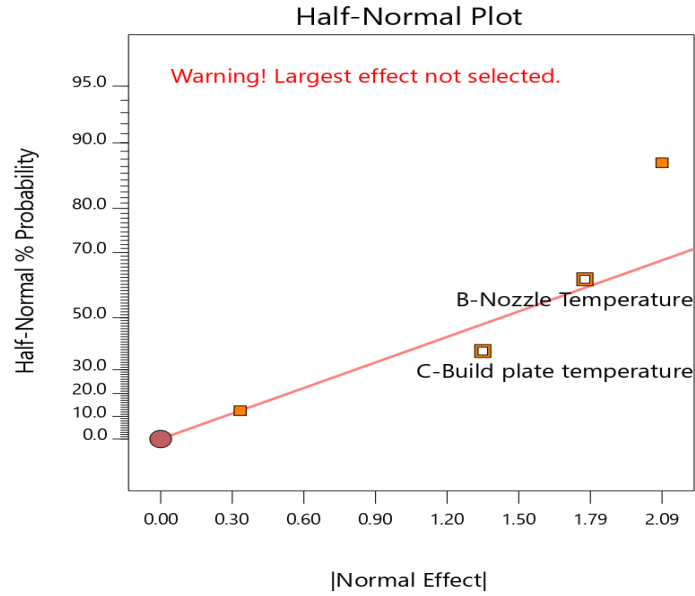


Figure 5.19. Half-Normal plot of the processing parameters impacts on the layer thickness; 2nd step of selecting the effective parameters

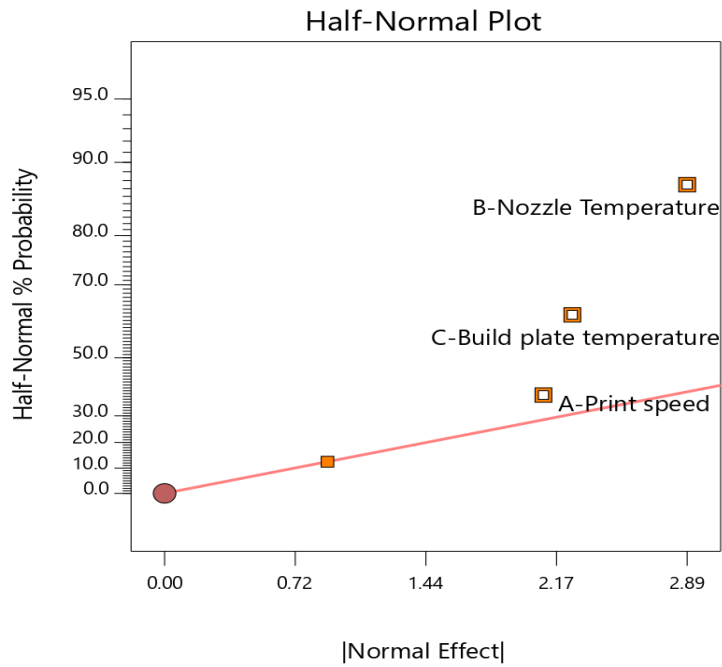


Figure 5.20. Half-Normal plot of the processing parameters impacts on the layer thickness; 3rd step of selecting the effective parameters

Table 5.5. Layer thickness response analyses

Source	Sum of Squares	df	Mean Square	F-value	p-value
Model	2249.33	6	374.89	4.20	0.2049
A-Print speed	592.67	2	296.33	3.32	0.2316
B-Nozzle Temperature	992.00	2	496.00	5.55	0.1526
C-Build plate temperature	664.67	2	332.33	3.72	0.2119
Residual	178.67	2	89.33		
Cor Total	2428.00	8			

The next response to analyze is the structural integrity, which its half-normal plot and the consecutive selections of the important parameters are shown in Figures 5.21 to 5.23. Nozzle temperature and build plate temperature are the two selected parameters based on the plots. The selected parameters are highly significant as the model has a P-value of 0.0486, as shown in Table 5.6. The model's significance was mainly because of the nozzle temperature, which has a very low P-value. The last analyzed response was the mechanical properties of the 3D printed parts. The half-normal plot and the selected parameters are shown in Figures 5.24 to 5.26. Nozzle temperature has a very high impact on the compressive strength of the parts, as shown in Table 5.7. The P-value of the nozzle temperature was 0.0292, and this magnitude of significance made the whole model significant too. Build plate temperature was less important compared to the nozzle temperature.

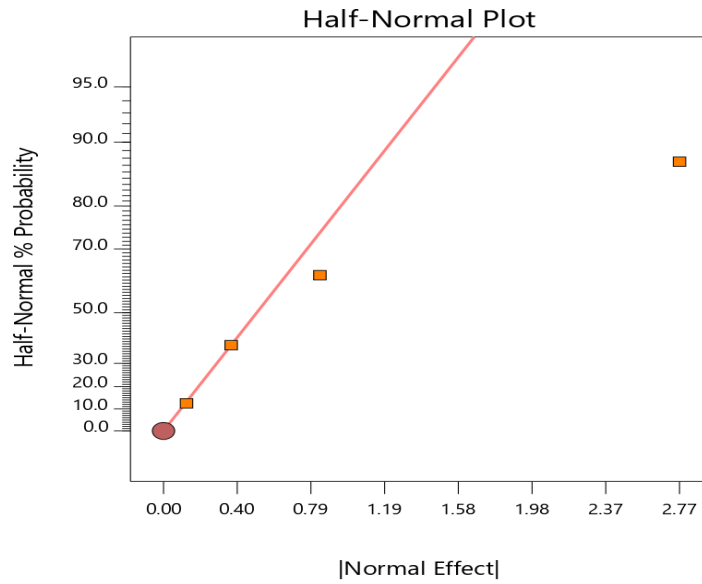


Figure 5.21. Half-Normal plot of the processing parameters impacts on the structural integrity

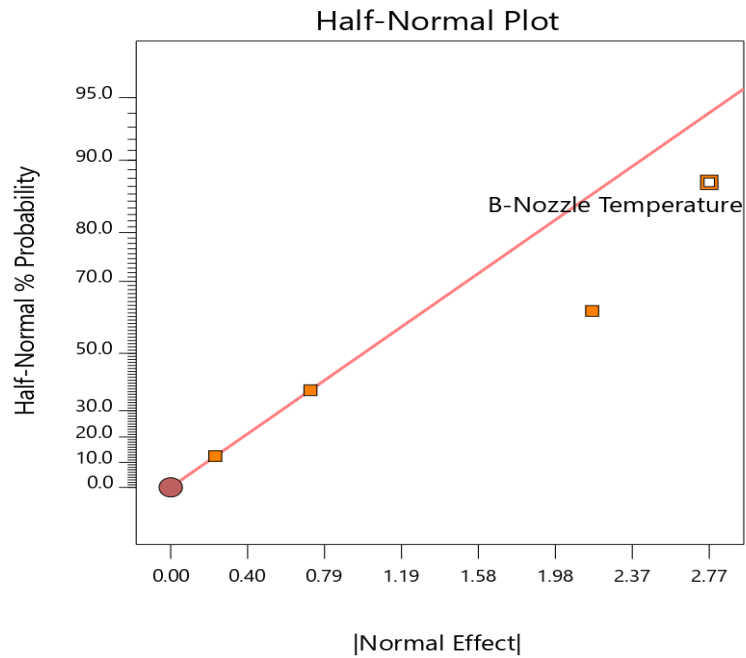


Figure 5.22. Half-Normal plot of the processing parameters impacts on the structural integrity; 1st step of selecting the effective parameters

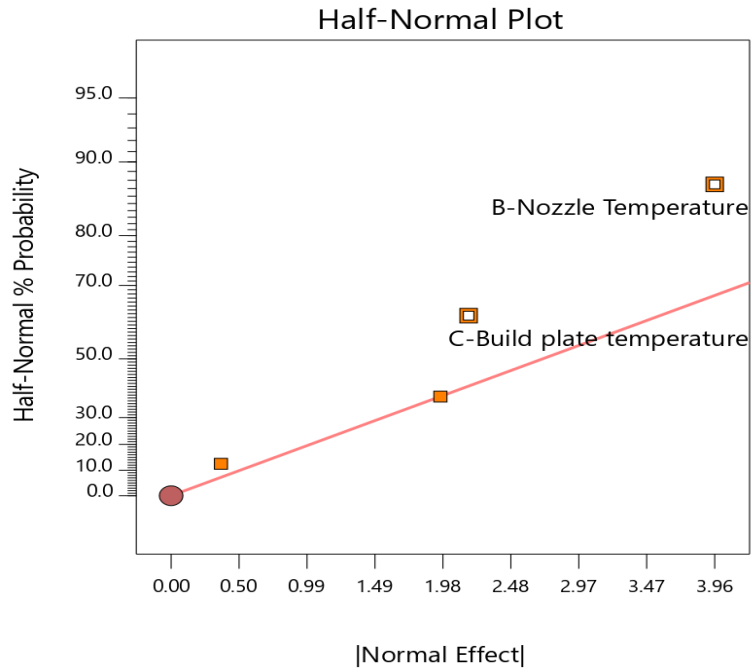


Figure 5.23. Half-Normal plot of the processing parameters impacts on the structural integrity; 2nd step of selecting the effective parameters

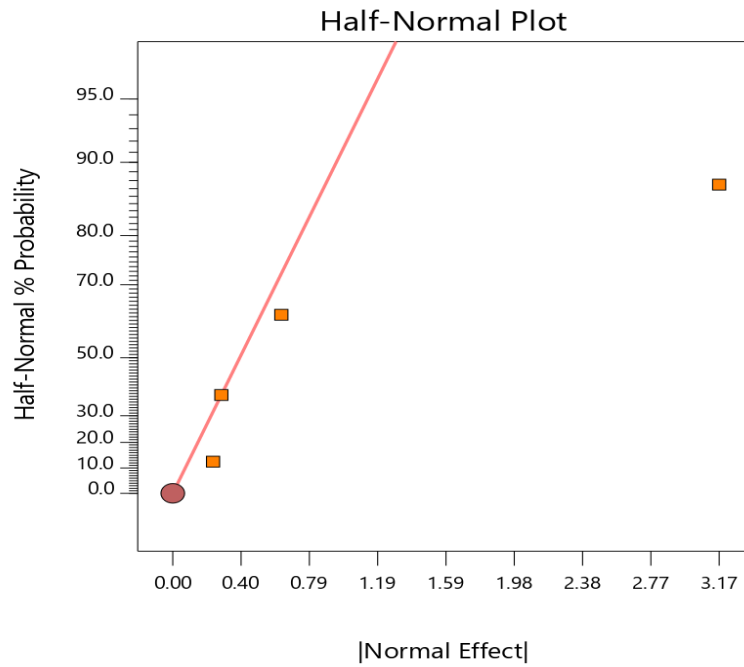


Figure 5.24. Half-Normal plot of the processing parameters impacts on the compressive strength

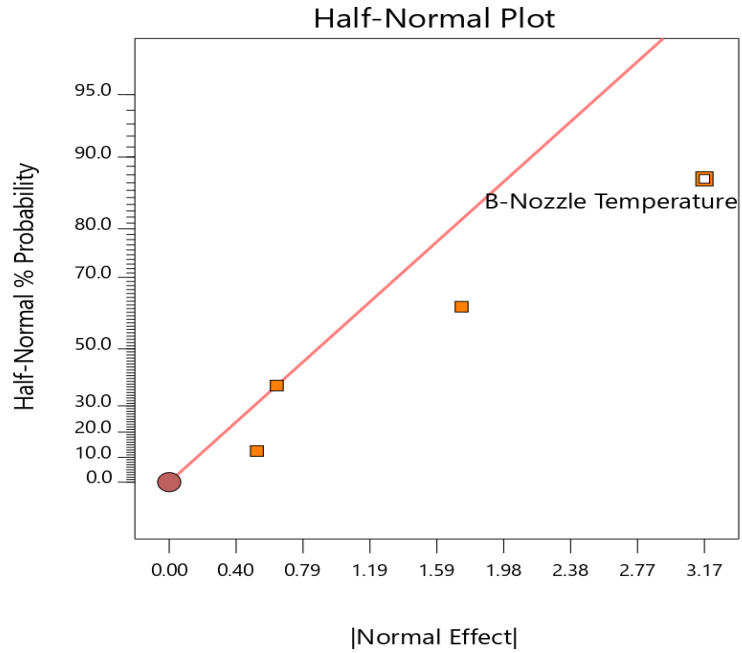


Figure 5.25. Half-Normal plot of the processing parameters impacts on the compressive strength; 1st step of selecting the effective parameters

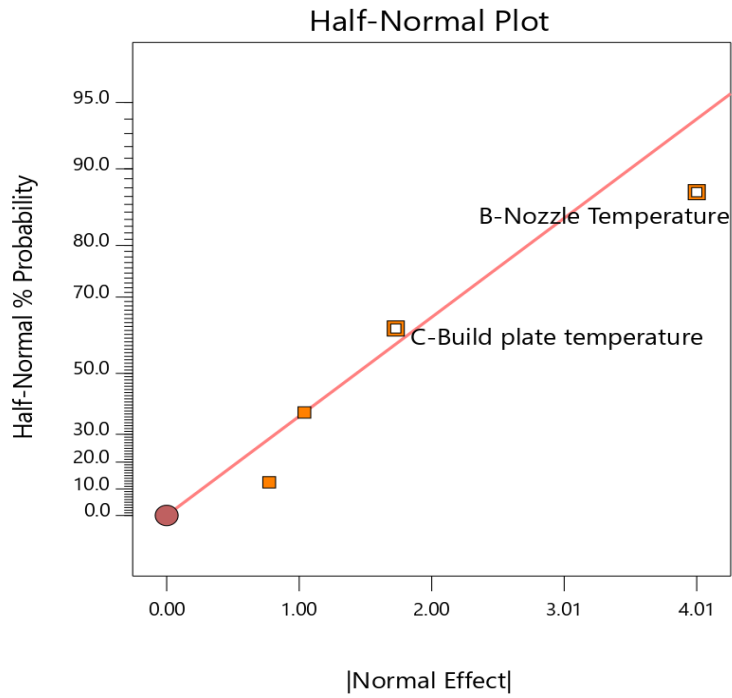


Figure 5.26. Half-Normal plot of the processing parameters impacts on the compressive strength; 2nd step of selecting the effective parameters

Table 5.6. Structural integrity response analyses

Source	Sum of Squares	df	Mean Square	F-value	p-value
Model	10833.33	4	2708.33	6.50	0.0486
B-Nozzle Temperature	7916.67	2	3958.33	9.50	0.0302
C-Build plate temperature	2916.67	2	1458.33	3.50	0.1322
Residual	1666.67	4	416.67		
Cor Total	12500.00	8			

Table 5.7. Compressive strength response analyses

Source	Sum of Squares	df	Mean Square	F-value	p-value
Model	563.14	4	140.78	6.09	0.0540
B-Nozzle Temperature	448.25	2	224.12	9.70	0.0292
C-Build plate temperature	114.89	2	57.45	2.49	0.1988
Residual	92.43	4	23.11		
Cor Total	655.57	8			

The next step was the numerical analyses of the experimental results, considering the selected factors and their importance. To achieve the optimal desired parameters, the optimal target for each response and the importance levels of the responses are defined, as shown in Figures 5.27 to 5.29 and reported in Table 5.8. The layer thickness target was 100µm, which is the defined layer thickness in the slicing software. The compressive strength was maximized, and the highest importance was set for this response. Structural integrity was maximized as well, with the same importance as layer thickness.

After numerical analysis of the reported information in Table 5.8, the best option with the optimal processing condition was achieved. The top five options are reported in Table 5.9,

and Figure 5.30 demonstrates the critical design factors' interactions in the limits of the optimal processing condition. Nozzle temperature of 100°C, print speed of 15 mm/s, build plate temperature of 30°C, and fan speed of 100% were recommended with the highest desirability, equal to 98.7%. Because the PCL matrix is the dominant component of the nanocomposites, these processing conditions were used to 3D print all of the nanocomposites.

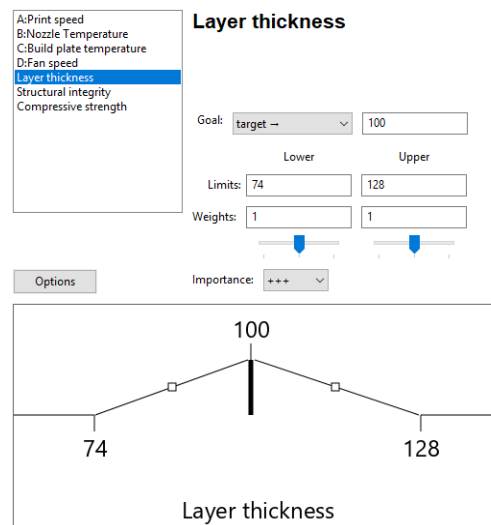


Figure 5.27. Setting the optimal target for numerical analyses of the layer thickness

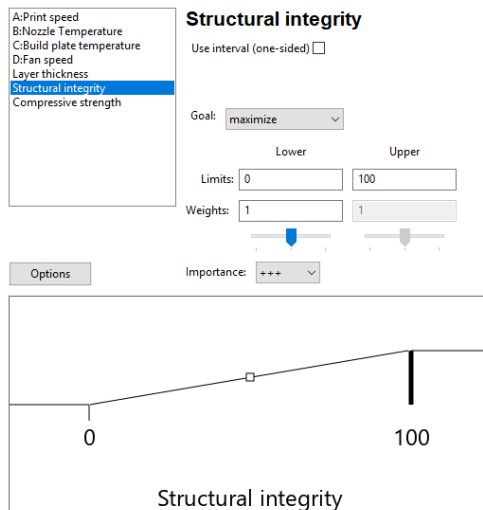


Figure 5.28. Setting the optimal target for numerical analyses of the structural integrity

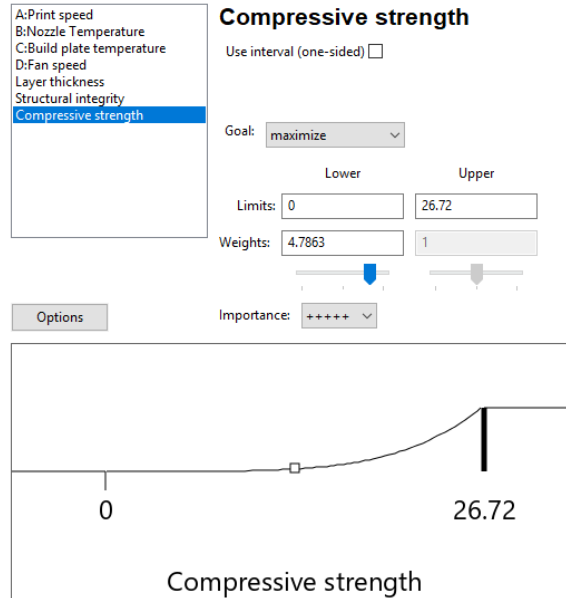


Figure 5.29. Setting the optimal target for numerical analyses of the compressive strength

Table 5.8. The defined parameters of the numerical analysis

Name	Goal	Lower Limit	Upper Limit	Lower Weight	Upper Weight	Importance
Print speed (mm/s)	is in range	10	20	1	1	3
Nozzle Temperature (°C)	is in range	80	120	1	1	3
Build plate temperature (°C)	is in range	30	50	1	1	3
Fan speed (%)	is in range	80	100	1	1	3
Layer thickness (µm)	is target = 100	74	128	1	1	3
Structural integrity	maximize	0	100	1	1	3
Compressive strength (MPa)	maximize	0	26.72	4.7863	1	5

Table 5.9. Optimal FDM printing processing conditions

Optimal options	1	2	3	4	5
Print speed (mm/s)	15	20	15	15	15
Nozzle Temperature (°C)	100	100	100	100	100
Build plate temperature (°C)	30	30	30	30	40
Fan speed (%)	100	100	90	80	100
Layer thickness (µm)	101.33	107	112	104.67	85
Structural integrity	100	100	100	100	100
Compressive strength (MPa)	29.61	26.72	25.85	24.52	23.35
Desirability (%)	98.7	92.5	79.9	78.9	59

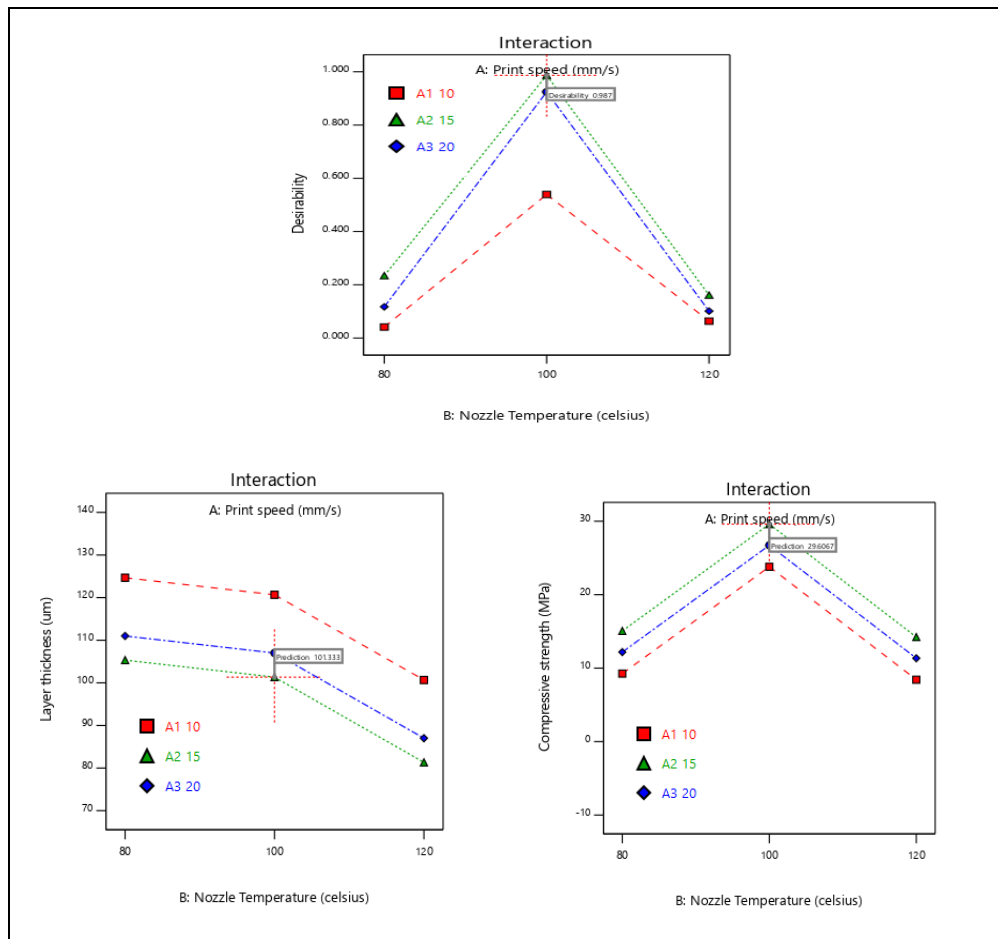


Figure 5.30. Interaction of critical design factors in the limits of the optimal processing condition

5.4 Mechanical Properties of the 3D Printed Nanocomposite Polymeric Bone Tissue Scaffolds

The mechanical properties of the manufactured nanocomposite Polymeric Bone Tissue Scaffolds (PBTSs) are reported in Table 5.10. Figure 5.31 demonstrates the statistical analysis for the average compressive strength of the composites containing nHA or CNW nanofillers. The nHA content increased the mechanical properties of the scaffolds considerably, as shown in Table 5.10 and Figures 5.31 and 5.32. The mechanical properties enhancement by adding 1% nHA nanofiller to the matrix was noticeable but not statistically significant, as shown in Figure 5.31. The increases caused by 2% and 3% nHA content were significant, which proves the effectiveness of the nanofiller. Comparing P-nHA3 compressive strength with P-nHA2, revealed that the improvement in the properties by increasing nHA content from 2% to 3% was statistically significant too. In general, by increasing the nHA nanofiller percentage from one to three percent, the improvement in mechanical properties was gradually increased, and in P-nHA3 composites, the average compressive strength and apparent modules were increased by almost 44% and 78% compared to PCL, respectively.

CNW was initially employed as a nanofiller to improve the biological properties of the scaffolds, but because of its distinguished fibrous morphology, it was expected to do not decrease the mechanical properties of the composites and even improve them. As demonstrated in Table 5.10 and Figures 5.31 and 5.33, the mechanical properties of the composites were slightly increased, and in general, adding the CNW content did not diminish the mechanical properties of the nanocomposites. The statistical analysis in

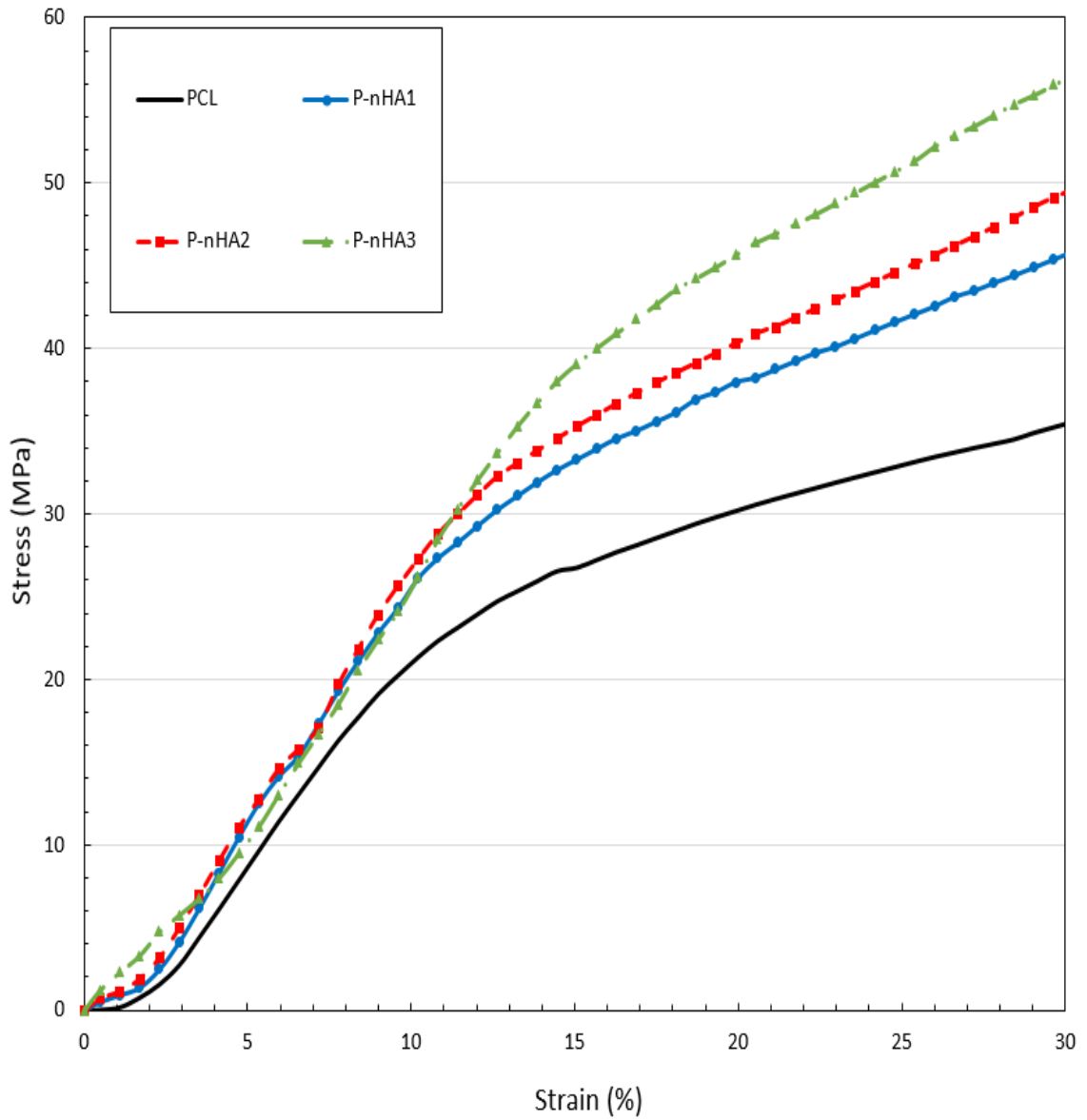


Figure 5.32. Stress-strain curves of the 3D printed nanocomposite PBTSs with nHA nanofiller

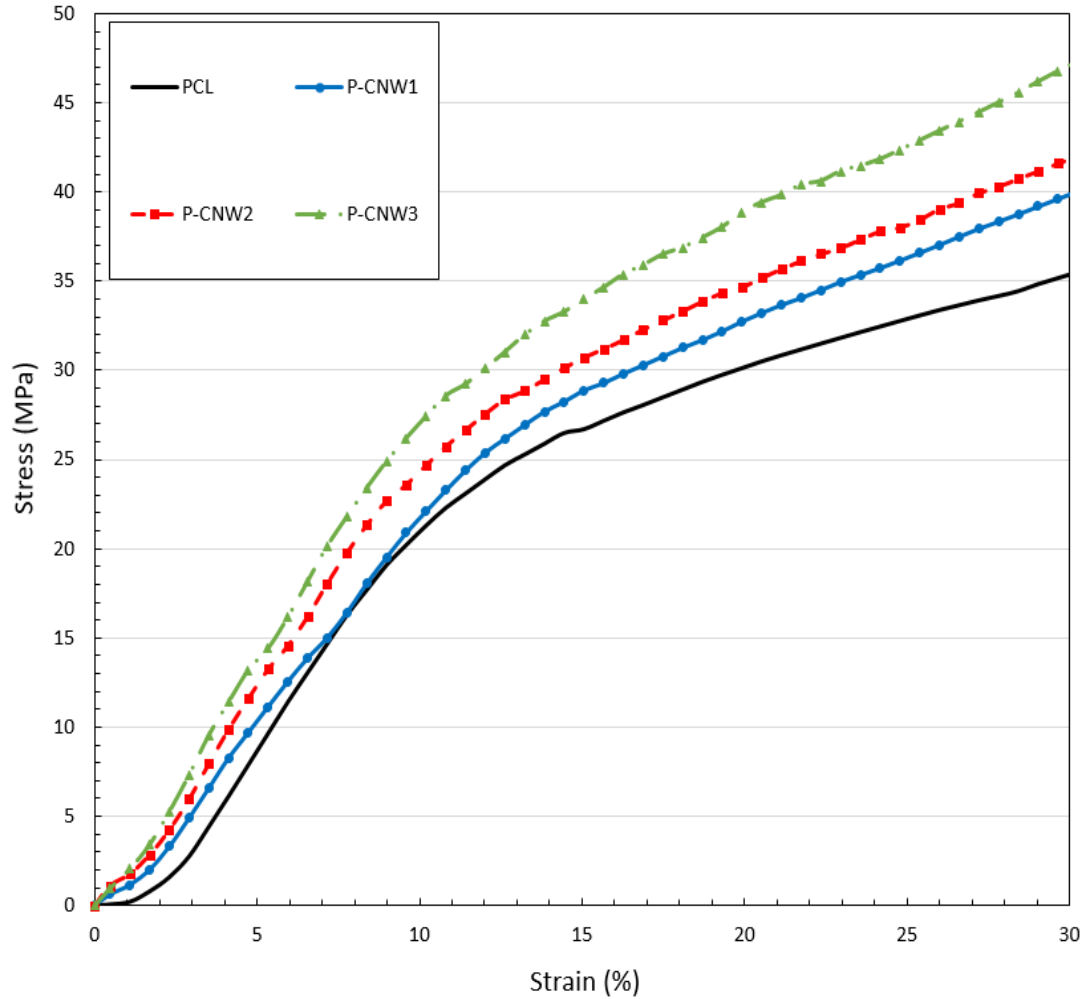


Figure 5.33. Stress-strain curves of the 3D printed nanocomposite PBTs with CNW nanofiller

The mechanical properties of the nanocomposites with nHA/CNW nanofillers are presented in Table 5.10 and Figures 5.34 and 5.35. P-nHA2-CNW1 and P-nHA1.5-CNW1.5 nanocomposites showed significant improvement in both average compressive strength and apparent modulus and contained a fair percentage of CNW in their matrix, which can improve the biological properties of the composites. In Figure 5.34, the average compressive strengths of the hybrid filler nanocomposites were compared with PCL, P-nHA2, and P-CNW2 to statistically analyze the impact of the nHA/CNW nanofillers. The

results indicated that the increases in the mechanical properties caused by P-nHA2-CNW1 and P-nHA1.5-CNW1.5 were statistically significant compared to the PCL matrix and P-CNW2. The comparison of P-nHA2-CNW1 and P-nHA1.5-CNW1.5 with P-nHA2 revealed that the increase caused by P-nHA1.5-CNW1.5 was statistically significant, but P-nHA2-CNW1 was not significant. The improvement in the mechanical properties by P-nHA1-CNW2 was not statistically significant compared to PCL and P-CNW2. The P-nHA1-CNW2 nanocomposites had lower mechanical properties than P-nHA2, but the statistical analysis indicated that the differences are not significant.

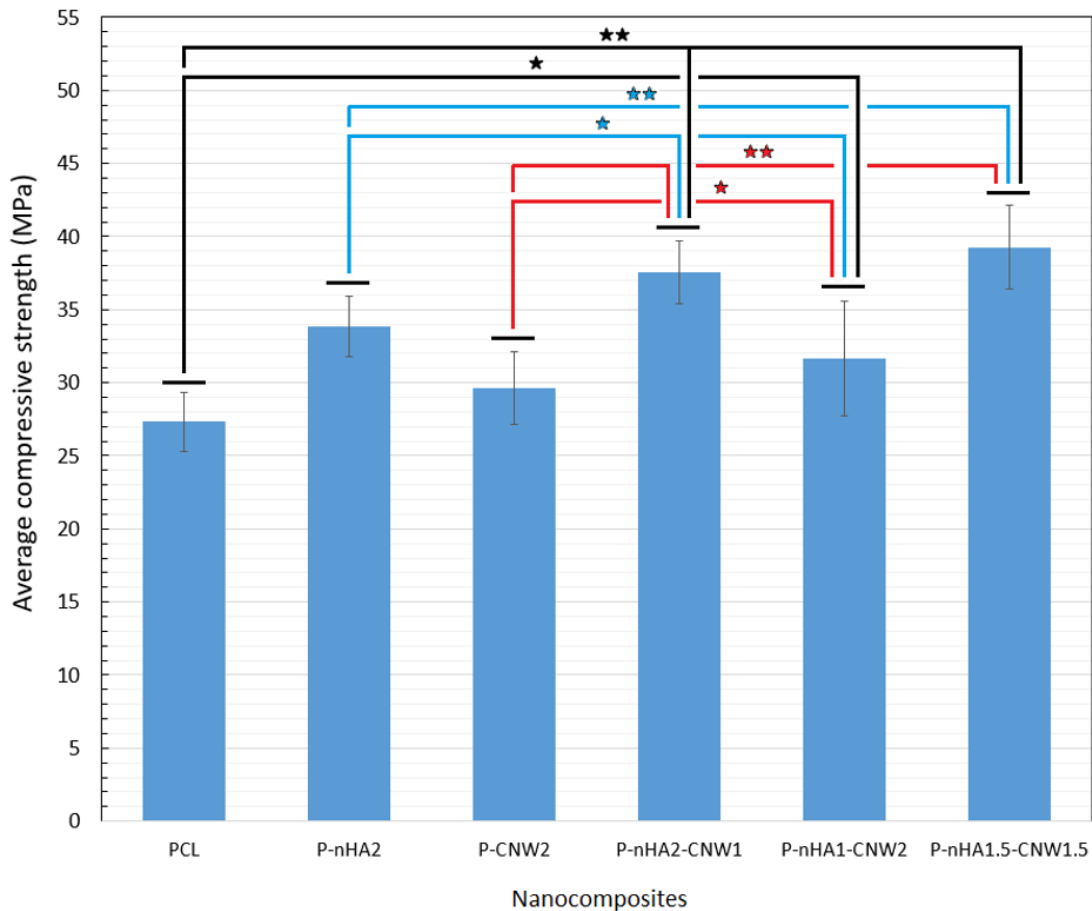


Figure 5.34. Average compressive strength (MPa) of 3D printed nanocomposite PBTs with nHA/CNW nanofillers, including statistical analysis (statistically significant: P-value ≤ 0.05). ★ stands for not statistically significant and ★★ for significant.

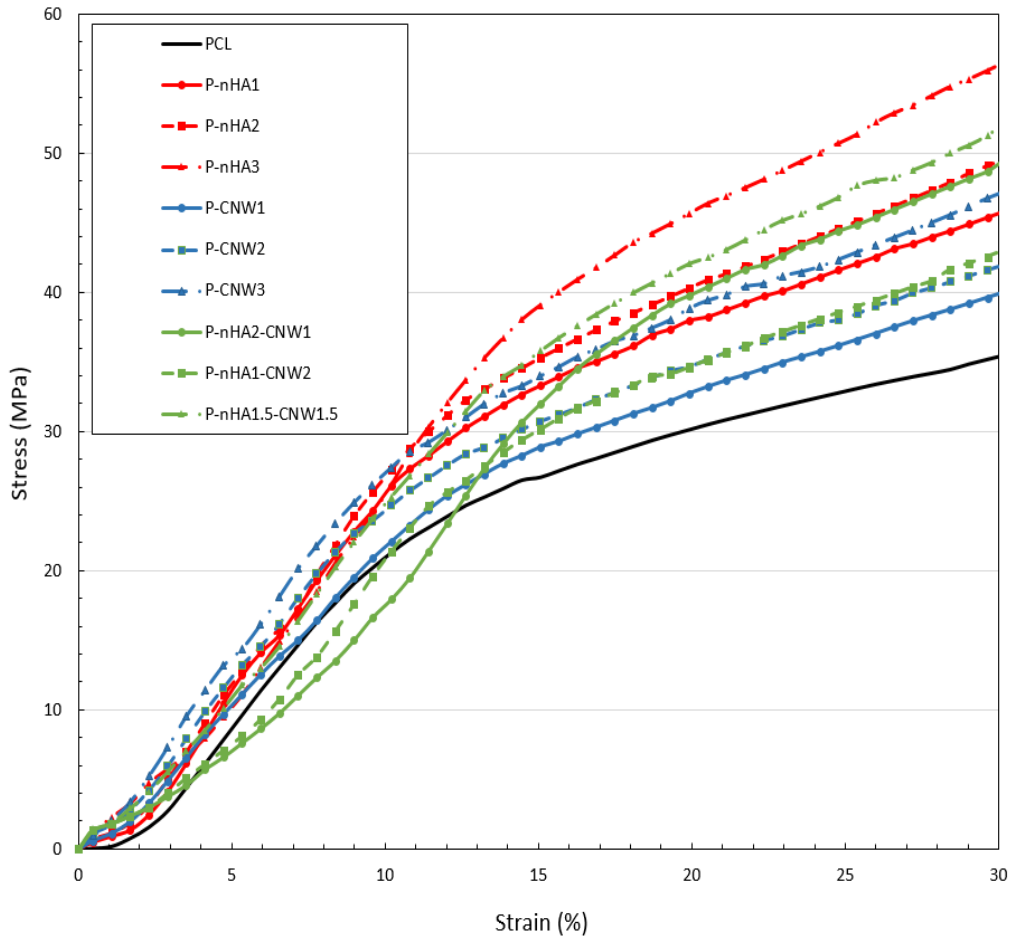


Figure 5.35. Stress-strain curves of the manufactured 3D printed nanocomposite PBTs

5.5 Biological Properties of the Manufactured 3D Printed Nanocomposite PBTs

Biological properties of the 3D printed bone tissue scaffolds were investigated using MTT assay, fluorescent microscopy, and biodegradation experiments. MC3T3-E1 preosteoblast cells proliferation and attachment on the scaffolds were assessed quantitatively based on MTT assay results in 1, 3, and 7 days, which was followed by qualitative analyses by fluorescent microscopy images in the same periods. The impact of the nanocomposite fillers on the biodegradation rate of the scaffolds was analyzed, and the effect of released materials due to biodegradation on the pH of the media was assessed.

5.5.1 Cell Proliferation and Attachment

Cell proliferation assay (MTT) results were generated for 1, 3, and 7 days of culture on all of the 3D printed nanocomposite PBTSSs, as shown in Figure 5.36 (control samples results are included to demonstrate the scales of OD (optical density) for cell growth on top of wells with no scaffolds on them). The cell viability on all of the scaffolds, after one day, was very similar, and there were no noticeable differences. After three days of cell culture, a slight gradual advantage of having CNW nanofiller in the nanocomposites was noticeable. After seven days of cell culture, P-CNW3 indicated an exceptional cell proliferation compared to PCL. Also, P-CNW2, P-nHA1-CNW2, and P-nHA1.5-CNW1.5 showed more than 20% higher cell viability than PCL after seven days of cell culture.

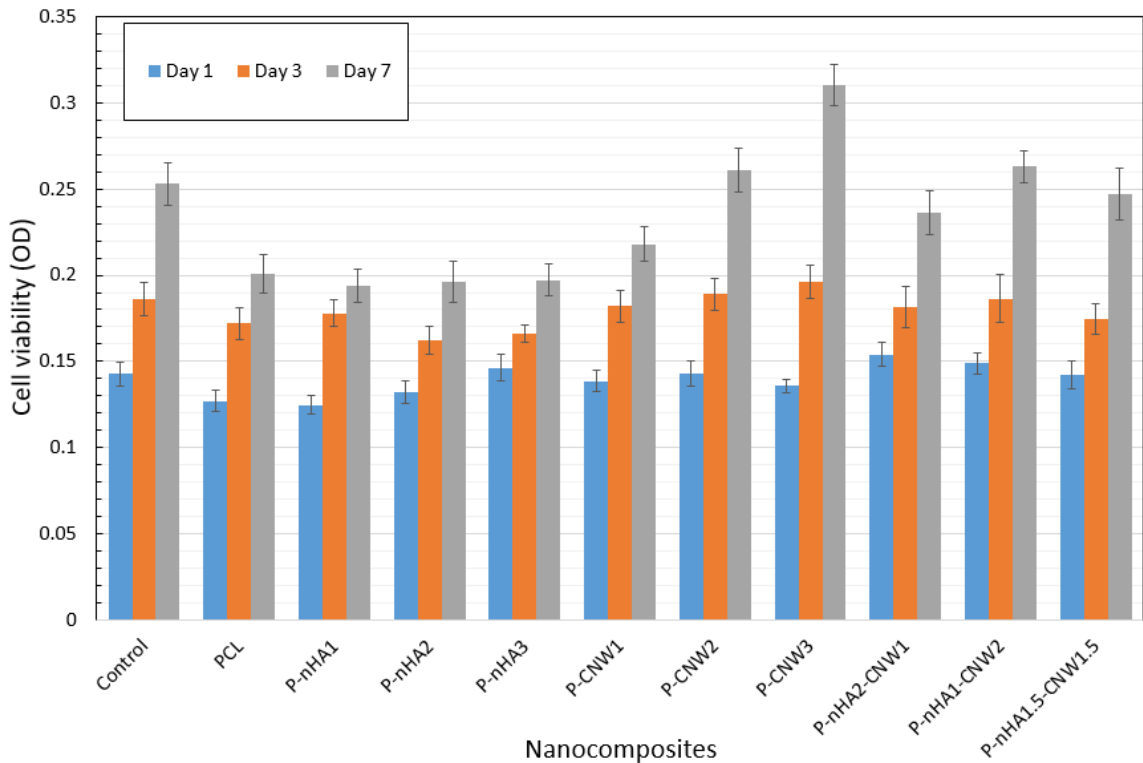


Figure 5.36. Cell viability results after 1, 3, and 7 days of MC3T3-E1 cells culture on the 3D printed nanocomposite PBTSSs

Figure 5.37 presents the statistical analyses of the cell proliferation results after seven days of cell culture (statistical significant is defined as P-values smaller than 0.05). These results demonstrated that the CNW nanofiller facilitates the cell proliferation properties of the scaffolds significantly. Because MTT assays only measure the live and viable cells attached to the scaffolds, these results suggest that CNW improves both cell attachment and proliferation properties of the scaffolds.

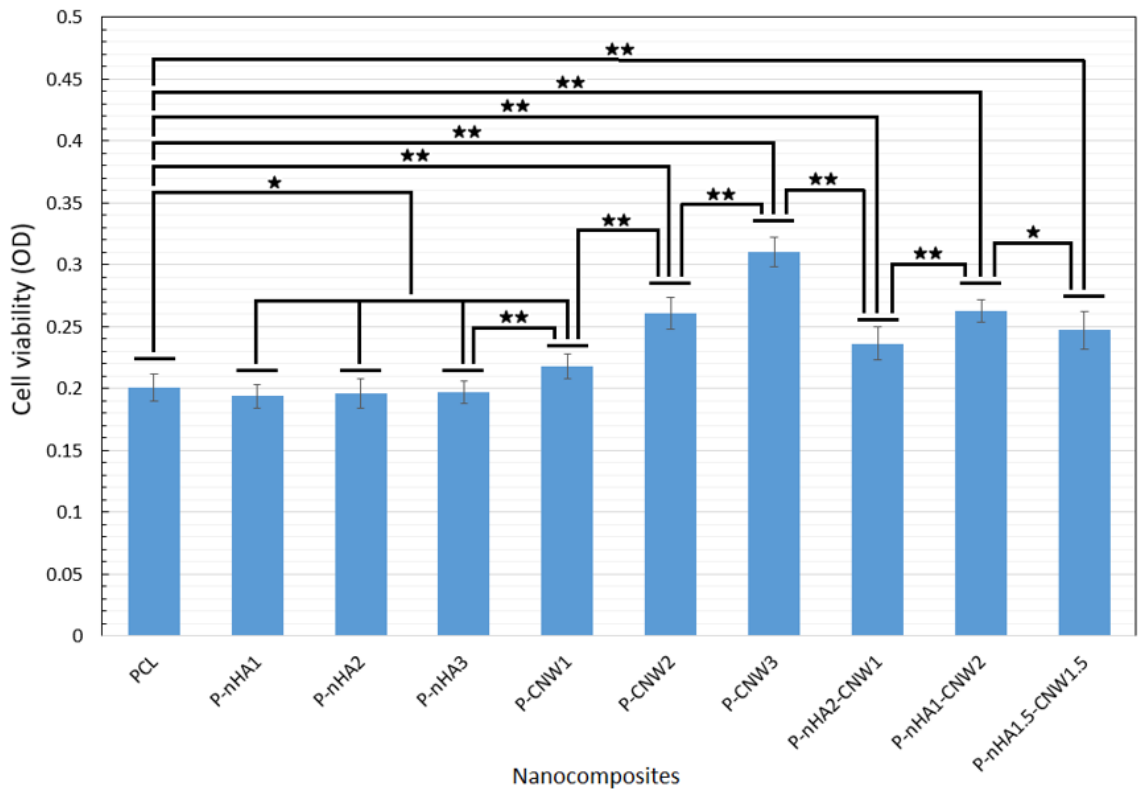


Figure 5.37. Cell viability results after seven days of cell culture on the 3D printed nanocomposite PBTs including statistical analysis. ★ stands for not statistically significant and ★★ for significant.

In Figures 5.38, 5.39, and 5.40, the fluorescent microscopy results of the MC3T3-E1 cells cultured on the scaffolds are presented. As shown in Figure 5.38, the cells' nuclei were

clustered together, representing healthy cell division, signaling, and growth behavior. DAPI staining of nuclei was robust, and in conjunction with actin filament staining, it is evident that the cells are adequately attached and displaying normal growth and stretch characteristics on the scaffolds. Figures 5.39 and 5.40 present the DAPI and Phalloidin CF®640R staining results for four selected scaffolds after 1, 3, and 7 days to compare the visualized results of fluorescent microscopy with the MTT assay. Based on MTT assay, PCL, P-CNW3, P-nHA3, and P-nHA1.5-CNW1.5 composites were selected for fluorescent microscopy.

After one day of cell culture, the nuclei and actin filaments staining support the cell growth and viability demonstrated by MTT results. Initial cell growth was on limited areas on the scaffolds, and there were almost more than 50 percent empty areas on the scaffolds, as expected at low seeding numbers. After three days of cell culture, the covered areas on the scaffolds increased and were similar for all of the composites, with P-CNW3 and P-nHA1.5-CNW1.5 nanocomposites showing the most vigorous cell growth and spread across the whole surface of the scaffolds. In contrast, PCL and P-nHA3 materials only supported limited and restricted growth across the scaffolds. After seven days of cell culture, the preosteoblast cells covered the P-CNW3 surface completely and evenly. The visualized actin filaments of the cells on the P-CNW3 demonstrated a genuine biological cell connection and attachment to the scaffolds. P-nHA1.5-CNW1.5 also showed growth and attachment, but to a lesser extent compared to P-CNW3. The results suggest the significant effectiveness of CNW nanofiller in long-term cell proliferation, attachment, and spread on the scaffolds. After seven days, cells were growing well on the PCL scaffolds, but as expected, the rate was lower than the composites with CNW content. P-nHA3

scaffolds experienced cell growth concentrated in just certain areas, and still, there were considerable uncovered areas on the surface of the scaffold after seven days of cell culture, although the cell growth rate and attachment in total were comparable to PCL.

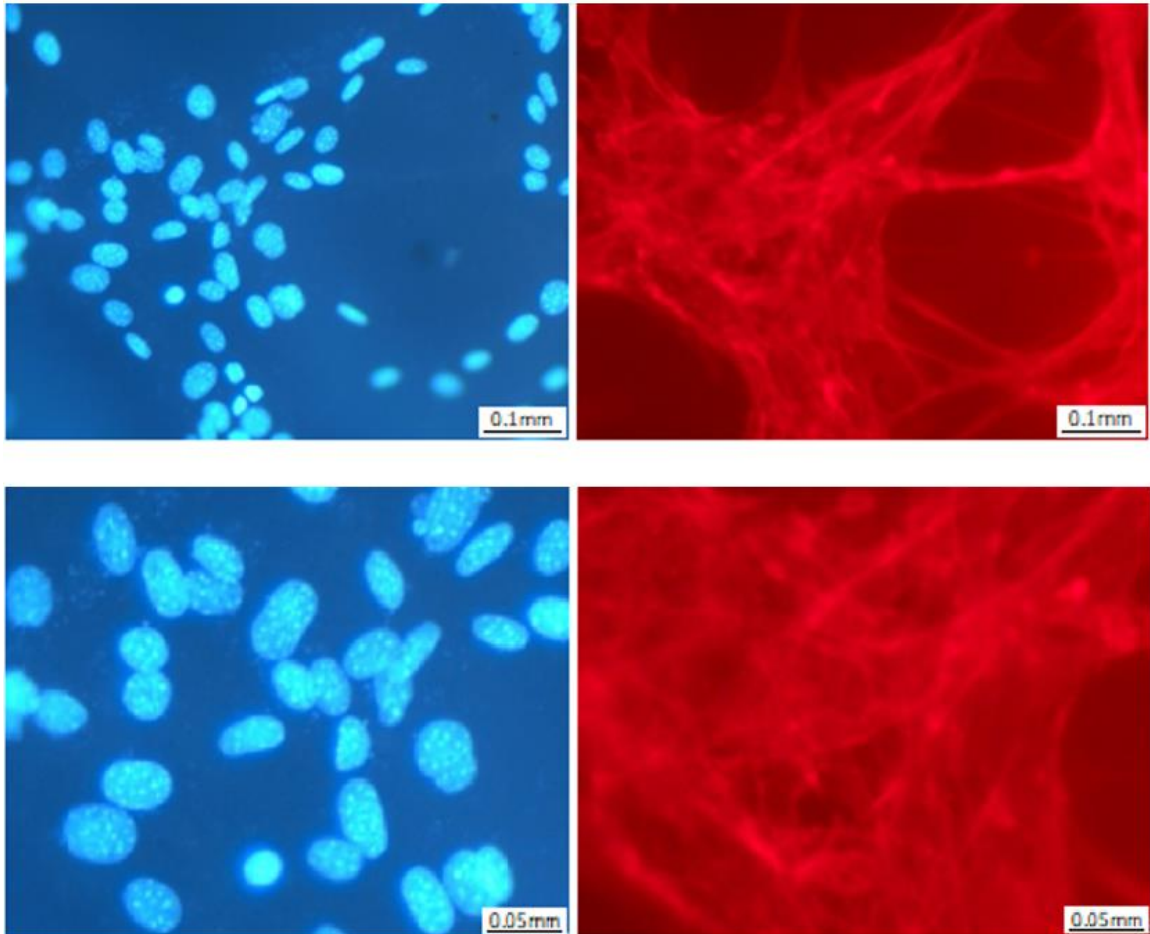


Figure 5.38. Nuclei and actin filaments of MC3T3-E1 cells growing on top of the 3D printed nanocomposite PBTSs (P-nHA1.5-CNW1.5 was employed as a representative)

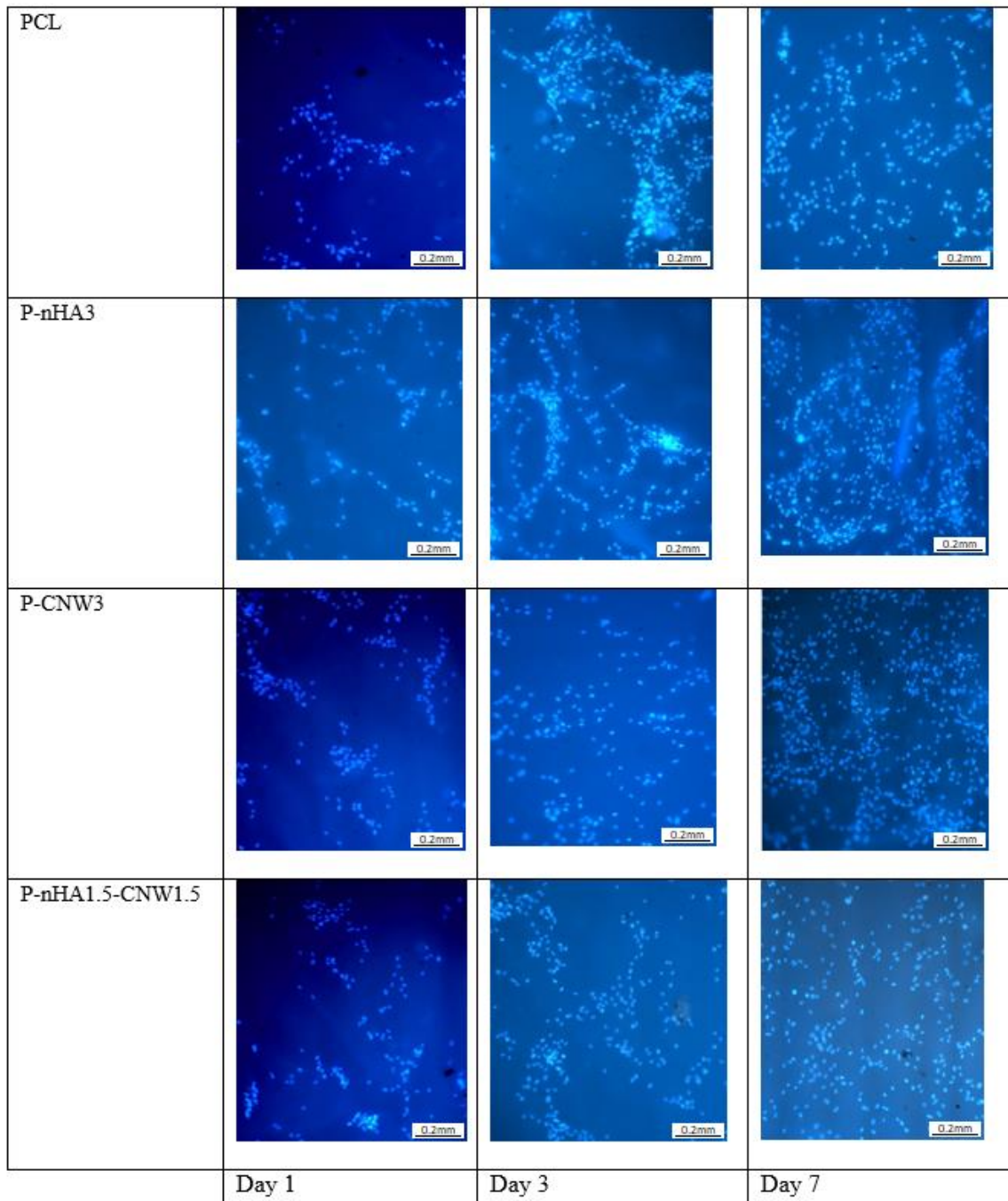


Figure 5.39. Nuclei of MC3T3-E1 cells (fluorescent microscopy results of DAPI staining) after 1, 3, and 7 days of cell culture on the 3D printed nanocomposite PBTSs

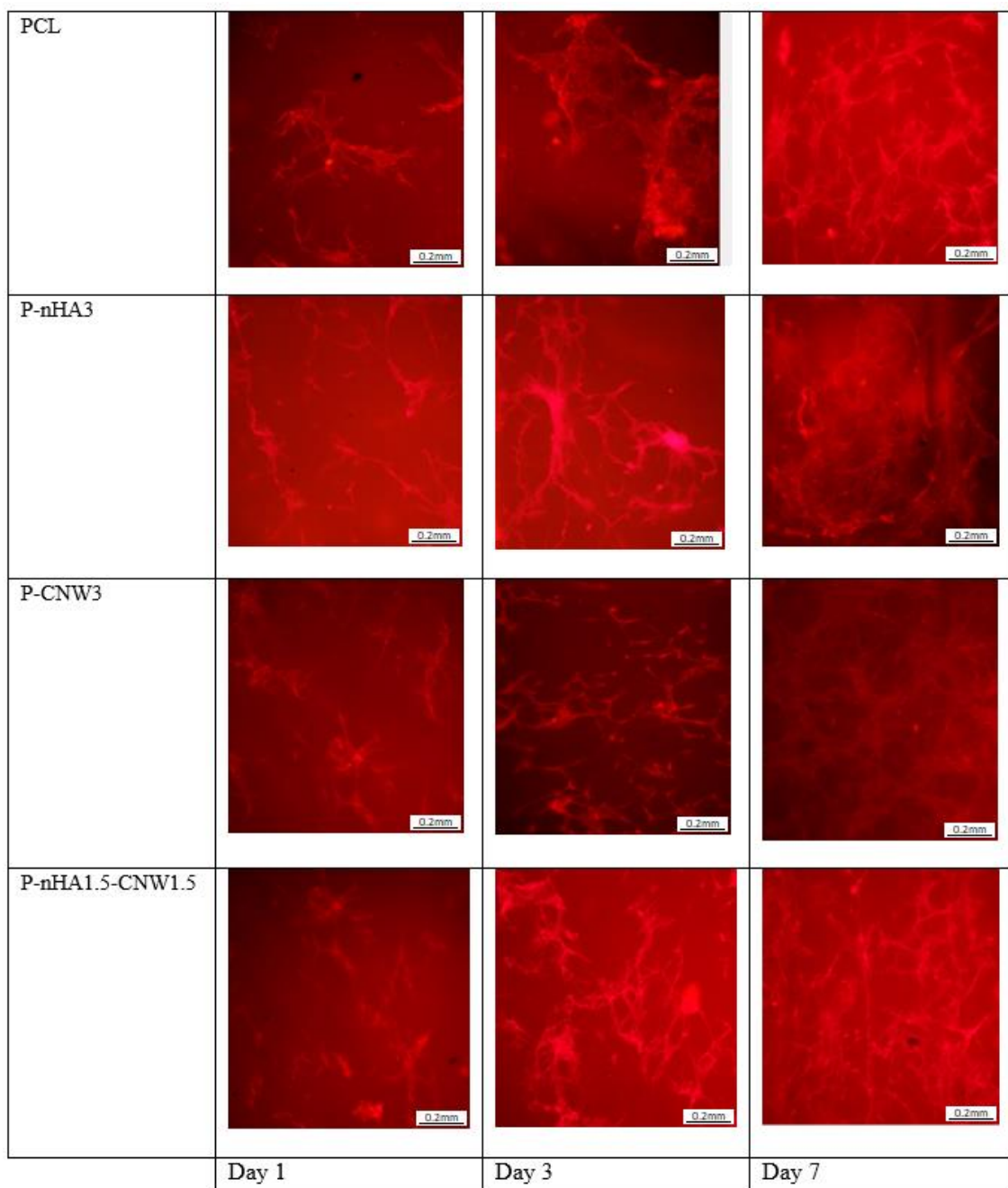


Figure 5.40. Actin filaments of MC3T3-E1 cells (fluorescent microscopy results of Phalloidin CF@640R staining) after 1, 3, and 7 days of cell culture on the 3D printed nanocomposite PBTSS

5.5.2 Biodegradation

Figure 5.41 presents the biodegradation rate of the nanocomposites after 7, 14, and 28 days and Figure 5.42 demonstrates the statistical analyses of the biodegradation rates after 28 days. In general, the fillers caused a significant increase in the biodegradation rate of the PCL matrix. The reason can be media penetration into the matrix in higher paces due to the presence of the fillers. CNW content increased the biodegradation rate more significantly, and after 28 days of biodegradation, P-CNW3 exhibited rates higher than 4%. The statistical analyses in Figure 5.42 revealed that the increase in the percentage of the nHA nanofiller from 1% to 3% did not cause a significant increase in the biodegradation rate. The results for the nanocomposites with CNW filler demonstrate that P-CNW3 significantly increased the biodegradation rate compared to P-CNW1, which indicates the high impact of the CNW content on the biodegradation rate. The P-nHA1-CNW2 and P-nHA1.5-CNW1.5 demonstrated high biodegradation rates too, which were in the range of 4-5% after 28 days. The increases in their biodegradation rates were statistically significant compared to the PCL matrix, P-CNW1, and P-nHA1 nanocomposites, emphasizing the impact of having both of the nanofillers in the matrix at the same time. The CNW impact along with nHA in these nanocomposites caused the high biodegradation rate, which can be the reason that P-nHA1.5-CNW1.5 had the highest biodegradation rate among the manufactured nanocomposites. Table 6 reports the data for pH variation of the media due to degradation of the nanocomposites after 7, 14, and 28 days. The results did not show any significant change in the pH, and the levels had remained in the range of 7.4, indicating a safe, osteogenic environment.

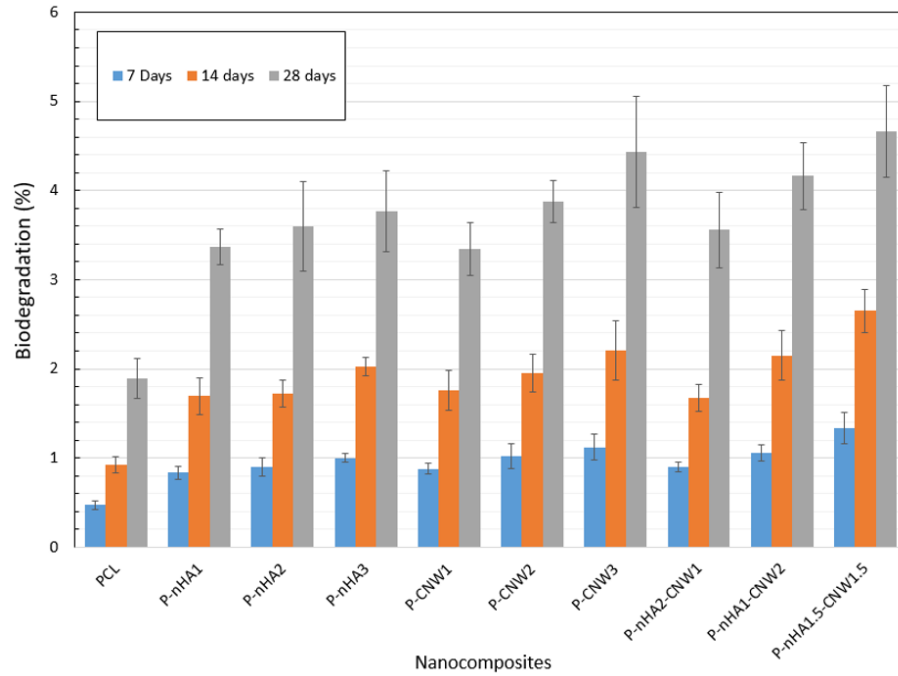


Figure 5.41. Biodegradation rates of the manufactured nanocomposites after 7, 14, and 28 days

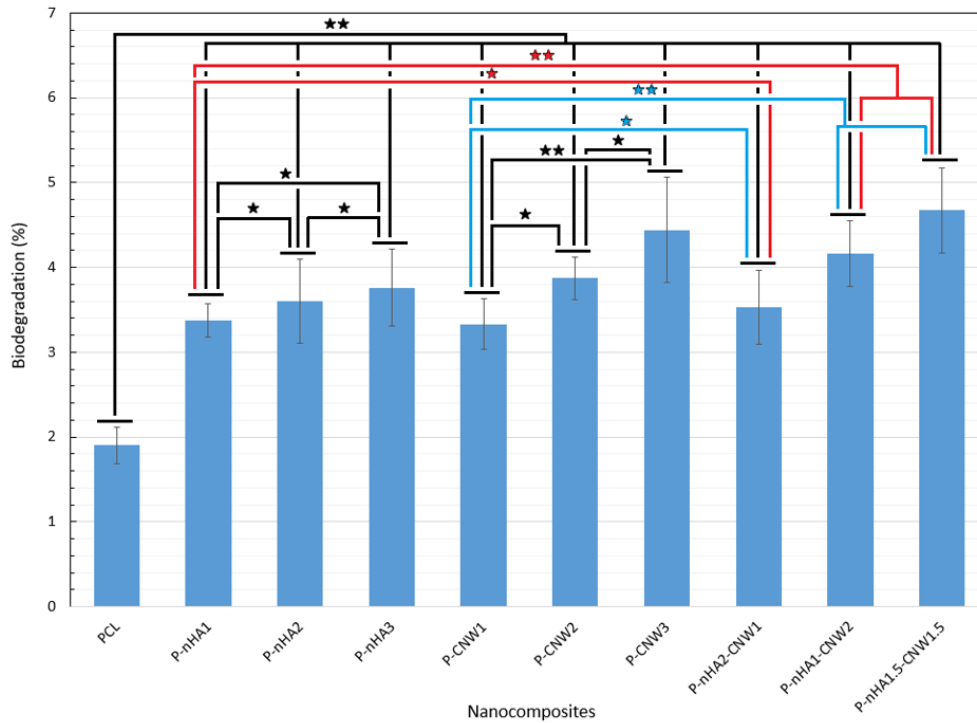


Figure 5.42. Biodegradation rate of the nanocomposites after 28 days, including statistical analysis. ★ stands for not statistically significant and ★★ for significant.

Table 5.11. pH level of the media after biodegradation of the nanocomposites

Nanocomposite	7 Days	14 days	28 days
PCL	7.4	7.42	7.39
P-nHA1	7.41	7.41	7.43
P-nHA2	7.42	7.43	7.45
P-nHA3	7.41	7.43	7.44
P-CNW1	7.42	7.4	7.39
P-CNW2	7.39	7.37	7.36
P-CNW3	7.4	7.38	7.37
P-nHA2-CNW1	7.41	7.4	7.41
P-nHA1-CNW2	7.42	7.39	7.37
P-nHA1.5-CNW1.5	7.42	7.41	7.43

5.6 Biodegradation Rate Estimation in the Long Term

In this section, the numerical simulations were analyzed, and the methods were developed to make an educated estimation of the biodegradation rate of the 3D printed nanocomposite PBTSs with Gyroid design in the long term. As mentioned before, many factors affect the degradation rate of 3D scaffolds, and precise prediction of the polyesters' biodegradation rate is not feasible. However, the methods used in this section can develop an understanding of the biodegradation rate to do a comparative study on the manufactured nanocomposites.

5.6.1 Mesh Sensitivity Analysis

Three different mesh sizes were defined to test the independence of the result from the employed meshing system. Free tetrahedral cells were used to produce the mesh. The inverted curved, very large, and very small elements were avoided to achieve high-quality mesh networks. The generated mesh networks are shown in Figure 5.43. Mesh sensitivity

analysis was performed by comparing the variations of the normalized molecular weight (Mn) for the Gyroid design. Table 5.12 reports the number of produced tetrahedral elements for each of the meshing networks.

The normalized molecular weight over volume is presented in Figure 5.44 for a 10-week period of biodegradation. The results were completely independent of the mesh size, and by increasing the mesh sensitivity, there were no noticeable variations in the results. Therefore, the mesh network with the lowest computational cost (Mesh-1) was selected as the mesh size for the simulations in this study.

Table 5.12. Number of elements for each meshing networks of the mesh sensitivity analysis

Title	Number of elements
Mesh-1	23103
Mesh-2	31522
Mesh-3	42264

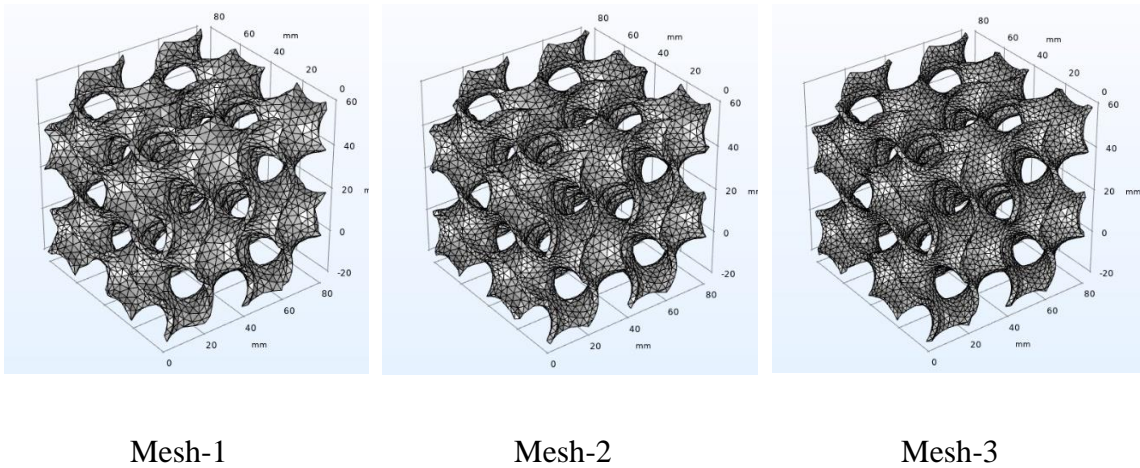


Figure 5.43. The defined meshing systems of the mesh sensitivity analysis

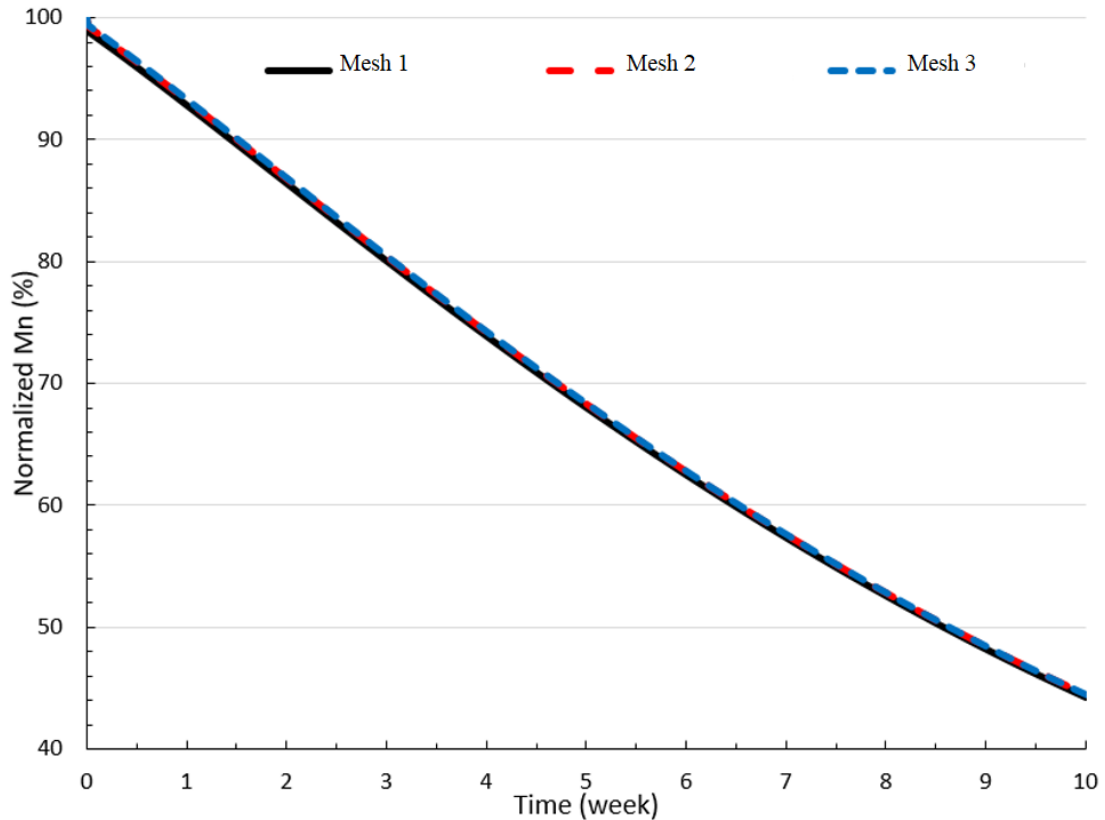


Figure 5.44. Normalized molecular weight variations in a 10-week period of biodegradation for meshing networks of the mesh sensitivity analysis

5.6.2 Validation of the Numerical Results

The experimental data presented by Grizzi et al. [179] for the average molecular weight (Mn) were employed to validate the numerical results. A PLA plate with dimensions of 15*10*2 mm was designed to match the experimental specimen. All of the simulation parameters in this paper were considered as reported in the experimental study. In Figure 5.45, the numerical simulation results are compared with the experimental data [179] for 20 weeks of biodegradation. The simulation results closely follow the same trend as the experimental data, especially in the long term as they coincide entirely. Therefore, the

numerical model could adequately predict the hydrolytic biodegrading over an extended period.

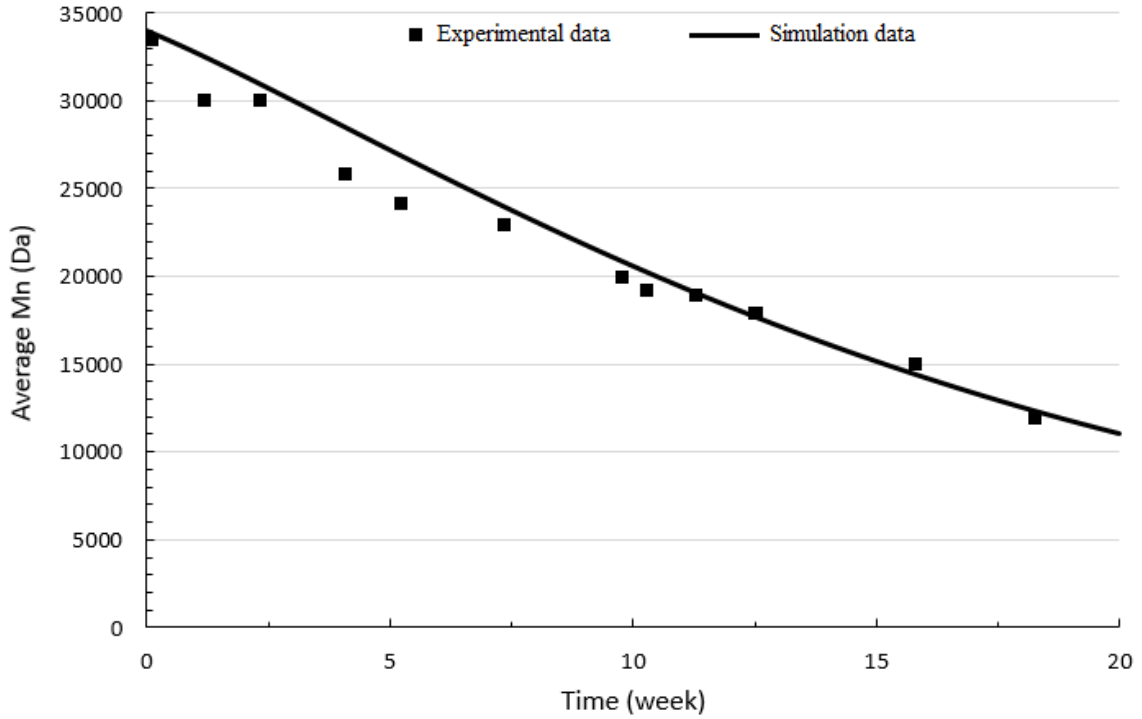


Figure 5.45. Comparison of simulation results in this study with the experimental data presented by Grizzi et al. [179]

5.6.3 Impact of 3D Printing Structure on the Average Normalized Molecular Weight Variations

The 3D printed structures have a noticeable difference in mass distribution over the wall thickness compared to structures with uniform walls. The 3D printed structures by the FDM method are consist of repeating units of the extruded filaments. For example, by using an extruder nozzle with 250 μm in diameter and setting the extrusion thickness of 240 μm in the FDM manufacturing process, the final Gyroid structure is supposed to be

made of repeating units of cylindrical extruded filaments with a diameter of 240 μm . To assess this factor, the results for a cube consist of 100 overlapping cylinders with a diameter of 240 μm were compared with a solid cube of the exact total dimensions. Figure 5.46 indicates that the decrease in the average Mn overtime was considerably lower in the 3D printed cube sample. The lower reduction rate in the average Mn overtime means that the mass loss due to internal erosion will be delayed in the FDM printed parts; the reason can be the drastic difference in the mass concentration of the 3D printed products with a uniform solid cube. This observation shows that simulation results for the solid Gyroid designs made in SOLIDWORKS (not extruded) have to be approximated in order to reflect the manufacturing process. For the assessed cubic structures, the approximation factor was calculated to be 1.55.

Before applying the approximation factor, the next step was to assess the impact of increasing FDM products' wall thickness on the average Mn. The increase in wall thickness of these products corresponds to adding more extruded filament units. Therefore, the samples shown in Figure 5.47 were designed to reflect this matter on the average Mn. Figure 5.48 shows that the Mn in these designs did not vary by increasing the structure wall thickness. By considering the mentioned conclusion, the 3D printed Gyroid designs in this study would have the same decline in the average Mn over time due to hydrolytic biodegradation that will be achieved by considering the approximation factor of 1.55. The finalized average Mn result for 3D printed Gyroid structures is shown in Figure 5.49. The average Mn is a critical factor in analyzing the mass loss due to biodegradation over time.

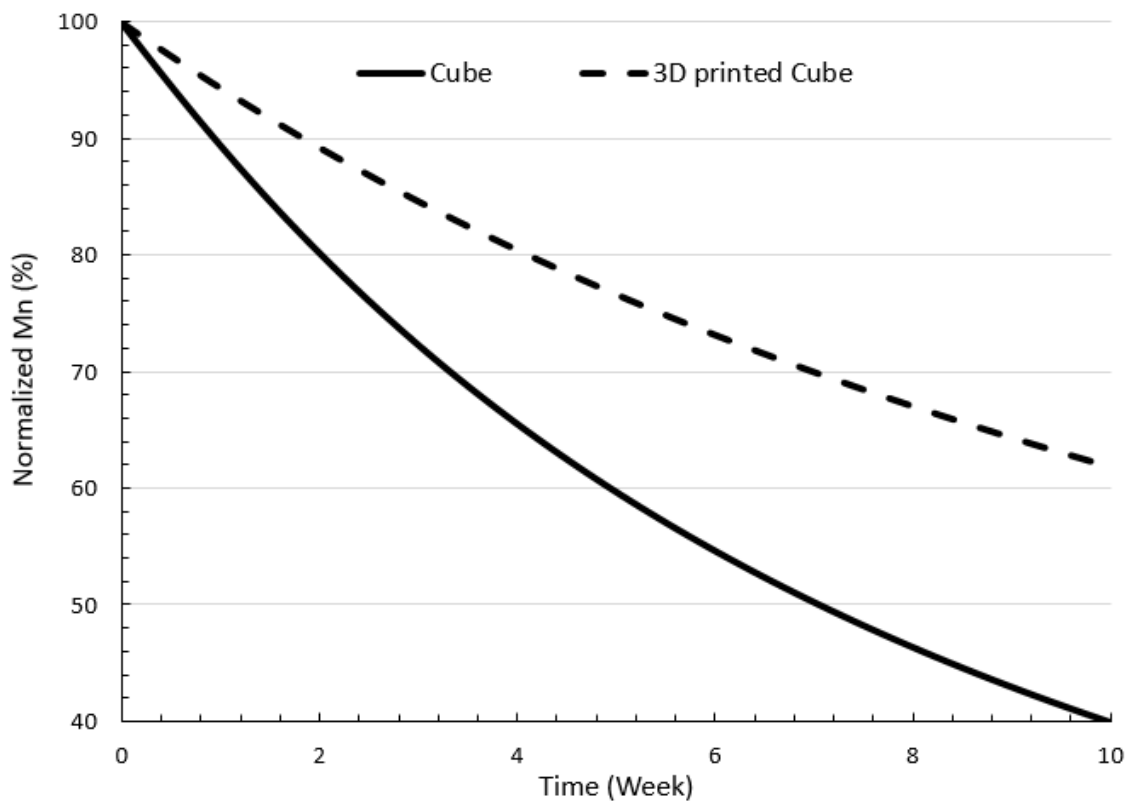
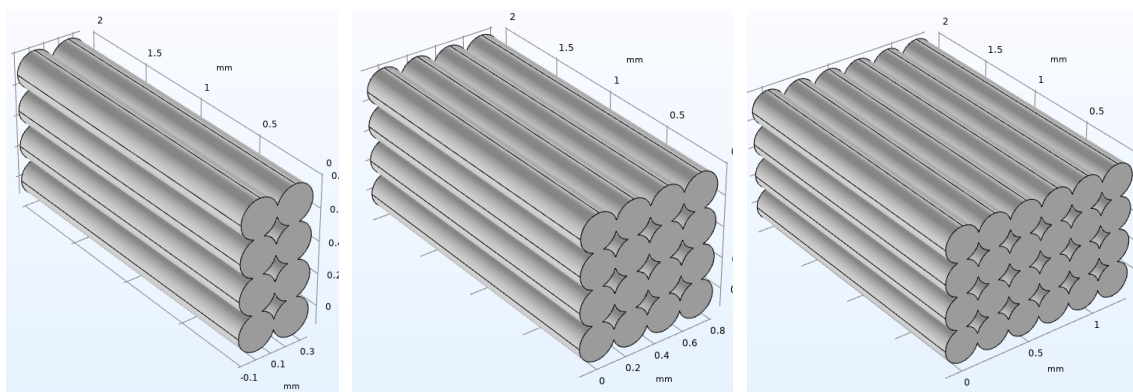


Figure 5.46. Normalized molecular weight variations for a 3D printed and a solid cube



F-TH0.5mm

F-TH1mm

F-TH1.5mm

Figure 5.47. The designs with the repeating overlapped extruded shape units

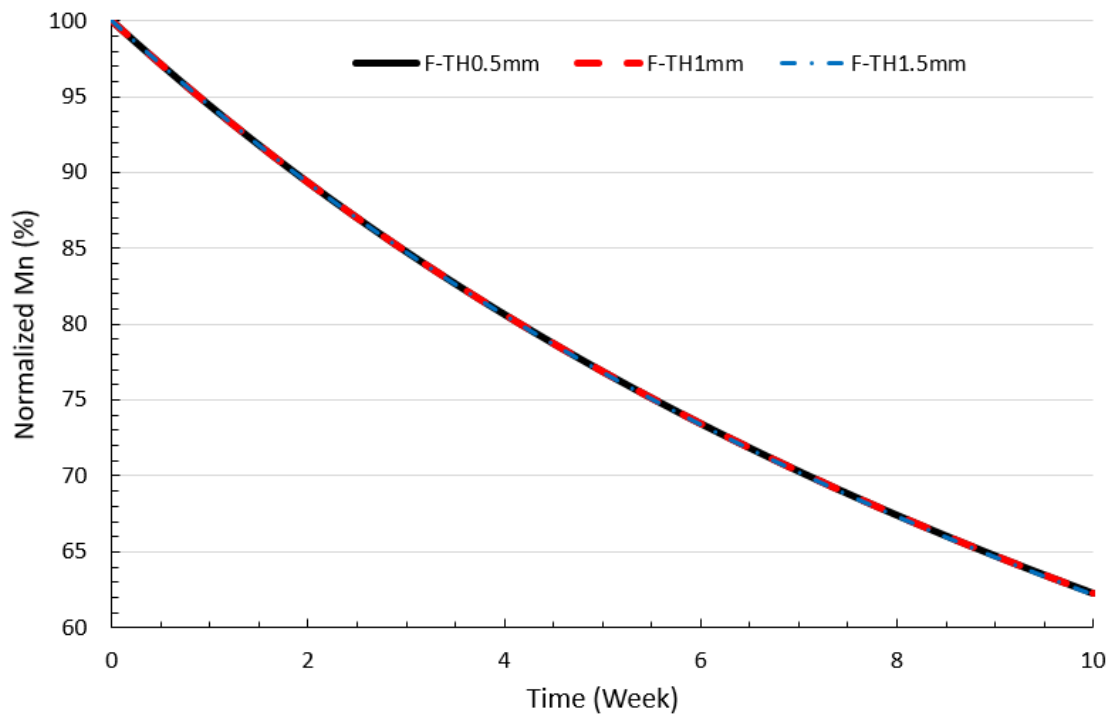


Figure 5.48. Normalized molecular weight variation of the designs with repeating overlapped extruded shape units

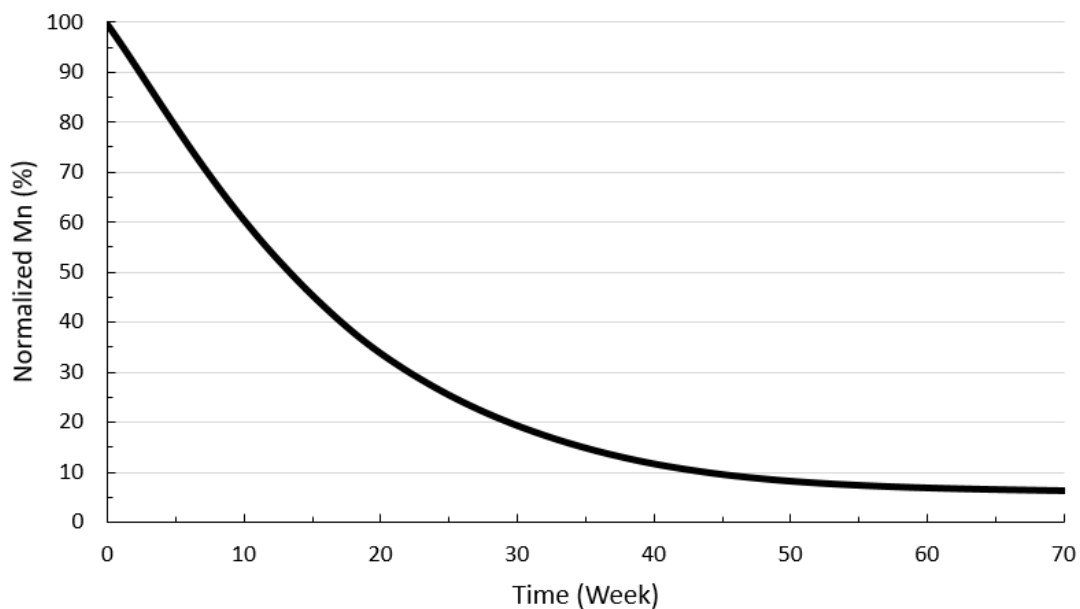


Figure 5.49. Normalized molecular weight variations of the 3D printed Gyroid structures in 70 weeks of biodegradation

5.6.4 Mass Loss Prediction (Biodegradation Percentage) of the FDM Printed Gyroid Scaffolds

Biodegradation causes mass loss in the biomedical devices by diffusion of the polymer short chains, internal erosion, and external erosion. In general, internal and external erosions are the dominant cause of mass loss, and the impact of diffusion of short chains is ignorable [186]. Therefore, estimation of the FDM scaffolds mass loss due to biodegradation is dependent on the internal and surface erosion.

When M_n reaches below a critical value and the target mass is in contact with an eroded neighboring mass, the internal erosion occurs [191]. By reaching the critical M_n , mass loss of the interior regions of the scaffolds starts that can promote either a sudden or a gradual mass loss. To model the internal mass loss, an incubation period have to be defined to capture the processing speed [175]. Surface erosion starts immediately after the media surrounds the scaffold, which is independent of the critical M_n [221]. Figure 5.50 represents the mass loss trends due to surface and internal erosion based on the mentioned theories [186].

The Gyroid 3D printed designs with the same extruded filament diameter reach the critical M_n simultaneously due to the hydrolytic degradation. Therefore, the most critical factor to estimate the mass loss of a tissue scaffold is the amount of mass reaching the critical M_n that is in contact with an eroded neighboring mass. To predict the mass loss due to internal erosion, the critical M_n was considered equal to 17000 g/mol, and the incubation period was set to a one-half week [186]. By considering these factors, Gyroid FDM structures would experience the mass loss just due to surface erosion in the first 15 weeks. After reaching the critical M_n , internal erosion starts, and the erosion rate was superimposed on

the surface erosion. The rate of internal erosion is highly dependent on the wall thickness, and the number of repeating units would play the primary role in the mass loss (due to the critical parameter of the mass contact with an eroded neighboring mass). Figure 5.51 represents the estimated mass loss for the FDM Gyroid scaffolds with three different wall thicknesses (G-TH0.5, G-TH1, and G-TH1.5 are the designs with 0.5 mm, 1 mm, and 1.5 mm wall thickness, respectively.). The results indicate that the mass loss percentage was reduced by almost 8% in the structure with 1 mm wall thickness (four adjacent filament units) compared to the scaffolds with 0.5 mm wall thickness. Therefore, in general, by increasing the wall thickness of the 3D printed parts, the mass-loss rate will reduce.

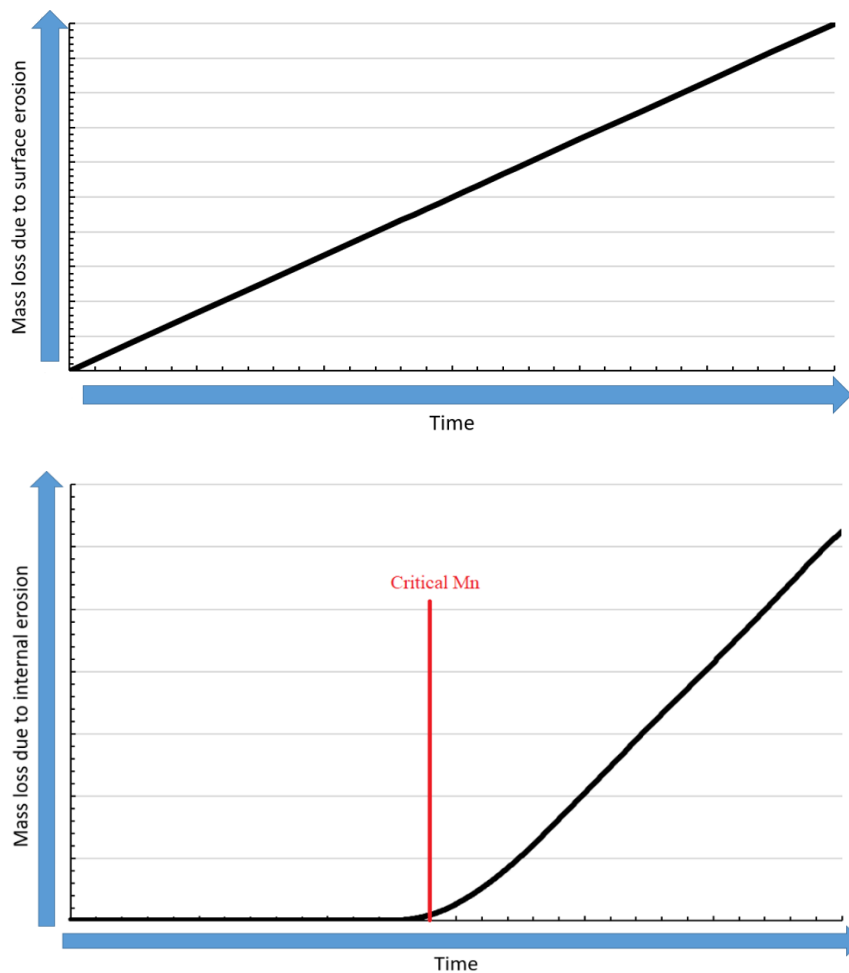


Figure 5.50. Mass loss trends due to internal and surface erosion over time

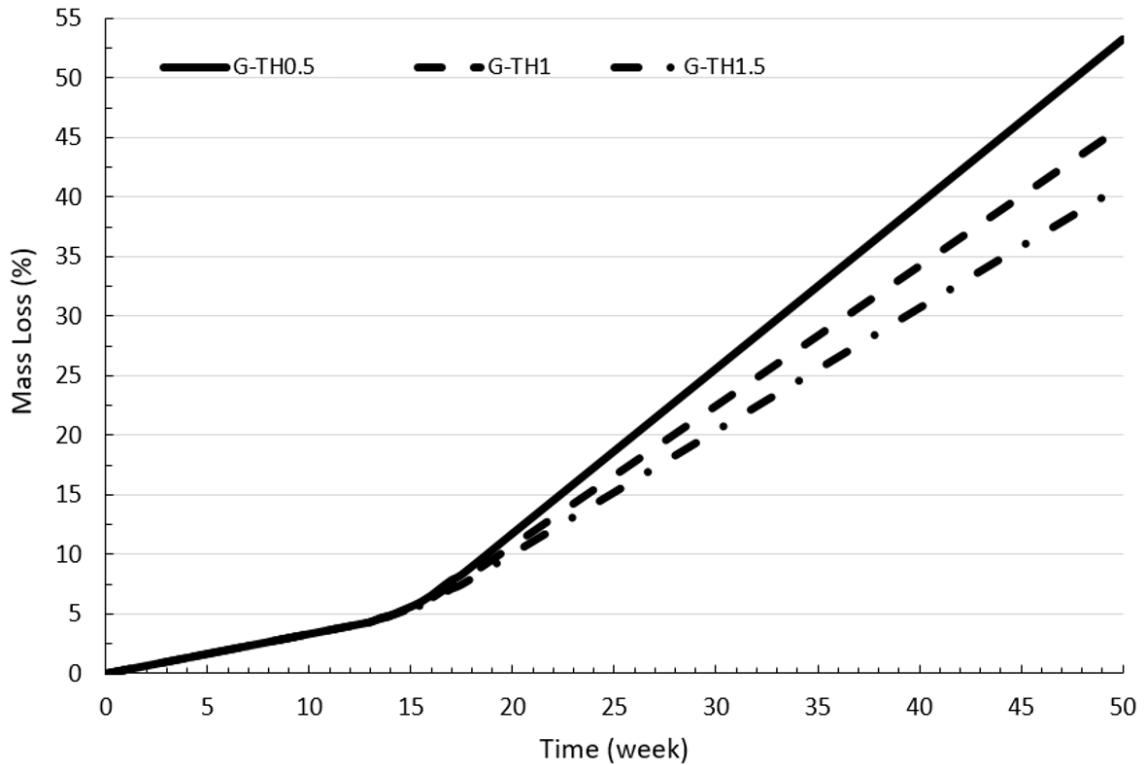


Figure 5.51. Mass loss estimation of the FDM Gyroid scaffolds over time

5.6.5 Mass Loss Prediction (Biodegradation Percentage) of the FDM Printed Nanocomposite Polymeric Bone Tissue Scaffolds

PCL is another type of polyester with the same dominant mechanisms for biodegradation. The analyses and methods presented in the previous sections (5.6.1 to 5.6.4) are employed to estimate the biodegradation behavior of the nanocomposites. Experimental results of the nanocomposites were employed to predict the slope of the surface erosion part of the degradation graph over time and to estimate the critical point (critical Mn), which initiates the internal erosion (based on the previous sections, the critical point was estimated in the range of 12 to 18 weeks, so more experiments were performed in this specific range). These two factors are the most critical parameters in predicting the long-term biodegradation rate,

which were achieved using the experimental results. Figure 5.52 represents the biodegradation rate prediction of PCL compared to the experimental data, which indicates the critical point estimation process. The selected critical point for the PCL matrix was considered the same, for all of the nanocomposite Polymeric Bone Tissue Scaffolds (PBTSs), during the prediction process. The incubation period of the nanocomposite PBTSs was considered the same as the PCL scaffolds; thus, the internal erosion superimposed slope on the graphs was considered equal for all of the nanocomposites.

Therefore, by considering the estimation mechanisms developed in section 5.6.4 and the above hypothesis, the biodegradation rate estimations over 60 weeks were achieved. Figures 5.53-5.55 present the estimated biodegradation results over time.

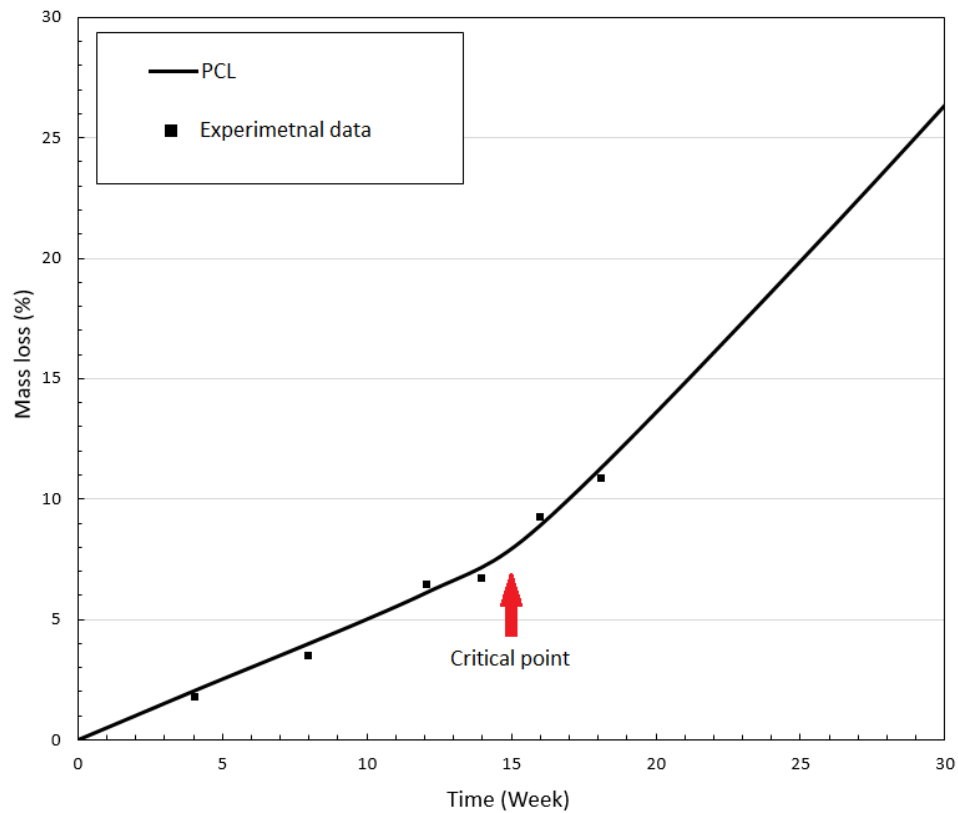


Figure 5.52. Estimation of the slope of surface erosion biodegradation and the critical point of the internal erosion initiation, using the experimental results

In Figure 5.53, the degradation rates of the 3D printed nanocomposite PBTs with nHA nanofiller, and PCL are compared. After 60 weeks (420 days) of degradation, PCL had lost almost 66% of its mass, but the PCL/nHA composites had lost more than 86% of their mass over the same period. In shorter terms, like six months, the differences were still noticeable, as the PCL lost almost 20% of its mass compared to 28-32% mass loss of the PCL/nHA nanocomposites.

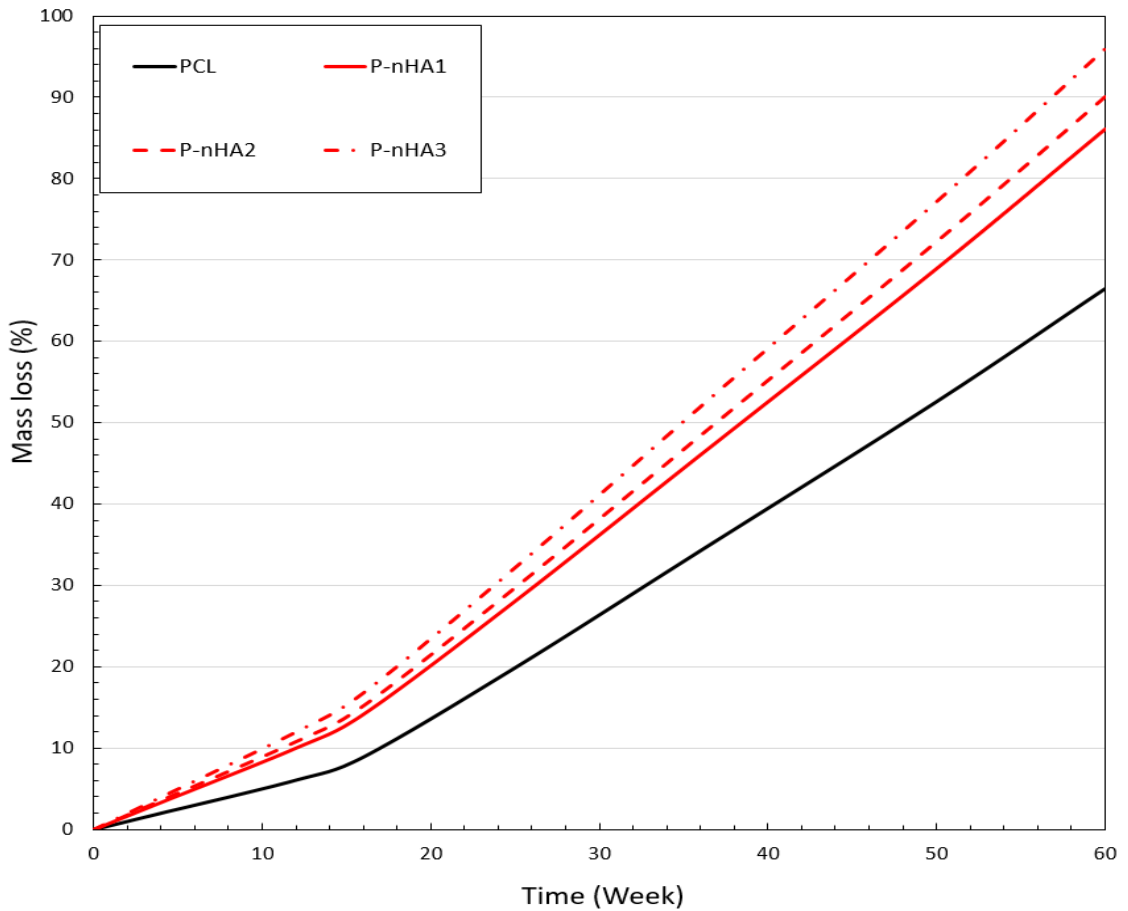


Figure 5.53. Estimated biodegradation rate of the 3D printed nanocomposite PBTs with nHA nanofiller over 60 weeks

Figure 5.54 presents the estimations for the 3D printed nanocomposite PBTs with CNW nanofiller compared to PCL. After 60 weeks of biodegradation, P-CNW3 was completely

degraded, and P-CNW2 had lost more than 97% of its mass. P-CNW1 has a considerably higher biodegradation rate than PCL as well, and lost almost 90% of its mass in the same period. In shorter periods like six months of biodegradation, P-CNWs had lost substantial mass too, reaching to almost 35% for P-CNW3.

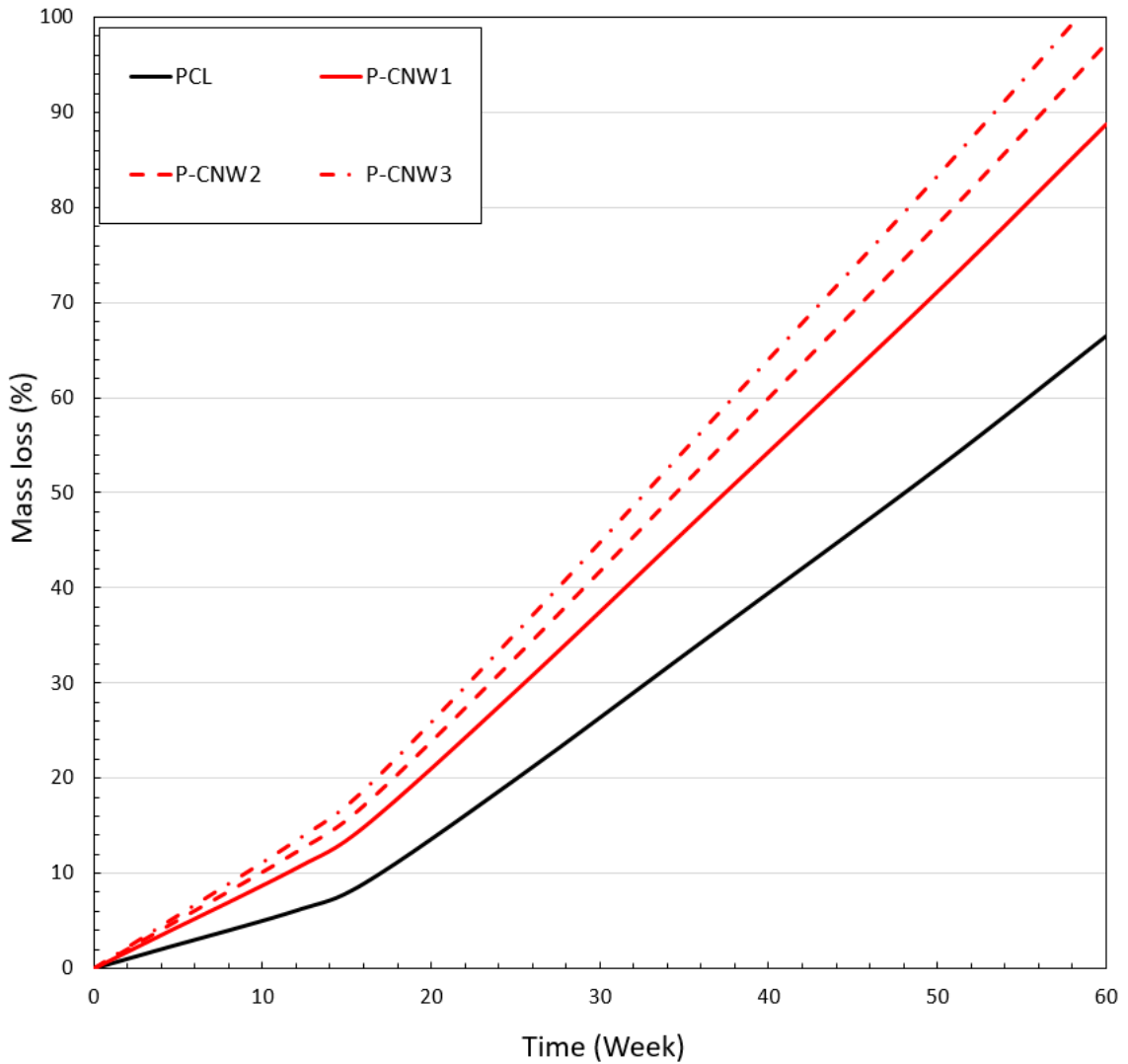


Figure 5.54. Estimated biodegradation rate of the 3D printed nanocomposite PBTSs with CNW nanofiller over 60 weeks

The hybrid nHA/CNW composites exhibited even higher increases in the biodegradation rate of the PCL matrix, as shown in Figure 5.55. P-nHA1.5-CNW1.5 had the highest

biodegradation rate among the manufactured composites and completely degraded after almost 52 weeks. Also, after six months of degradation, it already lost more than 40% of its mass. P-nHA1-CNW2 was degraded entirely after 60 weeks of biodegradation and reached to 33% mass loss after six months. Although P-nHA2-CNW1 had a high degradation rate compare to PCL and lost almost 90% of its mass after 60 weeks, its rate is significantly lower than P-nHA1.5-CNW1.5 and P-nHA1-CNW2.

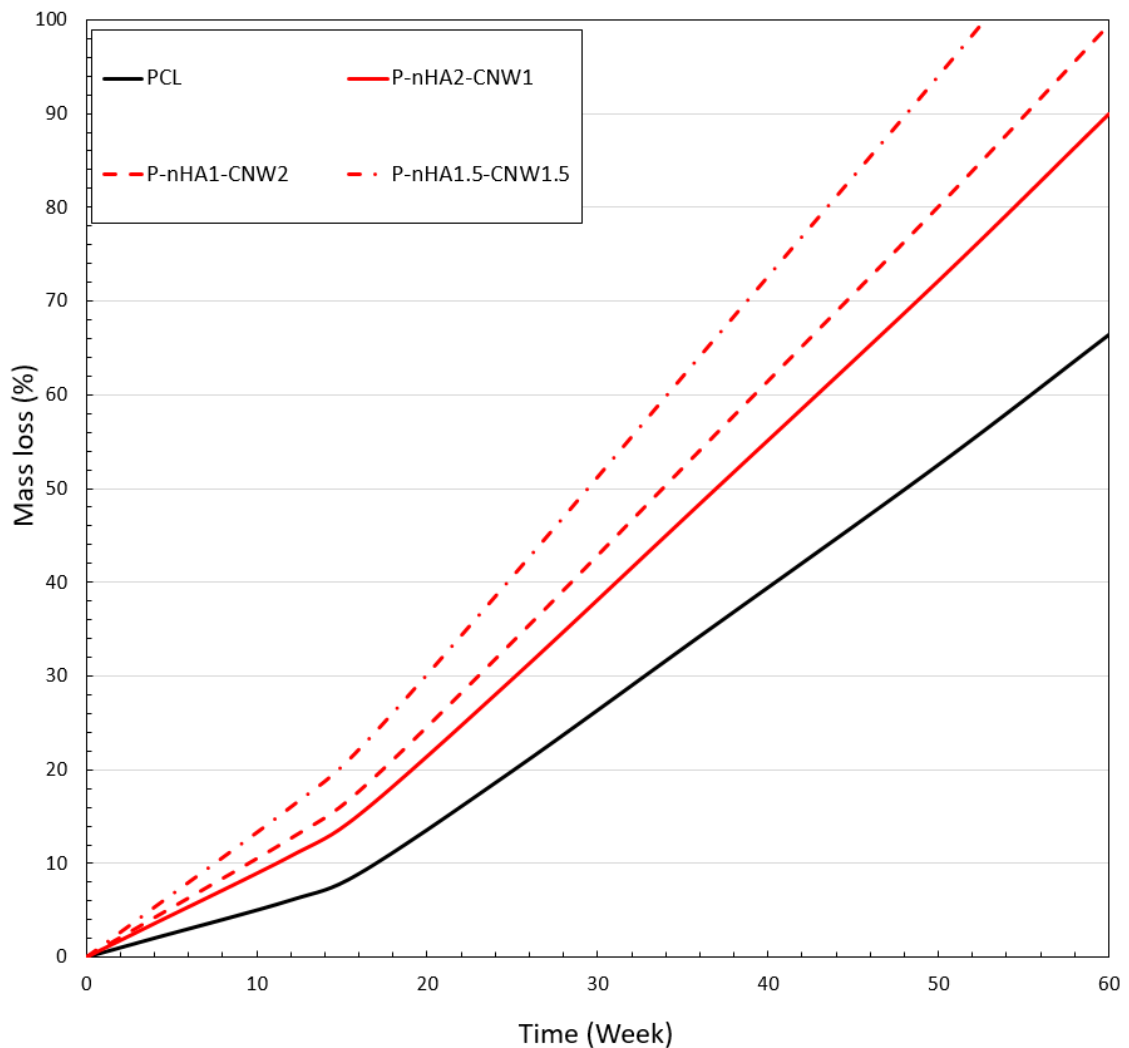


Figure 5.55. Estimated biodegradation rate of the 3D printed nanocomposite PBTSs with hybrid nHA/CNW nanofillers over 60 weeks

5.7 Meta-Modeling and Multi-Objective Optimization

5.7.1 Meta-Modeling

Six essential properties of the PCL/nHA/CNW 3D printed nanocomposite PBTSs were formulated using the meta-modeling technique. The equations are defined based on three variables, including nHA (X1) and CNW (X2) percentages in the polymeric matrix of the nanocomposites and the porosity percentage of the Gyroid design (X3). All of the formulations were achieved with “R-squared Goodness of Fit” higher than 99.5%, except the f_5 (Biodegradation percentage after 6 months), which had “R-squared Goodness of Fit” of 98% because of the complicated correlations and the hardship to fit the formula with very high precision. The extracted equations for the properties are presented in Equations 5.1-5.6.

$$f_1(\text{compressive strength}) = 44.1 + 11.4X_1 + 4.59X_2 + (2.68X_1^2)^{X_2} \operatorname{atan}(11.4X_1^2 - 2.68) - 0.0616X_1X_3 - 7.33X_1X_2 - 0.0013X_3^2 \quad (5.1)$$

$$f_2(\text{average apparent modulus}) = 3290 + 2801X_1 + 1233X_2 - 13.3X_3 - 19.1X_1X_3 - 177X_2^2 - 190X_1^2 - 1014X_2 \operatorname{tanh}(2801X_1) \quad (5.2)$$

$$f_3(\text{compressive strength after 4 months of biodegradation}) = 29 + 0.856X_2 + 0.751X_1 + 0.634X_1^3 + 3.1(0.314X_1^3)^{X_2} - 0.248X_3 - 0.0201X_3X_1^2 \quad (5.3)$$

$$f_4(\text{Average apparent modulus after 4 months of biodegradation}) = 1632 + 489X_1 + 62X_2 + 16.8X_2^2 - 2.61X_1X_3 - 117X_1X_2 - 0.146X_3^2 - 39.2X_1^2 \quad (5.4)$$

$$f_5(\text{Biodegradation percentage after 6 months}) = 12.9 + 0.182X_3 + 0.195X_1X_3 + 0.075X_2X_3 - 2.03X_1X_2 - 1.53X_1^2 - 0.001X_1X_3^2 \quad (5.5)$$

$$f_6(\text{Cell proliferation (OD} \times 1000)) = 32.3 + 3.48X_3 + X_1^{4.37} + 32.3X_1X_2 + 4.5X_2^3 + X_1X_2^2 + 0.183X_3X_2^2 - 13.1X_1 - 29.7X_2 \quad (5.6)$$

A graph was plotted for each equation for a specific range of the nanofillers percentages and a certain porosity to analyze the extracted equations' correctness and precision. In these graphs, the porosity was fixed at 70% to analyze a 3D graph instead a 4D complicated one. The graphs were plotted in the range of 0.5% to 1.5% for both of the nHA and CNW nanofiller percentages. These ranges of the nanofillers were selected because their impact on the properties was more significant after 1%. Also, the 3D printed nanocomposite PBTS of P-nHA1.5-CNW1.5 demonstrated a very significant enhancement in the properties, and by selecting the mentioned range, the properties on the graphs were more easily trackable to validate the results.

Figure 5.56 presents the compressive strength of the 3D printed nanocomposite PBTSs for a Gyroid design with 70% porosity, which was plotted using Equation 5.1. The results were satisfactory as the trends and the values were in the acceptable range. The graph indicates that the compressive strength was improving by the increase of nHA percentage, and there was a slight improvement by the increase in the CNW percentage. In higher percentages of nHA and CNW, the impact of CNW and nHA percentages (the other nanofiller) on the mechanical properties increased, respectively.

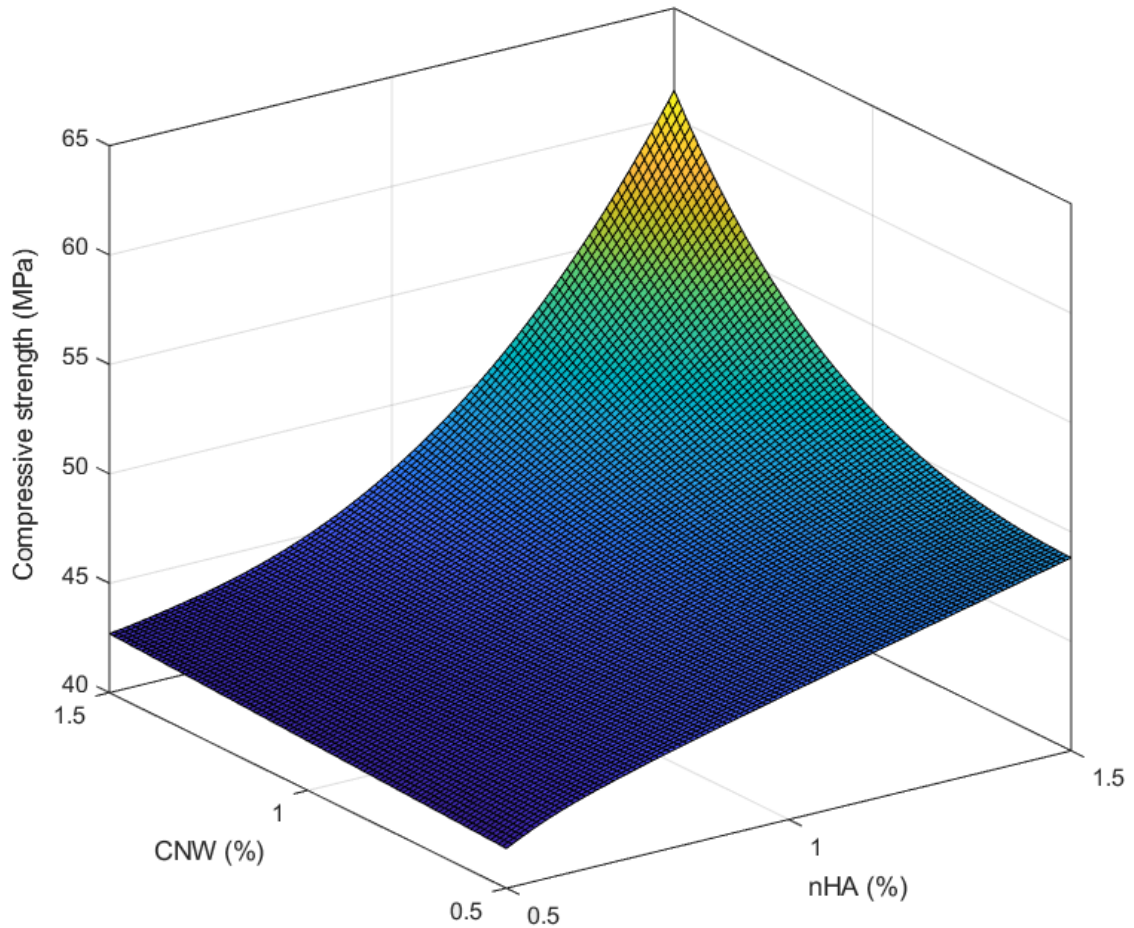


Figure 5.56. Compressive strength of the 3D printed nanocomposite PBTs for 70% porosity Gyroid design

Equations 5.2 was partly plotted in Figure 5.57, which presents the average apparent modulus of the 3D printed nanocomposite PBTs with 70% porosity. The apparent modulus was increasing by the nHA nanofiller significantly, and the widespread impact of the nHA on the apparent modulus dominated the impact of CNW. CNW had an ignorable impact on the apparent modulus, and the trend in the graph shows just an insignificant decrease in the property by increasing the CNW percentage. The decrease even in the higher percentages of nHA is less than 0.2 GPa which is entirely ignorable. In general, the extracted equation was acceptable to model the average apparent modulus of the products.

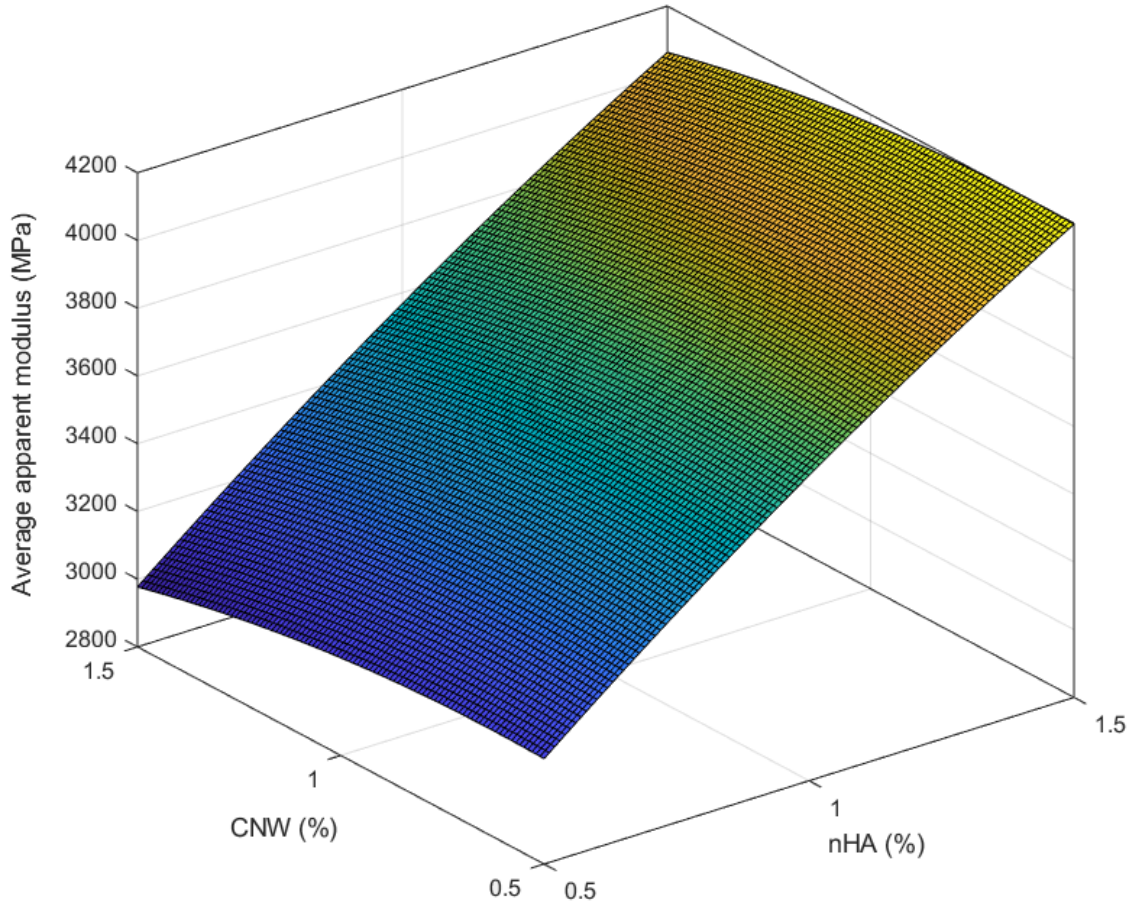


Figure 5.57. Average apparent modulus of the 3D printed nanocomposite PBTs for 70% porosity Gyroid design

The compressive strength of the scaffolds after four months of biodegradation was modeled in Equation 5.3, which is plotted in Figure 5.58 for the porosity of 70%. The observed trend for the nanofillers' impact was almost the same as their impact on the compressive strength before biodegradation. The nanofillers increase the biodegradation rate of the scaffolds and also increase their mechanical properties, so the trade of between the initial properties of the nanocomposites and their higher biodegradation rate leads to the presented graph. In Figure 5.58, the properties for the scaffolds with 70% porosity were in the range of 12.5-16.5 MPa for 0.5-1.5% of CNW and nHA, which the differences were not very significant.

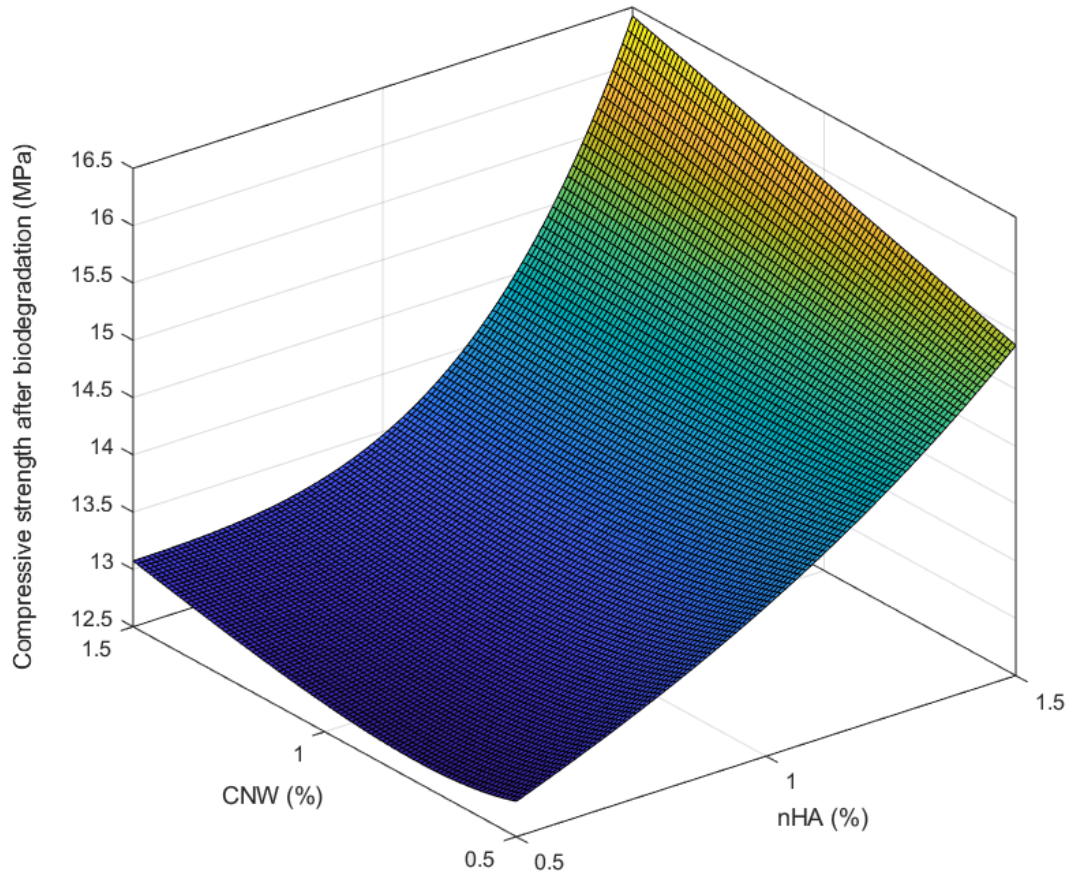


Figure 5.58. Compressive strength after four months of biodegradation of the 3D printed nanocomposite PBTs for 70% porosity Gyroid design

Figure 5.59 shows a plotted surface of Equation 5.4 for the average apparent modulus after four months of biodegradation of the PBTs with 70% porosity. In general, the average apparent modulus results after biodegradation were in the range of lower than 1.5 GPa, which was the same for the plotted area in Figure 5.59. Although the differences are not significant, the trend is interesting compared to the compressive strength after biodegradation. For the compressive strength, the impact of the increase in mechanical properties due to the nanofillers' presence was dominant, but in the apparent modulus, the high biodegradation rate of CNW was dominant in the high percentages of nHA, which caused reduction in the apparent modulus.

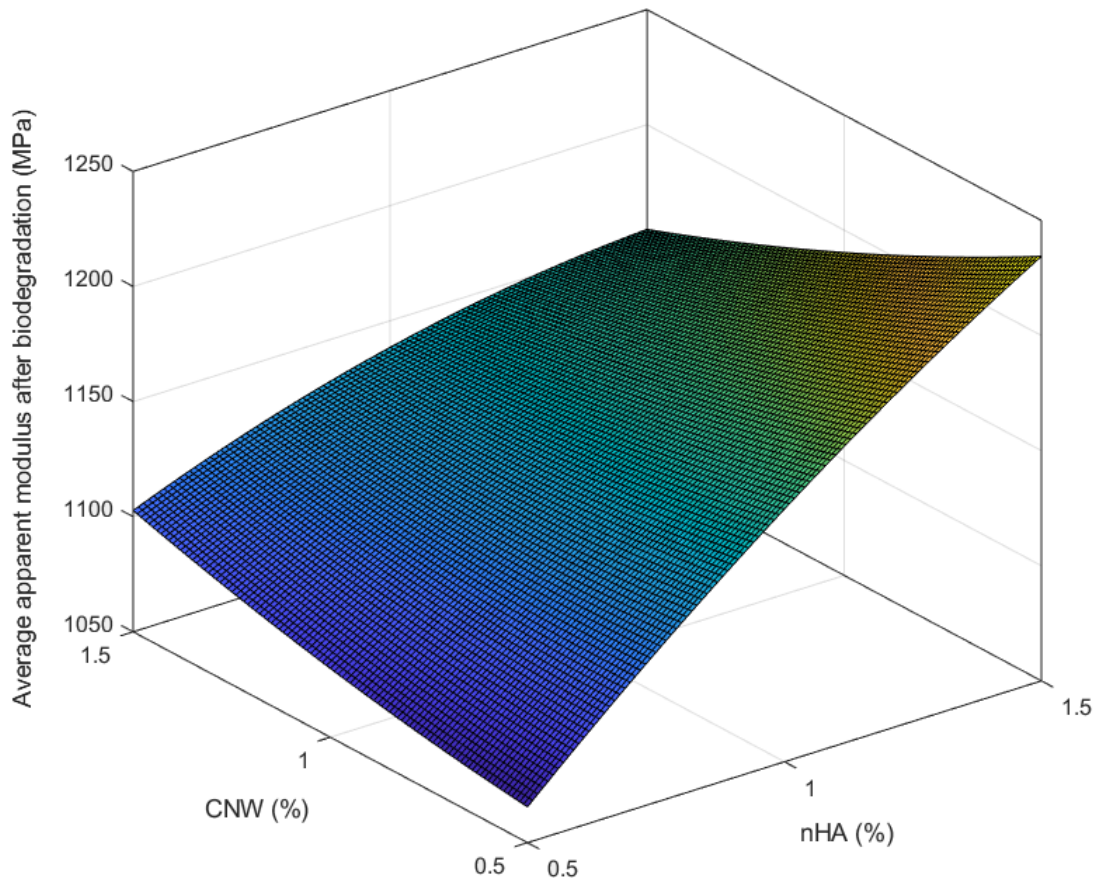


Figure 5.59. Average apparent modulus after four months of biodegradation of the 3D printed nanocomposite PBTs for 70% porosity Gyroid design

The meta-modeling results of the biodegradation rate after six months, had the lowest fitness percentage among all of the extracted equations. The partial plotted graph of Equation 5.5 is shown in Figure 5.60 for scaffolds with 70% porosity. The graph indicated that the high impact of the nanofillers' presence on the biodegradation rate was projected correctly. The graph's maximum line was close to the x-y plane's centerline, emphasizing the higher biodegradation rates in the nanocomposites with even and almost equal percentages of nHA and CNW. The maximum of the graph was reasonable and matched to the P-nHA1.5-CNW1.5 nanocomposite as expected. Therefore, Equation 5.5 was acceptable to model this property of the 3D printed nanocomposite PBTs.

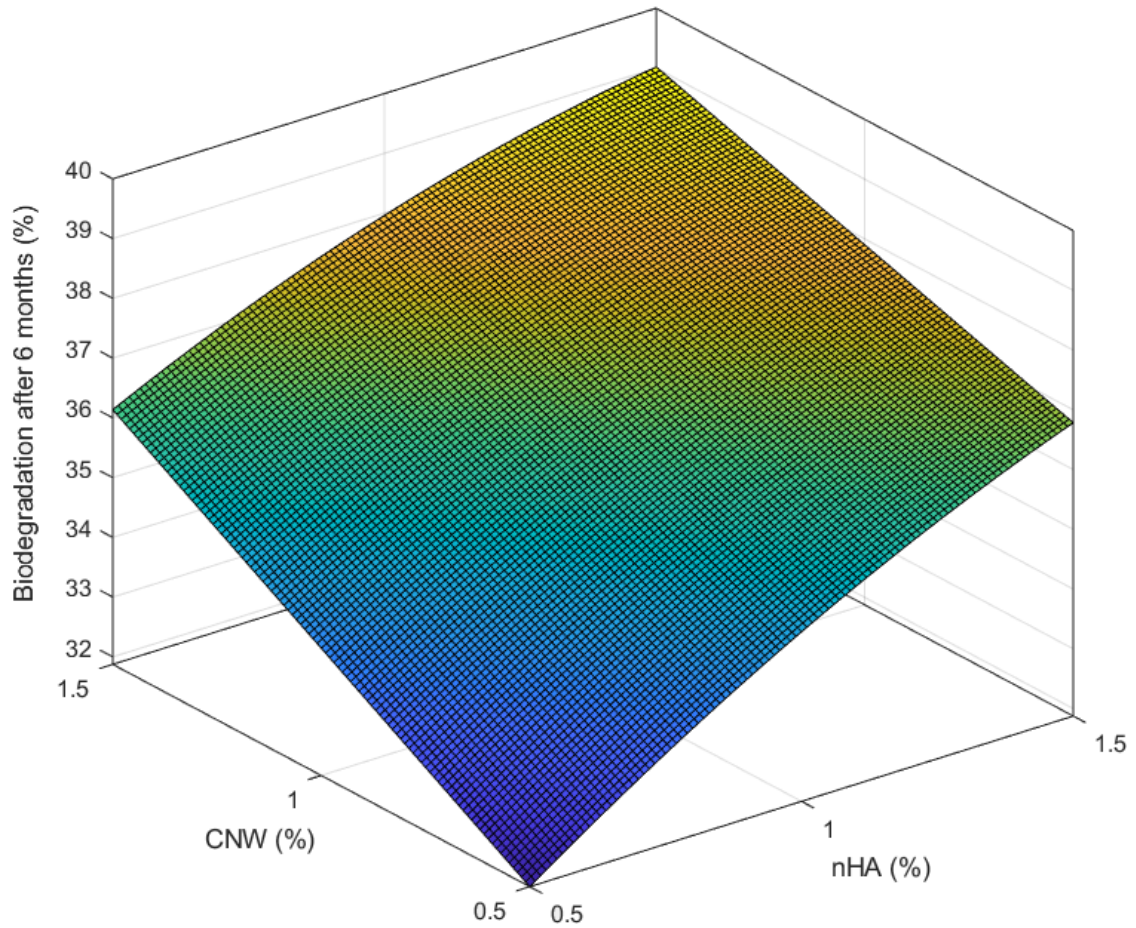


Figure 5.60. Biodegradation percentage of the 3D printed nanocomposite PBTs after six months for 70% porosity Gyroid design

The most stable extracted equation using meta-modeling was Equation 5.6 for the cell proliferation on the scaffolds. Figure 5.61 demonstrates the results of cell proliferation for the scaffolds with 70% porosity. The cell proliferation was improving significantly in the nanocomposites with a higher percentage of the CNW, and the impact of the CNW was dominant in the nanocomposite scaffolds with both nHA and CNW nanofillers. Based on the mentioned facts and the trend in the graph, the extracted equation was accurate to predict the cell proliferation properties of the 3D printed nanocomposite PBTs.

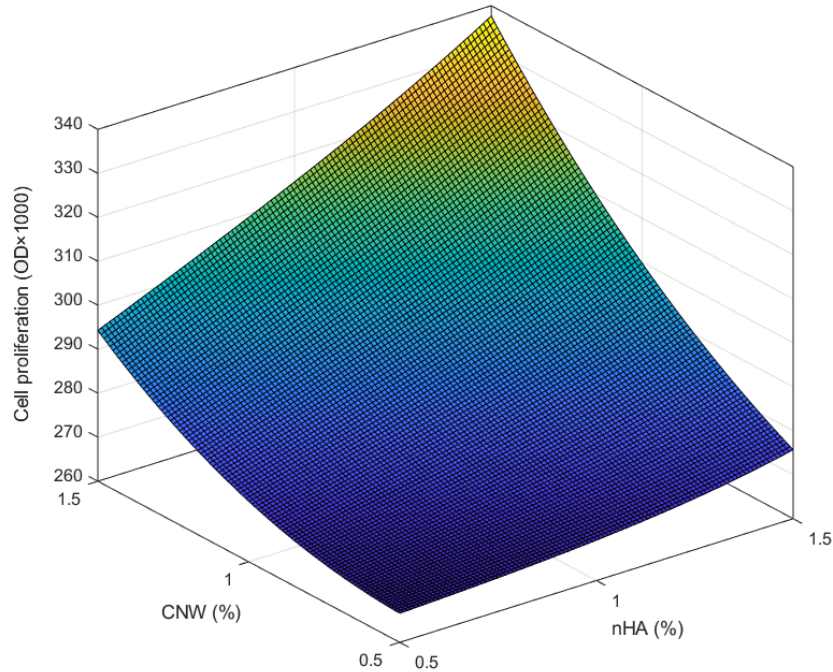


Figure 5.61. Cell proliferation of the 3D printed nanocomposite PBTs for 70% porosity Gyroid design

5.7.2 Multi-Objective Optimization

The NSGA-III optimization technique presents a few non-dominated optimal options as the result of simultaneous multi-objective optimization. The results are presented in Figures 5.62 and 5.63, and the detailed optimal options are reported in Table 5.13, in no order of preference as they are non-dominated. The optimization results are extensively validated with experimental results (at least 10 samples per property) and the errors for the validated optimal candidate solutions were less than 8%, 11% and 13% for the mechanical properties, cell proliferation and biodegradation, respectively.

In Figure 5.62, compressive strength, average apparent modulus, cell proliferation, and biodegradation after six months (the color bar) of the optimal results were plotted. As shown in the graph, the optimal results cover a considerable range of the output variables.

The points with red color (high biodegradation rates) had high cell proliferation properties, but their mechanical properties were in a more diverse range; all of these options had low average apparent modulus, but their compressive strengths were changing in the range of 40 GPa to 60 GPa. The options with lower biodegradation rates in Figure 5.62, mostly had higher average apparent modulus.

In Figure 5.63, the relationship of compressive strength and average apparent modulus properties after four months of biodegradation with cell proliferation and biodegradation after six months were indicated for the optimal non-dominated options. This graph exhibited a more clear division in the results. The options with high biodegradation rate and cell proliferation had lower mechanical properties with no exceptions, and by moving toward the options with lower biological properties, the mechanical properties were increased. The reason can be the dominant impact of biodegradation on the mechanical properties after a few months of degradation, in the optimal results.

The noticeable extracted information from the presented optimal results in Table 5.13 are as follow:

- The majority of the optimal responses are PCL/nHA/CNW 3D printed nanocomposite PBTSs with more than 1% nanofiller percentage for both of the nHA and CNW.
- The optimal results' porosity was over the whole range of 60-90% for different material compositions and covered a wide range of responses. The nanocomposite fillers were covering for the decrease in the mechanical properties as much as possible by the increase in the porosity. Also, by the increase in the porosity, cell proliferation and biodegradation were increasing as expected. Therefore, the results

indicated that based on the specific applications and requirement for any specific porosity, a non-dominated optimal response can be offered.

- The optimal non-dominated results for the PBTSs can have compressive mechanical strength as high as 51 to 61 MPa, average apparent modulus of 2.6 to 5.1 GPa, significant cell proliferation properties, and maintain up to 20 to 23 MPa of their compressive strength after four months of biodegradation.

In general, the multi-objective optimization based on the extracted equations of the meta-modeling was significantly beneficial in connecting the experimental and numerical results of this study. The technique connected all of the independent experimental studies and the numerical results, and in conclusion, presented a few non-dominated optimal options by considering all of the extracted information and trends in the previous sections.

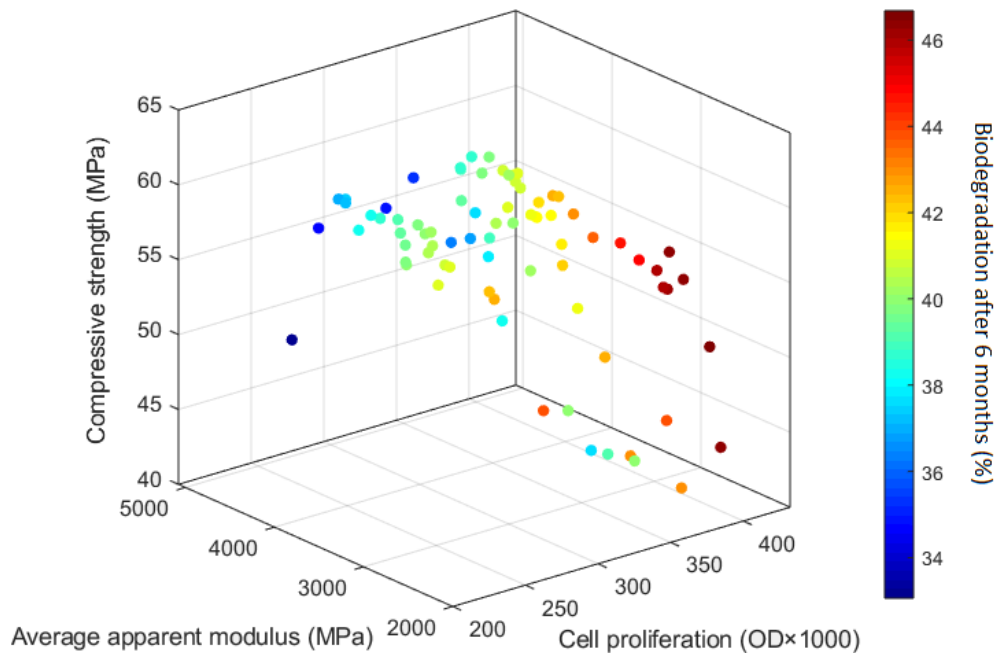


Figure 5.62. Non-dominated optimal options presented by the NSGA-III multi-objective optimization technique for compressive strength, average apparent modulus, cell proliferation, and biodegradation after six months

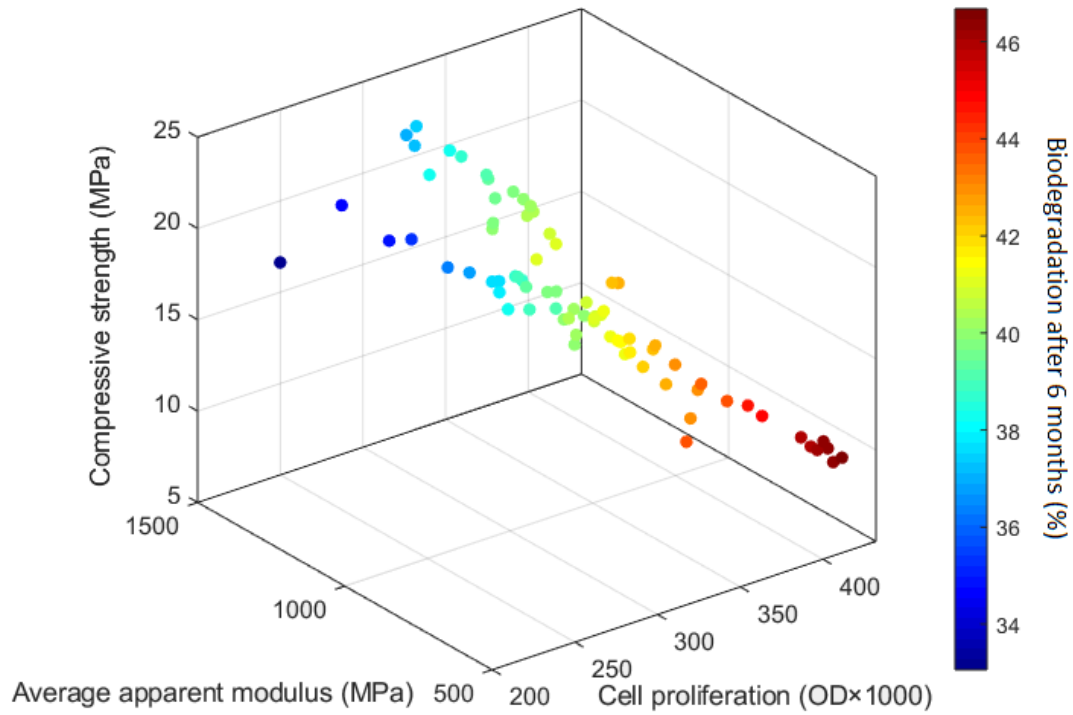


Figure 5.63. Non-dominated optimal options presented by the NSGA-III multi-objective optimization technique for compressive strength and average apparent modulus after four months of biodegradation, cell proliferation, and biodegradation after six months

Table 5.13. Non-dominated optimal options presented by the NSGA-III multi-objective optimization technique for the PCL/nHA/CNW 3D printed nanocomposite PBTSS

X_1	X_2	X_3	f_1	f_2	f_3	f_4	f_5	f_6
1.28	1.71	60	59.89	4161.66	17.44	1365.96	35.19	305.48
1.33	0.52	60	50.29	4426.55	17.59	1433.87	33.06	238.14
1.32	1.54	60.07	57.93	4267.1	17.68	1372.12	34.94	293.09
1.61	1.07	60.25	56.07	4688.24	19.83	1417.65	34.6	272.49
1.18	1.77	62.67	55.9	3918.5	16.12	1305.2	36.3	316.59
1.17	1.82	63.75	56.09	3848.38	15.79	1281.03	36.85	325.48
0.5	2.3	64.88	44.47	2734.31	15.03	1263.84	37.55	340.32
2.23	0.72	65.74	56.3	4988.34	23.07	1377.81	36.97	304.55
1.24	1.75	65.94	57.56	3883.19	15.55	1235.3	37.65	330.99
2.18	0.75	66.33	56.19	4922.71	22.66	1355.16	37.19	305.51
1.17	1.79	66.47	54.88	3767.75	15.03	1221.57	37.85	332.97

2.47	0.52	66.88	55.75	5078.44	23.01	1402.43	37.43	314.97
1.07	1.79	67.68	50.99	3615.8	14.36	1192.71	38.17	333.1
2.36	0.5	69.09	54.29	4882.65	21	1341.26	38.22	312.04
0.62	2.22	69.13	43.46	2832.87	13.87	1169.53	39.19	357.82
1.44	1.56	69.3	60.77	4021.03	16.07	1167.32	38.79	336.95
2.44	0.54	69.31	54.9	4914.85	22.11	1331.18	38.36	322.41
1.49	1.47	69.57	60	4080.23	16.41	1166.58	38.77	332.82
1.5	1.46	69.87	59.87	4082.54	16.42	1160.45	38.87	333.2
1.29	1.61	70.07	55.84	3828.4	14.66	1144.34	39	337.43
2.47	0.52	70.17	54.67	4879.45	21.8	1315.27	38.68	326.62
0.58	2.27	70.89	43.03	2707.78	13.47	1134.29	39.96	368.59
2.23	0.75	71.23	55.1	4684.43	21.56	1231.1	39.08	326.85
1.53	1.37	71.37	57.83	4067.95	16.17	1130.22	39.28	332.8
1.5	1.47	71.88	59.61	3989.23	15.79	1109.93	39.67	342.11
1.31	1.64	72.11	56.69	3757.56	14.22	1094.13	39.89	349.29
1.5	1.5	72.13	60.62	3972.2	15.78	1101.83	39.84	345.96
2.44	0.54	72.19	53.9	4741.95	20.96	1254.64	39.42	332.12
0.88	1.91	72.44	45.49	3209.53	12.82	1082.04	39.93	353.6
2.3	0.62	72.85	53.47	4635.2	20.37	1213.57	39.62	328.94
1.22	1.7	72.91	53.76	3619.81	13.46	1072.67	40.18	352.9
1.42	1.57	72.95	59.56	3850.1	14.86	1076.76	40.22	352.09
2.2	0.79	72.98	54.88	4564.78	20.94	1176.36	39.73	333.29
2.23	0.61	73.44	52.66	4558.9	19.32	1195.52	39.75	324.44
2.22	0.76	73.86	54.29	4531.28	20.61	1158.2	40.05	336.14
2.32	0.5	74.01	52.41	4572.68	18.86	1205.61	39.94	325.86
1.46	1.42	74.19	56.46	3880.72	14.77	1054.32	40.36	345.13
2.18	0.8	74.24	54.5	4481.73	20.38	1139	40.19	337.19
1.44	1.55	74.7	58.7	3798.42	14.44	1034.19	40.82	356.85
2.26	0.68	74.82	53.11	4496.74	19.81	1146.39	40.33	336.35
1.56	1.42	74.87	59.64	3928.3	15.56	1037.68	40.78	352.83
2.24	0.73	74.87	53.56	4482.38	20.06	1136.3	40.38	338.3
1.49	1.49	75.15	59.03	3842.97	14.8	1025.97	40.93	356.12
1.12	1.83	75.39	51.34	3389.82	12.43	1009.63	41.35	371.18

1.51	1.48	75.55	59.51	3848.82	14.93	1016.33	41.09	357.92
1.33	1.67	75.8	57.04	3623.01	13.3	1000.99	41.39	367.21
1.54	1.39	76.01	57.33	3872.42	14.92	1010.62	41.06	352.67
1.56	1.42	76.1	59.35	3878.22	15.23	1005.78	41.23	357.6
1.42	1.53	76.22	57.01	3730.7	13.85	996.04	41.3	359.97
1.28	1.69	76.42	55.24	3545.54	12.8	984.51	41.61	369.77
2.25	0.67	76.55	52.4	4399.06	19.09	1099.76	40.92	341.74
1.42	1.53	76.74	56.87	3709.82	13.7	982.58	41.49	361.99
1.42	1.53	76.86	56.83	3705.09	13.66	979.52	41.53	362.45
2.18	0.73	76.91	52.43	4338.92	18.74	1077.06	41.03	341.45
2.29	0.52	77.11	51.27	4380.99	17.74	1112.43	40.97	335.97
1.47	1.49	77.66	57.7	3726.52	13.91	960.25	41.83	365.06
1.31	1.6	78.28	53.88	3531.65	12.43	939.16	42.06	369.51
1.45	1.55	78.77	58.07	3642.06	13.38	927.44	42.35	373.51
1.07	1.81	78.9	48.24	3231.4	11.32	921.19	42.45	380.22
1.51	1.47	79.47	58.05	3685.76	13.76	912.81	42.49	372.26
1.43	1.55	80.4	56.95	3564.87	12.77	883.89	42.91	379.05
0.61	2.11	80.63	40.77	2602.29	10.84	892.68	43.02	394.39
2.17	0.73	80.89	50.99	4115.93	17.26	962.53	42.35	354.93
2.31	0.6	81.68	50.31	4132.29	17.08	965.57	42.59	359.37
0.92	1.98	81.96	44.16	2922.38	10.37	846.15	43.88	403.78
0.86	1.79	82.11	42.4	2947.31	10.19	839.24	42.9	380.42
1.4	1.57	82.18	55.46	3459.56	11.95	834.64	43.53	386.09
1.42	1.55	85.38	55.03	3352.58	11.22	744.85	44.65	398.33
1.34	1.65	85.69	53.97	3252.08	10.54	734.06	44.92	405.02
1.38	1.58	88.77	53.23	3181.02	9.94	645.97	45.83	412.92
1.36	1.58	89.54	52.16	3138.96	9.58	623.97	46.04	414.87
1.31	1.69	89.66	52.62	3065.8	9.25	618.26	46.39	424.11
0.94	1.91	89.82	42.16	2729	8.26	627.87	46.41	429.15
1.86	0.5	89.87	44.58	3525.08	10.78	715.84	43.74	355.99
1.15	1.83	89.92	48.32	2902.92	8.53	615.18	46.68	432.19
1.36	1.58	89.96	52.03	3122.28	9.46	611.33	46.18	416.54
1.41	1.58	90	54.35	3151.79	9.86	607.88	46.33	419.69

Chapter 6. Conclusions and Suggestions for Future Work

The main goal of this thesis was to introduce novel nanocomposite FDM filaments to manufacture biodegradable polymeric bone tissue scaffolds with advanced material compositions and geometries by 3D printing. As discussed in the background and literature review, the Polymeric Bone Tissue Scaffolds (PBTSs) have to achieve certain properties to be functional. Based on the type of bone tissue and the disease, the required characteristics vary case by case. In general, four fundamental characteristics have to be satisfied for a biodegradable PBTS to be practical, which can be summarized as follow:

- The scaffold should have a biomimetic design with high porosity (60-90%) to encourage and enhance cell proliferation and attachment to the scaffolds.
- The scaffolds' material compositions have to be non-toxic and enhance the regeneration and proliferation of the native cells.
- The scaffolds should degrade and metabolize by the body after 12-18 months. Also, it is more satisfactory if the scaffolds maintain part of their mechanical properties for almost six months.
- The compressive mechanical properties of bone tissue scaffolds should match the native tissue, which is in the range of 0.5 to 16 GPa for the elastic modulus and 6 to 124 MPa for the ultimate strength (this range covers the whole structural spectrum of the bone tissue from trabecular bones to cortical bones).

The products in this study were designed, manufactured, and characterized to meet these essential properties for a functional PBTS. The experimental analyses in the related sections to Triply Periodic Minimal Surfaces (TPMS) designed scaffolds indicated the

impact of the biomimetic designs, porosity, and biodegradation on the mechanical and morphological properties of the scaffolds, independent of the material composition. The scaffolds were manufactured by using a polyester polymer with the same dominant biodegradation properties of the main polymeric matrix of the manufactured nanocomposite PBTs in this study. The TPMS designs indicated significant improvement in the mechanical properties and kept part of their strength even after six months of biodegradation. The Gyroid design is recommended as the primary design for the scaffolds for further studies. These structures have higher mechanical properties, stable mechanical strength on increasing porosity of the scaffold, and maintain a considerable portion of the properties after six months of biodegradation. The experimental results for TPMS scaffolds fabricated with a neat polyester can be summarized as follow:

- The Schwarz-D scaffold with 60% porosity showed the highest mechanical properties compared to the other designs, but the mechanical properties were significantly reduced on increasing the porosity.
- The Gyroid scaffolds maintained their mechanical strength and apparent modulus with increase in the porosity.
- The Neovius scaffolds exhibited inferior mechanical properties compared to Schwarz-D and Gyroid scaffolds.
- Six months of biodegradation depleted the mechanical properties of the structures with Schwarz-D design much more than the Gyroid scaffolds. The Schwarz-D scaffolds with 80% porosity completely lost their mechanical strength, while the Gyroid structures with different porosities maintained their mechanical strength.

- Biodegradation transformed the ductile failure mode of the TPMS scaffolds to brittle mode.
- The Gyroid scaffold with 80% porosity was a very favorable design in terms of high porosity, compressive strength, and apparent modulus, as well as in preserving an acceptable percentage of its mechanical strength after six months of biodegradation.

In the next set of experimental studies, novel nanocomposites of PCL/nHA/CNW FDM filaments were manufactured, and 3D printed to address the essential required material composition for a practical PBTS. PCL/nHA/CNW nanocomposite filaments for FDM were designed, developed, and manufactured using a green manufacturing method. The Taguchi orthogonal array method was employed to optimize the 3D printing processing conditions of the nanocomposites. The material characterization of the nanocomposites were performed by Thermo-Gravimetric Analysis (TGA) using ASTM E1131 – 20 standard procedure and Fourier Transform Infrared Spectroscopy (FTIR) analysis. The mechanical and biological properties of the nanocomposite PBTSs fabricated by the FDM technique were investigated. MTT assay and fluorescent microscopy were employed to assess cell attachment and proliferation on the PBTSs. The assessments indicated that the employed materials and the 3D printed nanocomposite PBTSs were not toxic to the bone preosteoblast cells and significantly improved the cell proliferation and attachment to the scaffolds. The nanocomposites also increased the PCL matrix's overwhelmingly low biodegradation rate to fit into the practical range of the biodegradable PBTSs. The nanocomposite material selection improved the mechanical properties of the matrix, which was added to the increment in the mechanical properties caused by the 3D printing

processing conditions optimization using the Taguchi orthogonal array method. The nanocomposite fillers increased the average compressive strength and apparent modulus of the PBTs up to 44% and 78%, respectively. These parts of experiments were performed independent from the structural design, and the finding and understood relations were used for further analyses afterward. In general, the results of these parts of the experimental assessments can be summarized as follow:

- The optimal 3D printing processing conditions are the nozzle temperature of 100°C, print speed of 15 mm/s, build plate temperature of 30°C, and the fan speed of 100%, with desirability equal to 98.7%.
- The material characterization of the nanocomposites revealed that the proposed green manufacturing method was successful in the accurate fabrication of the nanocomposites.
- The manufactured PBTs that were fabricated by P-nHA3, P-nHA2-CNW1, and P-nHA1.5-CNW1.5 filaments had the highest mechanical properties. The nHA nanofiller significantly increased the mechanical properties of the PCL matrix. The CNW nanofiller did not diminish the mechanical properties of the PBTs and even increased them slightly.
- CNW significantly increased preosteoblast cells' proliferation on the scaffolds. P-CNW3, P-CNW2, P-nHA1-CNW2, and P-nHA1.5-CNW1.5 exhibited more than 20% higher cell proliferation than PCL, after seven days of cell culture.
- The visualized fluorescent microscopy results of the cells' nuclei and actin filaments confirmed the MTT assay results.

- Although CNW and nHA nanofillers both increased the PCL matrix's biodegradation rate, CNW had a more significant impact.
- After biodegradation, the nanocomposites did not considerably alter the pH of the media.

The experimental results, numerical simulation, and analytical assessment were combined to extend the experiments' biodegradation results and predict the behavior in an extended long-term period. The predicted results indicated that all 3D printed nanocomposite PBTSS introduced in this study will biodegrade in the practical range of 12 to 18 months. P-nHA1.5-CNW1.5 was predicted to biodegrade in almost 12 months completely, and P-nHA1 entirely degrades in 17 months. The rest of the manufactured nanocomposite PBTSS were predicted to biodegrade in the range of 12 to 17 months.

Based on the experimental results and numerical analyses, the final 3D printed PBTSS with Gyroid structure and using the PCL/nHA/CNW nanocomposites are practical products considering all of the mentioned critical requirements of the PBTSS. The meta-modeling was employed to formulate the relationship between the design and the nanocomposite material contents with the critical properties of the scaffolds and make a bridge between the independent experiments performed in this study. NSGA-III multi-objective optimization method was used to present a few non-dominated optimal options considering the design and nanocomposite contents of the 3D printed PBTSS. The final optimal products can have compressive mechanical strength of 51 to 61 MPa, average apparent modulus of 2.6 to 5.1 GPa, and significant cell proliferation properties. Also, they biodegrade in the practical range of less than 12 to 18 months and can maintain up to 20 to 23 MPa of their compressive strength after four months of biodegradation. These scaffolds

have advanced biomimetic TPMS designs and practical material compositions as well. Comparing the results of this study with the critical requirements of the practical bone tissue scaffolds reveals that the products significantly serve the purpose and are practical biodegradable PBTSSs.

For future works, there are a few recommendations in both experimental and numerical simulation research approaches. As mentioned above, the PCL/nHA/CNW nanocomposite 3D printed scaffolds were practical options for bone tissue scaffolds, and further experimental investigations on these types of nanocomposites can be done to continue the current research. Also, in the numerical simulation approach, there are few opportunities to investigate the biodegradation and mechanical properties of the scaffolds with advanced geometries. A few recommendations for future works can be listed as follow:

- Animal testing for the proposed PBTSSs in this study can be performed. The In-Vitro studies in this thesis indicated significant cell proliferation and attachment to the scaffolds by using CNW and nHA nanofillers. In-Vivo experimentations can be helpful for further investigation of the proposed scaffolds' properties.
- Further investigations can be done on the PCL/nHA/CNW nanocomposites, using other common manufacturing methods for the same application or employing FDM manufacturing for other biomedical applications.
- The biodegradation impact on the fracture pattern of TPMS scaffolds can be further investigated, especially by employing In-Vivo experimentations.
- A new numerical approach can be developed to simulate the impact of biodegradation on the mechanical properties for different designs and material compositions in the long term. The presented experimental results of this study can

be a significant start point to develop a new numerical approach and validate the model with the presented experimental results. This approach can be beneficial for other similar studies in the future.

References

- [1] K.-U. Lewandrowski, J. D. Gresser, D. L. Wise, and D. J. Trantolo, "Bioresorbable bone graft substitutes of different osteoconductivities: a histologic evaluation of osteointegration of poly (propylene glycol-co-fumaric acid)-based cement implants in rats," *Biomaterials*, vol. 21, no. 8, pp. 757-764, 2000.
- [2] G. F. Muschler, S. Negami, A. Hyodo, D. Gaisser, K. Easley, and H. Kambic, "Evaluation of collagen ceramic composite graft materials in a spinal fusion model," *Clinical Orthopaedics and Related Research®*, vol. 328, pp. 250-260, 1996.
- [3] O. Johnell and J. Kanis, "An estimate of the worldwide prevalence and disability associated with osteoporotic fractures," *Osteoporosis international*, vol. 17, no. 12, pp. 1726-1733, 2006.
- [4] T. Sözen, L. Özışık, and N. Ç. Başaran, "An overview and management of osteoporosis," *European journal of rheumatology*, vol. 4, no. 1, p. 46, 2017.
- [5] S. C. Marks Jr and P. R. Odgren, "Structure and development of the skeleton," in *Principles of bone biology*: Elsevier, 2002, pp. 3-15.
- [6] J.-Y. Rho, L. Kuhn-Spearing, and P. Zioupos, "Mechanical properties and the hierarchical structure of bone," *Medical engineering & physics*, vol. 20, no. 2, pp. 92-102, 1998.
- [7] R. Lanza, R. Langer, J. P. Vacanti, and A. Atala, *Principles of tissue engineering*. Academic press, 2020.
- [8] P. V. Giannoudis, H. Dinopoulos, and E. Tsiridis, "Bone substitutes: an update," *Injury*, vol. 36, no. 3, pp. S20-S27, 2005.

- [9] J. A. Goulet, L. E. Senunas, G. L. DeSilva, and M. L. V. Greenfield, "Autogenous iliac crest bone graft: complications and functional assessment," *Clinical Orthopaedics and Related Research*®, vol. 339, pp. 76-81, 1997.
- [10] E. D. Arrington, W. J. Smith, H. G. Chambers, A. L. Bucknell, and N. A. Davino, "Complications of iliac crest bone graft harvesting," *Clinical Orthopaedics and Related Research*®, vol. 329, pp. 300-309, 1996.
- [11] S. Froum, S. C. Cho, E. Rosenberg, M. Rohrer, and D. Tarnow, "Histological comparison of healing extraction sockets implanted with bioactive glass or demineralized freeze-dried bone allograft: A pilot study," *Journal of periodontology*, vol. 73, no. 1, pp. 94-102, 2002.
- [12] A. Barone, N. N. Aldini, M. Fini, R. Giardino, J. L. Calvo Guirado, and U. Covani, "Xenograft versus extraction alone for ridge preservation after tooth removal: a clinical and histomorphometric study," *Journal of periodontology*, vol. 79, no. 8, pp. 1370-1377, 2008.
- [13] Y. Deng and J. Kuiper, "Functional 3D tissue engineering scaffolds: materials, technologies, and applications," 2017.
- [14] T. M. Keaveny, E. F. Morgan, G. L. Niebur, and O. C. Yeh, "Biomechanics of trabecular bone," *Annual review of biomedical engineering*, vol. 3, no. 1, pp. 307-333, 2001.
- [15] V. Karageorgiou and D. Kaplan, "Porosity of 3D biomaterial scaffolds and osteogenesis," *Biomaterials*, vol. 26, no. 27, pp. 5474-5491, 2005.

- [16] D. Cooper, J. Matyas, M. Katzenberg, and B. Hallgrímsson, "Comparison of microcomputed tomographic and microradiographic measurements of cortical bone porosity," *Calcified tissue international*, vol. 74, no. 5, pp. 437-447, 2004.
- [17] Y. Kuboki *et al.*, "BMP-induced osteogenesis on the surface of hydroxyapatite with geometrically feasible and nonfeasible structures: topology of osteogenesis," *Journal of Biomedical Materials Research: An Official Journal of The Society for Biomaterials, The Japanese Society for Biomaterials, and the Australian Society for Biomaterials*, vol. 39, no. 2, pp. 190-199, 1998.
- [18] A. I. Itälä, H. O. Ylänen, C. Ekholm, K. H. Karlsson, and H. T. Aro, "Pore diameter of more than 100 μm is not requisite for bone ingrowth in rabbits," *Journal of Biomedical Materials Research: An Official Journal of The Society for Biomaterials, The Japanese Society for Biomaterials, and The Australian Society for Biomaterials and the Korean Society for Biomaterials*, vol. 58, no. 6, pp. 679-683, 2001.
- [19] S. Hulbert, F. Young, R. Mathews, J. Klawitter, C. Talbert, and F. Stelling, "Potential of ceramic materials as permanently implantable skeletal prostheses," *Journal of biomedical materials research*, vol. 4, no. 3, pp. 433-456, 1970.
- [20] A. R. Amini, C. T. Laurencin, and S. P. Nukavarapu, "Bone tissue engineering: recent advances and challenges," *Critical Reviews™ in Biomedical Engineering*, vol. 40, no. 5, 2012.
- [21] H. L. Holtorf, N. Datta, J. A. Jansen, and A. G. Mikos, "Scaffold mesh size affects the osteoblastic differentiation of seeded marrow stromal cells cultured in a flow perfusion bioreactor," *Journal of Biomedical Materials Research Part A: An*

- Official Journal of The Society for Biomaterials, The Japanese Society for Biomaterials, and The Australian Society for Biomaterials and the Korean Society for Biomaterials*, vol. 74, no. 2, pp. 171-180, 2005.
- [22] E. Volkmer *et al.*, "Hypoxia in static and dynamic 3D culture systems for tissue engineering of bone," *Tissue Engineering Part A*, vol. 14, no. 8, pp. 1331-1340, 2008.
- [23] M. Kruyt *et al.*, "Viable osteogenic cells are obligatory for tissue-engineered ectopic bone formation in goats," *Tissue Engineering*, vol. 9, no. 2, pp. 327-336, 2003.
- [24] J. Dong, H. Kojima, T. Uemura, M. Kikuchi, T. Tateishi, and J. Tanaka, "In vivo evaluation of a novel porous hydroxyapatite to sustain osteogenesis of transplanted bone marrow-derived osteoblastic cells," *Journal of Biomedical Materials Research: An Official Journal of The Society for Biomaterials, The Japanese Society for Biomaterials, and The Australian Society for Biomaterials and the Korean Society for Biomaterials*, vol. 57, no. 2, pp. 208-216, 2001.
- [25] E. Damien, K. Hing, S. Saeed, and P. A. Revell, "A preliminary study on the enhancement of the osteointegration of a novel synthetic hydroxyapatite scaffold in vivo," *Journal of Biomedical Materials Research Part A: An Official Journal of The Society for Biomaterials, The Japanese Society for Biomaterials, and The Australian Society for Biomaterials and the Korean Society for Biomaterials*, vol. 66, no. 2, pp. 241-246, 2003.
- [26] C. Zhang, J. Wang, H. Feng, B. Lu, Z. Song, and X. Zhang, "Replacement of segmental bone defects using porous bioceramic cylinders: A biomechanical and

- X-ray diffraction study," *Journal of Biomedical Materials Research: An Official Journal of The Society for Biomaterials and The Japanese Society for Biomaterials*, vol. 54, no. 3, pp. 407-411, 2001.
- [27] H. Yuan, J. D. de Bruijn, X. Zhang, C. A. van Blitterswijk, and K. de Groot, "Bone induction by porous glass ceramic made from Bioglass®(45S5)," *Journal of Biomedical Materials Research: An Official Journal of The Society for Biomaterials, The Japanese Society for Biomaterials, and The Australian Society for Biomaterials and the Korean Society for Biomaterials*, vol. 58, no. 3, pp. 270-276, 2001.
- [28] A. R. El-Ghannam, "Advanced bioceramic composite for bone tissue engineering: Design principles and structure–bioactivity relationship," *Journal of Biomedical Materials Research Part A: An Official Journal of The Society for Biomaterials, The Japanese Society for Biomaterials, and The Australian Society for Biomaterials and the Korean Society for Biomaterials*, vol. 69, no. 3, pp. 490-501, 2004.
- [29] H.-W. Kim, J. C. Knowles, and H.-E. Kim, "Hydroxyapatite/poly (ϵ -caprolactone) composite coatings on hydroxyapatite porous bone scaffold for drug delivery," *Biomaterials*, vol. 25, no. 7-8, pp. 1279-1287, 2004.
- [30] D. Lickorish, J. A. Ramshaw, J. A. Werkmeister, V. Glattauer, and C. R. Howlett, "Collagen–hydroxyapatite composite prepared by biomimetic process," *Journal of Biomedical Materials Research Part A: An Official Journal of The Society for Biomaterials, The Japanese Society for Biomaterials, and The Australian Society*

- for Biomaterials and the Korean Society for Biomaterials*, vol. 68, no. 1, pp. 19-27, 2004.
- [31] Z. M. Zhang Y, "Three-dimensional macroporous calcium phosphate bioceramics with nested chitosan sponges for loadbearing bone implants," *J Biomed Mater Res* vol. 61, no. 1, pp. 1-8, 2002.
- [32] Y. Y. Zhao F, Lu WW, Leong JC, Zhang W, Zhang J, et al. , "Preparation and histological evaluation of biomimetic three dimensional hydroxyapatite/chitosan-gelatin network composite scaffolds," *Biomaterials*, vol. 23, no. 15, pp. 3227-34, 2002.
- [33] W. M. Duan B., Zhou WY., Cheung WL., Li ZY., Lu WW. , "Three-dimensional nanocomposite scaffolds fabricated via selective laser sintering for bone tissue engineering," *Acta biomaterialia*, vol. 6, no. 12, pp. 4495-505, 2009.
- [34] A. G. Lee J.W., Kim D.S., Cho D-W. , "Development of nano-and microscale composite 3D scaffolds using PPF/DEF-HA and micro-stereolithography," *Microelectronic Engineering*, vol. 86, no. 4-6, pp. 1465-7, 2009.
- [35] H. D. W. Lam C.X., Schantz J.T., Woodruff M.A., Teoh S.H. , "Evaluation of polycaprolactone scaffold degradation for 6 months in vitro and in vivo. ," *Journal of Biomedical Materials Research Part A: An Official Journal of The Society for Biomaterials, The Japanese Society for Biomaterials, and The Australian Society for Biomaterials and the Korean Society for Biomaterials*, vol. 90, no. 3, pp. 906-19, 2009.
- [36] C. Shuai, J. Zhuang, H. Hu, S. Peng, D. Liu, and J. Liu, "In vitro bioactivity and degradability of β -tricalcium phosphate porous scaffold fabricated via selective

- laser sintering," *Biotechnology and applied biochemistry*, vol. 60, no. 2, pp. 266-273, 2013.
- [37] S. E. Russias J., Deville S., Gryn K., Liu G., Nalla R.K., et al. , "Fabrication and in vitro characterization of three-dimensional organic/inorganic scaffolds by robocasting," *Journal of Biomedical Materials Research Part A: An Official Journal of The Society for Biomaterials, The Japanese Society for Biomaterials, and The Australian Society for Biomaterials and the Korean Society for Biomaterials*, vol. 83, no. 2, pp. 434-45, 2007.
- [38] C. Zhou *et al.*, "Combination of fused deposition modeling and gas foaming technique to fabricated hierarchical macro/microporous polymer scaffolds," *Materials & Design*, vol. 109, pp. 415-424, 2016.
- [39] J. Park *et al.*, "Fabrication and characterization of 3D-printed bone-like β -tricalcium phosphate/polycaprolactone scaffolds for dental tissue engineering," *Journal of industrial and engineering chemistry*, vol. 46, pp. 175-181, 2017.
- [40] M. Z. Moghadam, S. Hassanajili, F. Esmaeilzadeh, M. Ayatollahi, and M. Ahmadi, "Formation of porous HPCL/LPCL/HA scaffolds with supercritical CO₂ gas foaming method," *Journal of the mechanical behavior of biomedical materials*, vol. 69, pp. 115-127, 2017.
- [41] L. Yang *et al.*, "Investigation on the orientation dependence of elastic response in Gyroid cellular structures," *Journal of the mechanical behavior of biomedical materials*, vol. 90, pp. 73-85, 2019.
- [42] E. Nyberg, A. Rindone, A. Dorafshar, and W. L. Grayson, "Comparison of 3D-printed poly- ϵ -caprolactone scaffolds functionalized with tricalcium phosphate,

- hydroxyapatite, bio-oss, or decellularized bone matrix," *Tissue Engineering Part A*, vol. 23, no. 11-12, pp. 503-514, 2017.
- [43] H. Doyle, S. Lohfeld, and P. McHugh, "Evaluating the effect of increasing ceramic content on the mechanical properties, material microstructure and degradation of selective laser sintered polycaprolactone/ β -tricalcium phosphate materials," *Medical engineering & physics*, vol. 37, no. 8, pp. 767-776, 2015.
- [44] O. Guillaume *et al.*, "Surface-enrichment with hydroxyapatite nanoparticles in stereolithography-fabricated composite polymer scaffolds promotes bone repair," *Acta biomaterialia*, vol. 54, pp. 386-398, 2017.
- [45] M. Chen, D. Q. Le, J. Kjems, C. Bünger, and H. Lysdahl, "Improvement of distribution and osteogenic differentiation of human mesenchymal stem cells by hyaluronic acid and β -tricalcium phosphate-coated polymeric scaffold in vitro," *BioResearch open access*, vol. 4, no. 1, pp. 363-373, 2015.
- [46] A. Grémare *et al.*, "Characterization of printed PLA scaffolds for bone tissue engineering," *Journal of Biomedical Materials Research Part A*, vol. 106, no. 4, pp. 887-894, 2018.
- [47] M. Arastouei, M. Khodaei, S. M. Atyabi, and M. J. Nodoushan, "The in-vitro biological properties of 3D printed poly lactic acid/akermanite composite porous scaffold for bone tissue engineering," *Materials Today Communications*, p. 102176, 2021.
- [48] B. Zhang *et al.*, "3D printed bone tissue regenerative PLA/HA scaffolds with comprehensive performance optimizations," *Materials & Design*, vol. 201, p. 109490, 2021.

- [49] P. Lichte, H. Pape, T. Pufe, P. Kobbe, and H. Fischer, "Scaffolds for bone healing: concepts, materials and evidence," *Injury*, vol. 42, no. 6, pp. 569-573, 2011.
- [50] D. W. Hutmacher, "Scaffolds in tissue engineering bone and cartilage," *Biomaterials*, vol. 21, no. 24, pp. 2529-2543, 2000.
- [51] G. Turnbull *et al.*, "3D bioactive composite scaffolds for bone tissue engineering," *Bioactive materials*, vol. 3, no. 3, pp. 278-314, 2018.
- [52] C. M. Agrawal and R. B. Ray, "Biodegradable polymeric scaffolds for musculoskeletal tissue engineering," *Journal of Biomedical Materials Research: An Official Journal of The Society for Biomaterials, The Japanese Society for Biomaterials, and The Australian Society for Biomaterials and the Korean Society for Biomaterials*, vol. 55, no. 2, pp. 141-150, 2001.
- [53] M. A. Velasco, C. A. Narváez-Tovar, and D. A. Garzón-Alvarado, "Design, materials, and mechanobiology of biodegradable scaffolds for bone tissue engineering," *BioMed research international*, vol. 2015, 2015.
- [54] S. Bose, M. Roy, and A. Bandyopadhyay, "Recent advances in bone tissue engineering scaffolds," *Trends in biotechnology*, vol. 30, no. 10, pp. 546-554, 2012.
- [55] L. Cristofolini, "A critical analysis of stress shielding evaluation of hip prostheses," *Critical Reviews™ in Biomedical Engineering*, vol. 25, no. 4-5, 1997.
- [56] K. Y. Lee, K. H. Bouhadir, and D. J. Mooney, "Degradation behavior of covalently cross-linked poly (aldehyde guluronate) hydrogels," *Macromolecules*, vol. 33, no. 1, pp. 97-101, 2000.
- [57] D. L. Butler, S. A. Goldstein, and F. Guilak, "Functional tissue engineering: the role of biomechanics," *J. Biomech. Eng.*, vol. 122, no. 6, pp. 570-575, 2000.

- [58] F. J. O'brien, "Biomaterials & scaffolds for tissue engineering," *Materials today*, vol. 14, no. 3, pp. 88-95, 2011.
- [59] D. P. Pioletti, "Biomechanics in bone tissue engineering," *Computer methods in biomechanics and biomedical engineering*, vol. 13, no. 6, pp. 837-846, 2010.
- [60] Y. H. An and R. A. Draughn, *Mechanical testing of bone and the bone-implant interface*. CRC press, 1999.
- [61] E. D. Sedlin and C. Hirsch, "Factors affecting the determination of the physical properties of femoral cortical bone," *Acta Orthopaedica Scandinavica*, vol. 37, no. 1, pp. 29-48, 1966.
- [62] A. Rohlmann, H. Zilch, G. Bergmann, and R. Kolbel, "Material properties of femoral cancellous bone in axial loading," *Archives of orthopaedic and traumatic surgery*, vol. 97, no. 2, pp. 95-102, 1980.
- [63] F. Linde and I. Hvid, "The effect of constraint on the mechanical behaviour of trabecular bone specimens," *Journal of Biomechanics*, vol. 22, no. 5, pp. 485-490, 1989.
- [64] N. Yaragatti and A. Patnaik, "A review on additive manufacturing of polymers composites," *Materials Today: Proceedings*, 2020.
- [65] S. C. Daminabo, S. Goel, S. A. Grammatikos, H. Nezhad, and V. K. Thakur, "Fused deposition modeling-based additive manufacturing (3D printing): Techniques for polymer material systems," *Materials today chemistry*, vol. 16, p. 100248, 2020.
- [66] U. Scheithauer, A. Bergner, E. Schwarzer, H.-J. Richter, and T. Moritz, "Studies on thermoplastic 3D printing of steel–zirconia composites," *Journal of materials research*, vol. 29, no. 17, pp. 1931-1940, 2014.

- [67] T. D. Ngo, A. Kashani, G. Imbalzano, K. T. Nguyen, and D. Hui, "Additive manufacturing (3D printing): A review of materials, methods, applications and challenges," *Composites Part B: Engineering*, vol. 143, pp. 172-196, 2018.
- [68] J. R. C. Dizon, A. H. Espera Jr, Q. Chen, and R. C. Advincula, "Mechanical characterization of 3D-printed polymers," *Additive Manufacturing*, vol. 20, pp. 44-67, 2018.
- [69] S. A. Tofail, E. P. Koumoulos, A. Bandyopadhyay, S. Bose, L. O'Donoghue, and C. Charitidis, "Additive manufacturing: scientific and technological challenges, market uptake and opportunities," *Materials today*, vol. 21, no. 1, pp. 22-37, 2018.
- [70] S. C. Ligon, R. Liska, J. Stampfl, M. Gurr, and R. Mülhaupt, "Polymers for 3D printing and customized additive manufacturing," *Chemical reviews*, vol. 117, no. 15, pp. 10212-10290, 2017.
- [71] J. Liu, L. Sun, W. Xu, Q. Wang, S. Yu, and J. Sun, "Current advances and future perspectives of 3D printing natural-derived biopolymers," *Carbohydrate polymers*, vol. 207, pp. 297-316, 2019.
- [72] R. Matsuzaki *et al.*, "Three-dimensional printing of continuous-fiber composites by in-nozzle impregnation," *Scientific reports*, vol. 6, no. 1, pp. 1-7, 2016.
- [73] R. A. Buswell, W. L. De Silva, S. Z. Jones, and J. Dirrenberger, "3D printing using concrete extrusion: A roadmap for research," *Cement and Concrete Research*, vol. 112, pp. 37-49, 2018.
- [74] A. Le Duigou, A. Barbé, E. Guillou, and M. Castro, "3D printing of continuous flax fibre reinforced biocomposites for structural applications," *Materials & Design*, vol. 180, p. 107884, 2019.

- [75] L. Serex, A. Bertsch, and P. Renaud, "Microfluidics: A new layer of control for extrusion-based 3D printing," *Micromachines*, vol. 9, no. 2, p. 86, 2018.
- [76] X. Wang, M. Jiang, Z. Zhou, J. Gou, and D. Hui, "3D printing of polymer matrix composites: A review and prospective," *Composites Part B: Engineering*, vol. 110, pp. 442-458, 2017.
- [77] A. International, "ISO/ASTM52900-15 Standard Terminology for Additive Manufacturing – General Principles – Terminology," 2015.
- [78] S. F. S. Shirazi *et al.*, "A review on powder-based additive manufacturing for tissue engineering: selective laser sintering and inkjet 3D printing," *Science and technology of advanced materials*, 2015.
- [79] E. O. Olakanmi, R. Cochrane, and K. Dalgarno, "A review on selective laser sintering/melting (SLS/SLM) of aluminium alloy powders: Processing, microstructure, and properties," *Progress in Materials Science*, vol. 74, pp. 401-477, 2015.
- [80] F.-H. Liu, R.-T. Lee, W.-H. Lin, and Y.-S. Liao, "Selective laser sintering of bio-metal scaffold," *Procedia Cirp*, vol. 5, pp. 83-87, 2013.
- [81] O. Alageel, M. N. Abdallah, A. Alsheghri, J. Song, E. Caron, and F. Tamimi, "Removable partial denture alloys processed by laser-sintering technique," *Journal of Biomedical Materials Research Part B: Applied Biomaterials*, vol. 106, no. 3, pp. 1174-1185, 2018.
- [82] M. N. Cooke, J. P. Fisher, D. Dean, C. Rinnac, and A. G. Mikos, "Use of stereolithography to manufacture critical-sized 3D biodegradable scaffolds for bone ingrowth," *Journal of Biomedical Materials Research Part B: Applied*

- Biomaterials: An Official Journal of The Society for Biomaterials, The Japanese Society for Biomaterials, and The Australian Society for Biomaterials and the Korean Society for Biomaterials*, vol. 64, no. 2, pp. 65-69, 2003.
- [83] Z. Zguris, "How mechanical properties of stereolithography 3D prints are affected by UV curing," *Formlabs Inc., Somerville, MA, USA*, 2016.
- [84] K. C. Hribar, P. Soman, J. Warner, P. Chung, and S. Chen, "Light-assisted direct-write of 3D functional biomaterials," *Lab on a chip*, vol. 14, no. 2, pp. 268-275, 2014.
- [85] C. Zhou, Y. Chen, Z. Yang, and B. Khoshnevis, "Development of multi-material mask-image-projection-based stereolithography for the fabrication of digital materials," in *Annual solid freeform fabrication symposium*, 2011, vol. 3.
- [86] P. K. Penumakala, J. Santo, and A. Thomas, "A critical review on the fused deposition modeling of thermoplastic polymer composites," *Composites Part B: Engineering*, p. 108336, 2020.
- [87] W. Gao *et al.*, "The status, challenges, and future of additive manufacturing in engineering," *Computer-Aided Design*, vol. 69, pp. 65-89, 2015.
- [88] J. U. Pucci, B. R. Christophe, J. A. Sisti, and E. S. Connolly Jr, "Three-dimensional printing: technologies, applications, and limitations in neurosurgery," *Biotechnology Advances*, vol. 35, no. 5, pp. 521-529, 2017.
- [89] S. M. Ahmadi *et al.*, "Additively manufactured open-cell porous biomaterials made from six different space-filling unit cells: The mechanical and morphological properties," *Materials*, vol. 8, no. 4, pp. 1871-1896, 2015.

- [90] P. Karimipour-Fard, A. H. Behraves, H. Jones-Taggart, R. Pop-Iliev, and G. Rizvi, "Effects of design, porosity and biodegradation on mechanical and morphological properties of additive-manufactured triply periodic minimal surface scaffolds," *Journal of the Mechanical Behavior of Biomedical Materials*, vol. 112, p. 104064, 2020.
- [91] W. Zhang *et al.*, "Interfacial bonding strength of short carbon fiber/acrylonitrile-butadiene-styrene composites fabricated by fused deposition modeling," *Composites Part B: Engineering*, vol. 137, pp. 51-59, 2018.
- [92] E. Pei, A. Lanzotti, M. Grasso, G. Staiano, and M. Martorelli, "The impact of process parameters on mechanical properties of parts fabricated in PLA with an open-source 3-D printer," *Rapid Prototyping Journal*, 2015.
- [93] S. T. Bendtsen, S. P. Quinnell, and M. Wei, "Development of a novel alginate-polyvinyl alcohol-hydroxyapatite hydrogel for 3D bioprinting bone tissue engineered scaffolds," *Journal of Biomedical Materials Research Part A*, vol. 105, no. 5, pp. 1457-1468, 2017.
- [94] Y. Jia, H. He, X. Peng, S. Meng, J. Chen, and Y. Geng, "Preparation of a new filament based on polyamide-6 for three-dimensional printing," *Polymer Engineering & Science*, vol. 57, no. 12, pp. 1322-1328, 2017.
- [95] S. Masood and W. Song, "Thermal characteristics of a new metal/polymer material for FDM rapid prototyping process," *Assembly Automation*, 2005.
- [96] A. R. T. Perez, D. A. Roberson, and R. B. Wicker, "Fracture surface analysis of 3D-printed tensile specimens of novel ABS-based materials," *Journal of Failure Analysis and Prevention*, vol. 14, no. 3, pp. 343-353, 2014.

- [97] J. Bustillos, D. Montero, P. Nautiyal, A. Loganathan, B. Boesl, and A. Agarwal, "Integration of graphene in poly (lactic) acid by 3D printing to develop creep and wear-resistant hierarchical nanocomposites," *Polymer composites*, vol. 39, no. 11, pp. 3877-3888, 2018.
- [98] P. Olesik, M. Godzierz, and M. Koziół, "Preliminary characterization of novel LDPE-based wear-resistant composite suitable for FDM 3D printing," *Materials*, vol. 12, no. 16, p. 2520, 2019.
- [99] J. F. Christ, N. Aliheidari, A. Ameli, and P. Pötschke, "3D printed highly elastic strain sensors of multiwalled carbon nanotube/thermoplastic polyurethane nanocomposites," *Materials & Design*, vol. 131, pp. 394-401, 2017.
- [100] M. Á. Caminero, J. M. Chacón, E. García-Plaza, P. J. Núñez, J. M. Reverte, and J. P. Becar, "Additive manufacturing of PLA-based composites using fused filament fabrication: Effect of graphene nanoplatelet reinforcement on mechanical properties, dimensional accuracy and texture," *Polymers*, vol. 11, no. 5, p. 799, 2019.
- [101] F. Alam, K. Varadarajan, and S. Kumar, "3D printed polylactic acid nanocomposite scaffolds for tissue engineering applications," *Polymer Testing*, vol. 81, p. 106203, 2020.
- [102] L. Lin, N. Ecke, M. Huang, X.-Q. Pei, and A. K. Schlarb, "Impact of nanosilica on the friction and wear of a PEEK/CF composite coating manufactured by fused deposition modeling (FDM)," *Composites Part B: Engineering*, vol. 177, p. 107428, 2019.

- [103] S. Dul, L. Fambri, and A. Pegoretti, "Fused deposition modelling with ABS–graphene nanocomposites," *Composites Part A: Applied Science and Manufacturing*, vol. 85, pp. 181-191, 2016.
- [104] I. Zein, D. W. Hutmacher, K. C. Tan, and S. H. Teoh, "Fused deposition modeling of novel scaffold architectures for tissue engineering applications," *Biomaterials*, vol. 23, no. 4, pp. 1169-1185, 2002.
- [105] S. J. Kalita, S. Bose, H. L. Hosick, and A. Bandyopadhyay, "Development of controlled porosity polymer-ceramic composite scaffolds via fused deposition modeling," *Materials Science and Engineering: C*, vol. 23, no. 5, pp. 611-620, 2003.
- [106] J. Kim *et al.*, "Rapid-prototyped PLGA/ β -TCP/hydroxyapatite nanocomposite scaffolds in a rabbit femoral defect model," *Biofabrication*, vol. 4, no. 2, p. 025003, 2012.
- [107] J. Zhang *et al.*, "3D-printed magnetic Fe₃O₄/MBG/PCL composite scaffolds with multifunctionality of bone regeneration, local anticancer drug delivery and hyperthermia," *Journal of Materials Chemistry B*, vol. 2, no. 43, pp. 7583-7595, 2014.
- [108] N. M. Ergul *et al.*, "3D printing of chitosan/poly (vinyl alcohol) hydrogel containing synthesized hydroxyapatite scaffolds for hard-tissue engineering," *Polymer Testing*, vol. 79, p. 106006, 2019.
- [109] A. Gloria *et al.*, "The influence of poly (ester amide) on the structural and functional features of 3D additive manufactured poly (ϵ -caprolactone) scaffolds," *Materials Science and Engineering: C*, vol. 98, pp. 994-1004, 2019.

- [110] L. Ambrosio, *Biomedical composites*. Woodhead Publishing, 2017.
- [111] M. A. Woodruff and D. W. Hutmacher, "The return of a forgotten polymer— Polycaprolactone in the 21st century," *Progress in polymer science*, vol. 35, no. 10, pp. 1217-1256, 2010.
- [112] D. Tadic, F. Beckmann, T. Donath, and M. Epple, "Comparison of different methods for the preparation of porous bone substitution materials and structural investigations by synchrotron μ -computer tomography," *Materialwissenschaft und Werkstofftechnik: Entwicklung, Fertigung, Prüfung, Eigenschaften und Anwendungen technischer Werkstoffe*, vol. 35, no. 4, pp. 240-244, 2004.
- [113] S. Stratton, N. B. Shelke, K. Hoshino, S. Rudraiah, and S. G. Kumbar, "Bioactive polymeric scaffolds for tissue engineering," *Bioactive materials*, vol. 1, no. 2, pp. 93-108, 2016.
- [114] S. Yin, W. Zhang, Z. Zhang, and X. Jiang, "Recent advances in scaffold design and material for vascularized tissue-engineered bone regeneration," *Advanced healthcare materials*, vol. 8, no. 10, p. 1801433, 2019.
- [115] A. R. Sarasam, R. K. Krishnaswamy, and S. V. Madihally, "Blending chitosan with polycaprolactone: effects on physicochemical and antibacterial properties," *Biomacromolecules*, vol. 7, no. 4, pp. 1131-1138, 2006.
- [116] C. Bastioli, A. Cerutti, I. Guanella, G. Romano, and M. Tosin, "Physical state and biodegradation behavior of starch-polycaprolactone systems," *Journal of environmental polymer degradation*, vol. 3, no. 2, pp. 81-95, 1995.
- [117] Y. Zhu, C. Gao, X. Liu, and J. Shen, "Surface modification of polycaprolactone membrane via aminolysis and biomacromolecule immobilization for promoting

- cytocompatibility of human endothelial cells," *Biomacromolecules*, vol. 3, no. 6, pp. 1312-1319, 2002.
- [118] M. G. Cascone, N. Barbani, C. C. P. Giusti, G. Ciardelli, and L. Lazzeri, "Bioartificial polymeric materials based on polysaccharides," *Journal of Biomaterials Science, Polymer Edition*, vol. 12, no. 3, pp. 267-281, 2001.
- [119] E. Khor and L. Y. Lim, "Implantable applications of chitin and chitosan," *Biomaterials*, vol. 24, no. 13, pp. 2339-2349, 2003.
- [120] P. M. Visakh and S. Thomas, "Preparation of bionanomaterials and their polymer nanocomposites from waste and biomass," *Waste and Biomass Valorization*, vol. 1, no. 1, pp. 121-134, 2010.
- [121] I. Aranaz *et al.*, "Functional characterization of chitin and chitosan," *Current chemical biology*, vol. 3, no. 2, pp. 203-230, 2009.
- [122] M. Ofem, A. Anyandi, and E. Ene, "Properties of chitin reinforces composites: a review," *Nigerian Journal of Technology*, vol. 36, no. 1, pp. 57-71, 2017.
- [123] J. Li, J. F. Revol, and R. Marchessault, "Effect of degree of deacetylation of chitin on the properties of chitin crystallites," *Journal of Applied Polymer Science*, vol. 65, no. 2, pp. 373-380, 1997.
- [124] M. A. Anwer, J. Wang, A. Q. Guan, and H. E. Naguib, "Chitin nano-whiskers (CNWs) as a bio-based bio-degradable reinforcement for epoxy: Evaluation of the impact of CNWs on the morphological, fracture, mechanical, dynamic mechanical, and thermal characteristics of DGEBA epoxy resin," *RSC advances*, vol. 9, no. 20, pp. 11063-11076, 2019.

- [125] L. Feng, Z. Zhou, A. Dufresne, J. Huang, M. Wei, and L. An, "Structure and properties of new thermoforming bionanocomposites based on chitin whisker-graft-polycaprolactone," *Journal of Applied Polymer Science*, vol. 112, no. 5, pp. 2830-2837, 2009.
- [126] A. Morin and A. Dufresne, "Nanocomposites of chitin whiskers from *Riftia* tubes and poly (caprolactone)," *Macromolecules*, vol. 35, no. 6, pp. 2190-2199, 2002.
- [127] Q. Wang, S. Chen, and D. Chen, "Preparation and characterization of chitosan based injectable hydrogels enhanced by chitin nano-whiskers," *Journal of the mechanical behavior of biomedical materials*, vol. 65, pp. 466-477, 2017.
- [128] M. Nikpour, S. Rabiee, and M. Jahanshahi, "Synthesis and characterization of hydroxyapatite/chitosan nanocomposite materials for medical engineering applications," *Composites Part B: Engineering*, vol. 43, no. 4, pp. 1881-1886, 2012.
- [129] L. L. Hench, "Bioceramics: from concept to clinic," *Journal of the american ceramic society*, vol. 74, no. 7, pp. 1487-1510, 1991.
- [130] M. Wang, R. Joseph, and W. Bonfield, "Hydroxyapatite-polyethylene composites for bone substitution: effects of ceramic particle size and morphology," *Biomaterials*, vol. 19, no. 24, pp. 2357-2366, 1998.
- [131] M. Huang, J. Feng, J. Wang, X. Zhang, Y. Li, and Y. Yan, "Synthesis and characterization of nano-HA/PA66 composites," *Journal of Materials Science: Materials in Medicine*, vol. 14, no. 7, pp. 655-660, 2003.
- [132] E. Ural, K. Kesenci, L. Fambri, C. Migliaresi, and E. Piskin, "Poly (D, L-lactide/ ϵ -caprolactone)/hydroxyapatite composites," *Biomaterials*, vol. 21, no. 21, pp. 2147-2154, 2000.

- [133] S. Zhang, F. Cui, S. Liao, Y. Zhu, and L. Han, "Synthesis and biocompatibility of porous nano-hydroxyapatite/collagen/alginate composite," *Journal of Materials Science: Materials in Medicine*, vol. 14, no. 7, pp. 641-645, 2003.
- [134] X. Xiao, R. Liu, Q. Huang, and X. Ding, "Preparation and characterization of hydroxyapatite/polycaprolactone–chitosan composites," *Journal of Materials Science: Materials in Medicine*, vol. 20, no. 12, p. 2375, 2009.
- [135] S. E. El-Habashy, H. M. Eltahir, A. Gaballah, E. I. Zaki, R. A. Mehanna, and A. H. El-Kamel, "Hybrid bioactive hydroxyapatite/polycaprolactone nanoparticles for enhanced osteogenesis," *Materials Science and Engineering: C*, vol. 119, p. 111599, 2021.
- [136] V. Trakoolwannachai, P. Kheolamai, and S. Ummartyotin, "Characterization of hydroxyapatite from eggshell waste and polycaprolactone (PCL) composite for scaffold material," *Composites Part B: Engineering*, vol. 173, p. 106974, 2019.
- [137] D. Ali and S. Sen, "Finite element analysis of mechanical behavior, permeability and fluid induced wall shear stress of high porosity scaffolds with gyroid and lattice-based architectures," *Journal of the mechanical behavior of biomedical materials*, vol. 75, pp. 262-270, 2017.
- [138] S. Limmahakhun, A. Oloyede, K. Sitthiseripratip, Y. Xiao, and C. Yan, "3D-printed cellular structures for bone biomimetic implants," *Additive Manufacturing*, vol. 15, pp. 93-101, 2017.
- [139] J. An, J. E. M. Teoh, R. Suntornnond, and C. K. Chua, "Design and 3D printing of scaffolds and tissues," *Engineering*, vol. 1, no. 2, pp. 261-268, 2015.

- [140] D. W. Hutmacher, J. T. Schantz, C. X. F. Lam, K. C. Tan, and T. C. Lim, "State of the art and future directions of scaffold-based bone engineering from a biomaterials perspective," *Journal of tissue engineering and regenerative medicine*, vol. 1, no. 4, pp. 245-260, 2007.
- [141] H. Zhu, J. Hobdell, and A. Windle, "Effects of cell irregularity on the elastic properties of open-cell foams," *Acta materialia*, vol. 48, no. 20, pp. 4893-4900, 2000.
- [142] H. Zhu *et al.*, "The effects of regularity on the geometrical properties of Voronoi tessellations," *Physica A: Statistical Mechanics and its Applications*, vol. 406, pp. 42-58, 2014.
- [143] Y. Deng and J. Kuiper, *Functional 3D tissue engineering scaffolds: materials, technologies, and applications*. Woodhead Publishing, 2017.
- [144] D. J. Yoo, "Porous scaffold design using the distance field and triply periodic minimal surface models," *Biomaterials*, vol. 32, no. 31, pp. 7741-7754, 2011.
- [145] P. J. Gandy, D. Cvijović, A. L. Mackay, and J. Klinowski, "Exact computation of the triply periodic D (diamond) minimal surface," *Chemical physics letters*, vol. 314, no. 5-6, pp. 543-551, 1999.
- [146] O. Al-Ketan and R. K. A. Al-Rub, "Multifunctional mechanical-metamaterials based on triply periodic minimal surface lattices: A review."
- [147] O. Al-Ketan and R. K. Abu Al-Rub, "Multifunctional mechanical metamaterials based on triply periodic minimal surface lattices," *Advanced Engineering Materials*, vol. 21, no. 10, p. 1900524, 2019.

- [148] Y. Lu, W. Zhao, Z. Cui, H. Zhu, and C. Wu, "The anisotropic elastic behavior of the widely-used triply-periodic minimal surface based scaffolds," *Journal of the mechanical behavior of biomedical materials*, vol. 99, pp. 56-65, 2019.
- [149] L. Hao, D. Raymont, C. Yan, A. Hussein, and P. Young, "Design and additive manufacturing of cellular lattice structures," in *The International Conference on Advanced Research in Virtual and Rapid Prototyping (VRAP)*. Taylor & Francis Group, Leiria, 2011, pp. 249-254.
- [150] P. Fucile *et al.*, "Reverse Engineering and Additive Manufacturing towards the design of 3D advanced scaffolds for hard tissue regeneration," in *2019 II Workshop on Metrology for Industry 4.0 and IoT (MetroInd4.0&IoT)*, 2019, pp. 33-37: IEEE.
- [151] S. Ma, Q. Tang, Q. Feng, J. Song, X. Han, and F. Guo, "Mechanical behaviours and mass transport properties of bone-mimicking scaffolds consisted of gyroid structures manufactured using selective laser melting," *Journal of the mechanical behavior of biomedical materials*, vol. 93, pp. 158-169, 2019.
- [152] B. Lozanovski *et al.*, "A Monte Carlo simulation-based approach to realistic modelling of additively manufactured lattice structures," *Additive Manufacturing*, vol. 32, p. 101092, 2020.
- [153] O. Al-Ketan, D.-W. Lee, R. Rowshan, and R. K. A. Al-Rub, "Functionally graded and multi-morphology sheet TPMS lattices: Design, manufacturing, and mechanical properties," *Journal of the Mechanical Behavior of Biomedical Materials*, vol. 102, p. 103520, 2020.

- [154] J. Shi, L. Zhu, L. Li, Z. Li, J. Yang, and X. Wang, "A TPMS-based method for modeling porous scaffolds for bionic bone tissue engineering," *Scientific reports*, vol. 8, no. 1, pp. 1-10, 2018.
- [155] M. Speirs, B. Van Hooreweder, J. Van Humbeeck, and J.-P. Kruth, "Fatigue behaviour of NiTi shape memory alloy scaffolds produced by SLM, a unit cell design comparison," *Journal of the mechanical behavior of biomedical materials*, vol. 70, pp. 53-59, 2017.
- [156] D. W. Abueidda, M. Elhebeary, C.-S. A. Shiang, S. Pang, R. K. A. Al-Rub, and I. M. Jasiuk, "Mechanical properties of 3D printed polymeric Gyroid cellular structures: Experimental and finite element study," *Materials & Design*, vol. 165, p. 107597, 2019.
- [157] P. Karimipour-Fard, R. Pop-Iliev, H. Jones-Taggart, and G. Rizvi, "Design of 3D scaffold geometries for optimal biodegradation of poly (lactic acid)-based bone tissue," in *AIP Conference Proceedings*, 2020, vol. 2205, no. 1, p. 020062: AIP Publishing LLC.
- [158] M. Wohlgenuth, N. Yufa, J. Hoffman, and E. L. Thomas, "Triply periodic bicontinuous cubic microdomain morphologies by symmetries," *Macromolecules*, vol. 34, no. 17, pp. 6083-6089, 2001.
- [159] H. Xie, S. Zhang, and S. Li, "Chitin and chitosan dissolved in ionic liquids as reversible sorbents of CO₂," *Green Chemistry*, vol. 8, no. 7, pp. 630-633, 2006.
- [160] R. Xiong, N. Hameed, and Q. Guo, "Cellulose/polycaprolactone blends regenerated from ionic liquid 1-butyl-3-methylimidazolium chloride," *Carbohydrate polymers*, vol. 90, no. 1, pp. 575-582, 2012.

- [161] X. Hu *et al.*, "Solubility and property of chitin in NaOH/urea aqueous solution," *Carbohydrate Polymers*, vol. 70, no. 4, pp. 451-458, 2007.
- [162] L. A. Blanchard and J. F. Brennecke, "Recovery of organic products from ionic liquids using supercritical carbon dioxide," *Industrial & engineering chemistry research*, vol. 40, no. 1, pp. 287-292, 2001.
- [163] H. Zhang, J. Wu, J. Zhang, and J. He, "1-Allyl-3-methylimidazolium chloride room temperature ionic liquid: a new and powerful nonderivatizing solvent for cellulose," *Macromolecules*, vol. 38, no. 20, pp. 8272-8277, 2005.
- [164] N. Hameed and Q. Guo, "Natural wool/cellulose acetate blends regenerated from the ionic liquid 1-butyl-3-methylimidazolium chloride," *Carbohydrate polymers*, vol. 78, no. 4, pp. 999-1004, 2009.
- [165] P. Karimipour-Fard, M. P. Jeffrey, H. J. Taggart, R. Pop-Iliev, and G. Rizvi, "Development, processing and characterization of Polycaprolactone/Nano-Hydroxyapatite/Chitin-Nano-Whisker nanocomposite filaments for additive manufacturing of bone tissue scaffolds," *Journal of the Mechanical Behavior of Biomedical Materials*, p. 104583, 2021.
- [166] T. S. Gaaz, A. B. Sulong, A. A. H. Kadhum, M. H. Nassir, and A. A. Al-Amiery, "Optimizing injection molding parameters of different halloysites type-reinforced thermoplastic polyurethane nanocomposites via Taguchi complemented with ANOVA," *Materials*, vol. 9, no. 11, p. 947, 2016.
- [167] T. S. Gaaz, A. B. Sulong, A. A. H. Kadhum, M. H. Nassir, and A. A. Al-Amiery, "Absolute variation of the mechanical characteristics of halloysite reinforced

- polyurethane nanocomposites complemented by Taguchi and ANOVA approaches," *Results in physics*, vol. 7, pp. 3287-3300, 2017.
- [168] T. S. Gaaz, A. B. Sulong, A. A. H. Kadhum, M. H. Nassir, and A. A. Al-Amiery, "Optimizing physio-mechanical properties of halloysite reinforced polyurethane nanocomposites by Taguchi approach," *Science of Advanced Materials*, vol. 9, no. 6, pp. 949-961, 2017.
- [169] H. Nosrati, R. Sarraf-Mamoory, D. Q. S. Le, and C. E. Bünger, "Enhanced fracture toughness of three dimensional graphene-hydroxyapatite nanocomposites by employing the Taguchi method," *Composites Part B: Engineering*, vol. 190, p. 107928, 2020.
- [170] K. Vasantharaj, M. Jerold, B. Deepanraj, M. Velan, and V. Sivasubramanian, "Assessment of a sulfidogenic system utilizing microalgal biomass of *Chlorella pyrenoidosa* as an electron donor: Taguchi based grey relational analysis," *International Journal of Hydrogen Energy*, vol. 42, no. 42, pp. 26545-26554, 2017.
- [171] B. Hartiti, S. Fadili, and P. Thevenin, "Nickel oxide optimization using Taguchi design for hydrogen detection," *International Journal of Hydrogen Energy*, vol. 43, no. 27, pp. 12574-12583, 2018.
- [172] P. D. Berger, R. E. Maurer, and G. B. Celli, "Introduction to Taguchi Methods," in *Experimental Design: With Application in Management, Engineering, and the Sciences*. Cham: Springer International Publishing, 2018, pp. 449-480.
- [173] K. A. Athanasiou, G. G. Niederauer, and C. M. Agrawal, "Sterilization, toxicity, biocompatibility and clinical applications of polylactic acid/polyglycolic acid copolymers," *Biomaterials*, vol. 17, no. 2, pp. 93-102, 1996.

- [174] C. Chu, "An in-vitro study of the effect of buffer on the degradation of poly (glycolic acid) sutures," *Journal of Biomedical Materials Research*, vol. 15, no. 1, pp. 19-27, 1981.
- [175] S. M. Li, H. Garreau, and M. Vert, "Structure-property relationships in the case of the degradation of massive aliphatic poly-(α -hydroxy acids) in aqueous media," *Journal of Materials Science: Materials in Medicine*, vol. 1, no. 3, pp. 123-130, 1990.
- [176] D. Gilding and A. Reed, "Biodegradable polymers for use in surgery— polyglycolic/poly (actic acid) homo-and copolymers: 1," *Polymer*, vol. 20, no. 12, pp. 1459-1464, 1979.
- [177] J. H. Zhu, Z. R. Shen, L. T. Wu, and S. L. Yang, "In vitro degradation of polylactide and poly (lactide-co-glycolide) microspheres," *Journal of applied polymer science*, vol. 43, no. 11, pp. 2099-2106, 1991.
- [178] T. G. Park, "Degradation of poly (lactic-co-glycolic acid) microspheres: effect of copolymer composition," *Biomaterials*, vol. 16, no. 15, pp. 1123-1130, 1995.
- [179] I. Grizzi, H. Garreau, S. Li, and M. Vert, "Hydrolytic degradation of devices based on poly (DL-lactic acid) size-dependence," *Biomaterials*, vol. 16, no. 4, pp. 305-311, 1995.
- [180] R. M. Ginde and R. K. Gupta, "In vitro chemical degradation of poly (glycolic acid) pellets and fibers," *Journal of Applied Polymer Science*, vol. 33, no. 7, pp. 2411-2429, 1987.
- [181] P. Törmälä, J. Vasenius, S. Vainionpää, J. Laiho, T. Pohjonen, and P. Rokkanen, "Ultra-high-strength absorbable self-reinforced polyglycolide (SR-PGA)

- composite rods for internal fixation of bone fractures: In vitro and in vivo study," *Journal of biomedical materials research*, vol. 25, no. 1, pp. 1-22, 1991.
- [182] S. Hurrell, G. E. Milroy, and R. E. Cameron, "The distribution of water in degrading polyglycolide. Part I: Sample size and drug release," *Journal of Materials Science: Materials in Medicine*, vol. 14, no. 5, pp. 457-464, 2003.
- [183] F. J. Buchanan, "Degradation rate of bioresorbable materials: prediction and evaluation," 2008.
- [184] J. Pan, "Modelling degradation of bioresorbable polymeric medical devices," 2014.
- [185] J. Siepmann and A. Göpferich, "Mathematical modeling of bioerodible, polymeric drug delivery systems," *Advanced drug delivery reviews*, vol. 48, no. 2-3, pp. 229-247, 2001.
- [186] K. Sevim and J. Pan, "A model for hydrolytic degradation and erosion of biodegradable polymers," *Acta biomaterialia*, vol. 66, pp. 192-199, 2018.
- [187] K. Zygorakis, "Development and temporal evolution of erosion fronts in bioerodible controlled release devices," *Chemical Engineering Science*, vol. 45, no. 8, pp. 2359-2366, 1990.
- [188] J. Siepmann, N. Faisant, and J.-P. Benoit, "A new mathematical model quantifying drug release from bioerodible microparticles using Monte Carlo simulations," *Pharmaceutical research*, vol. 19, no. 12, pp. 1885-1893, 2002.
- [189] Y. Chen, S. Zhou, and Q. Li, "Mathematical modeling of degradation for bulk-erosive polymers: applications in tissue engineering scaffolds and drug delivery systems," *Acta biomaterialia*, vol. 7, no. 3, pp. 1140-1149, 2011.

- [190] T. Zhang, S. Zhou, X. Gao, Z. Yang, L. Sun, and D. Zhang, "A multi-scale method for modeling degradation of bioresorbable polyesters," *Acta biomaterialia*, vol. 50, pp. 462-475, 2017.
- [191] A. Göpferich, "Polymer bulk erosion," *Macromolecules*, vol. 30, no. 9, pp. 2598-2604, 1997.
- [192] M. Husmann, S. Schenderlein, M. Lück, H. Lindner, and P. Kleinebudde, "Polymer erosion in PLGA microparticles produced by phase separation method," *International journal of pharmaceutics*, vol. 242, no. 1-2, pp. 277-280, 2002.
- [193] A. Gleadall, J. Pan, M.-A. Krufft, and M. Kellomäki, "Degradation mechanisms of bioresorbable polyesters. Part 1. Effects of random scission, end scission and autocatalysis," *Acta biomaterialia*, vol. 10, no. 5, pp. 2223-2232, 2014.
- [194] A. Gleadall, J. Pan, M.-A. Krufft, and M. Kellomäki, "Degradation mechanisms of bioresorbable polyesters. Part 2. Effects of initial molecular weight and residual monomer," *Acta biomaterialia*, vol. 10, no. 5, pp. 2233-2240, 2014.
- [195] Y. Wang, J. Pan, X. Han, C. Sinka, and L. Ding, "A phenomenological model for the degradation of biodegradable polymers," *Biomaterials*, vol. 29, no. 23, pp. 3393-3401, 2008.
- [196] X. Han and J. Pan, "A model for simultaneous crystallisation and biodegradation of biodegradable polymers," *Biomaterials*, vol. 30, no. 3, pp. 423-430, 2009.
- [197] F. Azimlu, S. Rahnamayan, M. Makrehchi, and P. Karimipour-Fard, "Designing Solar Chimney Power Plant Using Meta-modeling, Multi-objective Optimization, and Innovization," in *International Conference on Evolutionary Multi-Criterion Optimization*, 2019, pp. 731-742: Springer.

- [198] B. Can and C. Heavey, "A comparison of genetic programming and artificial neural networks in metamodeling of discrete-event simulation models," *Computers & Operations Research*, vol. 39, no. 2, pp. 424-436, 2012.
- [199] B. Can and C. Heavey, "Comparison of experimental designs for simulation-based symbolic regression of manufacturing systems," *Computers & Industrial Engineering*, vol. 61, no. 3, pp. 447-462, 2011.
- [200] W. Cai, A. Pacheco-Vega, M. Sen, and K.-T. Yang, "Heat transfer correlations by symbolic regression," *International Journal of Heat and Mass Transfer*, vol. 49, no. 23-24, pp. 4352-4359, 2006.
- [201] Y. Tian, R. Cheng, X. Zhang, and Y. Jin, "PlatEMO: A MATLAB platform for evolutionary multi-objective optimization [educational forum]," *IEEE Computational Intelligence Magazine*, vol. 12, no. 4, pp. 73-87, 2017.
- [202] K. Deb and H. Jain, "An evolutionary many-objective optimization algorithm using reference-point-based nondominated sorting approach, part I: solving problems with box constraints," *IEEE transactions on evolutionary computation*, vol. 18, no. 4, pp. 577-601, 2013.
- [203] H. Jain and K. Deb, "An evolutionary many-objective optimization algorithm using reference-point based nondominated sorting approach, part II: Handling constraints and extending to an adaptive approach," *IEEE Transactions on evolutionary computation*, vol. 18, no. 4, pp. 602-622, 2013.
- [204] G. C. Ciro, F. Dugardin, F. Yalaoui, and R. Kelly, "A NSGA-II and NSGA-III comparison for solving an open shop scheduling problem with resource constraints," *IFAC-PapersOnLine*, vol. 49, no. 12, pp. 1272-1277, 2016.

- [205] P. Karimipour-Fard, I. Naeem, A. Mohany, R. Pop-Iliev, and G. Rizvi, "Enhancing the accuracy and efficiency of characterizing polymeric cellular structures using 3D-based computed tomography," *Journal of Cellular Plastics*, p. 0021955X20948556, 2020.
- [206] P. Karimipour-Fard, W. Pao, G. Rizvi, and R. Pop-Iliev, "The use of microcomputed tomography to evaluate integral-skin cellular polyolefin composites," *Abstract Book; Unilever Res Dev Netherlands: Vlaardingen, The Netherlands*, 2018.
- [207] R. Pop-Iliev, W. Pao, P. Karimipour-Fard, and G. Rizvi, "Visualization and morphological characterization of integral skin cellular polymeric composites using X-ray microtomography," *Radiation and applications*, vol. 3, pp. 143-146.
- [208] P. Karimipour-Fard, W. Pao, R. Pop-Iliev, and G. Rizvi, "3D characterization and mechanical analysis of polyethylene foams processed in rapid rotational foam molding," presented at the Annual Technical Conference - ANTEC, Conference Proceedings, 2018.
- [209] D. ASTM, "1621–16. Standard test method for compressive properties of rigid cellular plastics," *ASTM, West Conshohocken, Pennsylvania, USA*, 2016.
- [210] A. International, *ASTM E1131 – 20, Standard test method for compositional analysis by thermogravimetry*. ASTM International, 2020.
- [211] D. Wang, K. Christensen, K. Chawla, G. Xiao, P. H. Krebsbach, and R. T. Franceschi, "Isolation and characterization of MC3T3-E1 preosteoblast subclones with distinct in vitro and in vivo differentiation/mineralization potential," *Journal of Bone and Mineral Research*, vol. 14, no. 6, pp. 893-903, 1999.

- [212] Y. Mao *et al.*, "RAGE-dependent mitochondria pathway: a novel target of silibinin against apoptosis of osteoblastic cells induced by advanced glycation end products," *Cell death & disease*, vol. 9, no. 6, pp. 1-14, 2018.
- [213] S. Faghihi, F. Azari, A. P. Zhilyaev, J. A. Szpunar, H. Vali, and M. Tabrizian, "Cellular and molecular interactions between MC3T3-E1 pre-osteoblasts and nanostructured titanium produced by high-pressure torsion," *Biomaterials*, vol. 28, no. 27, pp. 3887-3895, 2007.
- [214] K. Suh, E. Choi, S. Rhee, and Y. Kim, "Methylglyoxal induces oxidative stress and mitochondrial dysfunction in osteoblastic MC3T3-E1 cells," *Free Radical Research*, vol. 48, no. 2, pp. 206-217, 2014.
- [215] J.-W. Kim, K.-H. Shin, Y.-H. Koh, M. J. Hah, J. Moon, and H.-E. Kim, "Production of poly (ϵ -caprolactone)/hydroxyapatite composite scaffolds with a tailored macro/micro-porous structure, high mechanical properties, and excellent bioactivity," *Materials*, vol. 10, no. 10, p. 1123, 2017.
- [216] A. Chanda *et al.*, "Electrospun chitosan/polycaprolactone-hyaluronic acid bilayered scaffold for potential wound healing applications," *International journal of biological macromolecules*, vol. 116, pp. 774-785, 2018.
- [217] K. Shalumon, K. Anulekha, C. Girish, R. Prasanth, S. Nair, and R. Jayakumar, "Single step electrospinning of chitosan/poly (caprolactone) nanofibers using formic acid/acetone solvent mixture," *Carbohydrate Polymers*, vol. 80, no. 2, pp. 413-419, 2010.
- [218] K. Gómez-Lizárraga, C. Flores-Morales, M. Del Prado-Audelo, M. Álvarez-Pérez, M. Piña-Barba, and C. Escobedo, "Polycaprolactone-and

polycaprolactone/ceramic-based 3D-bioplotting porous scaffolds for bone regeneration: a comparative study," *Materials Science and Engineering: C*, vol. 79, pp. 326-335, 2017.

- [219] T. Lertwattanaseri, N. Ichikawa, T. Mizoguchi, Y. Tanaka, and S. Chirachanchai, "Microwave technique for efficient deacetylation of chitin nanowhiskers to a chitosan nanoscaffold," *Carbohydrate research*, vol. 344, no. 3, pp. 331-335, 2009.
- [220] F. Miyaji, Y. Kono, and Y. Suyama, "Formation and structure of zinc-substituted calcium hydroxyapatite," *Materials Research Bulletin*, vol. 40, no. 2, pp. 209-220, 2005.
- [221] A. G. Thombre and K. J. Himmelstein, "Modelling of drug release kinetics from a laminated device having an erodible drug reservoir," *Biomaterials*, vol. 5, no. 5, pp. 250-254, 1984.